INEEL/EXT-02-01411

Advanced Proliferation Resistant, Lower Cost, Uranium-Thorium Dioxide Fuels For Light Water Reactors

September 2002

Idaho National Engineering and Environmental Laboratory
Bechtel BWXT Idaho, LLC

INEEL/EXT-02-01411

Advanced Proliferation Resistant, Lower Cost, Uranium-Thorium Dioxide Fuels for Light Water Reactors

Nuclear Energy Research Initiative
Project 99-0153

Progress Report for Work through September, 2002

12th Quarterly Report and 3rd Annual Report

Principal Investigator: Philip E. MacDonald
Idaho National Engineering and Environmental Laboratory (INEEL)
P.O. Box 1625
Idaho Falls, Idaho 83415-3870
Telephone: 208-526-9634
Fax: 208-526-2930
e-mail: pem@inel.gov

Participating Organizations

Argonne National Laboratory- **Chemical Technology Division** Chicago, IL Dr. James C. Cunnane Telephone: 630 252 4064 e-mail: Cunnane@cmt.anl.gov Dr. James Jerden Telephone: 630-252-5246 Fax: 630-252-5246 e-mail: jerden@cmt.anl.gov	**University of Florida** Gainesville, FL Prof. James S. Tulenko Telephone: (352) 392-1401 fax: 352 392-3380 e-mail: tulenko@ufl.edu Prof. Ronald Baney Telephone: 352 392 5167 Fax: 352 392 6359 e-mail: rbane@mse.ufl.edu
Framatome ANP Lynchburg, VA Joe Sapyta Telephone: 804 832 2806 Fax :804 832 2932 e-mail: jsapyta@framatech.com Timothy Ake Telephone: 434-832-2985	**Idaho National Engineering and Environmental Laboratory (INEEL)** Idaho Falls, ID Dr. J. Stephen Herring e-mail: sth@inel.gov Dr. Kevan Weaver e-mail: weavkd@inel.gov Larry Siefken e-mail: ljs@inel.gov
Korea Atomic Energy Research Institute Taejon, Korea Chan Bock Lee Telephone: +82 42 868 2257 Fax: +82 42 863 0565 e-mail: cblee@kaeri.re.kr Hyung-Kook Joo e-mail: hkjoo@kaeri.re.kr Kun Woo Song kwsong@kaeri.re.kr Prof. Kwangheon Park e-mail: kpark@nms.kyunghee.ac.kr	**Massachusetts Institute of Technology (MIT)** **Department of Nuclear Engineering** Cambridge, MA Prof. Mujid S. Kazimi Telephone: 617 253-4219 fax: (617) 253-7300 kazimi@mit.edu Prof. Michael J. Driscoll Telephone: 617 253 4219 e-mail: mickeyd@mit.edu Dr. Pavel Hejzlar Telephone: 617 253 4231 e-mail: hejzlar@alum.mit.edu
Purdue University **School of Nuclear Engineering** West Lafayette, IN Prof. Alvin Solomon Telephone: 765 494-5753 fax: 765 494-9570 e-mail: solomon@ecn.prudue.edu	**Siemens Power Corporation** **Nuclear Division** Richland, WA Dr. Roger S. Reynolds Telephone: 509 375-8431 fax: 509 375-8943 e-mail: Roger_Reynolds@nfuel.com
Westinghouse Electric Corporation **Science & Technology Center** Pittsburgh, PA Dr. E. J. Lahoda Telephone: 412 256-2238 fax: 412 256-1222 e-mail: lahodaej@westinghouse.com	

Executive Summary

The overall objective of this NERI project is to evaluate the potential advantages and disadvantages of an optimized thorium-uranium dioxide (ThO_2/UO_2) fuel design for light water reactors (LWRs). The project is led by the Idaho National Engineering and Environmental Laboratory (INEEL), with the collaboration of three universities, the University of Florida, Massachusetts Institute of Technology (MIT), and Purdue University; Argonne National Laboratory; and all of the Pressurized Water Reactor (PWR) fuel vendors in the United States (Framatome, Siemens, and Westinghouse). In addition, a number of researchers at the Korean Atomic Energy Research Institute and Professor Kwangheon Park at Kyunghee University are active collaborators with Korean Ministry of Science and Technology funding. The project has been organized into five tasks:

- Task 1 consists of fuel cycle neutronics and economics analysis to determine the economic viability of various ThO_2/UO_2 fuel designs in PWRs,
- Task 2 will determine whether or not ThO_2/UO_2 fuel can be manufactured economically,
- Task 3 will evaluate the behavior of ThO_2/UO_2 fuel during normal, off-normal, and accident conditions and compare the results with the results of previous UO_2 fuel evaluations and U.S. Nuclear Regulatory Commission (NRC) licensing standards,
- Task 4 will determine the long-term stability of ThO_2/UO_2 high-level waste, and
- Task 5 consists of the Korean work on core design, fuel performance analysis, and xenon diffusivity measurements.

The remainder of this Executive summary is organized by task.

Task 1. Reactor Core Analysis and Fuel Cycle Design

Due to the relatively poor economic performance of the homogeneously mixed urania-thoria fuel, the focus of the physics work under Task 1 during Year 2 and the first part of Year 3 was primarily on the performance and economics of using micro-heterogeneous fuel forms, where some small distance physically separates the uranium and thorium. When compared to the equivalent homogeneous case (i.e., the same urania-thoria weight percentages), an increase in burnup is observed, which improves the economics of using thorium-based fuels. However, the economic improvement due to the use of any of the various micro-heterogeneous fuel forms is not sufficient to compensate for the costs of the increased Seperative Work Units (SWUs) required for thorium oxide fuels. Therefore, the work at Framatome, INEEL, and MIT during most of Year 3 has focused on use of thorium to burn unwanted reactor or weapons grade plutonium. The work at Framatome was completed in the third quarter of Year 3 and is fully reported in our 11th Quarterly Progress Report (MacDonald et al. 2002) and in a final report prepared by Famatome ANP (Sapyta et al. 2002). The INEEL portion of this executive summary covers all their work during Year 3 whereas the MIT section (for Task 1) summarizes all their work over all three years of this project.

INEEL. In this fuel cycle, the LWR fuel assembly mainly consists of standard UO_2 fuel rods with typical ^{235}U enrichment, along with a small fraction of thoria-urania fuel rods containing the plutonium and minor actinides produced in earlier cores. The goal of this mono-recycling strategy or "twice through fuel cycle" is to transmute the great majority of the long lived actinides in existing LWRs and to discharge a fuel form that is a very robust waste form and whose

isotopic content is very proliferation resistant. The incorporation of plutonium into a ThO_2 matrix results in the consumption of already-separated plutonium without breeding significant additional ^{239}Pu. The minor actinides (MA, i.e. neptunium, americium, curium, berkelium, californium, etc.) are also included in the ThO_2 to further reduce the overall long-term radiotoxicity of the fuel cycle. Our analyses have shown that thorium-based fuels can reduce the amount of Pu-239 needing further transmutation or going to a repository by about 90%. Also, thorium-based fuels produce a mixture of plutonium isotopes high in ^{238}Pu. Because of the high decay heat and spontaneous neutron generation of ^{238}Pu, the isotope provides intrinsic proliferation resistance.

In these analyses, we have modeled a case consisting of nine fuel pins, eight (89%) of which are standard UO_2 pins and one (11%) of which is a [Th-U-Pu-MA]O_2 transmuter pin in which the plutonium and minor actinides (neptunium, americium and curium) from UO_2 fuel reprocessed 30 years after discharge has been concentrated. MOCUP was used with 60-day time-steps and the generation and depletion of 50 fission products and 38 actinides. In the 9th Quarterly Report for this NERI project, we showed that this fuel array could be approximately plutonium-neutral at standard power levels and refueling cycles. In other words the [ThUPuMA]O_2 pins would consume about as much plutonium as was produced by the UO_2 pins.

In the 11th Quarterly Report we extended that analysis in two ways. First we included a greater number of thorium-based pins in the array and secondly, we looked specifically at the consumption of reactor grade plutonium, without the inclusion of the minor actinides. This analysis is preliminary in that we believe that the fuel can be taken to higher burnups in the present configuration. Furthermore, we have not optimized the hydrogen to heavy metal ratio for the particular combinations of thorium, uranium, and plutonium used in the fuel. Parametric studies of the hydrogen to heavy metal ratio were presented in the 10th Quarterly.

In the 12th quarter of the NERI project, we performed additional analyses of the one-transmuter-pin-in-nine fuel assembly design to optimize the neutronic design of the converter pin and carefully track the generation and consumption of the plutonium. We were able to again demonstrate that thorium-based fuels can reduce the amount of Pu-239 needing further transmutation or going to a repository by about 90%.

MIT. The work performed at MIT within Task 1 consisted of neutronic and thermal-hydraulic evaluations of micro-heterogeneous concepts of thoria-urania fuels and investigation of the potential of thoria-plutonia fuels for plutonium destruction in PWR lattices.

Micro-heterogeneous UO_2-ThO_2 concepts. The goal was to determine the potential of micro-heterogeneous fuel arrangements to achieve burnups higher than homogeneous thorium-uranium oxide mixtures and current UO_2 fuels. MIT focused on axial micro heterogeneity where pellets of UO_2 are sandwiched between ThO_2 or ThO_2-UO_2 pellets in a typical PWR fuel pin geometry and on checkerboard arrangements of UO_2 and ThO_2 pins. Typical reactivity limited batch burnup results are presented in the table below. In each case shown below, the thoria-urania fuel contained 35%UO_2 (enriched in U-235 to about 19.9%) and 65%ThO_2, the same amount of fissile material is initially invested and burnup stopped at a k-infinity of 1.03.

As shown in the table below, the homogeneous thoria-urania fuel is only able to reach about 90% of the burnup of the reference UO_2 core. Duplex fuel pellets with the ThO_2 on the outside provide about an 11% improvement in burnup over the homogeneous thoria-urania fuel option, but about the same burnup as the UO_2 fuel currently used in LWRs. This will not compensate for the higher enrichment costs of the thoria-urania fuel. However, denaturing of the thoria with

uranium to dilute the U-233 results in worse than all-uranium fuel burnup performance. This denaturing is necessary to achieve an acceptable power distribution to meet the thermal hydraulic constraints and to ensure that the end-of-life uranium composition will be below the non-proliferation limit.

Batch burnup available from various fuel types for the 35%UO_2 and 65%ThO_2 fuel.

Fuel Type	**Batch Burnup**	**Percent increase over Homogeneous ThO_2/UO_2 Fuel**	**Percent increase over All-UO_2 Base Case**
Duplex, ThO_2 inside	48.49	1	-10
Duplex, ThO_2 outside	53.57	11	-
Axial micro-heterogeneous, 2 cm of ThO_2 and 1 cm of UO_2	57.10	19	7
Axial micro-heterogeneous, 8.2 cm of ThO_2 and 4 cm of UO_2	60.48	25	13
Axial micro-heterogeneous, duplex –9.1 cm of ThO_2 with UO2 core and 4.0 cm of annular, graphite filled UO_2*	55.94	16	5
Axial micro-heterogeneous, 8.2 cm of ThO_2 and 5.0 cm of annular, voided UO_2	61.78	28	15
Radial micro-heterogeneous - ThO_2 and UO_2 pins in a 1x1 array (un-denatured)	57.32	19	7
Radial micro-heterogeneous - ThO_2 and UO_2 pins in a 1x1 array (denatured)	51.20	6	-5
Homogeneous ThO_2/UO_2 fuel	48.16	-	-10
All-UO_2 Reference Base Case	53.55	11	-

*Thorium section contains uranium central pellet region to denature bred-in U233

The axial micro-heterogeneous fuel, with pure ThO_2 segments (no denaturing of the thoria), increases the fuel discharge burnup by a significant amount over the UO_2 base case, about 13% to 15% for the cases analyzed. Note that there appears to be an improvement in reactivity and burnup when the length of the axial micro-heterogeneity is longer than a traditional pellet or when annular, graphite filled driver fuel is used, rather than solid UO_2 pellets. The analyses show that the optimum burnup performance for the axial micro-heterogeneous fuel is for the case of about 4cm-long UO_2 driver spaced apart with 9cm-long ThO_2 sections.

These gains are achieved due to a combination of spectral and mutual shielding effects. The spectral shift was identified as a key underlying phenomenon for the observed benefits and is also responsible for a "burnable poison-like effect". A local, highly thermalized spectrum in the ThO_2 section results in a high capture rate in the Th-232 at beginning-of-life, depressing reactivity. Thus, excess neutrons at beginning-of-life are used to breed U-233, which is available later during the cycle to fission thus increasing reactivity. Moreover, the harder spectrum at end-of-life reduces the conversion ratio (primarily due to less captures in the Th-232) thus increasing the reactivity. Separation of the thorium and uranium further improves the reactivity due to the reduction of the mutual resonance shielding of the overlapping resonances of the U-233 and U-238. However, the reduction in total resonance absorption in the U-233 shielded by the U-238 was found to be only about 2%. Therefore, the major benefits due to the spatial separation of the thorium and uranium come from the spectral effects; the effect of mutual shielding of resonances on reactivity and burnup performance is small.

The major challenge for the axial micro-heterogeneous arrangements is to meet the thermal hydraulic margins because of a large local power peaking in the UO_2 driver section. The power peaking problem is illustrated in the figure to the right, which is a plot of the normalized power along the fuel rod axis in the region of a UO_2-ThO_2 interface at beginning-of-cycle. Note that the power peaking for the un-denatured case is about a factor of 4.5 at the beginning of the fuel cycle; but it can be brought down to 2.4 when enriched UO_2 is added to thoria.

Normalized power density distribution at the UO2/ThO2 interface in axially micro-heterogeneous LWR fuel.

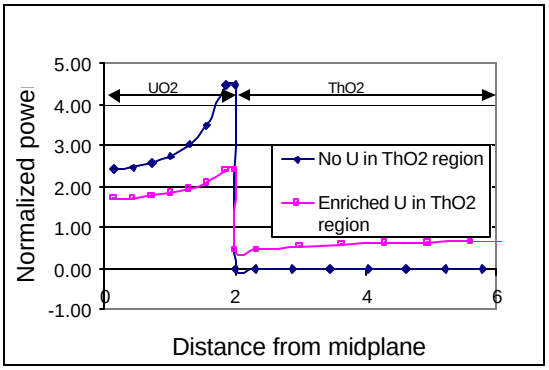

However, it has been found that homogeneously mixing uranium in the thorium section to reduce this power peaking in the axial heterogeneous fuel rods impairs the burnup performance; hence a duplex pellet configuration in place of the thoria section (UO_2 core surrounded by thoria annulus) was proposed and analyzed. Although this strategy results in significant reduction in the power peaking (as indicated in the figure by the curve "enriched U in ThO_2 region), the new design still exhibited significant local peaking (about a factor of 2.4). However, the DNBR performance is predicted to be satisfactory. The movement of the coolant from the low power regions to the high power regions of the rods, then back to the low power regions, tends to average the coolant conditions in the driver and blanket sections of the rods. This CHF performance had been observed experimentally for similar oscillatory heat flux profiles within the LBWR program. Use of annular fuel in the driver region significantly reduces the peak fuel temperatures, which remain below the melting point of the UO_2. Full 3-D heat conduction calculations showed appreciable heat fluxes in the axial direction due to large temperature gradients, resulting in a further reduction of the peak fuel temperatures in the driver section by several hundred °C. On the other hand, the large temperature gradients raise other concerns, such as hydriding of cladding, excessive gas release, and pellet/cladding mechanical interactions in the driver section.

The burnup potential of radial micro-heterogeneous (checkerboard) arrangements was also explored with a focus on the effects of denaturing and the size of the thorium region. Fuel compositions with total core U-235 content of 6.825 and 7.75w/o were studied. To achieve reasonable power sharing at beginning-of-life (local peaking $\leq$ 1.5) 20w/o uranium with an enrichment of at least 15w/o of U-235 (total of 3% of heavy metal in the thorium pins) is needed for practical designs. The discharged burnup modestly increases with the size of heterogeneous regions. All considered heterogeneous geometries with un-denatured fuel could achieve higher burnup than the all-uranium or homogeneously mixed thorium-uranium fuels (less than 9% improvement versus the all-uranium case and up to 20% improvement versus the homogeneous case). The effect of thorium fuel denaturing was found to be significant, degrading the burnup performance to values comparable to all-uranium fuel.

Proliferation-resistance was evaluated in terms of plutonium production rate, uranium discharge rate, spontaneous neutron source, decay heat, critical mass, and enrichment barrier. In terms of plutonium generation, micro-heterogeneous fuel is more proliferation-resistant than the homogenous fuel, while the homogenous fuel is more proliferation-resistant than the all-uranium fuel. Although the uranium discharged in the thorium zone of the axial micro-heterogeneous un-denatured design is a proliferation concern with high U-233 weight percent and small critical

mass, the multiple of critical mass is smaller than the all-uranium case. On a pellet-average basis, the axial micro-heterogeneous duplex fuel (modified design for lower peaking) is the most proliferation-resistant case. Whether the duplex arrangement can be credited as an effective means to denature U-233 must be resolved. Self-protection from the U-232 was not evaluated.

The economics of the axial micro-heterogeneous fuels were assessed in terms of heavy metal resource utilization and SWU utilization, which account for most of the cost of a fuel cycle. The thorium/uranium homogenous fuel can never outperform the all-uranium fuel neutronically, but micro-heterogeneous thorium/uranium fuel has the potential to outperform the all-uranium fuel when the mixing ratio is at or above 50%UO_2-50%ThO_2. However for the 35%UO_2-65%ThO_2 ratio the axial micro-heterogeneous fuel still has poorer SWU utilization (heavy metal resource utilization is equivalent to the all-uranium case). Based on the assumption of equal fabrication costs per kg of heavy metal and under "fissile content equivalency", the 4cm/9cm axial micro-heterogeneous case (having a 35%UO_2-65ThO_2 ratio) was found to be 5% more expensive than the all-U case. However, the thermal-hydraulically-feasible case in the duplex arrangement achieves smaller burnup and is 9% more expensive than the all-U case, even when discounting the significantly higher fuel fabrication cost.

Thorium-based fuels for plutonium burning. Thorium-based fuels are very good candidates for plutonium burning in light water reactors because they do not generate transuranics. Therefore, in the final stage of the project, a study of Trans-Uranic nuclides (TRU) destruction capabilities in homogeneously mixed thorium-based fuels in LWRs has been performed for various hydrogen-to-heavy-metal (H/HM) ratios. The study considered a one-pass irradiation only, without recycling of residual contents. The analysis was performed in three stages. First, PuO_2-ThO_2 fuel mixtures were evaluated. Then, the PuO_2-ThO_2 fuel mixtures with small additions of natural uranium (needed for denaturing of generated U-233) were considered. Finally, the capabilities of the thorium-based fuel to burn plutonium as well as minor actinides were assessed.

As a first step, benchmarks of the analysis tools CASMO4 and MCODE were performed using the international benchmark within the framework of IAEA's Coordinative Research Program (CRP) to establish confidence in the analysis of plutonia-thoria lattices. Both the MCODE and CASMO4 results were found to be in good agreement with the results of the other participants for all parameters and these benchmark calculations confirmed that CASMO4 and MCODE are suitable for scoping studies of thorium – plutonium fuel designs.

In the analysis of the PuO_2-ThO_2 mixtures, the plutonium destruction rate was found to be relatively insensitive to the H/HM ratio within the practical range of PWR lattice optimization. For the un-denatured PuO_2-ThO_2 cases, over 1000 kg of plutonium can potentially be destroyed per GWe-yr. The residual plutonium fraction (relative to initially loaded plutonium) in discharged fuel can be minimized by increasing the H/HM ratio and can potentially be as low as 25%. However, the total amount of plutonium loaded at the minimum residual point may be smaller, which requires more core loadings.

Denaturing of the mixed plutonium-thorium fuel impairs the plutonium destruction effectiveness. An addition of 15% natural uranium will decrease the plutonium destruction rate by 20% to about 800 kg of plutonium per GWe-yr. This penalty can also be minimized by increasing the H/HM ratio, where less U-233 is generated and therefore less natural uranium is required for denaturing. The residual plutonium fraction in the denatured cases is almost doubled in comparison with un-denatured cases at the reference H/HM ratio; however, changing to a

wetter fuel lattice can reduce this penalty to only about 5% difference in residual plutonium fraction between denatured and un-denatured cases.

The addition of minor actinides to the fuel mixture degrades the burning efficiency in a PWR spectrum. The theoretically achievable limit for total TRU destruction per path is 50%, while the transmutation rates can still be as high as 1000 kg of TRU per GWe year. Efficient minor actinide and plutonium destruction in the thorium-based fuel in a thermal spectrum generally requires a higher degree of neutron moderation and, therefore, a higher fuel lattice H/HM ratio than typically used in the current generation of PWRs. It should also be noted that actinide destruction efficiency in thorium-based fuels can potentially be higher in fast neutron spectra reactors.

The results of the reactivity coefficient evaluations indicate that mixed plutonium-thorium fuel can be used for plutonium disposition in conventional PWRs with some changes in reactor reactivity control systems. The Doppler coefficient (DC), moderator temperature coefficient (MTC), and boron worth (BW) have values comparable to those of MOX fuels. However, the delayed neutron fraction ($ß_{eff}$) of plutonium-thorium fuel is smaller than that of all-uranium fuel by approximately a factor of two and smaller than the MOX fuel values at end-of-life by a factor of up to 1.7. Such small values impose a major challenge for reactivity control. Detailed analyses of the effects of the magnitude of the individual reactivity coefficients and kinetic parameters on the range of limiting accidents/transients and on reactor control will have to be performed in the future as it was beyond the scope of current exploratory studies. In addition, various options to increase $ß_{eff}$ will have to be studied.

For Th-Pu-MA fuel, the results indicated the potential feasibility of designing such a fuel with negative Doppler and moderator temperature coefficients. However, the $ß_{eff}$ values for Th-Pu-MA fuel are smaller than those typically encountered for UO_2 and even for MOX fuel by more than a factor of 2, raising a significant concern about reactor controllability if based completely on such fuels. Approaches to overcome this challenge were not explored in the present study.

In summary, thorium-based fuels exhibit a good potential to perform the task of burning plutonium and minor actinides in current generation of light water reactors. These fuels can be effectively used for the reduction of existing TRU stockpile and can be of use in a sustainable PWR fuel cycle with essentially complete recycling and transmutation of TRUs. Introduction of TRU containing fuels to a PWR core inevitably leads to lower control materials worths and smaller delayed neutron yields in comparison with conventional UO_2 cores. Therefore, a major challenge associated with the introduction of thorium-based TRU fuels to PWRs will be the design of the whole core and reactor control features to ensure safe reactor operation.

Task 2. Fuel Manufacturing Costs

This task was organized into three major activities:

1. An engineering study of the feasibility of producing the thorium/uranium fuel in current nuclear fuel production facilities.
2. An effort to estimate the cost of fabricating ThO_2/UO_2 oxide fuel.
3. A developmental effort to make fuel pellets with appropriate densities and to use this material to determine fundamental heat transfer properties to use in the modeling efforts.

The Westinghouse Electric Co. has completed the first two tasks and the results were reported in the 7th and 8th Quarterly Progress Reports of this NERI project.

Purdue University has been evaluating the fabrication issues associated with co-precipitation of the powder and with pressing, sintering and grinding ThO_2-UO_2 fuel pellets. High quality and geometrically uniform pellets of $(U_{.3}Th_{.7})O_2$ or "30/70"have been fabricated at Purdue in the composition desired and at a target density of at least 95%TD using commercially-accessible conditions and the co-precipitation route. The co-precipitated powders were optimized and completely characterized. However, the as-produced fine powders formed very stable agglomerates making sintering to high density difficult, even after extensive ball milling. Therefore, a new technique called Wet-Dry Processing, or WDP, needed to be developed to break up the agglomerates. This process is based on the knowledge gained from the wet processing studies from Purdue's associated NERI Program to produce microspheres of U,ThO_2 [Solomon et al. 2002]. This new technique resulted in an increase in the sintered density of the co-precipitated powders from ~85 %TD to over 97%TD under the same pelletizing and sintering conditions. The pellet microstructures have been characterized by optical and SEM microscopy, and the existence of complete solid solutions established by X-ray diffraction measurements.

Because of the high sinterability of the WDP powder, the question of re-sintering stability was raised. Therefore, re-sintering tests were conducted in the course of thermal etching at 1700°C for 1hr. At first the pellets *swelled* considerably and irregularly during the re-sintering tests. It was hypothesized that carbon from the high organic addition was slowly reacting with the hydrogen in the flowing atmosphere even after pore closure, thus causing swelling during the re-sintering experiments. Consequently, the hold time of the binder burnout step was increased from 2h to 8h and the temperature was increased to 1000°C. This eliminated the swelling problem during re-sintering. A WDP pellet with an initial thickness of 2.67mm was sintered and the thickness after sintering was found to be 2.32mm. The same pellet after a re-sintering run was found to have a thickness of 2.32mm. Hence the WDP pellets are stable under re-sintering.

Task 3. Fuel Performance

This task will provide tools to evaluate the thermal, mechanical, and chemical aspects of the behavior of ThO_2-UO_2 fuel rods during normal, off-normal, and design basis accident conditions. The behavior of the ThO_2-UO_2 fuel will be compared with the current USNRC licensing standards and with the behavior of UO_2 fuel rods under corresponding conditions.

MIT. The objective of the MIT work has been to develop appropriate models for the behavior of thorium oxide based fuels for LWRs, including a fission gas release model for ThO_2-UO_2 fuel, and to incorporate the models into the FRAPCON-3 fuel performance code. The code has been modified for analyses of mixed thoria-urania fuels with newly developed models for the appropriate thermal conductivity, thermal expansion, radial power distributions, and fission gas yield fraction. Fission gas release predictions from the modified FRAPCON code were compared to measured fission gas release data for mixed thoria–urania fuels from the Light Water Breeder Reactor (LWBR) program. Sufficiently detailed information is available in the open literature for only a few test rods, which therefore became the basis for validating our modeling efforts. Because the mechanisms of fission gas release in ThO_2-UO_2 fuel are expected to be essentially similar to those of UO_2 fuel, the general formulations of the existing fission gas release models in FRAPCON-3 were retained. However, the gas diffusion coefficient was adjusted to a lower level to account for the smaller release fraction in thoria fuel. In addition, a model for athermal gas release at high burnup was introduced. The modified version of FRAPCON-3 represents the

available fission gas release data reasonably well. It also predicts significantly lower fission gas release from thoria -based fuel under PWR conditions compared with urania fuel at the same high burnup.

A model for high burnup ThO_2-UO_2 fuel behavior during a Reactivity Initiated Accident (RIA) has been developed. Under RIA conditions, a significant amount of energy will be deposited in the fuel in a very short time. The failure threshold of energy deposition is reduced for fuel rods operated to very high burnup. There are several factors contributing to the reduction of this threshold: 1) heavily oxidized and hydrided, thus degraded, cladding; 2) reduced fuel thermal conductivity; 3) pellet-cladding gap closure due to fuel swelling; and 4) large porosity in the fuel rim region. The behavior of high burnup fuel under RIA conditions has been modeled based on observations from UO_2 tests, and extrapolated to ThO_2–UO_2 fuels through the use of the FRAP-T6 computer code. Modifications to FRAP-T6 included: thoria fuel properties (heat capacity, thermal expansion, thermal conductivity); the low temperature cladding burst stress model; and gaseous swelling contribution to the cladding strain.

The data from RIA tests with high burnup UO_2 fuel has been reviewed. The FRAP-T6 code seems to reasonably predict the residual cladding strains in the tests. However, most of the RIA simulation tests were performed under different power ramp and coolant temperature conditions than expected during an accident in a LWR and this negates the validity of a direct extrapolation of the results. But, experiments have been performed at both hot and cold conditions and with different power pulse widths. The test reactor pulse widths that are too narrow produce enhanced stresses in the cladding at a time when the cladding is cooler than it would be in power reactors. Therefore, real PWR fuel was found to have a higher safety margin due to higher cladding temperatures and wider power pulses than most of the reported tests (except the IGR tests in Russia which had a very long pulse). ThO_2-UO_2 fuel is predicted to have better performance than UO_2 fuel under RIA conditions due to its lower thermal expansion and flatter power distributions in the fuel pellets (less power and less fission gas in the rim region).

Based on the developed model, the performance of thoria fuel using current PWR fuel designs was assessed and the results showed that there would be extensive fission gas release and cladding corrosion when the fuel is operated to very high burnup. Recommendations for fuel rod design and operation strategy were proposed and assessed for satisfactory performance of very high burnup homogeneous and micro-heterogeneous ThO_2-UO_2 fuel. With the adoption of advanced cladding materials, such as M5 or DX Zr1Nb, corrosion and hydriding may not pose problems for these fuel designs. However, a larger fuel grain size and a decreasing power history might be needed to mitigate the fission gas release, and an increased free gas volume (i.e. larger plenum volume) should be provided to accommodate the increased fission gas release for high burnup fuel.

INEEL. MIT has shown that the most promising micro-hetrogeneous thoria-urania arrangement with respect to achievable burnup is the axial micro-heterogeneous design with UO_2 and thorium section lengths of about 4 and 8 cm, respectively. In addition, this design offers the benefit of substantial reduction of poison to compensate for the reactivity excess at beginning-of-life. Although this design manifests appreciable neutronic advantages, the absence of fissile material in the ThO_2 section at beginning-of-life results in large local power peaking. The most effective way to reduce the local peaking is to add uranium with fissile U-235 into the ThO_2 section. However, because homogeneous mixing of uranium in the thorium slug significantly impairs the reactivity-limited burnup performance, a modified axial and radial micro-heterogeneous fuel pin design (DuUAx4) was developed by introducing a 25 vol% central void in

the UO_2 driver zone and moving the extra UO_2 into the blanket zone as an inner ring with ThO_2 as an outer ring.

During the first part of Year 3 calculations were performed at the INEEL to compare the temperature behavior of DuUAx4 fuel rods and conventional 100% UO_2 fuel rods during a large break LOCA. The calculations were performed with the SCDAP/RELAP MOD3.3 code extended for the analysis of ThO_2-UO_2 fuel rods and extended for the modeling of axial heat conduction as discussed in the 9th and 10th Quarterlies for this project. The affect of the fuel rod axial heat conduction on the calculated temperature behavior of the DuUAx4 fuel rods was also assessed. The maximum cladding temperature of the DuUAx4 fuel during a LOCA is not significantly greater than that in conventional 100% UO_2 fuel.

During the 4th Quarter of Year 3 the steady state and transient temperature performance of fuel rods with 96wt%ThO_2-4wt%PuO_2 fuel was analyzed and compared with the behavior of 100% UO_2 fuel. The in-service fuel temperatures of the 96%ThO_2-4%PuO_2 fuel rods are significantly less than those of 100% UO_2 fuel rods, and the cladding temperatures during a LOCA are significantly less in the 96%ThO_2-4%PuO_2 fuel rods than in the 100% UO_2 fuel rods. These favorable comparisons are primarily due to the thermal conductivity of the 96%ThO_2-4%PuO_2 fuel being greater than that of 100% UO_2 fuel. Since the model used for the thermal conductivity of the 96%ThO_2-4%UO_2 fuel was based on only one set of measurements, these results are preliminary in nature.

Task 4. Long Term Stability of ThO_2-UO_2 Waste

The leaching of radionuclides from spent UO_2 fuel is a major concern when addressing the long-term storage of these materials. Mixed oxide (U, Th)O_2 fuels are being considered as an alternative due to the large quantity of thorium material available, non-proliferation benefits of the material, and the potential for significantly improved long term spent fuel storage capability. The research in this task was focused on measuring uranium dissolution from (U, Th)O_2 solid solutions as a function of the uranium content to determine the degree to which the mixed oxide is superior to UO_2 as a waste form.

The dissolution of irradiated (U, Th)O_2 pellets with compositions in the range 2–5.2% UO_2 was studied at Argonne National Laboratory East (ANL-E). The irradiated pellets were taken from the Shippingport Light Water Breeder Reactor. Pellet dissolution was carried out in J-13 well water inside sealed vessels at 90ºC. Uranium dissolution rates for these materials are between $2x10^{-3}$ and 2.510^{-5} mg m^{-2} d^{-1}, which is at least 2 orders of magnitude lower than values found in the literature for pure UO_2 irradiated fuel. A significant initial release of fission products, including ^{137}Cs, ^{99}Tc, and ^{90}Sr, has been observed, which is attributed to the accumulation of these species in macro-pores with the fuel pellets.

The studies on unirradiated (U, Th)O_2 pellets were performed at the University of Florida. Pellets with compositions of 5%, 23.6%, 36,8%, 50%, and 100% UO_2 were fabricated by blending, compacting, and sintering UO_2 and ThO_2 powders. Dissolution was monitored by measuring the uranium concentration in J-13 leachate solutions over a period of 120 days. The dissolution of whole pellets was performed at 90ºC, and the dissolution of crushed and sieved pellet fragments was performed at room temperature.

The dissolution rates for all of the unirradiated materials decrease rapidly in the first several days of leaching. The uranium dissolution rates of crushed UO_2 pellets (2 to 0.01 mg m^{-2} d^{-1}) are

very similar to values reported previously in the literature for unirradiated UO_2 under similar conditions. However, the results indicate that the normalized uranium dissolution rates of crushed $(U,Th)O_2$ pellets are less than that of pure UO_2 by as much as one and a half orders of magnitude. All of the $(U,Th)O_2$ compositions exhibit very similar fractional uranium release rates. The dissolution rate for unirradiated 5% UO_2 crushed pellets is between approximately 10^{-3} and 10^{-4} mg m^{-2} d^{-1} at 10 to 120 days.

The dissolution rate of an unirradiated UO_2 pellet is roughly 0.1 to 0.01 mg m^{-2} d^{-1} over a period of 7 to 93 days. The dissolution rates of $(U,Th)O_2$ pellets (36.8% and 50% UO_2) are lower than that of UO_2 by up to approximately one order of magnitude. The extremely low concentrations of soluble uranium species in the leachate solutions of the unirradiated $(U,Th)O_2$ pellets, compared to the background value, which makes reliable calculation of the dissolution rates for these materials difficult, particularly in the case of 5% UO_2 pellets.

These overall results from dissolution studies demonstrate an advantage for the $(U,Th)O_2$ fuel versus UO_2 with respect to dissolution in groundwater, with the uranium dissolution rates for the solid solution thoria-urania fuel lower than those of UO_2 by one to two orders of magnitude.

The oxidation behavior of unirradiated $(U, Th)O_2$ has been studied using thermal gravimetric measurements to monitor the weight gain of samples oxidized in air under both isothermal and non-isothermal conditions. The mean uranium valence of all $(U, Th)O_2$ samples after complete isothermal oxidation at different temperatures remained lower than that of pure UO_2, indicating lower O/U ratios for these materials. X-ray diffraction analysis of oxidized $(U, Th)O_2$ samples showed that all compositions retained the cubic fluorite crystal structure, in contrast to pure UO_2, which underwent a phase transformation first to tetragonal, then to an orthorhombic crystal structure as the oxidation proceeds.

Various kinetic models have been applied to the isothermal gravimetric data in order to find the best fit and calculate activation energies for oxidation. The results for 23.6% and 36.8% UO_2 samples suggest that the oxidation follows a three dimensional diffusion model. Data for 50% and 100% UO_2 samples, however, did not produce a satisfactory fit to any of the reaction models applied. A model-free method was also applied to the data to calculate activation energies. The results indicated that the activation energy is relatively independent of the $(U, Th)O_2$ composition, with values determined from both isothermal and non-isothermal data falling between approximately 80–100 kJ/mol. These values are slightly lower than that found for pure UO_2 (108 kJ/mol).

Task 5. Korean Work

The Koreans have been working on four tasks: core design analyses, fuel pellet manufacturing technologies, fuel rod performance analysis, and xenon diffusivity measurements. In the area of core design analyses, the Koreans continued their analysis of the mixed core concepts of $(Th,U)O_2$ and UO_2 fuels discussed in the previous quarterlies. The HELIOS/MASTER code system was modified for the neutronic analyses of thorium-fuelled reactor cores. The k-infinite and isotopic number densities of 25% UO_2 + 75% ThO_2 fuel pins were calculated with the HELIOS/MASTER code and compared with the results of CASMO4 and MOCUP calculations (both the MIT and INEEL versions). The HELIOS results were found to in good agreement with the MOCUP and CASMO4 results. Then, three kinds of thorium-uranium fueled PWR cores were investigated homogeneous ThO_2-UO_2 fuel, duplex $(Th,U)O_2$ fuel, and a mixed core of

duplex $(Th,U)O_2$ and UO_2 fuel assemblies. Also, a series of reference UO_2 only cores were analyzed.

The reference plant core had 157 fuel assemblies with fifty-two fresh fuel assemblies newly loaded for each cycle according to a three-batch reloading strategy. The power distributions in the various cores were controlled by using various numbers of gadolinia rods. The cycle lengths of the homogeneous thorium-uranium fuel cores were shorter than that of the reference uranium cores (at any given initial U-235 enrichment level). However, the differences between the cycle lengths of the thorium-uranium cores and the reference uranium core become smaller as the cycle length becomes longer. The cycle lengths of the alternative thorium cores with duplex fuel and/or mixed ThO_2-UO_2 fuel and UO_2 only fuel assemblies are longer than the cycle lengths of the homogenous ThO_2-UO_2 cores and similar to the cycle lengths of the reference all-uranium cores at very long cycle lengths (i.e. at high enrichment and burnup). The Doppler temperature coefficients of the cores with thorium-based fuel are more negative than that of the reference UO_2 cores, however, there were no significant systematic differences in the other physics parameters between the various thorium-based fueled cores and the reference UO_2 cores.

In order to assess the economic potential of the homogeneous thorium-uranium fuel and the alternative thorium fuel cycles, the natural uranium utilization and the separative work unit (SWU) utilization were considered. The results of the fuel economics assessment as a function of cycle length are shown in the figure to the right. The fuel costs of the thorium-based fuel cycles are decreased as the cycle lengths become longer, while that of uranium fuel cycle increases with cycle burnup. At a cycle length of about 500 EFPDs the mixed core of duplex $(Th,U)O_2$ and UO_2 fuel assemblies becomes cost competitive with the all-uranium reference.

Uranium ore purchase and SWU costs of homogeneous thorium-uranium cores, uranium cores, and alternative thorium cores versus cycle length (110US$/Kg-SWU).

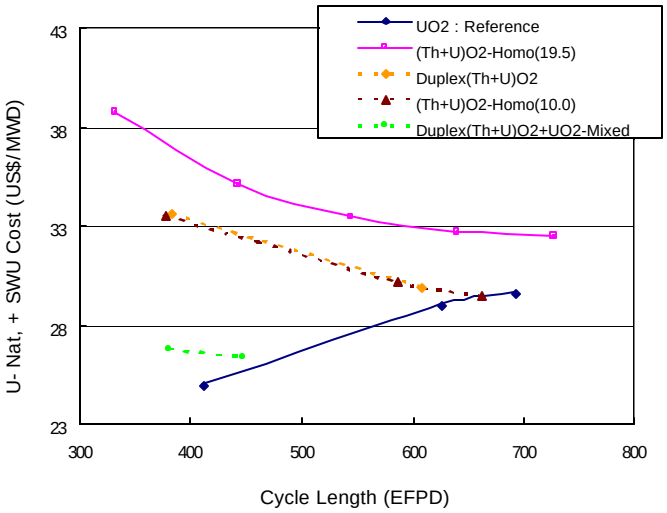

To further improve their fuel pellet manufacturing technologies, three kinds of pellets -ThO_2, ThO_2-35%UO_2, ThO_2-65%UO_2 - were fabricated by conventional powder processing using as-received and then milled powder. At first, the as-received thorium oxide powder was milled in a mortar for 40 min. Then the ThO_2 powder was mixed with the UO_2 powder in a tumbling mixer for 1 hour in order to form the various ThO_2-UO_2 powder mixtures. The thoria-urania powder was then further milled 6 times using an attrition mill, which was designed to allow the powder charge to be removed from the mill and then loaded again. In addition to the above dry milling, the powder mixtures were ball-milled for 24h in a jar containing zirconia balls and alcohol. The prepared powders were pressed at various pressures into compacts (green pellets) and then heated up to 1700°C at 5°C/min and then held for 4 hours in a H_2 atmosphere to fabricate the pellets. Milling of the ThO_2-UO_2 powders and sintering at 1700°C produced $(Th,U)O_2$ pellets with densities ranging from 93% to 98% TD. Compared to the dry milling method, wet milling of the

ThO_2-UO_2 powders increases the density of the pellets and enhances the homogeneity of the uranium and thorium distribution. This work is now successfully completed.

The thermal diffusivity of the various pellets was measured and the thermal conductivity calculated. ThO_2 has a higher thermal conductivity than UO_2, but $(Th,U)O_2$ - 65 or 35wt% ThO_2 - is similar in thermal conductivity to UO_2.

In the area of fuel rod performance, a ThO_2-UO_2 irradiation test, called IFA-652.1, was started in June 2000 in the Halden Reactor. The IFA-652.1test rods are instrumented with thermocouples and pressure transducers. The fuel centerline temperature and rod internal pressure data from two rods in IFA-652.1 at beginning-of-life and at a burnup of about 5 MWD/kgHM was compared with predictions from the INFRA-Th computer code. The agreement of the INFRA-Th predictions with the measured fuel centerline temperatures and rod internal pressures from Rods 4 and 5 in the Halden IFA-652.1 ThO_2-UO_2 experiment indicates that the models for the ThO_2-UO_2 fuel in the INFRA-Th code such as the thermal conductivity, thermal expansion, and radial power and burnup distributions are appropriate.

Also, the performance of homogeneous ThO_2-UO_2 fuel rods during irradiation in both a 900 MWe PWR and the 330 MWth SMART reactor were analyzed. Four different power histories were considered for the 900 MWe PWR case. The INFRA-Th fuel rod performance calculations indicate that the integrity of the ThO_2-UO_2 fuel rods could be maintained up to a burnup 100 MWD/kgHM.

To measure the xenon diffusivity in thoria-urania fuel, 2mm cubic specimens of polycrystalline $(Th,U)O_2$ and UO_2 were made. The cubes were irradiated in the HANARO reactor for 30 minutes. After cooling for 10 days, annealing tests were performed with various ambient gas oxygen potentials. The xenon diffusion coefficients from the polycrystalline $(Th,U)O_2$ are coincident with or lower than those from polycrystalline UO_2. The diffusion coefficient for the polycrystalline $(Th,U)O_2$ under a higher oxygen potential (–160kJ/mol) turned out to be higher than under a lower oxygen potential(–370 kJ/mol). Based on the comparison between the diffusion coefficients from single crystal (work previously report in these quarterlies) and polycrystalline UO_2, the diffusion coefficients in a single crystal of $(Th,U)O_2$ are expected to be much lower than that in polycrystalline $(Th,U)O_2$.

Contents

Introduction

The overall objective of this NERI project was to evaluate the efficacy of high burnup mixed thorium-uranium dioxide (ThO_2-UO_2) fuels for light water reactors (LWRs). A mixed thoria-urania fuel that can be operated to a relatively high burnup level in current and future LWRs may have the potential to:

- Improve fuel cycle economics (allow higher sustainable plant capacity factors);
- Improve fuel performance;
- Increase proliferation resistance; and
- Be a more stable and insoluble waste product than UO_2.

The project was led by The Idaho National Engineering and Environmental Laboratory (INEEL), with the collaboration of three universities, the University of Florida, Massachusetts Institute of Technology (MIT), and Purdue University; Argonne National Laboratory; and all of the pressurized water reactor (PWR) fuel vendors in the United States. The project was organized into four tasks:

- Task 1 consisted of fuel cycle neutronics and economics analysis to determine the economic viability of a ThO_2-UO_2 fuel cycle in PWRs,
- Task 2 was focused on determining whether or not ThO_2-UO_2 fuel can be manufactured economically,
- Task 3 evaluated the behavior of ThO_2-UO_2 fuel during normal, off-normal, and accident conditions and compare the results with the results of previous UO_2 fuel evaluations and U.S. Nuclear Regulatory Commission (NRC) licensing standards, and,
- Task 4 determined the long-term stability of ThO_2-UO_2 waste.

A demonstration irradiation of ThO_2-UO_2 fuel will also probably be needed before ThO_2-UO_2 fuel can be loaded into commercial reactors.

Task 1. Fuel-Cycle Analysis

This task evaluated the economic viability of a ThO_2-UO_2 fuel cycle in commercial reactors operating in the United States. Three organizations collaborated on this work: a nuclear fuel vendor (Framatome ANP), a university (MIT), and a DOE National Laboratory (INEEL). Framatome ANP has performed two- and three-dimensional fuel-lattice calculations and calculated power distributions for both assemblies and individual rods, in both uranium and plutonium enriched PWR 17×17 cores. Framatome ANP has also contributed to the other vendors and the DOE the results of 17 critical experiments containing thorium and uranium, and that data has been used to benchmark the thorium cross-sections (see Figure 1). The final Framatome ANP results were presented in the 11th Quarterly Progress Report for this project and in a final report prepared by Framatome ANP and are not repeated here. MIT further optimized various core designs by investigating such things as fuel rod geometry, metal-water ratio, and ThO_2-UO_2 ratios using the CASMO-4 and SIMULATE-4 lattice codes. Both MIT and the INEEL have been performing benchmark quality calculations at the rod, cell, and assembly levels using the Monte Carlo code MOCUP, which combines MCNP and ORIGEN.

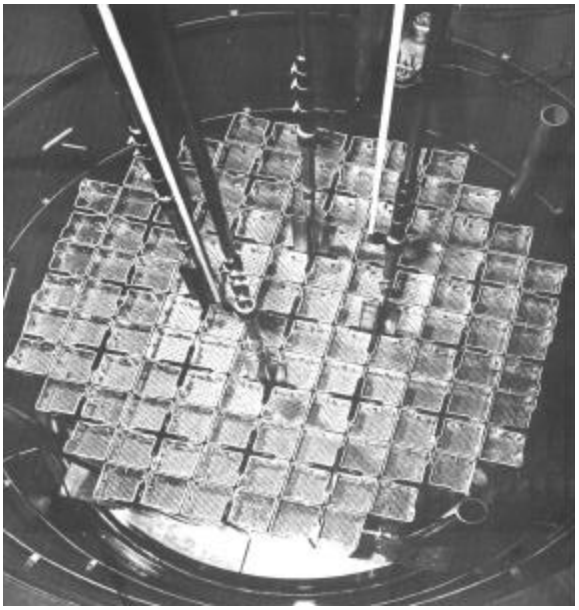

Figure 1. ThO_2-UO_2 Critical Experiment

Due to the relatively poor economic performance of the homogeneously mixed urania-thoria fuel, the focus of the work under Task 1 during Year 2 of this NERI project was primarily on the performance and economics of using micro-heterogeneous fuel forms, where some small distance physically separates the uranium and thorium. When compared to the equivalent homogeneous case (i.e., the same urania-thoria weight percentages), an increase in burnup is observed, which improves the economics of using thorium-based fuel. However, the physical separation of the uranium and thorium has its own set of challenges depending on the type of separation, and higher enrichment may still be required to achieve the desired burnup. Therefore, the work during Year 3 has focused on use of thorium to burn unwanted U-233 or plutonium.

Task 1 Progress in Neutronics at the INEEL - Thorium-Based Transmuter Fuels For Use In Light Water Reactors

J. Stephen Herring

When used in a transmutation mode, thorium-based fuels may have an advantage over conventional UO_2-PuO_2 mixed oxide (MOX) fuels because the thorium-based fuels reduce the total amount of plutonium produced and produce a mixture of plutonium isotopes high in ^{238}Pu. Because of the high decay heat and spontaneous neutron generation of ^{238}Pu, the isotope provides

intrinsic proliferation resistance. Thoria is also a fuel and waste form that is difficult to dissolve, thus making the diversion of spent fuel for weapons' production purposes more difficult.

The objective of this analysis is to demonstrate the value of using ThO_2-UO_2 fuels to burn unwanted plutonium. Some of the proliferation concern in the world today stems from plutonium that has already been separated from spent fuel. Currently separated plutonium is being incorporated in UO_2-PuO_2 mixed oxide (MOX) fuel. However, because MOX fuel contains ~90 wt % ^{238}U, substantial amounts of ^{239}Pu are produced in the MOX fuel and the net plutonium burnup rates are only 30-50% per cycle. The incorporation of plutonium into a ThO_2 matrix will allow the consumption of already-separated plutonium without breeding additional ^{239}Pu. The minor actinides (MA, i.e. neptunium, americium, curium, berkelium, californium, etc.) would be included in the ThO_2 to further reduce the overall long-term radiotoxicity of the fuel cycle. These analyses have shown that thorium-based fuels can reduce the amount of Pu-239 needing further transmutation or going to a repository by about 90%.

1.1. Introduction

Thoria fuels appear promising as a matrix for plutonium and the minor actinides during mono-recycling in light water reactors. The goals of this recycling strategy are to reduce overall inventories of plutonium, to render the resulting spent fuel as proliferation-resistant as possible through the accumulation of ^{238}Pu, ^{240}Pu, ^{242}Pu and ^{232}U, to consume the minor actinides, and to produce a very robust waste form. A schematic of the mono-recycling strategy is shown in Figure 2 for the case of one thoria-urania pin for every nine fuel rods. In this fuel cycle the LWR fuel assembly consists of 89% standard UO_2 fuel rods with a ^{235}U enrichment of 4.95 wt %. The plutonium and minor actinides produced in earlier standard rods are separated and placed in the thoria-urania pins occupying 11% of the positions in the fuel assembly. Thus the goal of the mono-recycling strategy or "twice through fuel cycle" is to transmute the great majority of the long lived actinides in existing LWRs and to discharge a fuel form that is a very robust waste form and whose isotopic content is very proliferation resistant. We have also evaluated some cases where five of the nine positions are occupied by thoria-urania fuel rods.

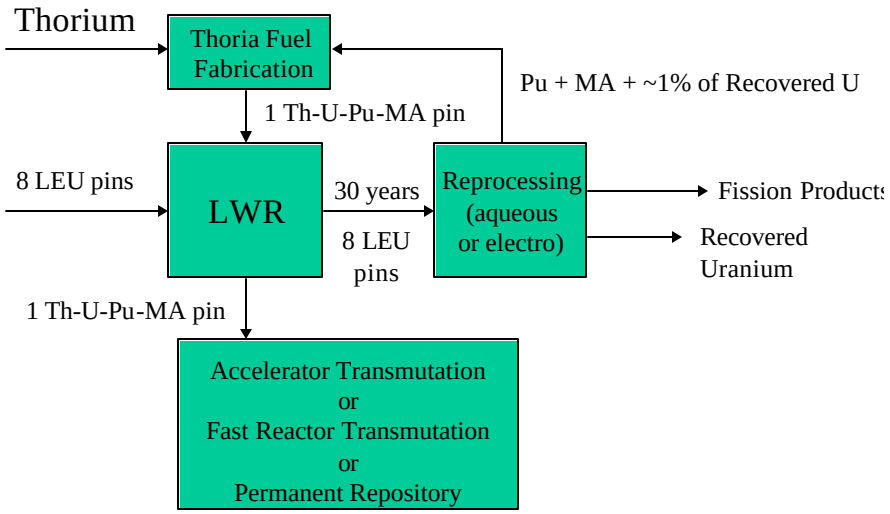

Figure 2. Mono-recycling strategy for light water reactors.

We have used the model shown in Figure 3 in this analysis, consisting of nine fuel pins, either with one [Th-U-Pu-MA]O_2 transmuter pin and eight standard UO_2 pins or with five transmuter pins and four UO_2 pins. The plutonium and minor actinides are derived from UO_2 fuel irradiated to 45 MW-d/kg and reprocessed 30 years after discharge.

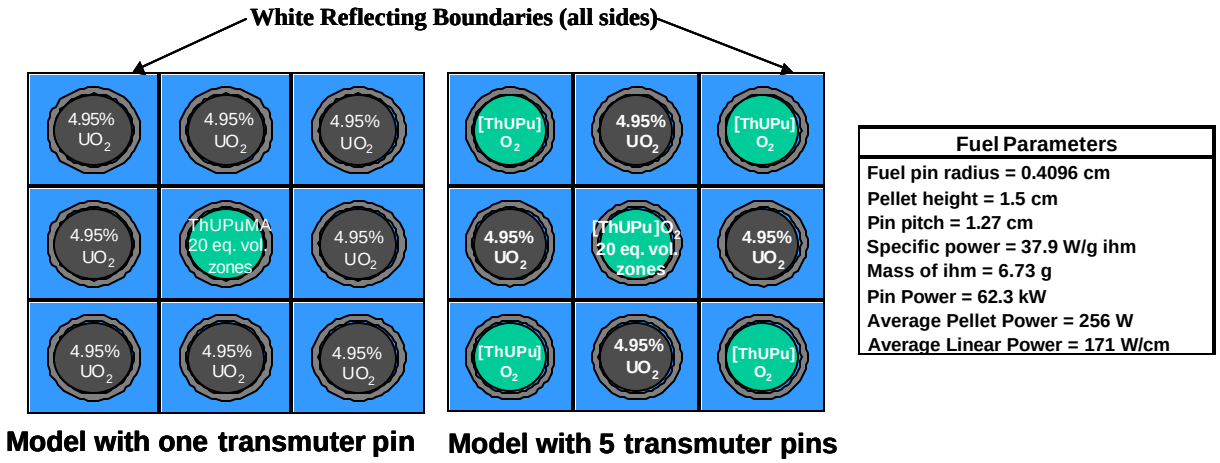

Figure 3. One and five thoria-urania pins in nine model and fuel parameters

In the various cases analyzed, the thoria-urania fuel contained 0-10 wt% recovered uranium and 6 - 15 wt% Pu+MA. The recovered uranium (98.5 wt% ^{238}U) was included to denature the ^{233}U below the 12 wt % limit for low enrichment uranium (LEU) [Forsberg et al. 1999]. For these analyses, the burnup code MOCUP [Moore et al. 1995], which uses the Monte Carlo transport code MCNP [Briesmeister 1997] and the exponential matrix generation and depletion code ORIGEN2 [Croff 1980], was used. MOCUP was used with 60-day time-steps and tracked the generation and depletion of 50 fission products and 38 actinides. The model has white reflecting boundaries to simulate an infinite array. The eight outer pins are modeled as eight individual fuel zones and the center pin is divided into twenty equal-volume zones. The isotopic constituents of the fresh UO_2 fuel and of the recovered uranium and plutonium plus minor actinides are shown in Tables 1 and 2.

Table 1. Uranium isotopic content.

	Fresh Fuel	Recovered U
U-234	0.00%	0.027%
U-235	4.95%	0.908%
U-236	0.00%	0.578%
U-237	0.00%	0
U-238	95.05%	98.487%

The uranium is included in the center pin only as a diluent for the ^{233}U to approach the LEU limit, 12% ^{233}U/total U.)

Table 2. Isotopic content of plutonium and minor actinides.

45 MWd/kg ihm UO2 fuel, 30 years after discharge		
	Fraction of Pu+MA	Elemental Fraction
Np-236	0.00%	0.00%
Np-237	6.03%	100.00%
Np-238	0.00%	0.00%
Pu-237	0.00%	0.00%
Pu-238	1.77%	2.16%
Pu-239	49.00%	59.99%
Pu-240	21.71%	26.59%
Pu-241	3.29%	4.03%
Pu-242	5.90%	7.23%
Pu-243	0.00%	0.00%
Am-241	10.79%	89.06%
Am-242m	0.01%	0.07%
Am-243	1.32%	10.87%
Cm-242	0.00%	0.01%
Cm-243	0.00%	1.75%
Cm-244	0.15%	84.74%
Cm-245	0.02%	11.89%
Cm-246	0.00%	1.59%
Cm-247	0.00%	0.02%
Cm-248	0.00%	0.00%

1.2. Results for Transmutation With a One of Nine Pin Geometry

We analyzed nine cases using the nine-pellet model shown in Figure 3 above. The constituents of the transmuter pins were varied to determine the most effective combination for extended burnup, proliferation resistance, and consumption of the minor actinides. In some cases the center pellet was irradiated for the entire lifetime of the surrounding UO_2 pellets, then removed from the first assembly and placed in a second, fresh UO_2 assembly. The isotopic concentrations in the center pellet were tracked both spatially and temporally through the entire irradiation. In addition, isotopic ratios that are important to proliferation resistance have been tracked both spatially and temporally for each of the ten cases.

The chief parameters for the nine cases are shown in Table 3. The results of the "5 of 9 pin" cases, the fifth and sixth on this list, were reported in the 11th Quarterly report. This report will concentrate on the "1 of 9 pin" third and fourth cases, with reference to the second case, containing 10% U and 15% PuMA, which was reported in the 10th Quarterly.

Table 3. Cases analyzed.

Advanced Fuels 9-pin Cases					
		Transmuter Pin Weight Fractions			
Name	# of Transmuter pins	Th	U	PuMA	Pu only
ThUPuMA 0010 9p	1	90%	0%	10%	
ThUPuMA 1015 9p	1	75%	10%	15%	
ThUPuMA 0812 9p	1	80%	8%	12%	
ThUPuMA 0609 9p	1	85%	6%	9%	
ThUPu 10-10 5 of 9p	5	80%	10%		10%
ThUPu 10-6 5 of 9p	5	84%	10%		6%
ZrYPuMA 08 9p	1	0%	0%	8%	
ZrYPuMA 22 9p	1	0%	0%	22%	
UO2 baseline	0		100%		

In all of the cases discussed in this quarterly, the transmuter pin is assumed to remain in for the same irradiation period as the surrounding UO_2 pins, for an average burnup of 61.5 MWth-d/kg. The k effective during the irradiation is shown in Figure 4.

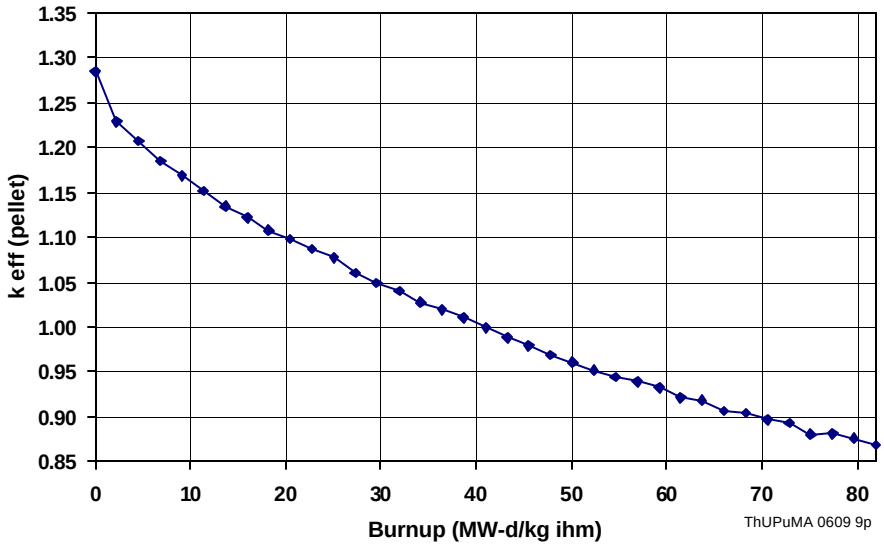

Figure 4. k-effective for 6% U, 9% PuMA transmuter pin in UO_2 array.

The variation of the Pu-239 concentration in the center pin is shown in Figure 5. Note that the ^{239}Pu, initially uniform across the diameter, is burned out on the periphery first because of the well-moderated flux near the coolant. After a burnup of 34.1 MW-d/kg (red curve), the center concentration is about 35% of the initial concentration and the peripheral concentration is about 10% of the beginning-of-life concentration. At the final burnup of 61.5 MW-d/kg, the distribution of Pu-239 is fairly uniform across the pellet cross-section.

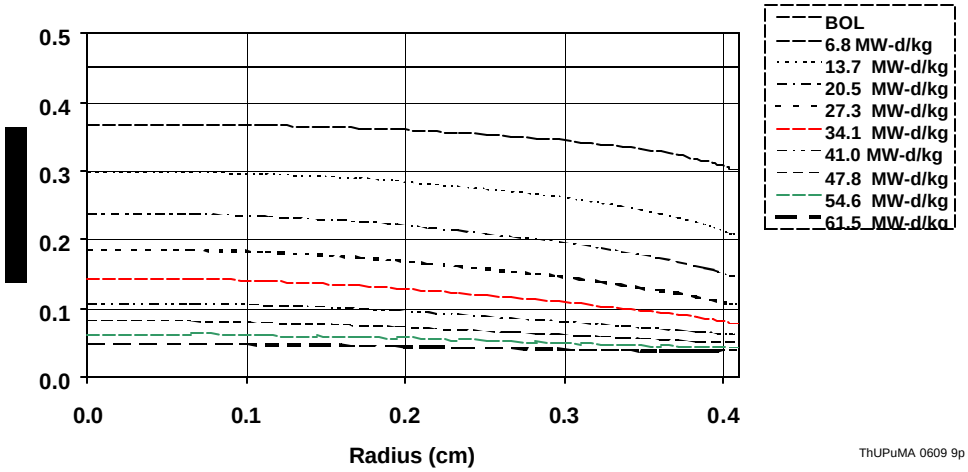

Figure 5. ^{239}Pu concentration in 6% U 9% PuMA transmuter pin.

The average plutonium concentrations in the transmuter pin are shown in Figure 6. Note that the ^{239}Pu concentration decreases quite rapidly, while the Pu-238 and Pu-240 concentrations increase during the irradiation.

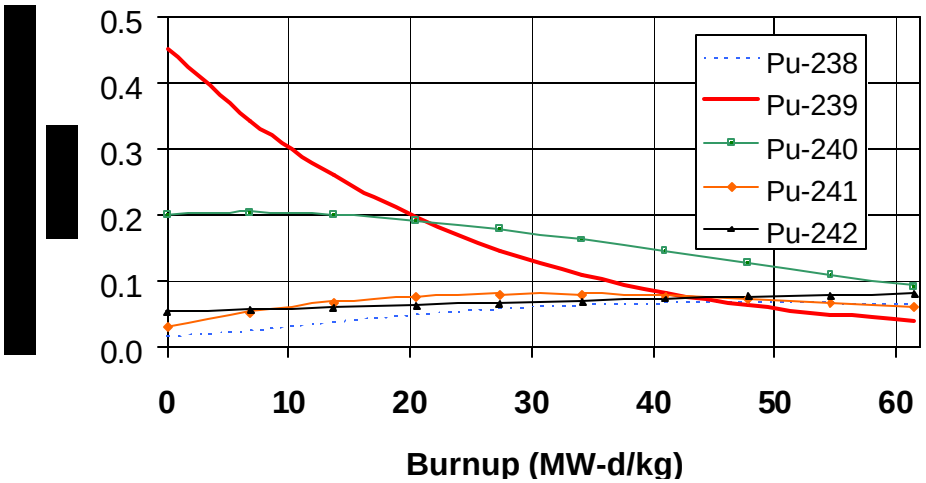

Figure 6. Average plutonium isotopic concentrations in the 6 % U, 9% PuMA transmuter pin.

1.3. Proliferation Resistance

The high spontaneous neutron generation and high decay heat of ^{238}Pu make any plutonium separated from the center pin mixture very difficult to use of weapons purposes. The ^{238}Pu content of the transmuter pin is significantly increased during the irradiation because of the high

loading of ^{237}Np, which produces ^{238}Pu via the ^{237}Np(n,γ)^{238}Np→^{238}Pu reaction. Note in Figure 7 that the initial ^{239}Pu/total plutonium ratio is about 65 %. However, because the thorium-based transmuter pin has only 6 wt % ^{238}U, little additional Pu-239 is bred during the irradiation and the ratio of ^{239}Pu/total plutonium decreases to about 15% after an average burnup of 61.5 MW-d/kg. On the other hand, because of the presence of significant amounts of ^{237}Np, the content of the ^{238}Pu increases during the irradiation and the ratio of ^{238}Pu/total plutonium is nearly 25% after 61.5 MW-d/kg. In fact the ^{238}Pu concentration in the transmuter pin actually exceeds the ^{239}Pu concentration after about 45 MW-d/kg.

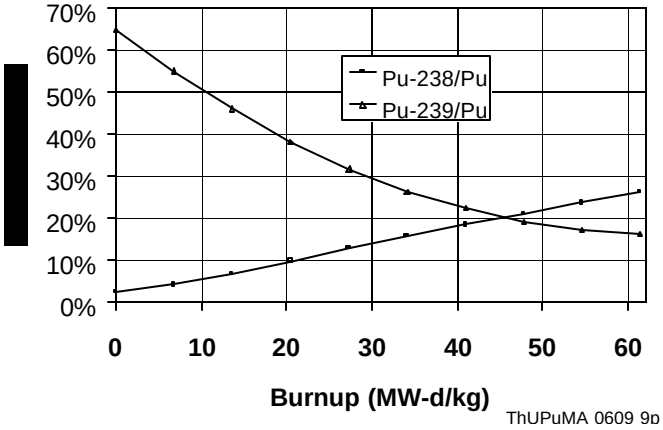

Figure 7. Plutonium isotopic ratios important to proliferation resistance.

Another measure of the proliferation resistant of spent fuel is the ratio of uranium isotopes. In order to be classed "Low Enriched Uranium" the ^{235}U/total U concentration ratio must be below 20 wt % and the ^{233}U/total U ratio must be below 12 wt %. When both ^{235}U and ^{233}U are present one uses the "sum of fractions rule." Thus a mixture containing 6 wt % ^{233}U and 10 wt % ^{235}U would be at the LEU limit. Recovered uranium, with the isotopic concentration shown in Table 1, has been added to the transmuter pin for the sole purpose of diluting the ^{233}U bred in the pin to a concentration below the LEU limit.

Another measure of the proliferation resistance of the uranium mixture is the content of ^{232}U. ^{232}U comes to secular equilibrium with its daughter product ^{208}Tl with a 3-year time constant. ^{208}Tl emits a 2.6 MeV gamma that makes handling difficult. A five-kg mass of ^{233}U containing 1% ^{232}U will produce a dose of 125 rem/hr at a distance 0.5 m 1 yr after separation of the uranium from the spent fuel.

In Figure 8, the uranium concentration ratios are shown a function of burnup. Note that the LEU sum-of-fractions the transmuter pin containing 6 wt % U and 9 wt % PuMA is about 1.8, meaning that the fissile uranium could not be classed at low enriched uranium. Therefore, additional recovered or depleted uranium will have to be added to the transmuter pin to satisfy the LEU limit. On the other hand, the ^{232}U

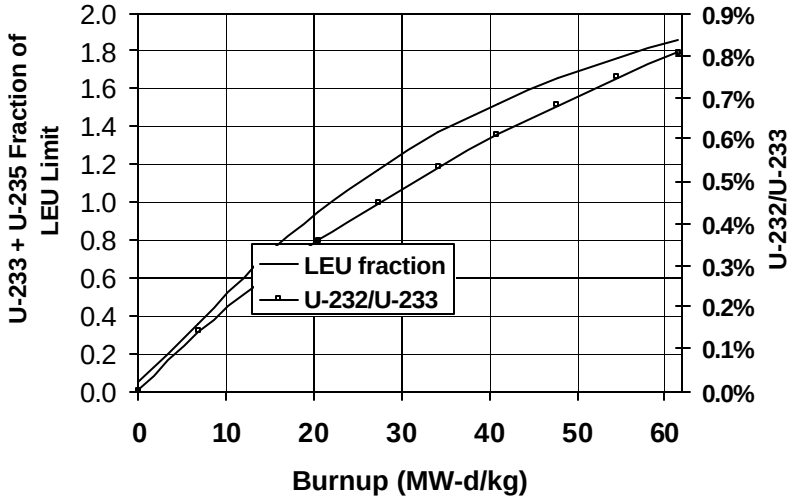

Figure 8. Uranium isotopic ratios important to proliferation resistance.

content of the transmuter pin is about 0.8 % at the end of the irradiation, meaning that the uranium would be self-protecting.

1.4. Overall Transmutation Effectiveness

In order to determine the effectiveness of the various transmutation schemes, we have calculated the amounts of the various actinides produced in the various "1 in 9 pin" cases listed in Table 3 and compared those amounts with the actinide production in the standard UO_2 once-through fuel cycle. The UO_2 Baseline case consists of a once-through irradiation of the UO_2 fuel to 61.5 MW-d/kg, followed by disposal of all the pins in a repository.

The comparison has been carried out for two scenarios. In the first scenario, we assume that the plutonium and minor actinides from previous cycles are placed in the transmuter pin and that all the pins in the assembly, both the surrounding UO_2 pins and the transmuter pins, are sent to a repository at the end of one 61-MW-d/kg irradiation. A comparison of the net actinide production in the first scenario for the various "1 in 9 pin" cases listed in Table 3 is shown in Figure 9. The case labeled ZrYPuMA 08 is an inert matrix transmuter pin consisting of a yttria-stabilized zirconia matrix containing 8 wt % of the PuMA mixture shown in Table 2. All the other cases, except the UO_2 Baseline case, have thorium fertile material with varying amounts of UO_2 (first two numbers in the label) and plutonium and minor actinide loadings (last two numbers in the label).

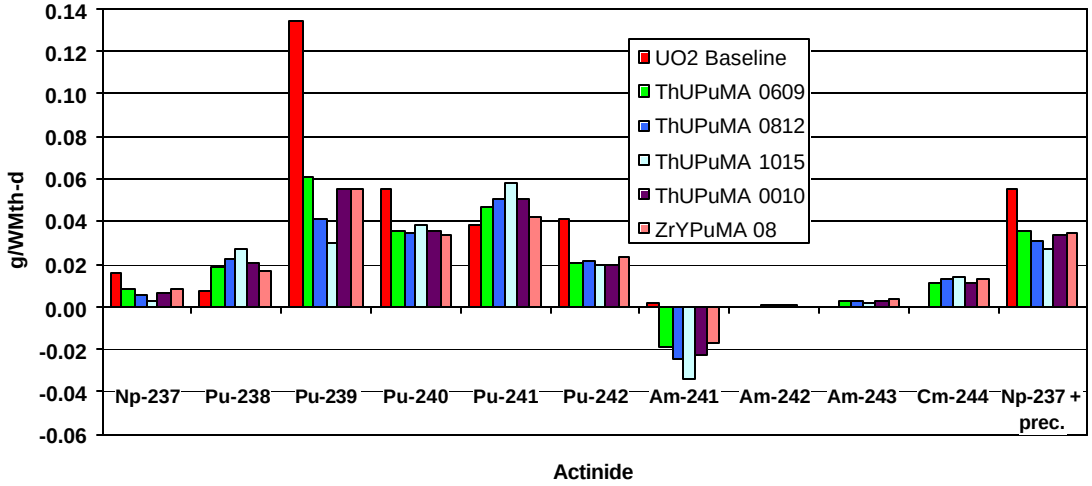

Figure 9. Net actinide production by the eight LEU pins and the transmuter pin

Note that the net production of ^{239}Pu for all the pins is reduced by at least a factor of 2 from the UO_2 baseline. The case with 10% UO_2 and 15%PuMA has the least ^{239}PU and the most ^{238}Pu at end-of-life. The net production of the higher plutonium isotopes is reduced by lesser factors, because of the higher initial loading of those isotopes in the transmuter pins. The net production of ^{241}Am is actually negative for the transmuter cases because the actinide mixture in the transmuter pins is assumed to have decayed for 30 years before separation from the original UO_2 fuel. During that time, most of the fissile ^{241}Pu ($t_{½}$ = 14.5 years) has decayed into non-fissile ^{241}Am. In the transmuter pins the ^{241}Am is first converted to the fissile ^{242}Am and then fissioned. More important, the long-term source term in a repository has been reduced through the lower net production of ^{237}Np and its precursors, ^{241}Pu and ^{241}Am. Finally, note that the net production of ^{238}Pu has been significantly increased in all the thorium and metal fuel cases compared to the UO_2 Baseline through the continued irradiation of the ^{237}Np in the transmuter pins.

The net production of selected actinides is compared with the UO_2 Baseline on a percentage basis in Figure 10. Note that the net production of ^{238}Pu in the overall assembly has increased by 150 to 250 % while the net production of the other plutonium isotopes has decreased by 50 to 75 %. The net ^{241}Pu production is higher than the once-through UO_2 Baseline because of the higher inventory of ^{240}Pu in the transmuter pins compared with the baseline. The net production of ^{237}Np and its precursors is reduced by about 50 % from the UO_2 Baseline. Again, the thorium fuel case with 10%UO_2 and 15%PuMA appears to result in the best isotopics.

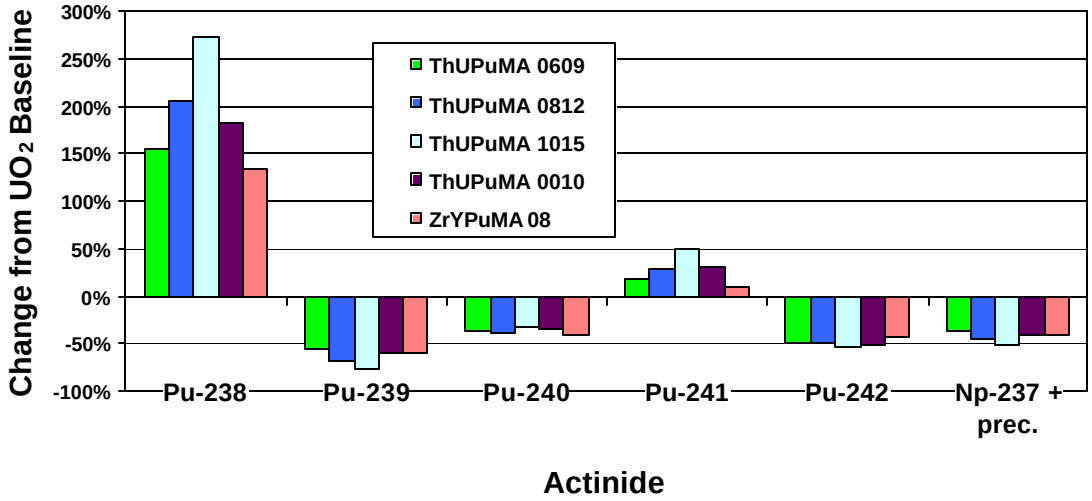

Figure 10. Change in net actinide production compared with the once-through UO_2 Baseline.

The second scenario assumes that only the transmuter pins are sent to further transmutation or to a repository. The plutonium and minor actinides and about 1 % of the uranium in the surrounding UO_2 pins are chemically separated after a 30-year decay time and fabricated into transmuter pins. Because the thorium-based or inert matrix transmuter pins would be more difficult to process chemically, those pins are assumed to be sent directly to a geologically repository (or maybe subjected to more advanced separation and transmutation technologies). The masses of each of the actinides sent to further transmutation or to a repository are shown in a logarithmic plot in Figure 11.

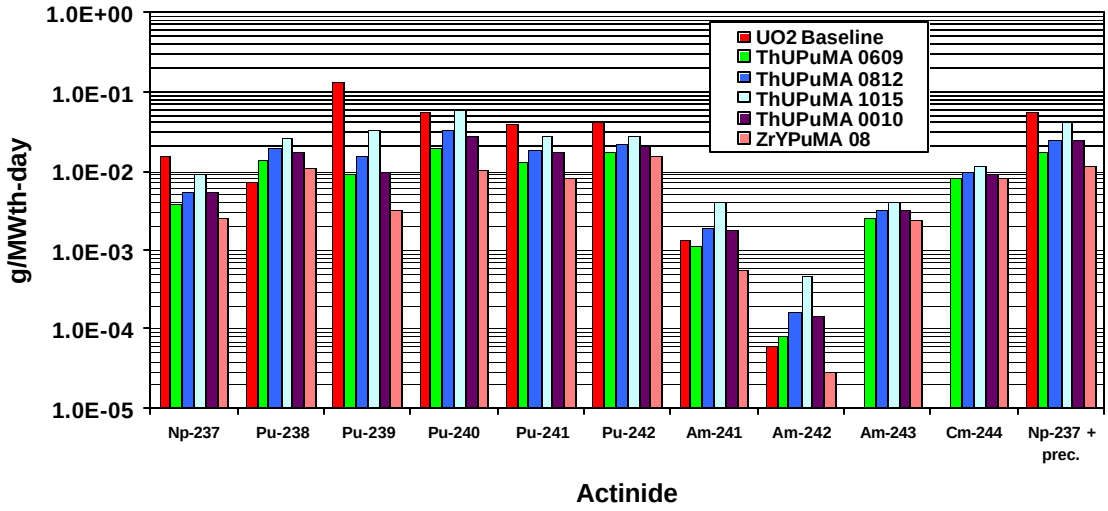

Figure 11. Actinides sent to further transmutation or repository.

Note that the ^{239}Pu leaving the LWR system has been reduced by as much as an order of magnitude, but that ^{238}Pu has been generally increased. Though small, the ^{242}Am going to further transmutation or to a repository is also generally higher than in the UO_2 Baseline case. On the other hand, the rest of the plutonium isotopes have been reduced. The percentage change in the amounts of actinides going to further transmutation or a geological repository are shown in Figure 12. As was the case with the net production comparisons, the amounts of ^{238}Pu leaving the LWR system are increased by 50 % to 250 %. The ^{239}Pu is reduced by 75% to 95% and the rest of the plutonium isotopes by lesser amounts. The ^{237}Np and its precursors is reduced by as much as 75 %.

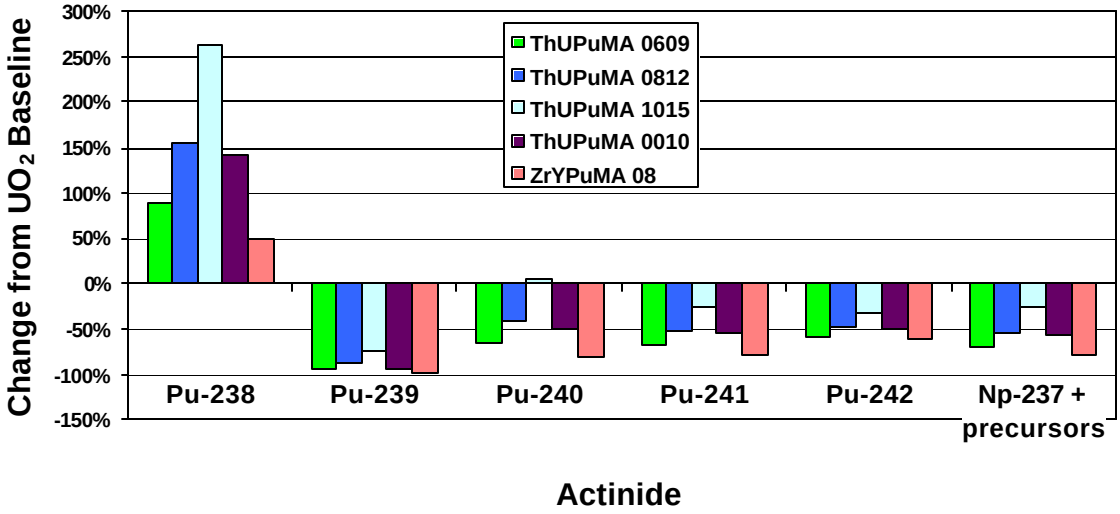

Figure 12. Change in actinides going to further transmutation of a geological repository.

1.5. Fission Heating Profile

Finally, we have tracked the fission heating in the transmuter pellet from beginning-of-life to an assembly-averaged burnup of 61 Mw-d/kg. The results are shown in Figure 13. In standard UO_2 pellets the fission heating is fairly uniform at beginning-of-life and becomes peaked at the rim as ^{239}Pu is produced at the periphery through resonance absorptions by ^{238}U. The opposite occurs in the transmuter pellets, which contain a much lower amount of ^{238}U. The ^{239}Pu is initially uniformly distributed in the transmuter pellet. However, because of the strong fission resonance at 0.3 MeV, the peripheral ^{239}Pu is more rapidly consumed in fission and the heat

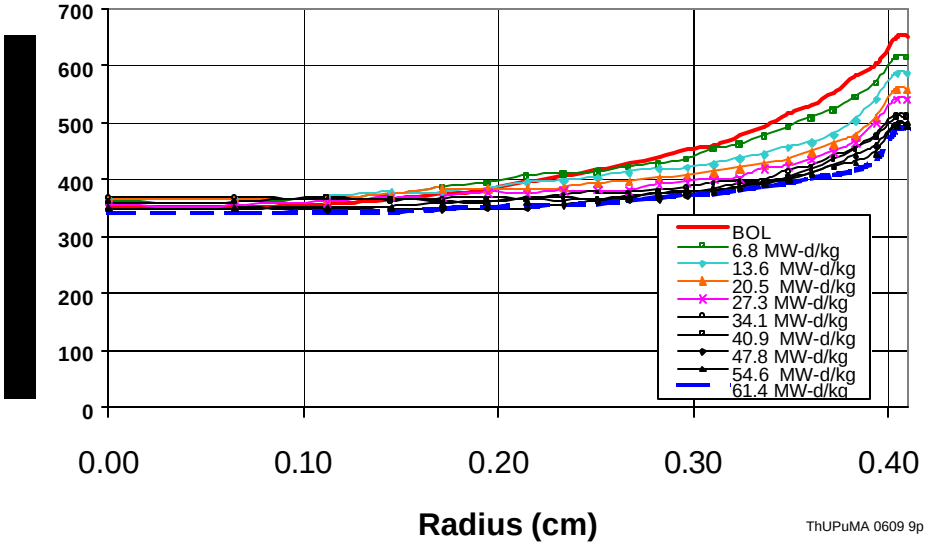

Figure 13. Fission Heating Profile in Transmuter Pellet.

profile flattens with high burnup.

The average volumetric fission energy deposition in the UO_2 pins and in the transmuter pins is shown in Figure 14. Since the UO_2 and transmuter pins are the same diameter, Figure 14 shows a comparison of the heat flux for the UO_2 and transmuter pins. Note that the transmuter pins have a heat flux that is about 50 % higher than the UO_2 pins at beginning-of-life and about 20% higher at the end-of-life. This peaking factor is greater than that allowed in LWR assemblies and indicates that either the actinide loading of the transmuter pins should be reduced from 9 % to about 6 % or that the transmuter pins should have a smaller diameter or an annular configuration to enhance heat removal.

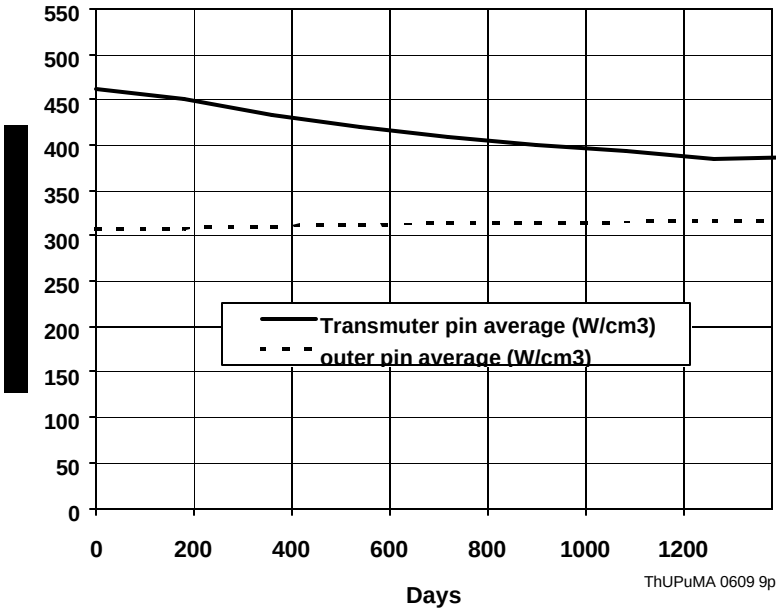

Figure 14. Fission Heating in UO_2 and Transmuter Pins

1.6. Conclusions

Thorium-based spent fuel is significantly more proliferation resistant than UO_2 fuel. In particular, the intrinsic proliferation resistance of plutonium mixtures with high ^{238}Pu loadings is enhanced through high decay heat and spontaneous neutron production.

Also, the use of thorium-uranium fuels, and perhaps fuels with non-fertile matrices, shows promise as LWR transmuter fuels that would significantly reduce the amount of plutonium, neptunium and its precursors going to a permanent repository or to long-term interim storage. Furthermore, these transmuter fuels used in a mono-recycling or "twice through fuel cycle" significantly decrease the volume of spent fuel going to a repository while greatly increasing the proliferation resistance and waste form durability of the resulting fuel. Work is continuing in the analysis of non-fertile and thorium-based LWR transmuter fuels.

Task 1 Progress at MIT

E. Shwageraus, X. Zhao, M. J. Driscoll, P. Hejzlar, and M. S. Kazimi

1.1. Neutronics of Micro-Heterogeneous ThO_2-UO_2 PWR Cores

The objective of this task has been to evaluate the neutronics performance of various micro-heterogeneous arrangements, where the ThO_2 and UO_2 fuel is separated on a micro-scale (up to several cm). The work has addressed three types of fuels: (1) axial micro-heterogeneous ThO_2-UO_2 fuel, where the ThO_2 fuel pellets and UO_2 fuel pellets are stacked in separate layers in the fuel rods, (2) duplex fuel where the thorium resides in an annulus around a UO_2 core, and (3) separate pins of UO_2 and ThO_2 fuels.

1.1.1. Computational Method

The computer program MOCUP [Moore et al. 1995] has been used as a primary tool for this study. MOCUP is the MCNP-ORIGEN2 Coupled Utility Program that employs the MCNP (here version 4B) generalized-geometry Monte Carlo transport code to provide the neutronics solution and the ORIGEN2 code to compute the time-dependent compositions of the individually selected MCNP cells. All data communication between the two codes is accomplished through the MCNP and ORIGEN2 input/output files. This allows a general material (target, fuel, control, etc.) to be depleted in a neutral particle field, with the accuracy of a transport neutronics solution. Since the MCNP version 4B library does not contain temperature-dependent neutron cross sections for most actinides, a number of libraries from the UTXS compilation were imported. Also for some fission products, the evaluated data files produced at Los Alamos National Laboratory were imported via INEEL. The benchmarking of this code with others can be found in Zhao et al. [2000]. As in the benchmarks, all the calculations were for fuel pin-cells; whole-assembly and whole-core calculations are left for the future. Sufficient neutron histories were accumulated to achieve a one-sigma uncertainty in k of ± 0.002. It should be noted that most state-of-the-art codes may not be accurate enough for micro-heterogeneous fuel because of its complicated resonance shielding configurations.

Checkerboard (radial micro-heterogeneous) cases were analyzed using the CASMO-4 computer code [Edenius et al. 1995]. Benchmarking of the criticality predictions was carried out in order to verify the capability of CASMO-4 to predict reactivity and reaction rates in thorium-based lattices. The Monte-Carlo MCNP-4B computer code was used for that purpose. The benchmark was performed using initial fuel composition in a 1x1 radial micro-heterogeneous geometry. The values of K_{inf} predicted by both computer codes were found to be in a fairly good agreement [MacDonald et al. 2001, Zhao et al. 2001]. Therefore, it was assumed that the CASMO-4 computer code can treat radial micro-heterogeneous thorium based lattices with sufficient accuracy for the purpose of this study.

1.1.2. Summary Of Achievements As Of September 2001

This section summarizes the key results and findings achieved during the first two fiscal years of this NERI project. Further details are found in the FY-02 annual report [MacDonald et al. 2001]. The basic configurations of micro-scale heterogeneous ThO_2-UO_2 fuel designs, in the form of interspersed uranium and thorium regions, are shown in Figure 15: checkerboard, duplex, and axial heterogeneous. The uranium dioxide is 19.5 w/o enriched in U-235, and the ThO_2 is pure thorium dioxide. There are many possible variations from these basic configurations such as

multi-pin checkerboard, and other combined designs of the base cases, but in this report, our discussion will be focused on checkerboard and axial cases. The operating parameters of current PWRs were adopted, except that the fuel compositions were based on 35%UO_2+65%ThO_2 fuel (the weight percent here is on a heavy metal basis) distributed appropriately among the respective fuel zones.

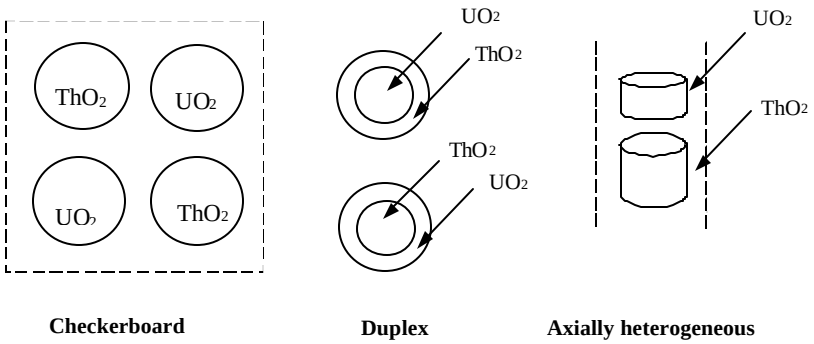

Figure 15. Representative basic configurations of micro-heterogeneous ThO_2/UO_2 fuel.

Configurations and burnup performance for various micro-heterogeneous fuel designs based on the same initial fissile content are given in Table 4 on the next page. Other parameters of the conventional PWR fuel assembly are typical of a standard Westinghouse 17x17 assembly and can be found in [Zhao et al. 2000 and 2001]. In terms of the reactivity-limited batch loaded burnup, B1 [Driscoll et al. 1990], (where K=1.03 to allow for core leakage), a slight improvement can be seen in going from homogeneously mixed ThO_2-UO_2 (Hom) fuel to duplex oxide fuel with the ThO_2 on the inside (ThU fuel). However, there is about a 12% improvement from Hom fuel to duplex oxide fuel with the UO_2 on the inside (UTh) fuel and about an 18% improvement from Hom fuel to axial micro-heterogeneous (Ax) fuel. However, as Table 4 shows, an improvement in the reactivity-limited burnup over the all-U case is realized only for the Ax case (by 6.6%) among these three alternatives.

Figure 16 compares the reactivity burnup curves for the Hom, Ax and Ax4 cases. The last configuration consists of successive 4 cm segments of UO_2 between 8.164 cm segments of ThO_2 and has about a 25% improvement in burnup over the Hom case and a 13% improvement over the all-uranium case. In addition, it has a suppressed reactivity or "burnable poison effect" at the beginning of burnup. These effects are achieved by merely rearranging the ThO_2 and UO_2 material on a micro-scale inside the fuel pins.

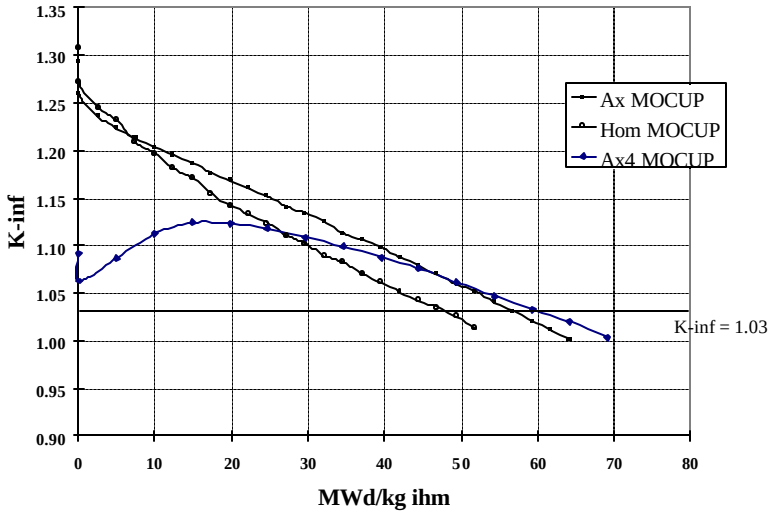

Figure 16. Comparison of K_∞ as a function of burnup for the Ax, Hom, and Ax4 cases.

In order to determine the effect on the neutronics of homogeneous denaturing of the ThO_2 to keep the fraction of U-233 below 12%, 12 w/o of the thorium was replaced by natural uranium (0.711 w/o) in the ThO_2 zone of the Ax case, which corresponds to the AxNU case in Table 4. It

can be observed that denaturing the thorium in the Ax design reduces the achievable burnup to below the all-uranium case, spoiling the benefit. The optimization of the local H/HM ratio for the axial micro-heterogeneous designs was not investigated, however the achievable burnup was found to improve by adding central voids inside the fuel pellets and graphite spacers between them, which correspond to the Ax4V and AxC cases in Table 4. The checkerboard pin pattern (Case ChK) fuel exhibits a 7% improvement over to the all-uranium case, but denaturing of the thorium eliminates this benefit.

Table 4. The configurations and burnup performance for various micro-heterogeneous designs (based on 35%UO_2-65%ThO_2)

	Symbol	Fuel	r (mm)	h **(mm)	Composition	B1** MWd/kg	DB1 over all-U (%)
Duplex, ThO_2 inside	ThU	ThO_2	3.3813	--*	100 w/o Th	48.49	-9.5%
		UO_2	4.1274	--	19.5 w/o U235		
Duplex, ThO_2 outside	UTh	ThO_2	2.3668	--	100 w/o Th	53.57	0
		UO_2	4.1274	--	19.5 w/o U235		
Axial micro-heterogeneous	Ax	ThO_2	4.1274	20.41	100 w/o Th	57.10	6.6%
		UO_2	4.1274	10.0	19.5 w/o U235		
Denatured Ax	AxNU	ThO_2-UO_2	4.1274	20.49	12w/o U/HM (0.711w/o U235)	51.08	-4.8%
		UO_2	4.1274	10.0	19.5 w/o U235		
Ax with 2.5mm graphite spacer	AxC	ThO_2	4.1274	20.41	100 w/o Th	60.73	13%
		UO_2	4.1274	10.0	19.5 w/o U235		
Axial micro-heterogeneous, taller stack	Ax4	ThO_2	4.1274	81.64	100 w/o Th	60.48	13%
		UO_2	4.1274	40.0	19.5 w/o U235		
Ax4 with 20vol/o central void	Ax4V	ThO_2	4.1274	81.64	100 w/o Th	61.78	15%
		UO_2	4.1274	50.0	19.5 w/o U235		
		Void	1.8458	50.0	Helium		
Ax4 with duplex ThO_2-UO_2 and UO_2 / graphite	DuUAx4	ThO_2/UO_2	4.1274/1.137	91.0	100 w/o Th/19.5 w/o U235	55.94	4.5%
		UO_2	4.1274	40.0	19.5 w/o U235		
		Center	2.0635	40.0	Graphite		
Checkerboard (1x1) un-denatured	ChK	ThO_2	4.7820	--	100 w/o Th	57.32	7.0%
		UO_2	3.3472	--	19.5 w/o U235		
Checkerboard (1x1) denatured	ChKD	ThO_2	4.7820	--	15 w/o U/HM (10.0 w/o U235)	51.20	-4.6%
		UO_2	3.3472	--	16.826 w/o U235		
Homogeneous Th andU fuel	Hom	ThO_2/UO_2	4.1274	--	65 w/o Th	48.16	-10%
All-UO_2 Ref. Case**	All-U	UO_2	4.1274	--	6.825 w/o U235	53.55	0

* -- means material is axially uniform.

** h = pellet layer stack height; B_1 = reactivity-limited batch burnup; All-U Ref Case has same U-235/HM ratio

In search of an optimal design, the k-infinity at beginning-of-cycle and B1 as functions of UO_2 segment height for an axial un-denatured case, an axial denatured (with natural uranium) case, and a checkerboard-axial un-denatured case were calculated and the results are shown in Figure 17. It can be seen that B1, the reactivity-limited batch burnup, of the un-denatured axial and checkerboard-axial (ChKAx) designs can slightly exceed 60 MWd/kg iHM at UO_2 segment heights of 4cm and 8cm respectively, but the B1 of the denatured axial case is about 10% less than that of the un-denatured axial case. The checkerboard-axial design behaves differently in that when its B1 peaks, its k-infinity at beginning-of-life is still high, which means that the "burnable poison effect" seen in the axial case disappears. Figure 17 shows that the most promising arrangement with respect to reactivity-limited achievable burnup is the axial micro-heterogeneous design with UO_2 and thorium section lengths of 4 and 8cm. In addition, this design offers the benefit of substantial reduction of poison to compensate for the reactivity excess at beginning-of-life.

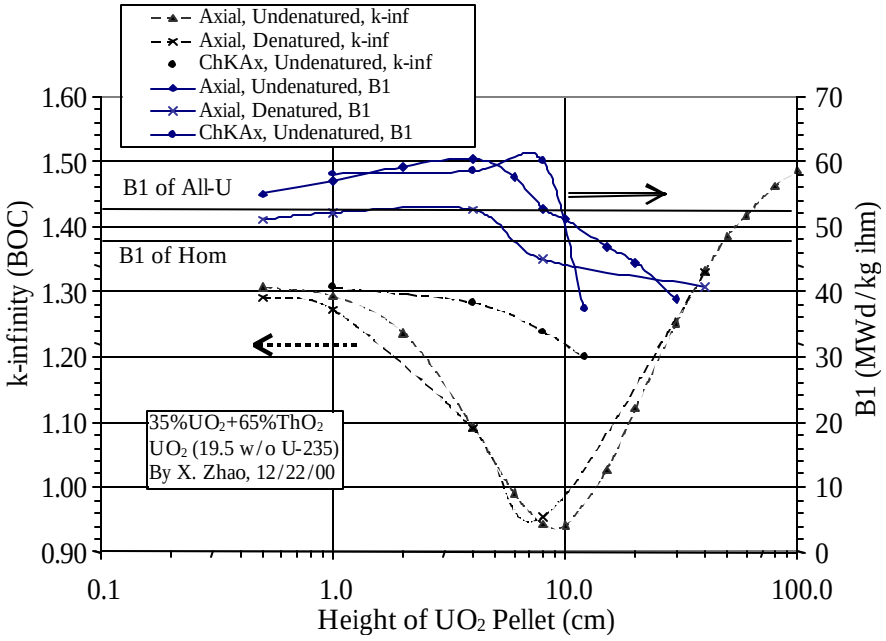

Figure 17. K_∞ (B=0) and B1 as functions of UO_2 segment height in axial micro-heterogeneous Th/U fuel.

The higher reactivity-limited burnup is due to a combination of spectral and mutual shielding effects. The spectral shift was identified as a key underlying phenomenon for the observed benefits and is also responsible for the "burnable poison effect". The local highly thermalized spectrum in the ThO_2 section results in a high capture rate in the Th-232 at beginning-of-life, depressing reactivity. Thus, excess neutrons at beginning-of-life are used to breed U-233, which is available later during the cycle for fissions to increase reactivity. Moreover, the harder spectrum at end-of-life reduces the conversion ratio thus increasing reactivity. Separation of thorium and uranium further improves reactivity-limited burnup due to the reduction of mutual resonance shielding of overlapping resonances of the two nuclides. However, the magnitude of this effect appears to be small. The reduction in total resonance absorption in U-233 shielded by U-238 was found to be only about 2%, whereas the corresponding value for U-235 is about 1%. Therefore, the major benefits of spatial separation of thorium and uranium come from spectral effects; the effect of mutual shielding of resonances on reactivity and burnup performance is marginal.

Although axial micro-heterogeneous designs of the Ax4 type manifest appreciable neutronic advantages, the absence of fissile material in the ThO_2 section at beginning-of-life results in a

large local power peaking (4.5). The most effective way to reduce local peaking is to add uranium with fissile U-235 into the ThO_2 section. However, because homogeneous mixing of uranium in the thorium slug significantly impairs the reactivity-limited burnup performance, a modified axial and radial micro-heterogeneous fuel pin design (DuUAx4), shown in Figure 18, was designed by introducing a 25 vol% central void in the UO_2 driver zone and moving the extra UO_2 into the blanket zone as an inner ring with ThO_2 as an outer ring. Figure 19 shows the power peaking for two different U-235 enrichments in the UO_2 core of the blanket section.

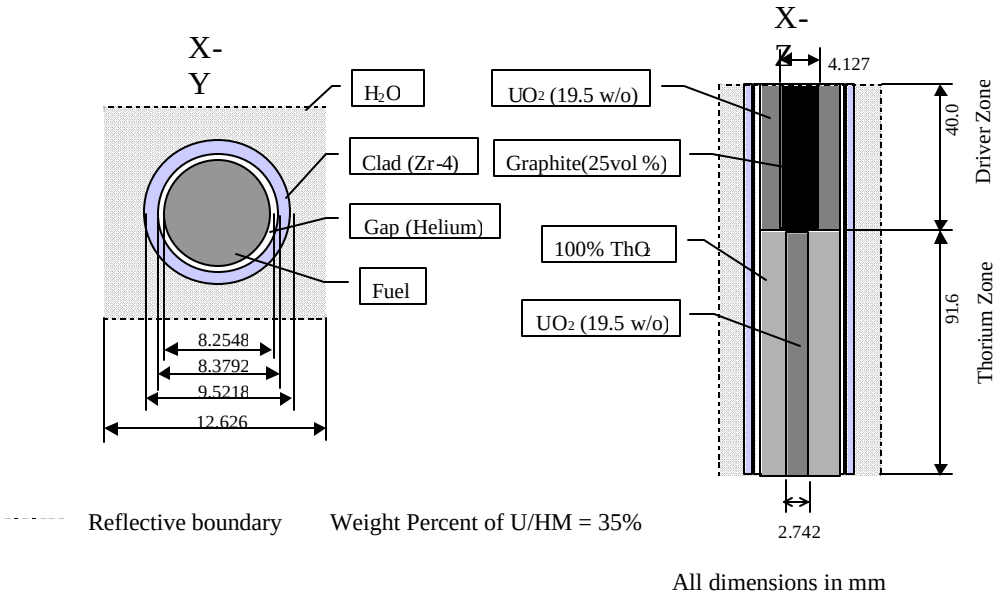

Figure 18. A modified axial and radial micro-heterogeneous fuel pin design (DuUAx4).

As can be seen from Table 4, the reactivity-limited burnup of the DuUAx4 design is significantly impaired in comparison with the optimized Ax4 design, albeit to a lesser extent than for the case of homogeneously mixed Th and U in the thorium section. In addition, the DuUAx4 arrangement loses the desirable "burnable poison-like" effect. However, the DuUAx4 configuration with a driver height of 4cm yields a combination of reasonable neutronics performance and power peaking, therefore, it was selected for further thermal hydraulic evaluations.

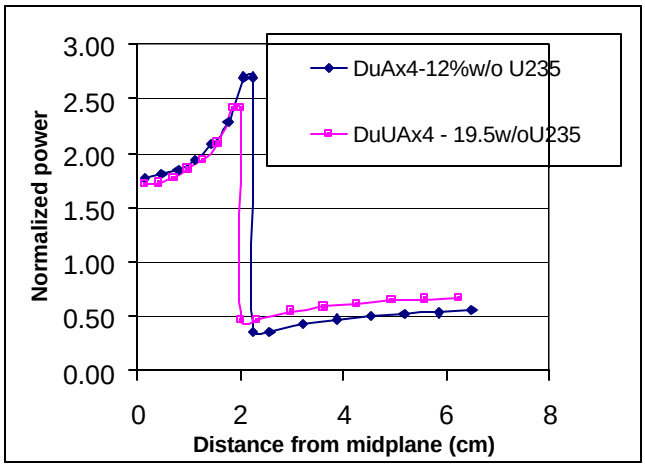

Figure 19. Power density profile for the DuUAx4 micro-heterogeneous fuel pin design.

Heavy metal resource utilization and enrichment services (or SWU) utilization account for most of the cost of a fuel cycle. The heavy metal resource utilization for the Hom Th/U, Ax4 Th/U, and all-uranium cases as a function of the mixing ratio (U/HM) is shown in Figure 20. The

SWU utilization plot [MacDonald et al., 2001] has the same trend. The performance of the Th/U Hom fuel asymptotically approaches that of the all-uranium fuel as the ratio of the uranium to total heavy metal increases, but the performance of the Th/U Ax4 fuel shows an almost constant 10% improvement over that of the Th/U Hom fuel. Two important conclusions are that: (1) Th/U Hom fuel can never outperform the all-uranium fuel neutronically, but (2) micro-heterogeneous Th/U fuel has the potential to outperform the all-uranium fuel when the mixing ratio is at or above 50%UO_2-50%ThO_2. However, for the 35%UO_2-65%ThO_2 ratio, the Ax4 Th/U fuel still has poorer SWU utilization (heavy metal resource utilization is equivalent to the all-U). Therefore, the ThO_2-UO_2 fuels were found to be more expensive than UO_2 fuels.

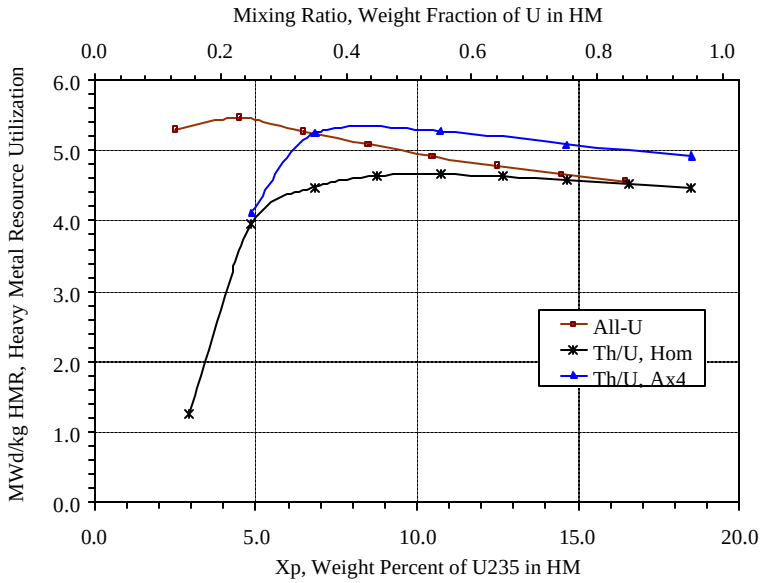

Figure 20. Comparison of heavy metal [U_{NAT}+Th] resource utilization of all-U, Th/U Hom, and Th/U Ax4 cases.

In terms of plutonium generation, micro-heterogeneous fuel is more proliferation-resistant than the Hom fuel, while the Hom fuel is more proliferation-resistant than the all-uranium fuel. Although the uranium discharged in the thorium zone of the Ax4 un-denatured design is a proliferation-prone material with high U-233 weight fraction and small critical mass, the multiples of critical mass available from the Ax4 un-denatured case is still smaller than that of the of plutonium produced in the all-uranium case. In addition, the separation of uranium from thorium is generally more difficult than extraction of plutonium from uranium. On a pellet-average basis, the DuUAx4 fuel is the most proliferation-resistant case. Whether the duplex arrangement can be credited as an effective means to denature U-233 must be resolved. Table 5 summarizes key neutronic and proliferation characteristics of axial micro-heterogeneous fuels.

Table 5. Key values of neutronics, thermal-hydraulics, and proliferation-resistance of various fuels, based on 35%UO_2 and 65%ThO_2 with the same U-235 initially invested.

	Ax4 Fuel	Ax4NU Fuel	DuUAx4 Fuel	Hom Fuel	All-U Fuel
B1 (MWd/kg)	60.48	52.85	55.94	48.16	53.55
Local Power Peaking Factor	4.5	4.3	2.4	1.0	1.0
Pu Production (kg/GWe-year)	70.72	110.3	77.87	108.0	232.2
Effective Uranium Fissile Ratio (U-233+0.6U-235)/U_{tot}	75.4%(1)	13.3%(1)	14.98%(1)(2)	7.9%	0.76%
Multiples of Critical Mass [Pu+U] / GWe-year	12.3	7.51	6.6	12.1	10.8

(1) uranium from the thorium zone. (2) pellet average

Local power peaking superimposed on a typical chopped cosine shape poses a challenge to the DNBR margin and the centerline fuel temperature, even for the DuUAx4 case, which exhibits the smallest power peaking among all axial micro-heterogeneous configurations. However, in spite of the large local power peaking (see Figure 21), the DNBR calculated by the W-3 correlation stays above the 1.3 limit, as shown in Figure 22. This is due to the immediate upstream effect of the relatively cold boundary layer coming from the thorium section that significantly alleviates the DNBR problem in the high flux driver region. These results are further supported by the experimental data from the LWBR program, where periodic heat flux spikes were applied and found to have no distinguishable effect on CHF in comparison with uniformly heated rod data.

Radial fuel temperature profiles in the UO_2/graphite duplex pellet and in UO_2/ThO_2 pellets of DuUAx4 design are presented in Figure 23. The case of a voided UO_2 pellet was also investigated, but the differences in peak fuel temperatures between the voided and graphite cases are small because the gamma and neutron heat generated in the central graphite section is negligible. Surprisingly, the centerline temperature in the UO_2/ThO_2 section is higher than the maximum temperature in the driver UO_2 section in spite of the small heat generation in this section. This is because all the heat at beginning-of-life is generated in the small UO_2 core with relatively high enrichment and must be conducted across the entire thorium thickness. The peak centerline temperatures remains below the melting point of the UO_2 in both sections, albeit by a lower margin than for the reference PWR UO_2 rods. Large axial temperature gradients result in non-negligible

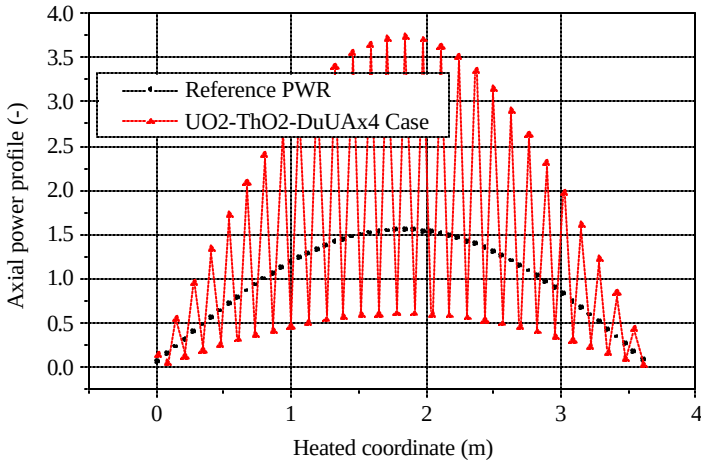

Figure 21. Axial heat flux profile for PWR and the DuUAx4 fuel case.

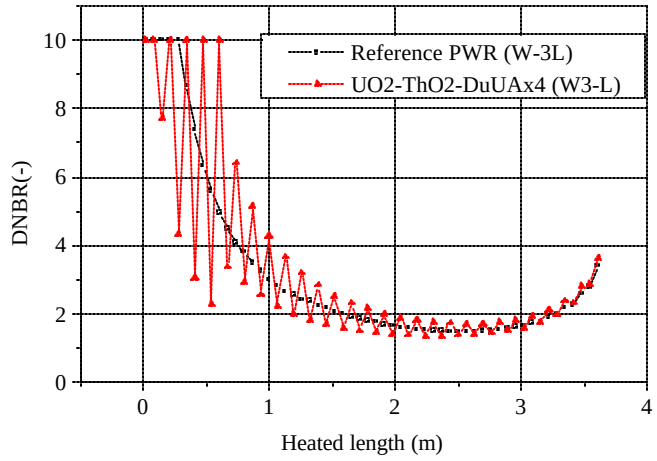

Figure 22. DNBR in the hot channel using the W-3 CHF correlation.

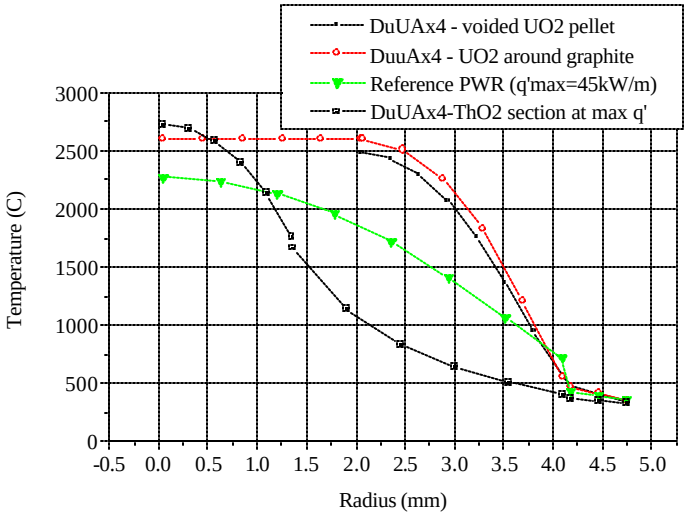

Figure 23. Radial temperature profiles at the hot spot.

conduction in the axial direction. To quantify this effect, a 3-D model using HEATING7 [Childs 1993] was used. Accounting for axial conduction reduces the peak fuel temperature in the UO_2 driver section by up to 500°C, depending on the contact resistance between the UO_2 and ThO_2 pellets. However, the peak centerline temperature in the UO_2 core of the ThO_2 section is only slightly smaller than that obtained by the 1-D conduction solution, thus the effect of the axial heat conduction on the peak temperature in the UO_2/ThO_2 section is marginal.

Even though the thermal hydraulic analyses of the DuUAx4 design suggests that the DNBR and fuel melting margins can be met, the high peaking in the driver section at beginning-of-life, and the large power density imbalance between the driver and thorium zones would have to be reduced further to alleviate other problems, such as zirconium hydride formation and subsequent embrittlement of cladding in the regions of large temperature gradients, enhanced fission gas release in the high-temperature driver section, and uneven thermal expansion of the pellets in these regions and excessive PCI in the driver section.

Because the 4.5% burnup increase achievable with DuUAx4 fuel is not sufficient to offset the significantly higher manufacturing cost of this relatively complex axially micro-heterogeneous duplex fuel, subsequent efforts were focused on the optimization of radial micro-heterogeneous fuel to identify if similar burnup improvement can be achieved in a simpler geometry.

The study of basic fuel configurations in Table 4 involved a checkerboard configuration in a 1x1 array without considering the different sizes of the heterogeneous regions. Various checkerboard arrangements were investigated in more detail including the more practical cases of radial checkerboard arrangements with denatured thorium pins. Four base cases (without guide tubes) with an increasing degree of heterogeneity, with and without denaturing (with enriched uranium), were considered – see Figure 24. The thorium fuel composition had 15 w/o of 10% enriched UO_2 in the ThO_2. The total fraction of ^{235}U in the assembly was maintained constant by adjusting the uranium enrichment of the seed fuel. This fraction of ^{235}U corresponds to the homogeneous 35 w/o UO_2 (19.5% enriched) – 65 w/o ThO_2 case; namely, 6.825 w/o ^{235}U in the entire fuel assembly. The reference PWR unit cell geometry has a fuel to moderator volume ratio of about 1.6, while all of the radial micro-heterogeneous cases have a global Vm/Vf ratio of about 2.0. Therefore, the homogeneous and all-uranium cases presented in this study included both a reference PWR unit cell geometry case and a 4x4 pin arrangement case with the dimensions presented in Figure 24 to allow for consistent comparisons with the other micro-heterogeneous arrangements. The results of the calculations are summarized in Figure 25.

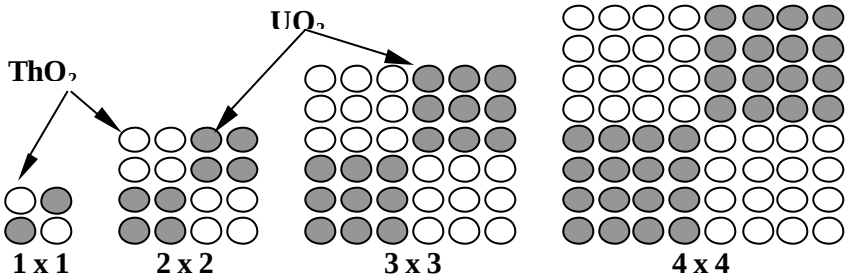

Dimensions	UO_2	ThO_2
Fuel pellet radius (mm)	3.322	4.746
Fuel rod radius (mm)	3.852	5.503
Pitch (mm)	12.60	12.60

Figure 24. Radial-heterogeneous fuel arrays.

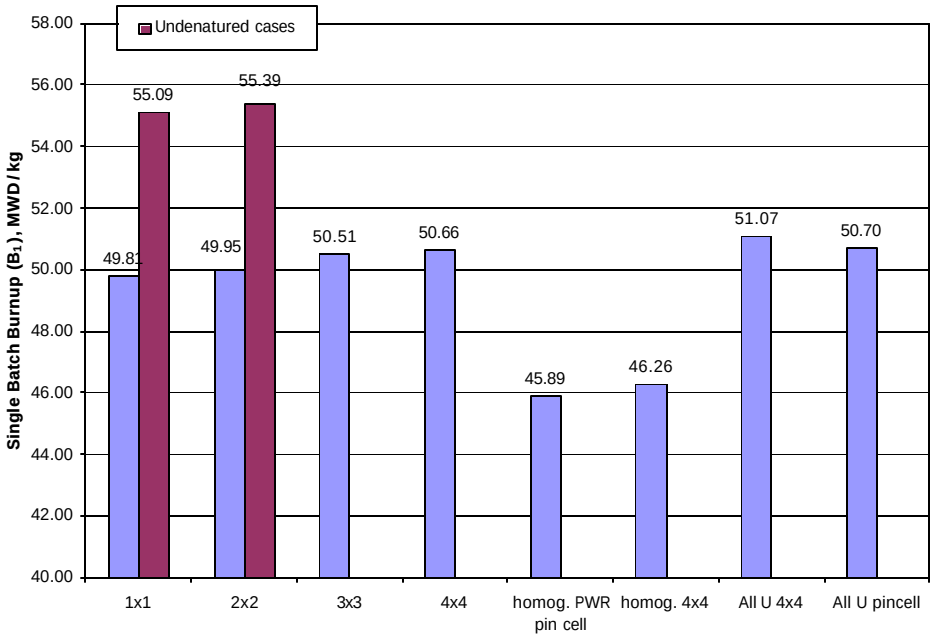

Figure 25. Single batch burnup for homogeneous and radial heterogeneous geometries.

The results showed that:

- There is a modest increase in discharge burnup with an increase in the size of heterogeneous regions.
- All considered heterogeneous geometries with denatured fuel have no advantage over the all-uranium case. The burnup improvement versus the homogeneous case is 7 to 9.5%.
- The effect of thorium fuel denaturing is significant. It results in lower burnup by about 11% compared to an un-denatured case for the 2x2 geometry configuration.
- The burnup of the uranium rods is very high in both the denatured and un-denatured cases (e.g. the 3 batch burnup will be roughly 1.5 times the B_1 value of Figure 25). This raises the issue of designing fuel rods that can withstand such high irradiation.

A more realistic study was carried out including the effects of the guide tube positions and water gaps between the fuel assemblies and varying the ^{235}U content to identify blanket fuel compositions that will result in acceptable power peaking and uranium isotopic composition in the discharged blanket fuel. The power peaking at beginning-of-life was found to decrease monotonically and the achievable burnup to increase monotonically with increasing ^{235}U content. The highest power peak value of about 1.7 corresponded to 10 w/o of 10% (about 1w/o U-235 in mixture) enriched uranium and the smallest value of about 1.2 corresponded to 30 w/o of 20% enriched uranium (6w/oU-235 in mixture). Based on the thermal hydraulic analyses, which showed that a power peaking ≤ 1.5 can be accommodated, 20w/o uranium with at least 15w/o enrichment (3w/o U-235 in mixture) is needed for a practical design.

Finally, the possibilities to increase the reactivity-limited burnup in the checkerboard configurations through variation of the moderator to heavy metal (V_m/V_f) ratio in the seed and blanket regions were explored. The V_m/V_f ratio was varied by introducing a void into the center of a fuel pellet and by changing the outside fuel pellet diameter and the ratio of uranium heavy metal to thorium heavy metal; the assembly average ^{235}U loading (6.82 w/o), which corresponds to the homogeneous (35 w/o U – 65 w/o Th) case, and the seed uranium enrichment (19.5 %)

were kept fixed in all cases calculated. A sensitivity analysis of the achievable reactivity limited burnup to the V_m/V_f ratio was performed separately for the seed and blanket unit cells.

The reference seed solid pin geometry (with the highest V_m/V_f ratio) was found to exhibit the best burnup performance and the decrease of the seed unit cell V_m/V_f ratio had a negative effect on the achievable burnup. An optimum value of V_m/V_f ratio was not observed, but cases with higher than the reference value of V_m/V_f were not investigated because further reduction of the fuel pin diameter increases the heat flux to the coolant significantly, thus challenging the MDNBR limit. An alternative arrangement of the seed and blanket fuel pins within an assembly with higher V_m/V_f ratio, where the seed fuel pins were located around the guide tubes in order to take advantage of extra water available in these regions, achieved a moderate increase of about 2% in the single batch burnup.

The sensitivity of the reactivity-limited achievable burnup to the V_m/V_f ratio in the blanket was analyzed by introducing a void into the center of the blanket fuel pellet and by increasing the number of blanket fuel pins. The reference seed unit cell geometry, which had the highest V_m/V_f ratio and achieved the highest burnup, was maintained fixed. Burnup was found to increase with the increase of V_m/V_f in the blanket, but the gain was not significant. The effect of an increase of V_m/V_f ratio through the reduction of the outside fuel pin diameter, not maintaining the uranium to thorium ratio on achievable burnup, was also investigated. As can be observed on Figure 26, the burnup curve in terms of the effective-full-power-days has a maximum at the blanket V_m/V_f ratio of about 1.5 despite the smaller amount of thorium in the assembly. The improvement in burnup performance is about 2.7 % in comparison with the reference seed and blanket unit cell geometries. However, note that this burnup improvement is a result of an increased neutron moderation effect and, therefore, more efficient utilization of the fissile ^{235}U. Should this higher V_m/V_f ratio be used with current UO_2 fuel pins, a similar increase of burnup would be observed.

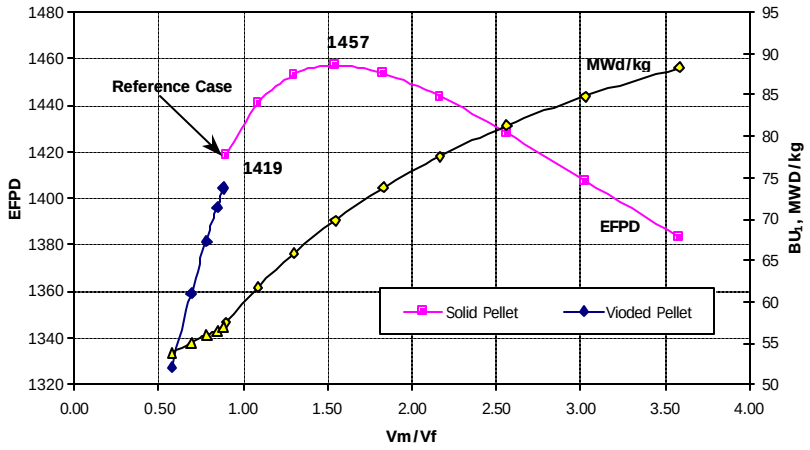

Figure 26. Single batch burnup for full assembly radial heterogeneous un-denatured case as a function of blanket Vm-to-Vf ratio.

The results of the analyses of the radial micro-heterogeneous arrangement show that these configurations can improve burnup capabilities of uranium-thorium fuel to some extent (up to 8%). However, denaturing of the thorium, which is necessary to prevent misuse of bred-in ^{233}U from the discharged thorium rods and to maintain acceptable power peaking at beginning-of-life, degrades the burnup performance to values that are about the same as for all-uranium fuel. More importantly, this micro-heterogeneous arrangement exhibits high burnup of seed fuel rods, which goes well beyond the current experience base. Therefore, radial micro-heterogeneous concepts are not as promising as the axial micro-heterogeneous configurations.

In summary, the studies on micro-heterogeneous ThO_2/UO_2 fuels confirmed that these fuels can increase fuel discharge burnup by 20-30% compared to the same fuel when homogenized, and reduce plutonium production 2 or 3 times in comparison with all-uranium fuel. However, denaturing of the thorium, to reduce the power peaking at beginning-of-life and deter the potential for extraction of bred-in U-233 from the discharged blanket regions, significantly reduces this benefit. The DuUAx4 fuel design was found to exhibit the largest reactivity-limited burnup and acceptable thermal hydraulic performance. However, its 4.5% burnup increase over the all-uranium fuel is not sufficient to offset the significantly higher manufacturing cost of such relatively complex axial micro-heterogeneous duplex fuel. Also, simple checkerboard micro-heterogeneity does not offer sufficient burnup improvements over the all-uranium fuel. Therefore, our recent work has focused on the use of thorium fuels for plutonium burning.

1.2. Thorium Based Fuel as a Plutonium Disposition Option

Thorium, as a fertile material, generates very little plutonium during its irradiation. As a result, thorium based fuels represent an excellent potential for disposition of the existing and future stockpiles of reactor and excess weapons grade plutonium. We discuss the different plutonium disposition options in the LWR thorium based fuel cycle in this section.

The objectives of this study are different from the objectives of the prior UO_2-ThO_2 fuel design optimization. In the investigation of the uranium – thorium fuel, the main goal was to maximize the amount of energy extracted from the fuel per initial investment of fissile ^{235}U. This parameter is directly related to the economic efficiency of the fuel cycle. In this study, each proposed disposition option will be assessed and optimized with respect to the following two most important performance parameters:

1. Plutonium destruction rate, i.e., the number of kilograms of plutonium burnt per unit energy produced by the fuel.
2. The residual amount of plutonium in the discharged fuel, i.e. the amount of plutonium per unit energy produced that will have to be recycled or finally disposed of in a geological repository. Optimization of this parameter is important because it indicates the "quality" of plutonium destruction. In addition, a diluted isotopic plutonium vector in discharged fuel will be desirable to enhance proliferation resistance.

In addition, each plutonium disposition option will be evaluated in terms of reactivity and reactor control related parameters in order to assure safe reactor operation.

The first step in this investigation was the assessment of the computational tools and data libraries available for neutronic analysis of plutonium disposition options. These include the CASMO-4 Fuel Assembly Burnup Code [Edenius et al. 1995] and MCODE – an MCNP4C and ORIGEN2 coupling code [Xu et al., 2002a]. Two benchmarks– a pin cell and a fuel assembly having a repeating typical PWR lattice – were evaluated.

1.2.1. Benchmark Calculations

1.2.1.1. Pin Cell Benchmark Description

The first benchmark calculations were performed using CASMO-4 and MCODE for homogeneously mixed PuO_2-ThO_2 fuel in PWR pin-cell and fuel assembly geometries. The fuel

composition used in this benchmark included 95.5 weight % of thorium and 4.5 weight % of reactor grade plutonium. The fuel composition, geometry and parameters for the benchmark runs were chosen to be identical to those used in a similar benchmarking task performed within the framework of IAEA Coordinative Research Program (CRP) on "Potential of Thorium-based Fuel Cycles to Constrain Plutonium and to Reduce the Long-Lived Waste Toxicity" [Ruetten et al. 2000]. CRP participants from 8 different countries performed this benchmark. Each participating team used its own computational tools and data libraries. None of the teams used either CASMO-4 or MNCP-ORIGEN type computer codes.

The description of PWR pin-cell geometry and operating conditions used for the first part of the benchmark is shown in Figure 27. The materials compositions for each zone in the fuel pin cell are summarized in Table 6.

The task of this benchmark was to calculate the fuel burnup at a constant power (211 W/cm) as a function of time, without using any burnable poison for reactivity control. The following parameters are reported for a burnup of 0, 30, 40 and 60 MWd / kg of initial heavy metal:

- Neutron multiplication (K_{inf}),
- Total neutron flux,
- Average energy per fission,
- Residual amount of plutonium,
- Fraction of fissile plutonium,
- Amount of generated minor actinides, and
- Amount of bred ^{233}U.

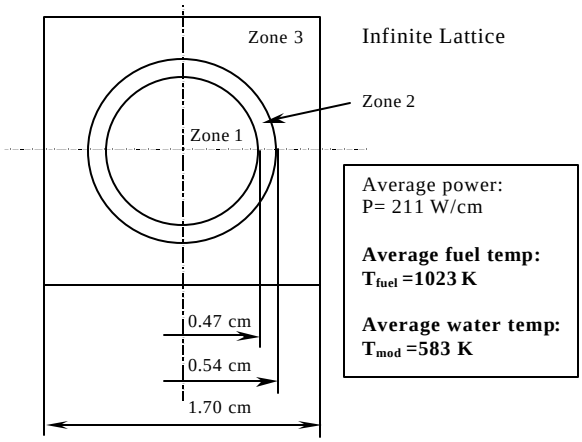

Figure 27. Reference pin cell geometry.

Table 6. Initial nuclide densities in the pin cell (atoms/cm^3).

	Zone 1	Zone 2	Zone 3
Th-232	2.11E+22		
Pu-238	9.72E+18		
Pu-239	5.99E+20		
Pu-240	2.32E+20		
Pu-241	7.69E+19		
Pu-242	4.78E+19		
Cr		8.14E+19	3.20E+20
Mn			2.11E+19
Fe		1.60E+20	8.46E+20
Ni			3.76E+20
Zr		4.37E+22	
C			2.68E+18
H			4.80E+22
O	4.41E+22		2.40E+22

1.2.1.2. Pin Cell Calculation Benchmark Results

The results of the PWR pin cell benchmark obtained from CASMO-4 and MCODE are compared with IAEA CRP results in Tables 7 through 11 and Figures 28 and 29. The fuel criticality is predicted with reasonable accuracy by all codes. The results for the average energy per fission, average neutron flux, plutonium isotopes destruction rate, as well as build-up of ^{233}U and minor actinides are also in a good agreement.

Since the details about the codes used by other participants were not available to us, the discussion on possible reasons behind the differences will be focused on CASMO4 versus MCODE results. The discrepancy on $k_{infinty}$ ranges between about 2% ? ? at beginning-of-life to about 5% at end-of-life. The beginning-of-life criticality predicted by CASMO4 is slightly higher than that predicted by MCODE and other codes. CASMO4-calculated reactivity versus MCODE

results is higher even though the fuel temperature used in MCODE was lower than the fuel temperature of 1023K defined in the benchmark. Note that the cross-section data for fuel nuclides used in MCODE calculations were available only at 900K. The reasons for this discrepancy most likely lies in different libraries used in MCODE and CASMO4, as discussed below.

Table 7. Infinite medium neutron multiplication factor as a function of burnup.

Burnup(MWd/kg)	0.0	30	40	60
Germany	1.136	0.908	0.862	0.810
Russia	1.123	0.915	0.876	0.838
China	1.131	0.913	0.868	0.824
Korea	1.118	0.910	0.870	0.830
India	1.112	0.889	0.851	0.822
USA	1.110	0.911	0.873	0.832
Japan	1.135	0.921	0.881	0.841
Netherlands	1.125	0.925	0.887	0.848
CASMO4 (MIT)	1.142	0.915	0.870	0.824
MCODE (MIT)	1.121± 0.0014	0.916±0.0013	0.874±0.0012	0.837±0.0012

Table 8. Residual amount of plutonium (Pu / Pu initial) as a function of burnup.

Burnup (MWd/kg)	0.0	30	40	60
Germany	1.00	0.42	0.29	0.13
Russia	1.00	0.43	0.31	0.16
China	1.00	0.40	0.28	0.12
Korea	1.00	0.41	0.28	0.14
India	1.00	0.41	0.29	0.14
USA	1.00	0.43	0.30	0.16
Japan	1.00	0.43	0.31	0.16
Netherlands	1.00	0.43	0.31	0.16
CASMO4 (MIT)	1.00	0.43	0.30	0.16
MCODE (MIT)	1.00	0.43	0.31	0.16

Table 9. Fraction of fissile plutonium (Pu fissile / Pu init.) as a function of burnup.

Burnup (MWd/kg)	0.0	30	40	60
Germany	0.70	0.42	0.34	0.23
Russia	0.70	0.40	0.32	0.19
China	0.71	0.39	0.31	0.23
Korea	0.70	0.39	0.29	0.18
India	0.70	0.38	0.30	0.17
USA	0.70	0.41	0.34	0.21
Japan	0.70	0.41	0.32	0.18
Netherlands	0.70	0.41	0.33	0.21
CASMO4 (MIT)	0.70	0.41	0.32	0.18
MCODE (MIT)	0.70	0.41	0.33	0.21

Table 10. Minor actinides fraction (MA / Pu initial) as a function of burnup.

Burnup(MWd/kg)	0.0	30	40	60
Germany	0.00	0.037	0.049	0.069
Russia	0.00	0.033	0.043	0.065
Korea	0.00	0.035	0.048	0.069
USA	0.00	0.036	0.047	0.068
Japan	0.00	0.037	0.048	0.069
Netherlands	0.00	0.037	0.049	0.070
CASMO4 (MIT)	0.00	0.034	0.044	0.062
MCODE (MIT)	0.00	0.039	0.052	0.074

Table 11. Bred ^{233}U fraction (^{233}U / Pu initial fissile) as a function of burnup.

Burnup(MWd/kg)	0.0	30	40	60
Germany	0.00	0.37	0.44	0.50
Russia	0.00	0.40	0.47	0.53
China	0.00	0.39	0.45	0.51
Korea	0.00	0.41	0.48	0.54
India	0.00	0.40	0.47	0.51
USA	0.00	0.41	0.48	0.54
Japan	0.00	0.38	0.44	0.50
Netherlands	0.00	0.41	0.48	0.54
CASMO4 (MIT)	0.00	0.36	0.42	0.47
MCODE (MIT)	0.00	0.38	0.44	0.50

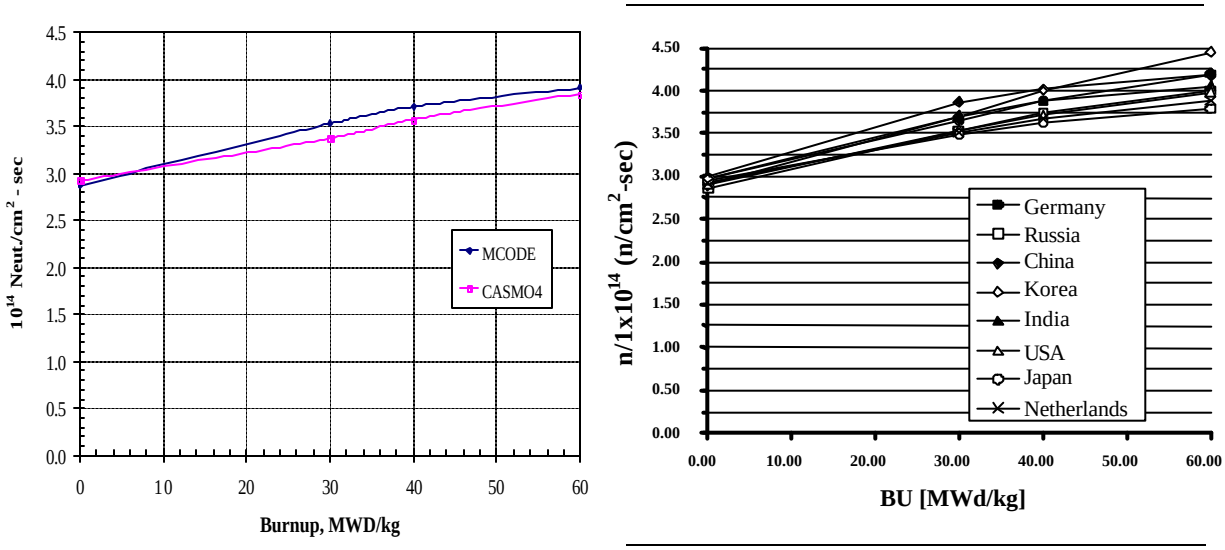

Figure 28. Total neutron flux: MIT vs. IAEA benchmark comparisons.

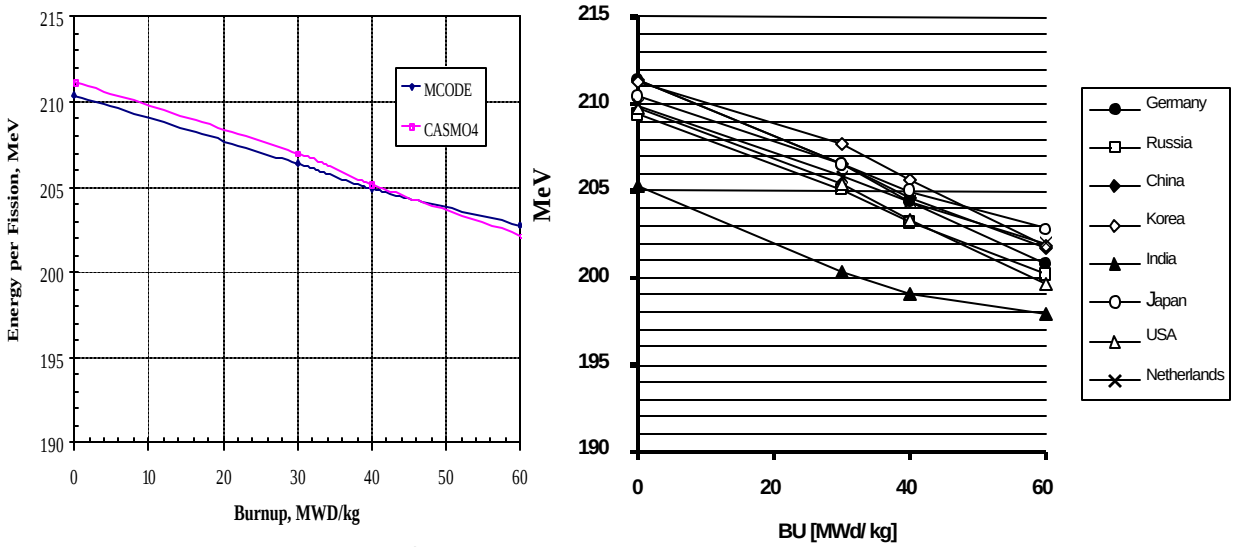

Figure 29. Energy per fission: MIT vs. IAEA benchmark comparisons.

The slope of the criticality curve calculated by CASMO4 is steeper than that obtained by MCODE. There are two reasons for this disagreement:

1. Differences in the number of fission products and actinides tracked in MCODE. One hundred fission products and 29 actinides were tracked in MCODE calculation while one hundred and eight individual nuclides are considered in CASMO4 depletion calculations.
2. Differences in libraries between these two codes. MCODE utilized primarily ENDF-VI cross-section data. CASMO4 cross-section data are based on evaluated data files JEF-2.2 and ENDF/B-VI that are processed by NJOY-91.91 to generate libraries in 70 energy groups in CASMO4 format.

Also it is to be noted that CASMO4 has a higher recoverable energy per fission than ORIGEN2.1 but exhibits a faster burnup rate, i.e. against the expectations based on fission energy difference. Thus, the effect of differences in fission products and cross sections is more important than the differences in recoverable energy per fission.

1.2.1.3. PWR Lattice Benchmark Description

This part of the benchmark was performed in order to assure the capability of CASMO-4 and MCODE computer codes to manage assembly level 2D transport calculations with fuel depletion. As in the first part of the benchmark, the results obtained with CASMO-4 and MCODE will be compared with the results obtained by the participants of the IAEA Coordinative Research Program.

The calculations were performed for a 17x17 PWR fuel assembly with octant symmetry. The assembly included 25 water hole positions without guide tubes. The assembly cans were not considered. The calculations were carried out at a constant power density of 37.7 kW/kg of initial heavy metal and with zero buckling. The assembly and fuel pin geometry are described in Table 12. The material compositions are given in Table 13.

Table 12. PWR assembly and fuel pin geometry description.

Outer dimensions (cm):	22.662×22.662
Cell pitch (cm):	1.33306
Fuel pellet radius (cm):	0.4127
Cladding thickness (cm):	0.0617
Equiv. Cell radius (cm):	0.7521

Table 13. PWR assembly material composition (atoms / barn – cm).

Fuel - 5% PuO2 + 95% ThO2. Temperature 900 K	
Th-232	2.0592e-2
Pu-238	2.2900e-5
Pu-239	7.4780e-4
Pu-240	2.9030e-4
Pu-241	1.5340e-4
Pu-242	5.0100e-5
O-16	4.3710e-2
Cladding - Natural Zr. Temperature 600 K	
Zr (natural)	4.3241e-2
Moderator - Light water, with 500 ppm Natural Boron. Temperature 573 K	
H-1	4.7708e-2
O-16	2.3854e-2
B-10	3.9518e-6
B-11	1.5906e-5

The task of the second part of benchmark was to calculate and compare the following parameters:

- Criticality as a function of burnup for burnup range between 0 and 60 MWd/kg,
- Fuel composition as a function of burnup (major actinides),
- Local pin-by-pin power distribution,
- Moderator temperature coefficient (MTC) for 0 and 60 MWd/kg,
- Doppler coefficient (DC) for 0 and 60 MWd/kg, and
- Soluble boron worth (BW) for 0 and 60 MWd/kg.

The reactivity coefficients are defined as follows.

$$\text{Moderator temperature coefficient - MTC} = \frac{\Delta K}{K_1 * K_2 * \Delta T_m},$$

where ΔT_m is the moderator temperature difference between two moderator temperatures T_1 and T_2 and K_1 and K_2 are neutron multiplication factors corresponding to temperatures T_1 and T_2, respectively.

$$\text{Doppler coefficient - DC} = \frac{\Delta K}{K_1 * K_2 * \Delta T_f},$$

where ΔT_f is fuel temperature difference between two fuel temperatures T_1 and T_2.

$$\text{Soluble Boron Worth - BW} = \frac{\Delta K}{K_1 * K_2 * \Delta C},$$

where ΔC is boron concentration difference in ppm.

1.2.1.4. PWR Benchmark Calculation Results

The results of this part of the benchmark are compared in Tables 14 through 16 and in Figures 30 and 31. The criticality predictions from the various codes agree within about 2.5% at the beginning-of-life and within 3.5% at 60 GWd/t. The results obtained from both CASMO4 and MCODE fall within this range of uncertainty. The beginning-of-life eigenvalue predicted by CASMO4 is slightly higher (by 1.7%) than that predicted by MCODE. Although the fuel temperature was the same in both codes (900K), the trend of higher reactivity prediction by CASMO4 at beginning-of-life and lower reactivity prediction at end-of-life remained the same as in the pin cell benchmark. The reasons for the differences are the same as discussed above for the unit cell calculations.

As in the pin cell benchmark task, the same number of nuclides (100 fission products and 29 actinides) was tracked in the MCODE depletion calculations. All of the fuel pins in the MCNP (MCODE) assembly model were defined as a single material. Thus, the effects of local neutron flux differences on the burnup of the individual pins could not be fully accounted for. Despite this simplification, the agreement in fuel isotopics prediction between MCODE, CASMO4, and the IAEA benchmark results is plausible. This is not surprising because the differences in neutron flux within the assembly are small. The good agreement of assembly-average fuel composition prediction between CASMO4 and MCODE suggests that a simplified MCODE full core model, which uses one material in an axial section of a fuel assembly, may yield good results. This would allow full core burnup simulation with MCNP-based codes at reasonable computer time.

Table 14. Infinite medium neutron multiplication factor versus burnup.

Burnup, MWd/kg	Russia	Japan	Korea	India	Israel	**CASMO**	**MCODE**
0	1.1890	1.1987	1.1734	1.2076	1.1956	**1.2035**	**1.1836± 0.0013**
0.5	1.1569	1.1670	1.1384	1.1736	1.1643	**1.1721**	**-**
20	1.0298	1.0521	1.0123	1.0372	1.0290	**1.0360**	**1.0233± 0.0013**
40	0.9147	0.9527	0.9057	0.9104	0.9119	**0.9115**	**0.9124± 0.0011**
60	0.8315	0.8657	0.8310	0.8294	0.8314	**0.8188**	**0.8318± 0.0011**

Table 15. Assembly-average fuel composition (actinides) as a function of burnup.

Assembly-Average Number Density (atoms/barn*cm)							
Burnup, GWd/T	Russia	Japan	Korea	India	Israel	**CASMO4**	**MCODE**
Th232							
0.0	$2.059*10^{-2}$	$2.059*10^{-2}$	$2.059*10^{-2}$	$2.059*10^{-2}$	$2.059*10^{-2}$	$2.059*10^{-2}$	$2.059*10^{-2}$
0.5	$2.059*10^{-2}$	$2.059*10^{-2}$	$2.059*10^{-2}$	-	-	-	-
20.0	$2.037*10^{-2}$	$2.036*10^{-2}$	$2.037*10^{-2}$	$2.036*10^{-2}$	$2.037*10^{-2}$	$2.038*10^{-2}$	$2.037*10^{-2}$
40.0	$2.011*10^{-2}$	$2.008*10^{-2}$	$2.011*10^{-2}$	-	$2.010*10^{-2}$	$2.013*10^{-2}$	$2.009*10^{-2}$
60.0	$1.977*10^{-2}$	$1.975*10^{-2}$	$1.978*10^{-2}$	$1.970*10^{-2}$	$1.977*10^{-2}$	$1.980*10^{-2}$	$1.975*10^{-2}$
Pu238							
0.0	$2.290*10^{-5}$	$2.290*10^{-5}$	$2.290*10^{-5}$	$2.290*10^{-5}$	$2.290*10^{-5}$	$2.290*10^{-5}$	$2.290*10^{-5}$
0.5	$2.279*10^{-5}$	$2.279*10^{-5}$	$2.279*10^{-5}$	-	-	-	-
20.0	$1.940*10^{-5}$	$1.952*10^{-5}$	$1.928*10^{-5}$	$1.829*10^{-5}$	$1.937*10^{-5}$	$1.929*10^{-5}$	$1.925*10^{-5}$
40.0	$1.834*10^{-5}$	$1.879*10^{-5}$	$1.798*10^{-5}$	-	$1.793*10^{-5}$	$1.744*10^{-5}$	$1.777*10^{-5}$
60.0	$1.687*10^{-5}$	$1.816*10^{-5}$	$1.636*10^{-5}$	$7.488*10^{-6}$	$1.611*10^{-5}$	$1.515*10^{-5}$	$1.607*10^{-5}$
Pu239							
0.0	$7.478*10^{-4}$	$7.478*10^{-4}$	$7.478*10^{-4}$	$7.478*10^{-4}$	$7.478*10^{-4}$	$7.478*10^{-4}$	$7.478*10^{-4}$
0.5	$7.348*10^{-4}$	$7.351*10^{-4}$	$7.349*10^{-4}$	-	-	-	-
20.0	$3.174*10^{-4}$	$3.270*10^{-4}$	$3.175*10^{-4}$	$2.993*10^{-4}$	$3.147*10^{-4}$	$3.154*10^{-4}$	$3.130*10^{-4}$
40.0	$0.810*10^{-4}$	$0.961*10^{-4}$	$0.820*10^{-4}$	-	$0.773*10^{-4}$	$0.7726*10^{-4}$	$0.773*10^{-4}$
60.0	$0.118*10^{-4}$	$0.170*10^{-4}$	$0.121*10^{-4}$	$0.479*10^{-4}$	$0.105*10^{-4}$	$0.0999*10^{-4}$	$0.106*10^{-4}$
Pu240							
0.0	$2.903*10^{-4}$	$2.903*10^{-4}$	$2.903*10^{-4}$	$2.903*10^{-4}$	$2.903*10^{-4}$	$2.903*10^{-4}$	$2.903*10^{-4}$
0.5	$2.911*10^{-4}$	$2.909*10^{-4}$	$2.911*10^{-4}$	-	-	-	-
20.0	$2.826*10^{-4}$	$2.678*10^{-4}$	$2.820*10^{-4}$	$2.846*10^{-4}$	$2.853*10^{-4}$	$2.810*10^{-4}$	$2.816*10^{-4}$
40.0	$1.981*10^{-4}$	$1.845*10^{-4}$	$1.991*10^{-4}$	-	$2.014*10^{-4}$	$1.951*10^{-4}$	$1.975*10^{-4}$
60.0	$0.809*10^{-4}$	$0.839*10^{-4}$	$0.874*10^{-4}$	$0.670*10^{-4}$	$0.846*10^{-4}$	$0.783*10^{-4}$	$0.838*10^{-4}$
Pu241							
0.0	$1.534*10^{-4}$	$1.534*10^{-4}$	$1.534*10^{-4}$	$1.534*10^{-4}$	$1.534*10^{-4}$	$1.534*10^{-4}$	$1.534*10^{-4}$
0.5	$1.540*10^{-4}$	$1.543*10^{-4}$	$1.541*10^{-4}$	-	-	-	-
20.0	$1.591*10^{-4}$	$1.703*10^{-4}$	$1.605*10^{-4}$	$1.545*10^{-4}$	$1.578*10^{-4}$	$1.613*10^{-4}$	$1.632*10^{-4}$
40.0	$1.233*10^{-4}$	$1.360*10^{-4}$	$1.231*10^{-4}$	-	$1.214*10^{-4}$	$1.236*10^{-4}$	$1.265*10^{-4}$
60.0	$0.650*10^{-4}$	$0.741*10^{-4}$	$0.641*10^{-4}$	$0.539*10^{-4}$	$0.639*10^{-4}$	$0.621*10^{-4}$	$0.662*10^{-4}$
Pu242							
0.0	$0.5010*10^{-4}$	$0.5010*10^{-4}$	$0.5010*10^{-4}$	$0.5010*10^{-4}$	$0.5010*10^{-4}$	$0.5010*10^{-4}$	$0.5010*10^{-4}$
0.5	$0.5050*10^{-4}$	$0.5043*10^{-4}$	$0.5051*10^{-4}$	-	-	-	-
20.0	$0.7088*10^{-4}$	$0.6813*10^{-4}$	$0.7248*10^{-4}$	$0.7203*10^{-4}$	$0.7020*10^{-4}$	$7.018*10^{-4}$	$6.8240*10^{-4}$
40.0	$0.9877*10^{-4}$	$0.9245*10^{-4}$	$1.0380*10^{-4}$	-	$0.9832*10^{-4}$	$0.990*10^{-4}$	$0.9517*10^{-4}$
60.0	$1.1890*10^{-4}$	$1.1030*10^{-4}$	$1.2880*10^{-4}$	$1.1624*10^{-4}$	$1.1940*10^{-4}$	$1.216*10^{-4}$	$1.1530*10^{-4}$
U233							
0.0	-	-	-	-	-	-	-
0.5	$0.7319*10^{-6}$	$0.7918*10^{-6}$	$0.7378*10^{-6}$	-	-	-	-
20.0	$1.5150*10^{-4}$	$1.5996*10^{-4}$	$1.5350*10^{-4}$	$1.5960*10^{-4}$	$1.5330*10^{-4}$	$1.4594*10^{-4}$	$1.5690*10^{-4}$
40.0	$2.6120*10^{-4}$	$2.7492*10^{-4}$	$2.6400*10^{-4}$	-	$2.6750*10^{-4}$	$2.539*10^{-4}$	$2.7180*10^{-4}$
60.0	$3.1350*10^{-4}$	$3.3109*10^{-4}$	$3.1600*10^{-4}$	$3.1910*10^{-4}$	$3.2350*10^{-4}$	$3.060*10^{-4}$	$3.2732*10^{-4}$
U234							
0.0	-	-	-	-	-	-	-
0.5	$0.2361*10^{-7}$	$0.2522*10^{-7}$	$0.1556*10^{-7}$	-	-	-	-
20.0	$0.8565*10^{-4}$	$0.9714*10^{-5}$	$0.8025*10^{-5}$	$0.9627*10^{-5}$	$0.7913*10^{-5}$	$0.7834*10^{-5}$	$0.856*10^{-5}$
40.0	$2.6680*10^{-4}$	$2.8855*10^{-5}$	$2.5200*10^{-5}$	-	$2.5290*10^{-5}$	$2.484*10^{-5}$	$2.658*10^{-5}$
60.0	$5.3200*10^{-4}$	$5.4315*10^{-5}$	$4.9070*10^{-5}$	$6.1950*10^{-5}$	$5.0450*10^{-5}$	$4.987*10^{-5}$	$5.1981*10^{-5}$

Water								
1.071 1.068 1.066 1.075	1.025 1.019 1.022 1.015			xxxx xxxx xxxx xxxx	Russia Japan Korea Israel			
1.069	**1.013**			**xxxx**	CASMO			
1.064±0.006	1.018±0.006			**xxxx**	MCODE			
1.059 1.068 1.067 1.076	1.014 1.02 1.023 1.016	1.015 1.021 1.025 1.018						
1.069	**1.016**	**1.016**						
1.071±0.006	1.008±0.004	1.01±0.006						
Water	1.068 1.068 1.067 1.075	1.072 1.071 1.071 1.078	Water					
	1.069	**1.069**						
	1.076±0.004	1.072±0.004						
1.063 1.066 1.065 1.074	1.016 1.018 1.023 1.015	1.009 1.023 1.027 1.02	1.084 1.084 1.084 1.091	1.08 1.068 1.085 1.074				
1.066	**1.014**	**1.018**	**1.083**	**1.0744**				
1.077±0.006	1.017±0.004	1.018±0.004	1.089±0.004	1.063±0.006				
1.072 1.061 1.061 1.069	1.013 1.014 1.019 1.011	1.005 1.019 1.024 1.017	1.08 1.085 1.085 1.092	1.122 1.107 1.124 1.124	Water			
1.063	**1.011**	**1.015**	**1.083**	**1.115**				
1.061±0.006	1.012±0.004	1.013±0.004	1.089±0.004	1.125±0.004				
Water	1.053 1.051 1.053 1.06	1.058 1.054 1.057 1.064	Water	1.099 1.081 1.098 1.1	1.049 1.045 1.049 1.055	0.963 0.965 0.968 0.964		
	1.055	**1.059**		**1.095**	**1.051**	**0.966**		
	1.058±0.004	1.069±0.004		1.095±0.004	1.056±0.004	0.961±0.006		
1.051 1.021 1.026 1.034	0.979 0.977 0.985 0.98	0.98 0.978 0.987 0.981	1.033 1.024 1.03 1.036	0.973 0.976 0.982 0.976	0.922 0.941 0.932 0.931	0.91 0.915 0.904 0.904	0.886 0.899 0.883 0.884	
1.033	**0.981**	**0.986**	**1.032**	**0.980**	**0.935**	**0.912**	**0.891**	
1.025±0.006	0.975±0.004	0.983±0.004	1.033±0.004	0.972±0.004	0.934±0.004	0.905±0.004	0.905±0.006	
0.925 0.929 0.925 0.926	0.924 0.925 0.923 0.921	0.921 0.925 0.923 0.921	0.93 0.929 0.924 0.924	0.922 0.921 0.914 0.914	0.907 0.91 0.897 0.897	0.889 0.901 0.883 0.885	0.889 0.896 0.869 0.876	0.876 0.898 0.895 0.872
0.928	**0.927**	**0.927**	**0.930**	**0.919**	**0.906**	**0.892**	**0.886**	**0.880**
0.926±0.007	0.927±0.005	0.922±0.005	0.930±0.005	0.915±0.005	0.900±0.005	0.889±0.005	0.888±0.005	0.881±0.007

Figure 30. Pin-by-pin relative power distribution in PWR fuel assembly at beginning-of-life.

Water								
1.071 1.068 1.066 1.075	1.025 1.019 1.022 1.015			xxxx xxxx xxxx xxxx	Russia Japan Korea Israel			
1.069	**1.013**			**xxxx**	CASMO			
1.059 1.068 1.067 1.076	1.014 1.02 1.023 1.016	1.015 1.021 1.025 1.018						
1.069	**1.016**	**1.016**						
Water	1.068 1.068 1.067 1.075	1.072 1.071 1.071 1.078	Water					
	1.069	**1.069**						
1.063 1.066 1.065 1.074	1.016 1.018 1.023 1.015	1.009 1.023 1.027 1.02	1.084 1.084 1.084 1.091	1.08 1.068 1.085 1.074				
1.066	**1.014**	**1.018**	**1.083**	**1.0744**				
1.072 1.061 1.061 1.069	1.013 1.014 1.019 1.011	1.005 1.019 1.024 1.017	1.08 1.085 1.085 1.092	1.122 1.107 1.124 1.124	Water			
1.063	**1.011**	**1.015**	**1.083**	**1.115**				
Water	1.053 1.051 1.053 1.06	1.058 1.054 1.057 1.064	Water	1.099 1.081 1.098 1.1	1.049 1.045 1.049 1.055	0.963 0.965 0.968 0.964		
	1.055	**1.059**		**1.095**	**1.051**	**0.966**		
1.051 1.021 1.026 1.034	0.979 0.977 0.985 0.98	0.98 0.978 0.987 0.981	1.033 1.024 1.03 1.036	0.973 0.976 0.982 0.976	0.922 0.941 0.932 0.931	0.91 0.915 0.904 0.904	0.886 0.899 0.883 0.884	
1.033	**0.981**	**0.986**	**1.032**	**0.980**	**0.935**	**0.912**	**0.891**	
0.925 0.929 0.925 0.926 **0.928**	0.924 0.925 0.923 0.921 **.0927**	0.921 0.925 0.923 0.921 **0.927**	0.93 0.929 0.924 0.924 **0.930**	0.922 0.921 0.914 0.914 **0.919**	0.907 0.91 0.897 0.897 **0.906**	0.889 0.901 0.883 0.885 **0.892**	0.889 0.896 0.869 0.876 **0.886**	0.876 0.898 0.895 0.872 **0.880**

Figure 31. Pin-by-pin relative power distribution in PWR fuel assembly at 60 MWd/kg.

Table 16. Reactivity coefficients (× 10^4) for 0 and 60 MWd/kg.

	0 MWd/kg			60 MWd/kg t		
	MTC	DC	BW	MTC	DC	BW
Russia	-3.500	-0.280	-0.380	-1.500	-0.360	-1.100
Japan	-2.696	-0.283	-0.341	-0.969	-0.378	-0.864
Korea	-3.774	-0.319	-0.394	-2.928	-0.453	-0.107
Israel	-3.333	-0.292	-0.400	-1.142	-0.477	-1.119
CASMO	**-3.768**	**-0.235**	**-0.403**	**-2.544**	**-0.359**	**-1.175**

The reactivity coefficients were calculated only with the CASMO4 code because it has built-in capabilities for reactivity parameter calculations and, therefore, it will be used for these purposes in the future. The pin-by-pin power distribution was calculated with MCODE for the beginning-of-life only since the computational time required for the depletion calculation of each fuel pin within the assembly is large. The agreement of the pin-by-pin power distribution predictions was found to be very good. All the codes identified the hot fuel pin at the same location at beginning-of-life. The discrepancy in pin power prediction at end-of-life for the different pin locations is between 5 and 10%.

The beginning-of-life values of reactivity coefficients are in reasonable agreement. Some discrepancies in reactivity coefficients predictions were observed at end-of-life. These discrepancies may be attributed to different plutonium isotope concentrations. However, the trend of change with burnup is predicted correctly by all the computer codes.

1.2.1.5. Conclusions

The benchmark calculations confirm that the CASMO4 and MCODE computer codes are suitable for scoping studies of thorium–plutonium based fuel designs. They predict reasonably well the criticality and composition of the fuel, and their results fall within the uncertainties of the other codes used by the participants in the IAEA international benchmark. The CASMO4 computer code can also be used for estimation of the fuel reactivity coefficients with a reasonable degree of confidence.

1.2.2. Potential Of Thorium-Based Fuels To Burn Plutonium And Minor Actinides

Plutonium and the minor actinides in spent nuclear fuel represent a considerable nuclear proliferation concern and have a major contribution to the long-term radiotoxicity of the nuclear waste. Extensive research is currently in progress aimed at a reduction in the existing plutonium and minor actinides in the spent LWR fuel stockpiles. However, many of the proposed solutions require a significant development effort and very likely high costs. For example, many accelerator driven and critical fast spectrum systems use advanced materials and components that have yet to be proven economically. Alternatively, use of uranium-plutonium MOX fuel in LWRs is less costly to implement but the production of plutonium from uranium in the fuel reduces the effectiveness of plutonium destruction.

In order to accelerate the plutonium and minor actinide destruction, the amount of uranium loaded into the core must be minimized. Two options seem to be promising in that respect – fertile-free and thorium based fuels. The utilization of the existing PWR fleet makes both of these options economically attractive.

Fuel cores based on fertile-free fuels exhibit a large reactivity swing. Cores with mixed fertile-free and UO_2 fuel may have high power peaking and impose some additional requirements on reactor control. As a result, only a limited number of fertile-free assemblies can be placed in the core.

Thorium-based fuels can potentially reduce the reactivity swing due to the continuous build up of U-233 and would have a more favorable Doppler reactivity coefficient. At the same time, similar to non-fertile fuels, thorium as a primary fertile material in the core allows effective burning of plutonium and minor actinides because virtually no plutonium and minor actinides are generated from thorium. ThO_2 is the preferable form to be used as a fuel due to substantial

accumulated experience, mostly in the 70's and 80's, as well as its compatibility with light water coolant.

The effectiveness of TRU transmutation in thermal reactors can be argued by the fact that the minor actinides have large capture cross-sections in a thermal spectra. In such a spectra, the minor actinides can be rapidly transmuted by neutron capture to fissile isotopes with high fission cross-sections, and thus eventually destroyed. In addition, the thermal spectrum cross-sections for neutron absorption are 200-300 times larger than for fast neutrons. Thus, at a given power level a thermal spectrum system requires a significantly smaller actinide inventory, even though fast systems operate at higher neutron flux levels than thermal systems. This ultimately implies that thermal spectrum systems will discharge a smaller amount of minor actinides for reprocessing and, therefore, potentially reduce reprocessing costs due to smaller heavy metal throughput. On the other hand, somewhat larger amounts of Cm and Cf are expected to build up in thermal systems, which will increase the cost of reprocessing because of high shielding requirements against neutrons from spontanesous fissions of these nuclides. Hence the cost aspects need to be evaluated against particular designs for both the manufacturing and reprocessing facilities (for example, IFR may have less costly reprocessing).

In this work, we focus on establishing the practical limits for plutonium and minor actinide burning efficiency and on the feasibility of thorium based fuel in PWRs. The main parameters of interest are the rate of total plutonium and minor actinide destruction and residual fraction of transuranic nuclides (TRU) in discharged fuel. The former parameter is, effectively, the number of kilograms of TRU that are burnt per unit energy produced by the fuel. The latter parameter indicates the amount of TRU that will have to be recycled or disposed of in the nuclear waste repository.

The fuel composition (relative amounts of Th, Pu, MAs, and U in the fuel) and lattice geometry will affect both of these indices: the burning efficiency and rate of TRU destruction. Therefore, the study reported here consists of several parts. First, homogenous reactor grade PuO_2-ThO_2 mixtures are studied covering a wide range of possible compositions and geometries. Then, the effect of the addition of a small amount of natural uranium to the fuel was investigated. This option is important for the once-through TRU burning scenario where the discharged fuel will be sent directly to the repository. In this case, the U-233 generated from the Th-232 has to be isotopically diluted (denatured) in order to eliminate potential nuclear proliferation threats. Next, the minor actinides were also considered as part of the fuel and the efficiency and destruction rates of the plutonium, minor actinides, and total TRU were investigated.

The PWR fuel lattice allows a certain degree of freedom in optimization of the fuel to moderator volume ratio. This ratio defines the degree of neutron moderation and, therefore, absorption and fission reaction rates in different heavy metal nuclides in the fuel. For that reason, a scoping study was carried out to evaluate the effect of the fuel lattice geometry on plutonium and minor actinide destruction performance for each fuel composition considered.

Finally, the feasibility of utilization of TRU-loaded thorium based fuels in the current generation of PWRs was studied by a comparative analysis of the reactivity coefficients and soluble boron worths for a number of realistic TRU-thorium cases, typical MOX, and conventional all-uranium fuel.

1.2.2.1. Description of Methodology and Calculated Cases.

All burnup and criticality calculations in this study were performed using the CASMO4 fuel assembly burnup computer code, which uses a 70-energy group neutron cross-section library. The benchmark calculations demonstrated that CASMO4 is suitable for scoping studies of thorium – plutonium based fuel designs. It predicts reasonably well the criticality, the evolution of the fuel composition with burnup, and the fuel reactivity coefficients. The results obtained with CASMO4 fall within the uncertainties of other codes evaluated in the benchmark. However, careful evaluation of the accuracy of the different computational tools for fuel design with large loadings of minor actinides has yet to be performed. It should also be noted that the accuracy of the currently available nuclear data for minor actinide nuclides is limited to a considerable extent. For example, the differences in the thermal cross-sections of some of the minor actinides from the major nuclear data files can range up to 30% [Delpech et al. 1996].

The burnup calculations were performed for a fuel pin cell geometry of a typical PWR. The reference fuel pin cell geometry and operating parameters used in the calculations are summarized in Table 17. The effect of differences in the neutron energy spectrum was studied by changing the hydrogen to heavy metal atom ratio (H/HM). Different H/HM ratios were simulated by varying the water density in a fuel pin cell of fixed reference geometry. For the purposes of the current study, this approach of varying H/HM can be considered neutronically equivalent to other more realistic options as demonstrated in [Xu et al. 2002b]. The H/HM ratios were varied in a wide range from about 0.002 to about 70. All the fuel compositions analyzed in this study are summarized in Table 18.

Table 17. Reference pin-cell geometry and operating parameters.

Fuel pellet diameter, mm	8.192
Gap thickness, mm	0.082
Outer Cladding diameter, mm	9.500
Lattice Pitch, mm	12.6
Fuel temperature, K	900
Coolant temperature, K	583
Power density, kW/l	104
Reference H/HM ratio	3.64

Table 18. Summary of studied fuel compositions.

Case.	Description	Th, w/o	Natural Uranium, w/o	Pu, w/o	MA w/o	Isotopic vector
1	Pu-Th undenatured	93.0	-	7.0	-	Table 19
2	Pu-Th undenatured	91.0	-	9.0	-	Table 19
3	Pu-Th undenatured	89.0	-	11.0	-	Table 19
4	Pu-Th undenatured	85.0	-	15.0	-	Table 19
5	Pu-Th denatured	78.0	15.0	7.0	-	Table 19
6	Pu-Th denatured	76.0	15.0	9.0	-	Table 19
7	Pu-Th denatured	74.0	15.0	11.0	-	Table 19
8	Pu-Th denatured	70.0	15.0	15.0	-	Table 19
9	Pu-MA-Th denatured	63.58	13.54	19.82	3.05	Table 20
10	Pu-MA-Th denatured	61.89	13.18	21.60	3.32	Table 20
11	Pu-MA-Th denatured	58.51	12.47	25.15	3.87	Table 20
12	MOX	-	93.00	7.00	-	Table 19
13	All-U	-	100 (4.5% ^{235}U)	-	-	-

In the cases with zero minor actinide loading, the isotopic composition of the plutonium vector that was used is shown in Table 19. This composition corresponds to the plutonium immediately after discharge in the spent fuel from a typical LWR, using all-uranium fuel with an initial U-235 enrichment of 4.5% and a burnup of about 50 MWd/kg. Four different initial plutonium loadings of 7, 9, 11 and 15w/o relative to total heavy metal in the fuel (Cases 1 through 4 in Table 18) were analyzed to cover the whole range of possible fuel cycle lengths.

In Cases 5 through 8 in Table 18, 15w/o of natural uranium was added to the initial plutonium and thorium fuel composition, in order to assure that the uranium proliferation index in the discharged fuel is smaller than 0.12. The uranium proliferation index is defined as [Forsberg et al. 1999] as:

$$\frac{\text{Weight of } {}^{233}\text{U} + 0.6 \times \text{Weight of } {}^{235}\text{U}}{\text{Total Weight of Uranium}} < 0.12$$

The initial plutonium and minor actinide isotopic composition of the Pu-MA-Th fuel (Cases 9 through 11 in Table 18) is shown in Table 20. This composition corresponds to the isotopics of 4.2% enriched conventional UO_2 fuel irradiated to 50 MWD/kg and then decayed for 10 years. Three different loadings of TRU in thorium were studied, again, to cover a broad range of possible fuel cycle lengths. In the reference fuel pin cell geometry these three fuel compositions will result in 12, 18 and 36 months operating cycle lengths respectively.

In this part of the study, the amount of natural uranium added for denaturing the bred U-233 was chosen to be about 20% relative to the amount of thorium in the fuel. It was assumed that all the minor actinides in the fuel have the chemical form of $(MA)O_2$ with densities equal to the theoretical density of PuO_2. Core leakage was neglected in these scoping studies and the reactivity limited single batch burnup (BU1) and fuel cycle length were estimated by calculating the burnup at which k-infinity of the fuel equals unity. The discharge fuel burnup was estimated using a 3-batch linear reactivity model, as 1.5×BU1 [Driscoll et al. 1990].

In current PWRs, only reasonably moderate changes in the fuel assembly configuration are possible in order to optimize the fuel performance parameters. Additionally, denaturing of bred U-233 is a required constraint for a practical design. In light of these two considerations, only denatured cases with H/HM ratios between the reference case and the reference +40% case were evaluated in terms of reactor operational characteristics.

The Doppler reactivity coefficient (DC), moderator temperature coefficient (MTC), void coefficient (VC) and

Table 19. Initial plutonium isotopic composition in Pu-Th fuel.

Isotope	Weight %
Pu-238	2.883
Pu-239	54.602
Pu-240	21.150
Pu-241	15.300
Pu-242	6.064

Table 20. Initial plutonium and minor actinide (TRU) isotopic composition in Pu-MA-Th fuel.

Isotope	Weight %
U-234	0.0001
U-235	0.0023
U-236	0.0019
U-238	0.3247
Np-237	6.641
Pu-238	2.7490
Pu-239	48.6520
Pu-240	22.9800
Pu-241	6.9260
Pu-242	5.0330
Am-241	4.6540
Am-242m	0.0190
Am-243	1.4720
Cm-242	0.0000
Cm-243	0.0050
Cm-244	0.4960
Cm-245	0.0380
Cm-246	0.0060

soluble boron worth (BW) were calculated for the Compositions 5 through 11 in Table 18 at 3 different H/HM ratios and at 3 time points: beginning, middle, and end of fuel irradiation. In order to simulate close to realistic operating reactor conditions, all the reactivity coefficients were calculated assuming that the soluble boron concentrations are 1000 ppm, 500 ppm, and 0 ppm at beginning, middle, and end-of-life respectively.

The MTC, DC and BW were calculated using the relations described in Section 1.2.1.3. The void coefficient (VC) is calculated as

$$VC = \frac{\Delta K}{K_1 \times K_2 \times \Delta V}$$

where ΔV is the difference between two coolant void fractions V_1 and V_2.

1.2.2.2. Results and Discussion – Un-denatured PuO_2-ThO_2 Fuel Cases

One of the most important characteristics of the fuel designed for plutonium disposition is the plutonium destruction rate; namely, the number of kilograms of plutonium destroyed per unit energy produced by the fuel. Figure 32 shows the plutonium destruction rates normalized per 1 $GWYear_e$. The plutonium destruction rate is relatively insensitive to the plutonium loading and to the H/HM ratio in the neighborhood of the reference H/HM value. The rate of plutonium destruction for low plutonium loadings at low H/HM ratios (in epithermal energy spectra) exhibits an increase due to the fact that the fuel cycle length in this region is relatively short (Figure 33) whereas fissile Pu-239 burns out rather rapidly at the beginning of fuel irradiation, increasing the total plutonium destruction rate. In contrast, the rate of plutonium destruction for the fuel with high plutonium loadings monotonically decreases as the H/HM ratio decreases (Figure 32). In this case, a significant amount of energy is generated from the U-233 due to the effective breeding in the epithermal and fast energy spectra. The initial plutonium loading is high enough to sustain core criticality until a

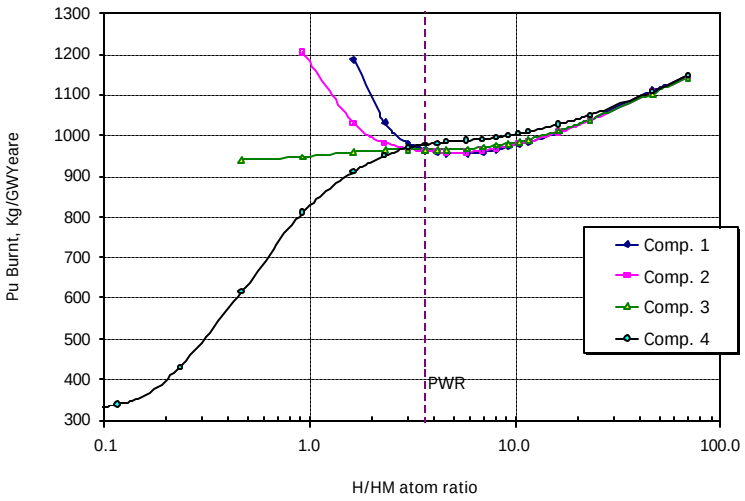

Figure 32. Normalized plutonium destruction rate vs. H/HM Ratio: un-denatured cases.

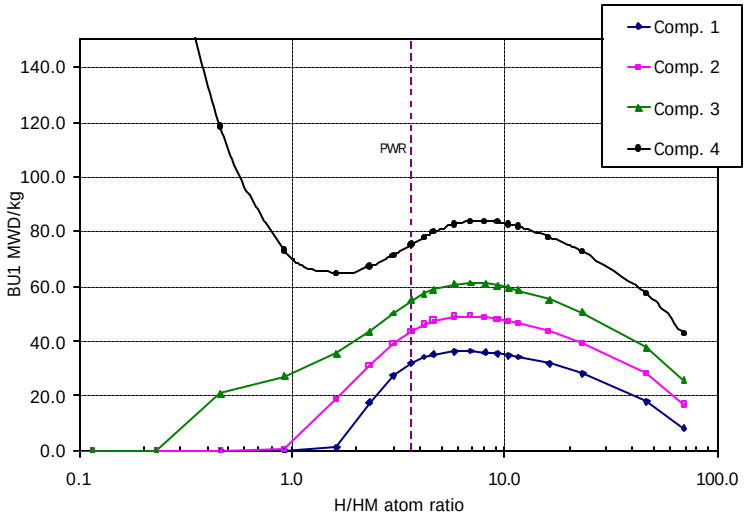

Figure 33. Reactivity limited burnup (BU1) vs. H/HM ratio: un-denatured cases.

significant amount of U-233 is generated. As a result, the plutonium destruction rate is reduced because of the competition between neutron absorption in the plutonium and U-233, although high burnup, in general, results in deep plutonium burning as shown in Figure 34. It should also be noted, however, that the stated achievable burnup is an overestimate since neutron leakage was not considered. Additionally, the leakage is expected to be higher in plutonium containing cores due to the harder neutron spectrum than for all-uranium cores. Similarly, the cases with very low H/HM will have significantly higher leakage than the cases with high H/HM because of an increased neutron migration area, resulting in smaller achievable burnups than those indicated on Figure 33. This will in turn lead to lower plutonium burnup rates and higher plutonium residual fractions for the low H/HM ratio cases than those shown in Figures 32 and 34.

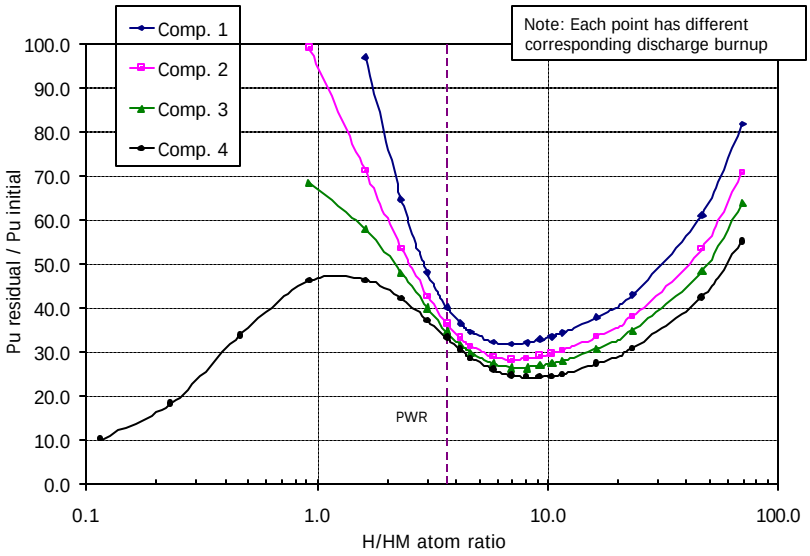

Figure 34. Residual plutonium fraction vs. H/HM ratio: un-denatured cases.

Figure 34 also suggests that an approach to achieve deeper plutonium burning (that is, to minimize the fraction of the residual plutonium in the discharged fuel) in a PWR core is to increase the H/HM ratio. Up to 75% of the initially loaded plutonium can be potentially destroyed by increasing the H/HM ratio from 3.64 to about 7. However, at high H/HM in a given core volume, the total initially loaded plutonium will be smaller.

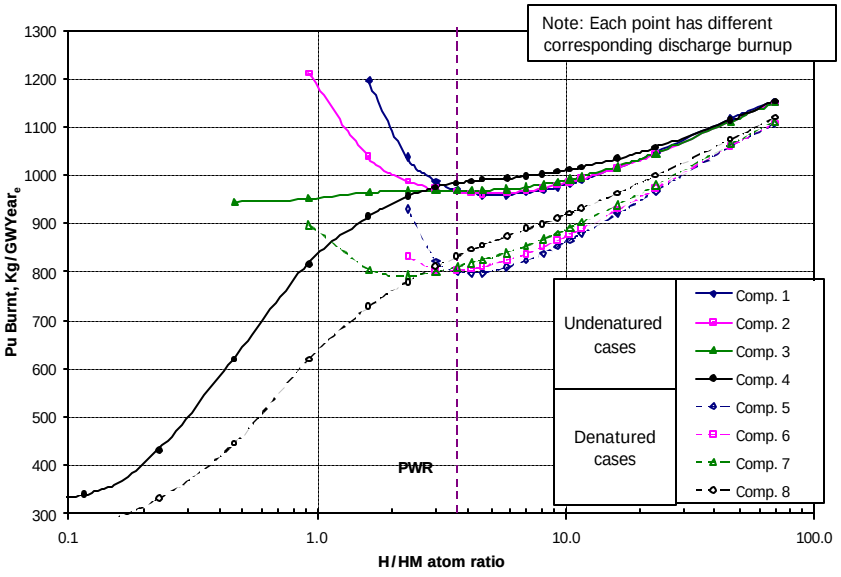

Figure 35. Normalized plutonium destruction rate vs. H/HM ratio.

1.2.2.3. Results and Discussion - Denatured PuO_2-UO_2-ThO_2 Mixture Cases

Addition of uranium to the fuel decreases the plutonium destruction rate as expected. Figure 35 illustrates this fact. At the reference H/HM ratio point, the addition of 15w/o natural uranium reduces the rate of plutonium destruction by about 20%, although, this relative reduction in the destruction rate becomes smaller for "wetter" than reference fuel lattices.

Figures 36 and 37 compare the quality of the plutonium destruction for the denatured and un-denatured cases for various plutonium loadings. At the reference H/HM ratio, denaturing can almost double the amount of residual plutonium. However, at higher than reference H/HM ratios, the difference between the denatured and un-denatured cases becomes smaller and even vanishes for highly over moderated lattices. This is partially due to the fact that denatured cases in the over moderated region achieve slightly higher burnup as illustrated by Figure 38.

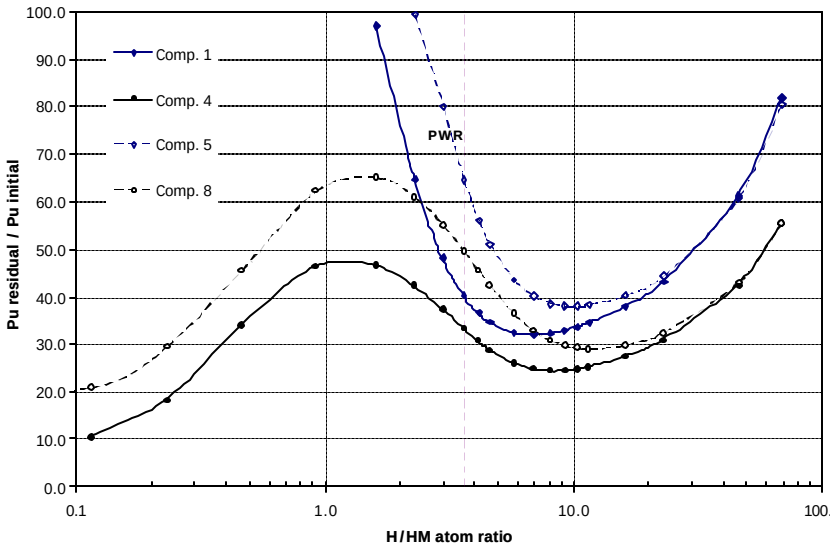

Figure 36. Residual plutonium fraction vs. H/HM ratio: plutonium loadings 7 and 15 w/o.

Figure 39 shows the effective fissile uranium ratio as a function of H/HM for denatured cases. The addition of 15 w/o natural uranium is sufficient to assure the proliferation resistance of the uranium in the discharged fuel for most of the calculated cases. In fact, the uranium fissile ratio decreases with H/HM which indicates that the amount of natural uranium can be reduced for wetter than reference fuel lattices, which also improves the plutonium burning performance.

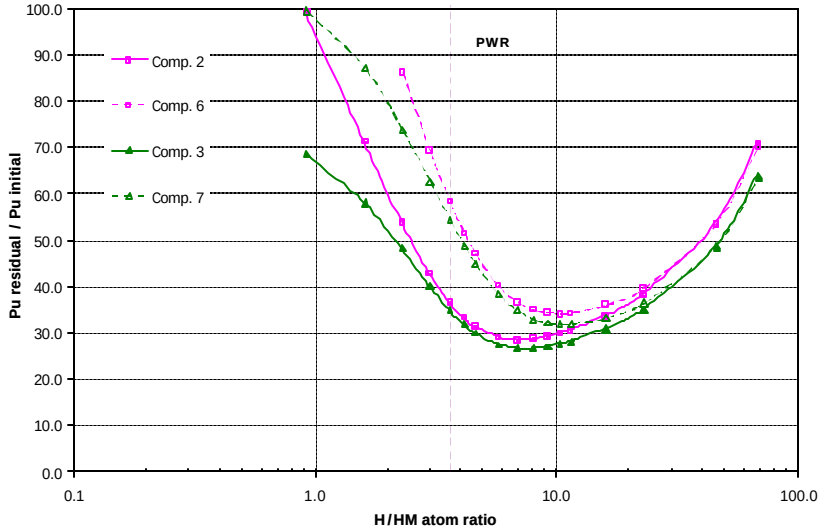

Figure 37. Residual plutonium fraction vs. H/HM ratio: plutonium loadings 9 and 11 w/o.

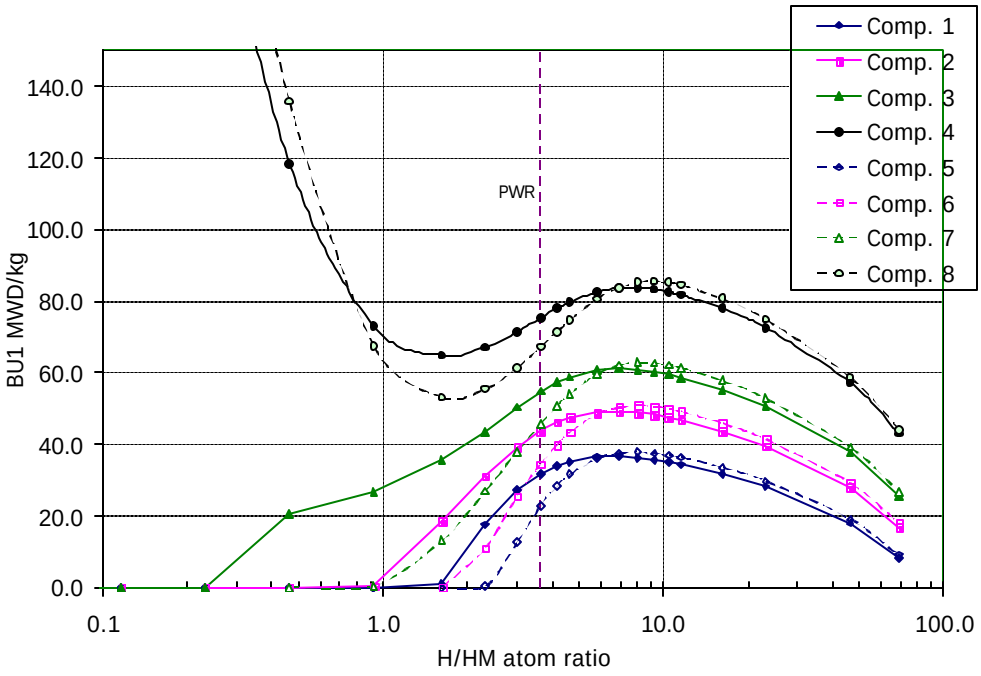

Figure 38. Reactivity limited burnup (BU_1) vs. H/HM ratio: denatured cases.

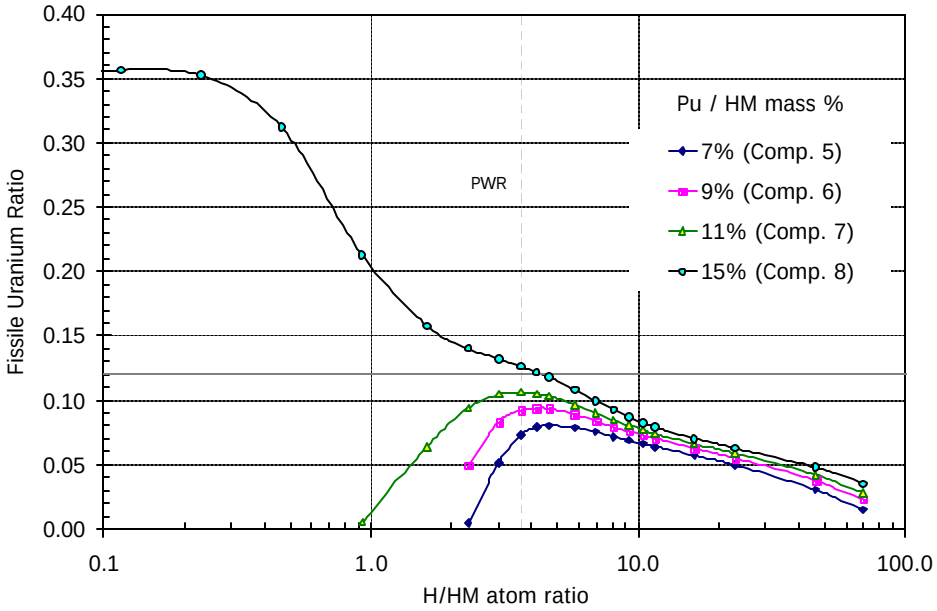

Figure 39. Effective fissile uranium ratio vs. H/HM ratio: denatured cases.

1.2.2.4. Results and Discussion - $(MA)O_2$ - PuO_2 - UO_2 - ThO_2 Mixture Cases

The potential for transuranic nuclide (TRU) destruction is an important feature of innovative fuel designs, which can help the effort to reach sustainable fuel cycles. Only systems that utilize fuel that burns the same amount, or more, TRU than originally loaded have the ability to reach an equilibrium state in a completely closed fuel cycle with zero net generation of TRU.

Thorium based fuels used for disposition of plutonium and minor actinides, although they do not create new plutonium and minor actinides, produce noticeable amounts of actinides originating from the Th-232. The most valuable nuclide for the sustainable closed fuel cycle scenario is U-233. It typically constitutes over 90% of all the thorium chain isotopes. It has a large thermal fission cross-section; thus, it can be efficiently recycled. However, small amounts of other thorium chain nuclides are long lived and radioactive. For example minute quantities of U-232 can significantly complicate fuel reprocessing and fabrication because of the presence of strong ?-emitters in its decay chain [Laughter et al. 2002].

To distinguish between the TRU and other non-natural actinides, all nuclides produced by neutron capture from Th-232 and subsequent decay have been added to the discharge waste stream. Therefore, two sets of curves were generated – the first set describes the consummation of TRU per path, while the second set includes also the contribution of non-natural actinides from the thorium chain to the TRU stream. However, it needs to be pointed out that more than 90% of actinides from the thorium chain are represented by the U-233, which is a valuable fissile isotope to be recycled and reused in LWRs, hence the net contribution of trans-thorium actinides to the overall actinide waste stream is very small. Figure 40 shows the destruction rates, normalized per 1 GweYear, for 3 different initial TRU loadings that in the reference PWR fuel pin cell geometry will result in 12, 18 and 36 month fuel cycle lengths.

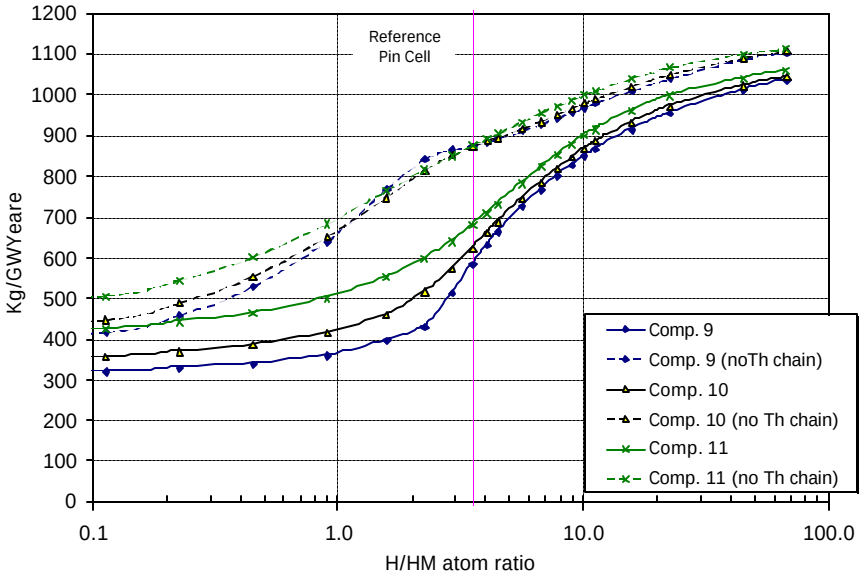

Figure 40. Energy normalized destruction rate for TRU and all non-natural actinides.

The following observations are made.

- The destruction rates of TRU only and all non-natural actinides monotonically increase with increasing H/HM ratio over the whole investigated range of fuel lattice geometries. Therefore, it is always beneficial to keep the H/HM ratio as high as possible from the destruction rate viewpoint.
- The destruction rates of the TRU, without the thorium chain nuclides, are not sensitive to the initial TRU loadings.
- The contribution of the thorium chain nuclides to the total destruction rate of the non-natural actinides varies with H/HM and initial TRU loading. This variation originates in the fact that the efficiency of the U-233 buildup depends on the H/HM ratio as well as on other actinide inventories.

Figure 41 shows the minor actinide-only contribution to the total TRU destruction rate. As can be observed from Figure 41, the actual reduction in minor actinide inventory can be achieved only for highly over-moderated lattices if the thorium chain nuclides are included in the balance.

If the thorium chain nuclides are not considered, the reduction of the minor actinide inventory is possible with a rate of about 100 kg per GWeYear. This rate appears to be remarkably insensitive to the initial TRU inventory and H/HM ratio in the range of practical interest (from 1 to 10).

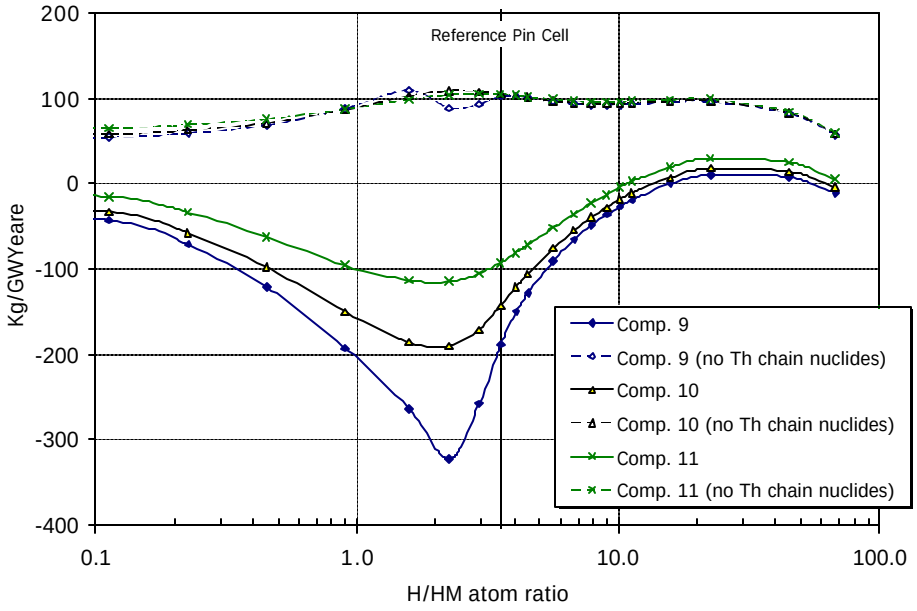

Figure 41. Energy normalized minor actinide destruction rate.

The fraction of residual TRU in the spent fuel, not including thorium chain nuclides, is shown in Figure 42. The data plotted in Figure 42 suggests that the reference pin cell geometry is not effective for TRU destruction. Higher initial TRU loadings are preferable as they result in deeper TRU burnout for the H/HM ratios close to the reference. However, this difference vanishes as the H/HM ratio approaches 10. The maximum theoretically achievable degree of TRU burnout is about 50% of the initial loading at a H/HM ratio of about 11.

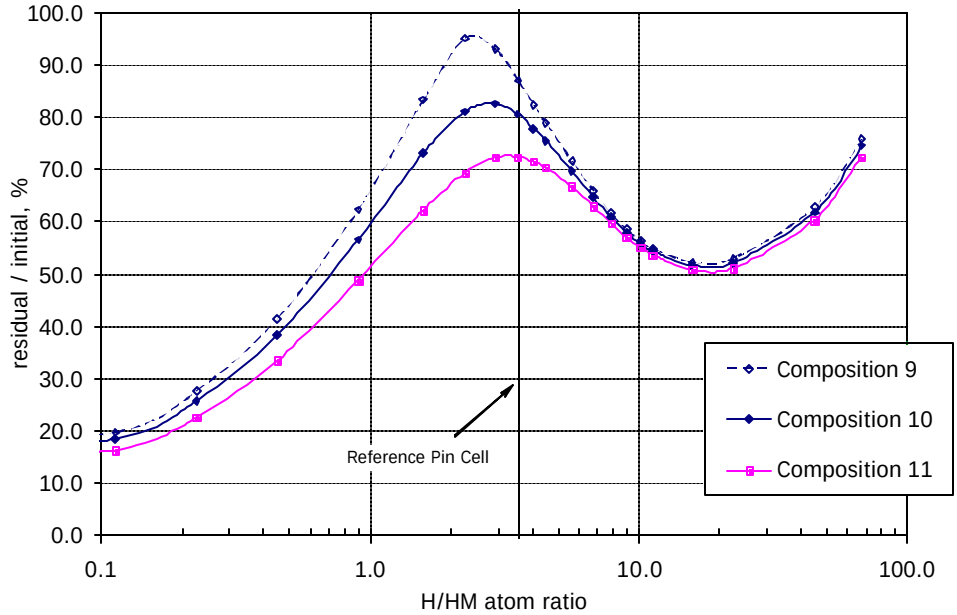

Figure 42. Residual fraction of TRU (no thorium chain nuclides).

1.2.2.5. Results and Discussion - Evaluation of Reactivity Coefficients

The results of the analysis presented above suggest that higher than reference H/HM ratios are preferable for effective plutonium destruction. Therefore, the reactivity coefficients were evaluated at H/HM values ranging from the reference PWR fuel pin cell to reference + 40% H/HM. All the reactivity coefficients were calculated on the basis of a pin cell geometry. The actual core average reactivity coefficients would be somewhat different as a core is composed of fuel assemblies with different accumulated burnup. The pin cell based calculations, however, can be used for comparison of different fuel designs with different compositions and H/HM ratios against a reference UO_2 fuel evaluated on the same basis.

Selected results of the reactivity coefficient calculations, as well as the soluble boron worth calculations are summarized in Table 21. All the fuel compositions presented in Table 21 correspond to the 18 months cycle length currently widely used by the nuclear industry. All the coefficients were evaluated assuming 1000, 500, and 0 ppm of soluble boron concentration in the coolant at beginning, middle, and end-of-life respectively in order to simulate close-to-realistic PWR operating conditions.

Table 21. Reactivity coefficients: selected results.

Case	Description	Reference H/HM			Reference + 40% H/HM		
		BOL	MOL	EOL	BOL	MOL	EOL
DOPLER COEFFICIENT, pcm/K							
6	Pu-Th den.	-4.32	-4.65	-5.04	-3.43	-3.78	-4.22
9	Pu-MA-Th den.	-2.98	-3.02	-3.15	-2.63	-2.80	-3.02
12	MOX	-2.92	-3.09	-3.20	-2.36	-2.57	-2.70
13	All-U	-2.20	-2.93	-3.33	-1.82	-2.31	-2.75
MODERATOR TEMPERATURE COEFFICIENT, pcm/K							
6	Pu-Th den.	-49.05	-58.68	-73.47	-38.91	-50.40	-66.73
9	Pu-MA-Th den.	-18.53	-17.69	-23.40	-29.57	-33.17	-44.86
12	MOX	-40.63	-54.65	-73.78	-32.37	-46.92	-66.39
13	All-U	-22.17	-51.62	-77.79	-2.21	-26.00	-50.07
VOID COEFFICIENT, pcm/%void							
6	Pu-Th den.	-128.0	-156.8	-198.3	-104.8	-142.9	-190.4
9	Pu-MA-Th den.	-42.8	-41.4	-51.7	-70.8	-85.3	-115.8
12	MOX	-104.8	-145.3	-200.7	-86.0	-130.8	-190.8
13	All-U	-62.5	-145.7	-228.0	-10.8	-83.5	-164.8
SOLUBLE BORON WORTH, pcm/ppm							
6	Pu-Th den.	-1.95	-2.28	-3.02	-2.82	-3.60	-5.15
9	Pu-MA-Th den.	-1.05	-1.03	-1.24	-1.73	-1.90	-2.24
12	MOX	-1.96	-2.37	-2.76	-2.88	-3.70	-4.85
13	All-U	-4.80	-5.22	-6.23	-6.65	-8.15	-11.90

The MOX fuel provides a somewhat stronger Doppler fuel temperature reactivity feedback (DC) than the all-uranium fuel, while the plutonium-thorium fuel has a more negative DC than the MOX and all-uranium fuel. Wetter lattices yield slightly less negative DCs than the reference, nevertheless, the plutonium-thorium fuel in a wetter lattice has still a more negative DC than the reference all-uranium fuel. A strongly negative DC is beneficial for transients associated with fuel temperature increases as it provides stronger negative reactivity feedback, however it results in larger reactivity insertion in startup and shutdown scenarios. A stronger DC

may also be a disadvantage in the reactor's response to sudden cool-down scenarios, such as a steam generator depressurization event.

The calculated moderator temperature and void coefficients (MTC and VC respectively) for thorium-based fuels are negative and exhibit smaller variations with burnup than the all-uranium and MOX fuel. The absolute values of the MTC and VC of the plutonium-thorium cases are close to those observed for the typical MOX fuel while Pu-MA-Th fuels have MTC and VC values close to those of the all-uranim case. The calculated values of the MTC and VC are consistent with those previously reported by Lombardi et al. [1999] and Gruppelaar et al. [2000]. The effect of the increased H/HM ratio is not particularly significant for the thorium-based cases. All the reactivity coefficients stay negative over the entire investigated range of H/HM values.

Table 22 shows an example of the beginning-of-life reactivity control requirements and soluble boron worth for a number of calculated cases. The beginning-of-life whole core excess reactivity was estimated assuming a 3 batch core with linear burnup-reactivity dependence for each batch. 3% of the ?? was allowed for leakage. No burnable poisons were considered. The soluble boron worth of the partially burned batches was assumed to be equal to the fresh batch soluble boron worth, which is a conservative assumption since soluble boron worth, generally, increases with the burnup.

Table 22. Soluble boron requirements for reactivity control at beginning-of-life.

Case	Description	k-infinity (BOL), Pin cell	Core Average Reactivity (BOL), pcm	Soluble Boron Worth pcm/ppm	ppm needed to control
Reference H/HM					
5	Pu-Th den.	1.119	4098	-2.41	1699
6	Pu-Th den.	1.146	5183	-1.95	2664
7	Pu-Th den.	1.170	6136	-1.66	3703
8	Pu-Th den.	1.216	7849	-1.24	6322
9	Pu-MA-Th den.	1.062	1533	-1.05	1456
10	Pu-MA-Th den.	1.078	2281	-0.97	2358
11	Pu-MA-Th den.	1.109	3672	-0.81	4525
12	MOX	1.206	7473	-1.96	3804
13	All-U	1.380	12953	-4.80	2698
Reference + 40% H/HM					
5	Pu-Th den.	1.195	7092	-3.41	2080
6	Pu-Th den.	1.216	7858	-2.82	2788
7	Pu-Th den.	1.235	8501	-2.42	3512
8	Pu-Th den.	1.269	9631	-1.92	5022
9	Pu-MA-Th den.	1.100	3289	-1.73	1903
10	Pu-MA-Th den.	1.111	3765	-1.62	2320
11	Pu-MA-Th den.	1.133	4680	-1.41	3324
12	MOX	1.275	9829	-2.88	3415
13	All-U	1.440	14528	-6.65	2185

Although the plutonium-thorium and Pu-MA-Th fuels require a much smaller initial excess reactivity for control, the soluble boron worth is much smaller than that of the all-uranium fuel. As a result, the soluble boron concentrations required to control the initial excess reactivity are comparable to the all-uranium fuel and in some cases considerably higher. Increasing the loading of the TRUs in the thorium based fuels leads to a harder neutron spectra and, therefore, lower

soluble boron worth. Higher than reference H/HM ratios increase the neutron moderation and, as a result, increases the soluble boron worth. In general, the relatively hard neutron spectrum in all TRU containing fuels necessitates that special attention be devoted to the design of the reactor control. Utilization of enriched boron or gadolinium in the control rods or as a burnable poison might be necessary to satisfy reactor safety criteria for some thorium-TRU fuel designs.

The prompt neutron lifetime and the effective delayed neutron fractions for the plutonium-thorium and plutonium-thorium-minor actinide fuel are presented in Tables 23 and 24 along with values for the all-uranium and MOX fuel.

Table 23. Prompt neutron lifetime (sec).

	H/HM Ratio					
	Reference			**Reference + 20%**		
Case	BOL	MOL	EOL	BOL	MOL	EOL
1 (Pu – unden.)	6.00E-06	6.58E-06	7.46E-06	6.01E-06	6.85E-06	8.06E-06
2 (Pu – unden.)	4.78E-06	5.64E-06	7.15E-06	4.85E-06	6.06E-06	8.18E-06
3 (Pu – unden.)	3.96E-06	4.81E-06	6.41E-06	4.07E-06	5.23E-06	7.47E-06
4 (Pu – unden.)	2.95E-06	3.81E-06	5.51E-06	3.09E-06	4.23E-06	6.58E-06
9 (Pu-MA-den.)	2.41 E-06	2.38 E-06	2.45 E-06	2.71 E-06	2.77 E-06	3.04 E-06
10 (Pu-MA-den.)	2.19 E-06	2.20 E-06	2.35 E-06	2.49 E-06	2.57 E-06	2.91 E-06
11 (Pu-MA-den.)	1.84 E-06	1.90 E-06	2.18 E-06	2.13 E-06	2.27 E-06	2.69 E-06
12 (All-U)	1.26E-05	1.37E-05	1.67E-05	1.25E-05	1.46E-05	1.95E-05
13 (MOX)	4.86E-06	5.82E-06	7.17E-06	4.97E-06	6.22E-06	8.09E-06

Table 24. Effective delayed-neutron yield ($ß_{eff}$) ´ 10^3.

	H/HM Ratio					
	Reference			**Reference + 20%**		
Case	BOL	MOL	EOL	BOL	MOL	EOL
1 (Pu – unden.)	2.98	2.76	2.46	2.99	2.84	2.42
2 (Pu – unden.)	3.00	2.81	2.39	3.00	2.89	2.36
3 (Pu – unden.)	3.01	2.77	2.41	3.01	2.88	2.44
4 (Pu – unden.)	3.02	2.74	2.41	3.02	2.86	2.45
5 (Pu – den.)	3.14	3.07	2.85	3.13	3.01	2.81
6 (Pu – den.)	3.14	2.96	2.75	3.13	3.01	2.76
7 (Pu – den.)	3.15	2.95	2.71	3.14	2.98	2.76
8 (Pu – den.)	3.15	2.89	2.62	3.14	2.95	2.70
9 (Pu-MA-den.)	2.63	2.57	2.53	2.69	2.65	2.63
10 (Pu-MA-den.)	2.66	2.58	2.51	2.68	2.63	2.60
11 (Pu-MA-den.)	2.62	2.50	2.43	2.65	2.58	2.55
12 (All-U)	7.23	5.49	4.80	7.20	5.54	4.81
13 (MOX)	4.01	4.10	4.15	3.92	4.06	4.15

The prompt neutron lifetime for all the plutonium-thorium, Pu-Th-MA, and MOX cases is significantly smaller than that of all-uranium fuel (Table 23). It decreases with increasing plutonium loading (depicted by increasing case number for the Pu-unden fuels) and with the addition of minor actinides, as a result of spectrum hardening. The cases more heavily loaded with plutonium and those containing minor actinides have prompt neutron lifetimes smaller than the MOX fuel, but this parameter is not of high importance. More importantly, the effective delayed neutron fractions of the plutonium-thorium fuel are smaller than the values for the all-uranium fuel by about a factor of two, and smaller than the MOX fuel values at end-of-life by more than 1.5 (Table 24). A smaller β_{eff} is a major challenge for the cores fully loaded with thorium-plutonium fuel and the feasibility of reactor controllability under such a low β_{eff} is questionable. For example, it is noted that fast reactors with plutonium fuel, such as the IFR, have a β_{eff} of 0.0035. This is appreciably higher than some end-of-life values for the plutonium-thorium fuel, where the lowest value is 0.0024. Moreover, a small reactivity worth of the control materials and low β_{eff} values in the plutonium-thorium containing PWR cores may lead to much higher reactivity in dollars vested in control rods and soluble boron in comparison with conventional UO_2 and MOX cores. A smaller effective delayed neutron fraction is the consequence of the smaller delayed neutron yield of the Pu-239 and U-233 in comparison to that of the U-235 and a smaller fast fission contribution from the Th-232, which has a higher delayed neutron yield than the U-238. Denatured plutonium-thorium fuels (Cases 5 through 9 in Table 24) have slightly more favorable β_{eff} values than the un-denatured plutonium-thorium fuels (Cases 1 through 4 in Table 24) because of the contribution from the U-238.

The prompt neutron lifetime values of all the plutonium-thorium cases *with minor actinides* indicate significantly faster reactor kinetics in comparison with the all-uranium, MOX, and even with the plutonium-thorium cases. More importantly, the effective delayed neutron yield is below 0.003 for all calculated Pu-Th-MA compositions. As a result, the feasibility of a PWR core with 100% loading of thorium based fuel assemblies containing plutonium and minor actinides is rather uncertain.

1.2.2.6. Summary and Conclusions

In this part of the work, we established the potential limits for the efficiency of plutonium and minor actinide destruction in thorium based fuels in PWRs. We primarily focused on two performance indexes: the rate of TRU destruction and residual fraction of TRU relative to initial TRU loading. The results of the study showed that thorium based fuel designs can be effectively used to reduce existing stockpiles of TRU in PWRs and, theoretically, can be part of a sustainable closed fuel cycle system with zero net generation of TRUs.

The reasonably achievable rate of TRU destruction in thorium based fuel is about 1000 kg of TRU destroyed per 1 GWeYear, while up to 50% of the initially loaded TRU can, theoretically, be destroyed per path.

Denaturing of the generated U-233 with natural uranium degrades the efficiency of the plutonium destruction. However, denaturing is required only for the once-through fuel cycle. In that case, denaturing reduces the plutonium destruction rates by approximately 20%. The difference in the destruction rate and the residual plutonium fraction between the denatured and un-denatured cases decreases for wetter than reference lattices.

The calculated reactivity coefficients and their comparison with MOX and all-uranium fuel indicate the potential feasibility of thorium-based fuels for transmutation of TRU in PWRs. However, the considerably smaller effective delayed neutron fraction in comparison with the MOX and all-uranium fuel is likely to impose a significant limitation on the feasibility of a PWR core with 100% loading of thorium-based fuel assemblies containing plutonium and minor actinides.

Somewhat wetter fuel lattices than present PWRs are more favorable from the TRU destruction efficiency and reactivity control perspectives. Plutonium and minor actinide containing thorium-based fuels have a significantly harder neutron spectra than for typical all-uranium fuel, which reduces the control material worth and imposes additional requirements on the design of the reactor control features.

In general, the plutonium and minor actinide transmutation option in thorium-based fuels is more challenging to implement than the plutonium-thorium option due to a rather low delayed neutron fraction in PWR cores with 100% loading of TRU containing assemblies. However, the option of using Pu-MA-Th fuel in combination with conventional all-uranium fuel as a part of a sustainable PWR fuel cycle, with complete recycling and transmutation of TRU, appear feasible and worthy of further examination. In the future, other strategies for improving the actinide burning efficiency and $ß_{eff}$ values should be explored. In addition, non-fertile fuel matrixes should be evaluated and compared to thorium based designs, MOX fuels, and conventional all-urnaium fuel.

Task 2. Fuel-Manufacturing Costs

This task will determine if the current nuclear fuel fabricators in the US have the capability to manufacture ThO_2-UO_2 fuel economically. The task was organized into three major activities:

1. An engineering study of the feasibility of producing the thorium/uranium fuel in current nuclear fuel production facilities.
2. An effort to estimate the cost of fabricating ThO_2/UO_2 oxide fuel.
3. A developmental effort to make fuel pellets with appropriate densities and to use this material to determine fundamental heat transfer properties to use in the modeling efforts.

The Westinghouse Electric Co. has completed the first two tasks and the results were reported in the 7th and 8th Quarterly Progress Reports of this NERI project. Purdue University has been evaluating the fabrication issues associated with co-precipitation of the powder and with pressing, sintering, and grinding ThO_2-UO_2 fuel pellets.

Task 2 Progress – Purdue

Professor Alvin Solomon and Dr. V. Chandramouli

2.1. Pellet Fabrication

2.1.1. Mixtures of Commercial DUO_2 and ThO_2 powders

Commercial samples of urania (provided courtesy of Siemens Corp.) and thoria (purchased from Rhodia Corp.) were selected for the initial fabrication runs to evaluate our processing procedures and study some of the processing variables. The purity of the starting oxide materials was extensively measured and reported in previous progress reports. The 99.98% pure ThO_2 appeared to be of "nuclear grade" but some of the rare earth impurities were not quantified by the ANL Analytical Chemistry Laboratory. For co-precipitation, we began with thorium nitrate that was only available in 99.8 % purity.

It was established that the sintering temperature and time as well as specimen composition and binder all played significant roles in controlling the desired high sintered densities in urania-thoria compacts, as shown in Table 25. The 30/70 mixture has been especially problematic in achieving the desired density. In order to optimize the sintering time, further sintering runs were carried out in this quarter. The new results are included in Table 1 (Run 8). For Run 8, the results of two sintering runs are averaged since the final densities varied only ±0.2%. Comparing Run 3 and Run 8, 10 hours sintering time at 1750°C in flowing Ar-5%H_2 appears to be adequate to achieve the target density. The processing methodology used for those runs includes (1) a ball-milling process with high precision WC balls of 9/16" diameter and 0.5 wt%PEG-8000 for 24h, (2) a pelletizing methodology using a special WC-lined die and hardened punches, (3) a binder burnout process at 500°C for 1 h in air,and (4) a particular sintering schedule with uniform ramps of 5°C/min up to the sintering temperature, and the same ramp for cooling.

Table 25. Sintered densities for mixed commercial oxides

Sinter Run	Sample	Condition	Green density (g/cc)	Sintering temperature and time (°C) / h	Sintering density (g/cc)	% T.D
1	$U_{.3}Th_{.7}O_2$	Milled 8h with 1 w/o PEG-12000	6.73	1750/10h	9.29	90.4
2	"	Milled 8h with 0.5 w/o PEG-12000	6.67	1750/10h	9.29	90.4
3	"	Milled 24h with 0.5 w/o PEG –8000	6.69	1750 /24h	9.79	95.2
4	$U_{.5}Th_{.5}O_2$	Milled 24h with 0.5 w/o PEG –8000	6.63	1650/5h	9.07	86.6
5	$U_{.3}Th_{.7}O_2$	Milled 24h with 0.5 w/o PEG –8000	6.37	1650/5h	9.17	89.2
6	$U_{.5}Th_{.5}O_2$	Milled 24h with 1w/o PVA	6.40	1750/10h	9.9	94.4
7	ThO_2	Milled 24h with 1 w/o PVA	6.43	1750/10h	9.28	92.8
8	$U_{.5}Th_{.5}O_2$	Milled 24h with 0.5 w/o PEG –8000	62.8	1750/10h	10.04	95.8
	$U_{.3}Th_{.7}O_2$	Milled 24h with 0.5 w/o PEG –8000	65.5	1750 /10h	9.76	94.95

2.1.2. Co-Precipitated Powders - Dry Milling

In the previous quarter, the reverse-strike method of co-precipitating a 30 w/o uranium and 70 w/o thorium mixture was modified so as to have a more uniform, fine, and controlled introduction of the nitrates into the large excess of ammonium hydroxide solution. This was done using a peristaltic pump and forcing the solution through a fine nozzle at a rate of 5 drops per sec. The precipitate thus obtained was filtered, washed, and de-agglomerated by sonication in ethyl alcohol and air-dried for 24 hours at 200°C. The dried precipitate was finally crushed using a mortar and pestle. The powders were then calcined at 700°C for 5h in a reducing atmosphere of argon-0.5% hydrogen to obtain oxide powders of near stoichiometric composition. The resultant powder was found to have a fine particle size (~0.2 μm) and high surface area (12 m^2/gm). However, the powders were also found to be highly agglomerated when examined by SEM and laser scattering (see below). When the dry milled powder was pelletized in the usual way, the green density was low, suggesting that the agglomerates were not broken up in pressing. The results are listed in Table 26. After sintering up to 1750°C for 5h, the immersion densities were significantly less than those obtained using the commercial powders. (It should be noted that these densities are somewhat lower than those previously reported for the same specimens because the measurements have now been corrected for open porosity.)

In order to explore whether increasing the sintering time would significantly increase the sintered density, a sintering run was carried out in this quarter and the resultant density was even lower, as shown in Table 26 (Run number 7).

Table 26. Sintered densities of $(U_{.3}Th_{.7})O_2$ obtained from co-precipitated powder

No.	Precipitation Method	Green density, g/cc	Sintering temperature and time (°C) / h	Immersion Density, %
1	Direct strike	4.65	1650 / 5h	86.0
2	Reverse strike [1]	4.52	1700 / 5h	89.1
3	Reverse strike [2]	5.15	1700 / 5h	83.7
4	Reverse strike [3]	5.3	1700 / 5h	89.6
5	Reverse strike [4]	5.52	1700 / 5h	85.8
6	Reverse strike [4]	5.53	1750 / 5h	87.7
7	Reverse strike	6.07	1750/10h	81.4

[1] As-calcined. [2] Manual addition & blended with PVA and stearic acid. [3] Addition of the nitrates using a squeeze bottle, and the calcined powder blended with PVA and stearic acid using WC balls. [4] Addition of the nitrates using a peristaltic pump and as-calcined.

Therefore effort was directed to breaking up the agglomerates and pelletizing and sintering in such a way that they do not reform during dry handling. Moreover, examination of the microstructures of the sintered co-precipitated powders revealed the key reason for the especially low sintered densities seen in Table 26. The sintered structures obtained with the previous standard processing techniques produced very large pores in a relatively dense matrix as shown in Figure 43. Therefore the focus was to prevent the formation of such large heterogeneities in the microstructure. Our immediate reaction was that some gas forming species like pore-formers were producing these large holes. But since care was taken to burn out the binders at low temperatures, and no pore formers were intentionally added, we focused on breaking up the agglomerates, without much success when following the dry route.

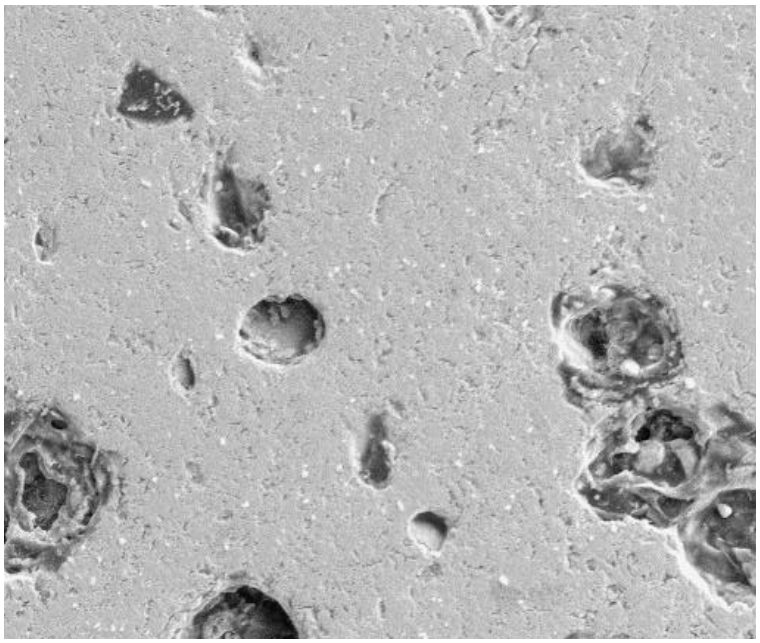

Figure 43. Large pores in co-precipitated dry milled urania/thoria powders.

2.1.3. Co-Precipitated Powders - WDP Powder Processing Route

We had learned from our wet processing studies for producing U,ThO_2 microspheres, [Solomon et al. 2002, Kuchibhotla and Solomon 2002] that uniform, concentrated and stable slurries could be obtained by controlling the zeta potential of the slurries by pH adjustment. Further, the use of certain new organics as binders in wet processing provided stearic constraints to forming hard Van der Waals bonds between the particles. Such slurries of the mixed oxide powders were found in the particle size analyzer to remain fine and suspended.

We therefore conjectured that a wet-milling step with the co-precipitated powders might produce the same excellent suspensions that might, with the presence of the organics, keep the particles isolated or un-agglomerated after drying. Finally, the wet milling step provides the opportunity of pressing a slightly moist powder that would flow during compaction. We call this the wet/dry process or "WDP" and WDP powder.

Therefore, the following processing procedures and relevant characterizations were carried out on co-precipitated powders that incorporated a wet-milling step:

Slurry preparation. A slurry was first prepared with 35 vol.% of the calcined co-precipitated 30/70 powder in de-ionized water. Then 0.5 vol.% triethanolamine or "TEA", and 0.5 vol.% of 3-aminopropyl triethoxysilane or "silane" were added, and the pH of the slurry adjusted to 3 by adding concentrated HCl. The slurry appeared to be more viscous compared to similar slurries of the mixed commercial oxides, probably due to the increased surface area of the co-precipitated powders.

The slurry was then ball milled using WC balls for 24 hours. After ball milling, the slurry was poured into a Petri dish and dried in air for 6 hours. The dried powder "flakes" were then ground well using a pestle (Powder A).

Particle size distributions. The WDP powder was analyzed for particle size distribution as shown in Figures 44 to 47 (designated as 'wet milling' in the figures). For comparison, the results for dry milled powder are also shown. Both powders originated from the same batch of co-precipitated powder (reverse strike) of the ammonium diuranate and thorium hydroxide to produce after calcination at 700°C, a 70/30 thoria/urania mixture. The size distributions of the oxide particles were measured by dispersing the powder in distilled water and performing laser scattering measurements with the Coulter LS230.

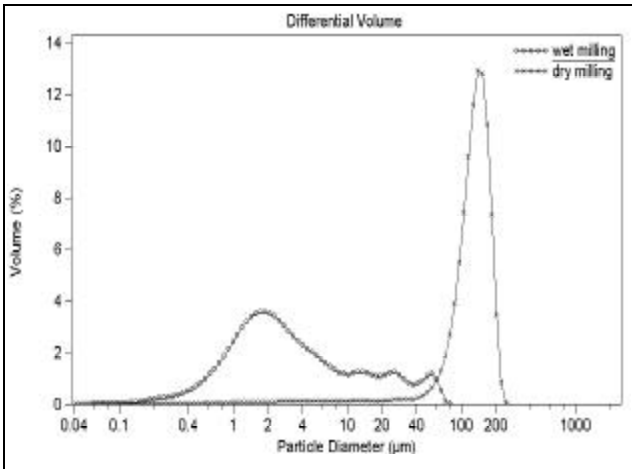

Figure 44. Initial particle size distribution of wet and dry milled coprecipitated powers at a re-circulating pump speed of "50" showing the improvement in agglomerate dispersal.

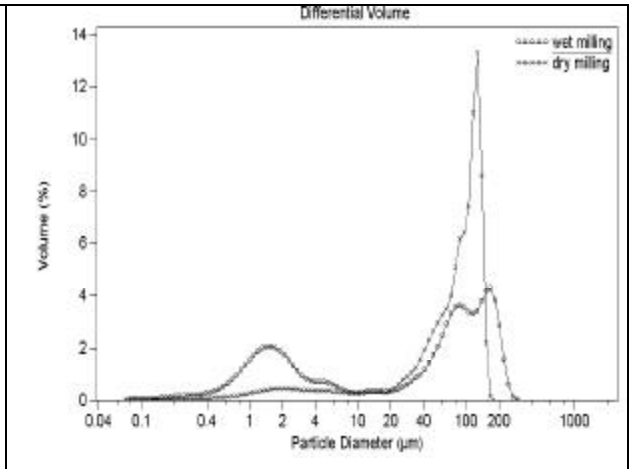

Figure 45. Particle size distribution of the wet and dry milled coprecipitated powers at a speed of 70 showing the WDP powder is beginning to agglomerate in the sampling cell at pH =7.

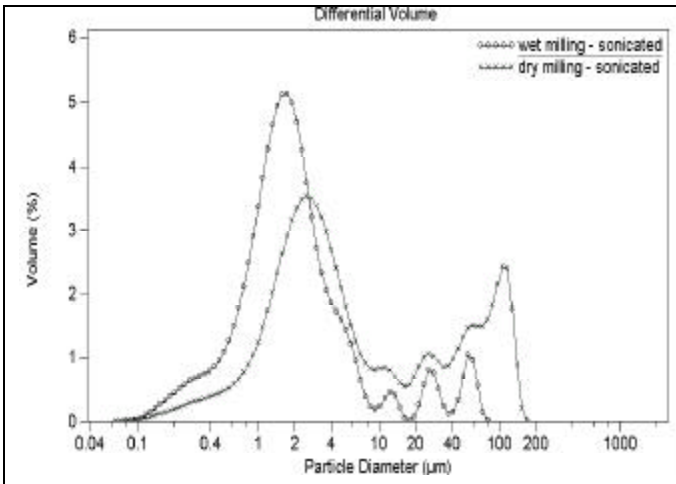

Figure 46. Particle size distribution of the wet and dry milled coprecipitated powers The slurry was sonicated (time: 2 min. and amplification: 20). Agglomeration occurs in spite of the sonication.

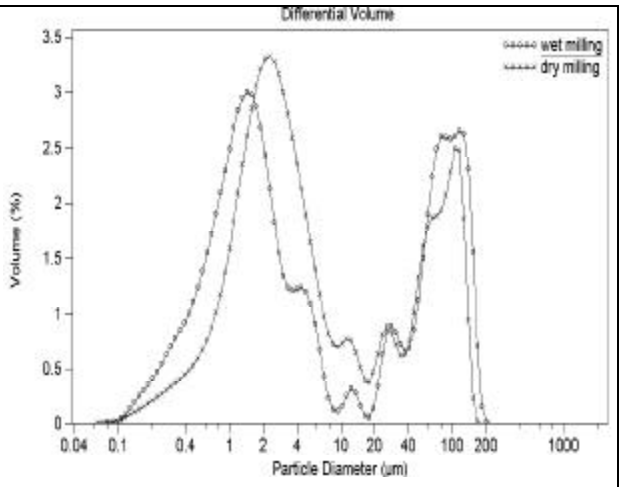

Figure 47. Particle size distribution of coprecipitated powers. The slurry was sonicated (time: 4 min. and amplification: 40). The agglomeration of the wet-milled powder was very near to that of the dry-milled powder.

The distributions shown are on a "volume" basis at different pump speeds with or without concurrent "sonication" (using a low energy ultrasonic horn). As previously observed, as agitation of the slurry increases, the agglomerates in the dry milled powder are broken up. However, for the WDP powder, as agitation of the slurry increases, the particles tend to re-agglomerate. This is expected in neutral solutions where the zeta potentials are near zero (the isoelectric point). However, before this process occurs, the improvement in the particle size distributions for the WDP powder is dramatic, Figure 44.

Pelletizing. The WDP powder was pressed into disks using at the usual 3 ton force and 30s hold time. Disk geometry was selected for subsequent thermal property measurements. Normal pellet geometry would be expected to have slightly lower densities. The green densities of the disks are listed in Tables 27 and 28. The first striking result was the uniformly high green densities. The green pellets were also very uniform in geometry with no breakage at the ends, as shown in Figure 48. These were clearly the most uniform high green density pellets we have ever produced with this fine co-precipitated powder.

Table 27. Densities and Porosities of a batch of pellets obtained from WDP Batch 1 sintered at 1700°C for 10h.

Disk No.	Green density (in %TD)	Sintered density g/cc	Immersion density, %TD	% open porosity	% Closed porosity	Geom. Density g/cc	% Geom. Density
1	63.26	10.08	98.0	0.96	0.94	9.97	96.94
2	63.69	10.04	97.68	1.1	1.22	9.98	97.04
3	63.84	10.06	97.87	1.3	0.83	9.78	95.12
4	63.18	10.02	97.5	0.79	1.71	9.71	94.43
5	63.83	10.08	98.0	1.12	0.88	9.68	94.18
6	63.66	9.9	96.3	0.52	3.18	9.97	97.0

Table 28. Densities and Porosities of a batch of pellets obtained from WDP Batch 2 sintered at 1650°C for 10h.

Disk No.	Green density (in %TD)	Sintered density g/cc	Immersion density %TD	% Open porosity	% Closed porosity	Geom. Density, g/cc	% Geom. Density
1	64.25	10.07	97.87	0.10	2.04	9.97	97.25
2	63.43	10.11	98.24	0.32	1.43	9.98	98.23

Sintering. The pellets were loaded into the Brew furnace and heated in a flowing argon-5% hydrogen gas mixture from room temperature to 500°C at a heating rate of 2°C per minute. The temperature of the furnace was maintained at 500°C for one hour in order to remove the organic materials in the compacts. This was different than our previous separate binder burnout step done in a separate furnace because of the different binders used.

After the removal of the organic materials, the temperature of the furnace was raised from 500°C to 1750°C at a rate of 5°C per minute. The furnace was maintained at that temperature for a period of 10 hours and then cooled to room temperature at a rate of 5°C per minute. The sintered pellets are shown in Figure 49, which again shows the uniformity and geometric perfection of these wet-milled pellets.

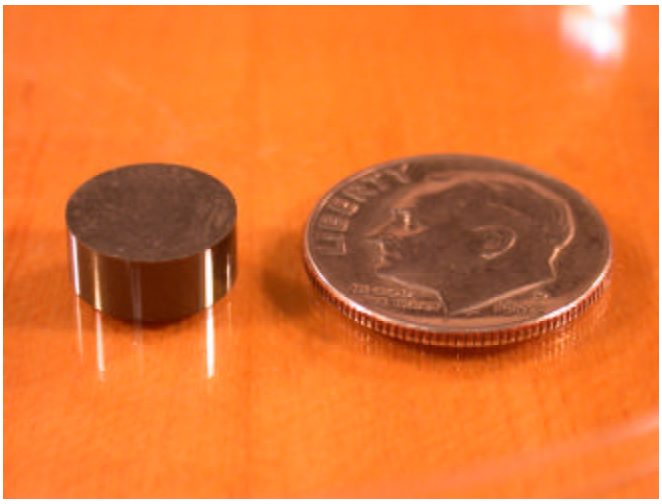

Figure 48. Pressed green disk of co-precipitated powder produced by the WDP route. The green pellet has a density of 63.6 %TD.

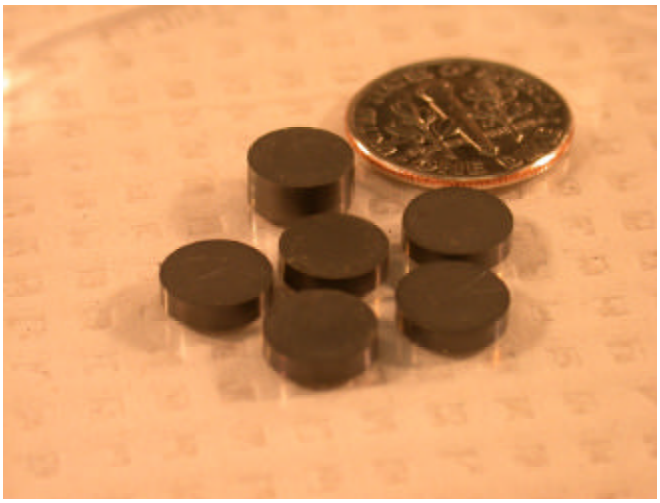

Figure 49. Sintered samples of WPD co-precipited powders.

X-ray analysis. The X-ray diffraction pattern of the sintered urania-thoria obtained by the above process is shown in Figure 50. A standard XRD pattern for $(U_{0.3}Th_{0.7})O_2$ is also shown in the figure for the purpose of comparison. The formation of the solid solution is thus confirmed.

Density measurements. The sintered densities of the wet-milled powder pellets were measured by liquid immersion using ethyl alcohol. The geometric densities of the green and sintered pellets were also measured. The results of these measurements are also listed in Tables 27 and 28. Vegard's Law was used to calculate the theoretical density of the U,Th O_2 mixtures.

It is seen that the green densities are uniformly high at 63.5%, and the immersion densities of the sintered specimens are also uniformly high at 97-98% TD. Therefore, the wet-milling process converts the difficult-to-sinter co-precipitated pellets using dry milling into pellets of uniform geometry, high density, and nearly perfect form. The high densities actually offer the possibility of reducing the sintering temperature and/or time. Therefore, a second batch was run at 1650°C/10h as shown in Table 28, but the sintered densities were still high for these disks.

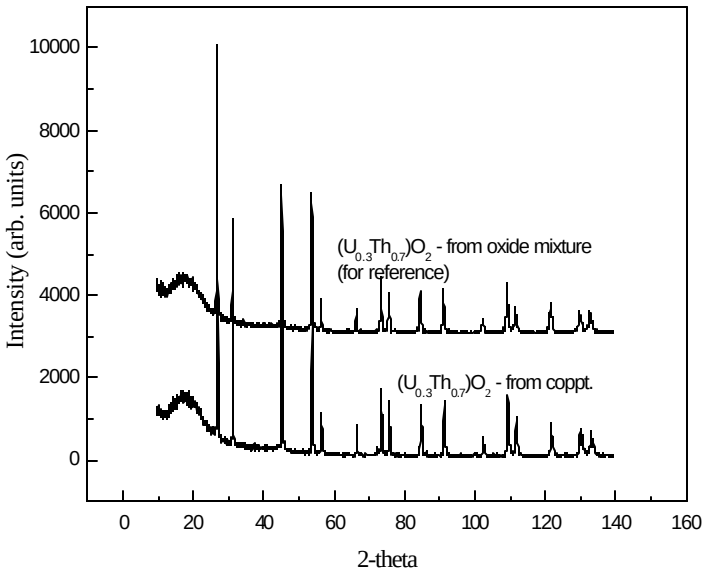

Figure 50. XRD patterns of sintered urania-thoria showing that complete solid solutions are formed.

Re-sintering. The high sinterability of the WDP powder raised the question of stability in service. Therefore a re-sintering run was carried with the sintered discs. It was found that the high density disks did not sinter but rather swelled during re-sintering and showed some evidence of macroscopic bubble growth and gas release. This was attributed to the slow reaction of the elemental carbon with hydrogen in the sintering atmosphere after pore closure. Hence, the binder removal time during sintering was lengthened from 1 to 8h, and the temperature at which this is carried out was increased from 500 to 1000°C. With these changes, the discs were found to be dimensionally stable. The stability is especially important for the thermal property measurements at very high temperatures.

2.2. Microstructural Examination

The setup of the facility, procedures to examine the microstructures of the U,ThO_2 specimens, and the results of the examinations are described in this section. Because of the differences in pressing and sintering behavior between the specimens made using commercial oxide powders ("mixed oxides") and the co-precipitated powders made at Purdue University, comparisons were made between the processing conditions and microstructures to help explain the differences.

Because of the low DAC's for thoria, a new hood system shown in Figure 51 was installed. A Buehler Minimet System was used for grinding and polishing, with the self-contained polishing cups seen in Figure 51. The hood ventilation system was ducted to our HEPA-filtered radioactive hood.

2.2.1. Mounting, Polishing, and Etching Procedures

Since sintered (U/Th)O_2 is a very hard ceramic, the mounting material also had to be hard to minimize "rounding" of the specimen during polishing. We chose the cold mount "Epoxicure" made by Buehler as the best castable and dissolvable material, but it still required casting three specimens in a single rubber mold to minimize rounding during polishing. Dissolution of the mount was necessary if subsequent thermal etching is performed after polishing (see below).

Alternatively, heating the mount to ~120°C in air rendered it brittle, and the specimens could be removed by breaking the mounting material.

Wet grinding was initially done successively with 320, 400, and 600 grit SiC papers, followed by polishing through 1-micron diamond. To prevent surface fracturing we reduced the load in the Buehler Minimet to ~1 pound and ground more gently beginning with 320 or 400 grit only and increased the grinding time. Ultrasonic cleaning was performed between all grinding and polishing steps. We verified that sufficient grinding was achieved for each step by examining the surface by optical microscopy between steps.

Figure 51. Dedicated fume hood for the ceramographic preparation of U,ThO_2 specimens using the Buehler Minimet. The color-coded polishing bowls contain the different media and polishing debris.

Chemical etching of this very stable compound was attempted first using various etchants proposed by Buehler or from published results [Ghosh *et al.* 1993]. Our initial etching attempts were done at room temperature. We first tried 30 parts phosphoric acid solution to 1 part hydrofluoric acid solution for 1 to 10 minutes following Ghosh *et al.* [1993] without any visible attack. We then tried a 1 to 1 ratio of phosphoric and hydrofluoric acid solutions for the same amounts of time, but still no attack was seen. We finally tried a 1 to 1 ratio of hydrofluoric and nitric acid, a very aggressive etchant for a maximum of 5 minutes and one could observe an attack on the mounting material, but no grain boundary attack.

Elevated temperature etching with a 50/50 mixture of HF and HNO_3 at 70 to 90°C yielded some grain boundary etching, but only *within* pores where thermal etching may also have occurred during prior sintering. On the other hand, the hot acids did effectively attack the mounting material so that specimens could be removed for thermal etching. Fortunately, SEM examination of the polished surfaces revealed that *thermal* etching could be successful in grain size measurements as described below.

2.2.2. Microstructural Observations

Because of the poor electrical conductivity of these materials, they were coated with an Au-Pd alloy before SEM examination. A typical SEM micrograph of the 70/30 co-precipitated WDP powder sintered at 1700°C/10h is shown in Figure 52 in the as-polished condition. As can be seen, the porosity is fine (~2 to 3 μm) and uniformly distributed. (The location of the porosity with respect to the grain boundaries is discussed below). This can be compared with the microstructure of the mixed commercial oxides sintered under the same conditions at a slightly lower density of 95% in Figure 53. Although the microstructures appear somewhat similar, the

coarser commercial powders lead to considerably coarser microstructures after undergoing the same sintering cycle.

The dry ball-milled co-precipitated samples exhibited strikingly different microstructures which were previously shown in low magnification optical microscopy in Figure 43. In this case, the microstructure was characterized by large stable pores in a dense matrix. Although quantitative image analysis has not been done, it is clear that these large pores dominate the density, and are the cause of the low measured sintered density of <90%TD. Examination of the large pores, shows an accumulation of residual material within the large pores that appear to contain some debris that could have derived from the low purity thorium nitrate used as a starting material, but this was never seen in other co-precipitated material.

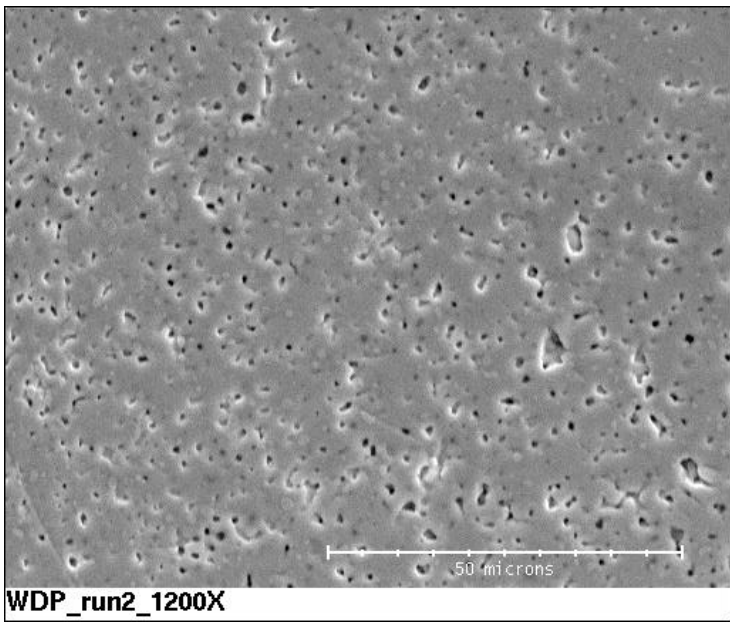

Figure 52. SEM image of polished surface of co-precipitated $U_{.3}Th_{.7}O_2$ powder processed using the new WDP methodology to produce 97%TD specimens.

As mentioned above, thermal etching was used because we were not able to chemically etch our samples. We had observed that the grain boundaries in large pores were nicely etched, so thermal etching was performed by removing the polished specimens from their mounts as described above, and annealing them along with other specimens to be sintered at 1700°C for 10 h in Argon-5%H_2.

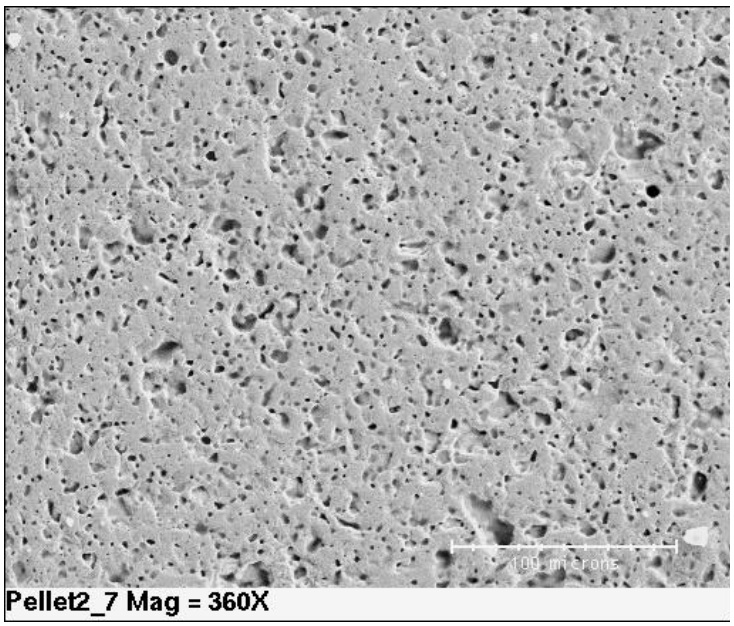

Figure 53. Scanning Electron Micrograph of polished surface of $U_{0.3}Th_{0.7}O_2$ sample from mixed commercial oxide powders sintered at 1700°C for 10h to 95%TD immersion density.

The results of the thermal etching are shown in Figure 54 for the sintered WDP powders. The grain size of this material is approximately 2 to 3µm. The pores are preferentially located at the grain boundaries. Thus pore breakaway has not occurred, and further sintering is possible, although at the highest densities, the entrapped gas pressure will eventually stop sintering. It is not known why the grain size is so small, but it may be due to the highly sinterable powder packing and green density. Residual carbon may also play a role.

Additional annealing will be performed for the thermal diffusivity specimens to determine the stability of the grain size.

The thermally etched specimen from commercial mixed oxides is shown in Figure 55. The grain size for the mixed commercial powders after our usual sintering at 1700°C for 10h was ~7 µm.

Figure 56 shows the thermally-etched co-precipitated powder samples that were dry ball-milled. For this slowly densifying material, the grain size was ~9µm.

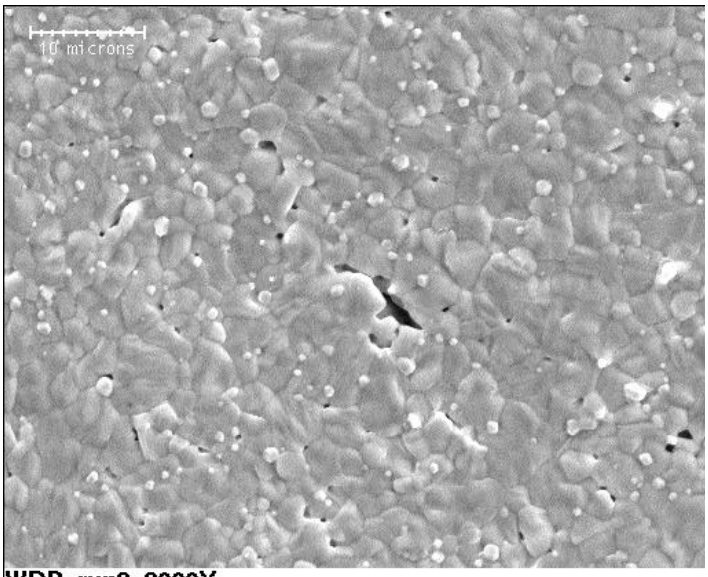

Figure 54. Thermally-etched specimen of $(U_{.3}Th_{.7})O_2$ produced from WDP co-precipitated powder and sintered at 1700°C for 10h in flowing Ar-5%H_2. Grain boundary porosity is seen.

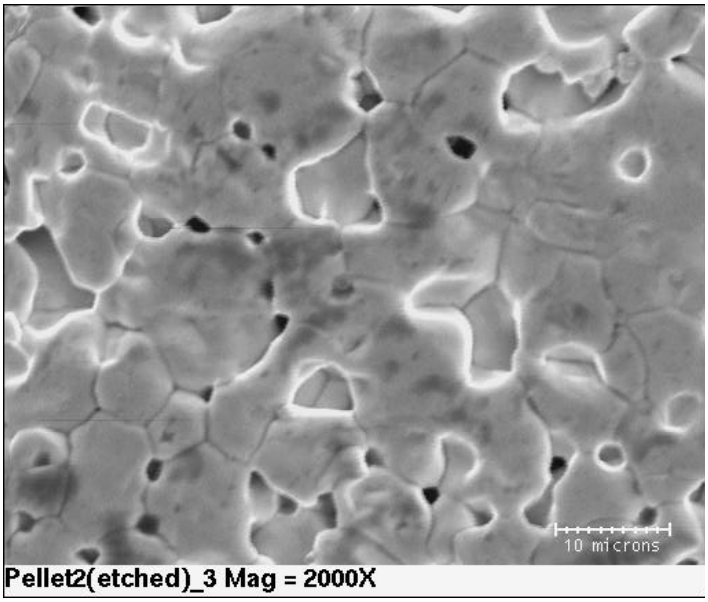

Figure 55. Thermally-etched $U_{.3}Th_{.7}O_2$ mixed commercial oxide sample showing grain boundary porosity and a grain size of ~10 microns.

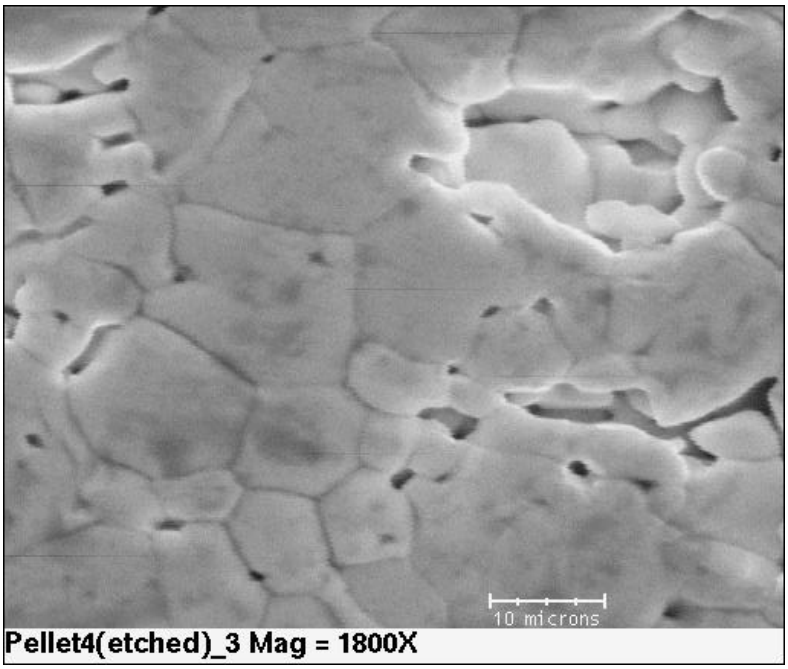

Figure 56. Polished and thermally-etched 30/70 co-precipitated powder processed using dry-milling.

Task 3. Fuel-Performance

This task is evaluating the thermal, mechanical, and chemical aspects of the behavior of ThO_2-UO_2 fuel rods during normal, off normal, and design basis accident conditions. The behavior of the ThO_2-UO_2 fuel will be compared with the current USNRC licensing standards and with the behavior of UO_2 fuel rods under corresponding conditions. Uniformly mixed ThO_2-UO_2 fuel has somewhat different properties than UO_2 fuel. These differences include

- Slightly higher decay heat,
- Higher thermal conductivity at low temperatures and lower thermal conductivity at high temperatures,
- Higher fission gas production per fission, but possibly a lower rate of release of fission gases,
- Higher melting temperature, and
- Less plutonium buildup near the surface of the fuel pellet.

During normal operation, ThO_2-UO_2 fuel will operate with somewhat lower fuel temperatures and internal gas pressures than UO_2 fuel at corresponding powers and burnups. During an accident such as a large break loss-of-coolant accident (LOCA), ThO_2-UO_2 fuel will have less stored energy but a slightly higher internal heat generation rate than UO_2 fuel at similar power levels.

Three U. S. organizations are involved in the evaluation of the performance of ThO_2-UO_2 fuel: INEEL, MIT, and Purdue. The planned work involved additional ThO_2-UO_2 material property measurements, adding ThO_2-UO_2 material properties to the MATPRO (INEEL 1996), FRAPCON-3 (Berna et al. 1997, Lanning et al. 1997a and 1997b), and SCDAP/RELAP5 (INEEL 1998) computer codes, and then applying the revised codes to evaluate the behavior of the ThO_2-UO_2 fuel. The activities to accomplish this task are summarized in Table 29 below.

Table 29. Tasks for evaluating the performance of ThO_2-UO_2 fuel.

Subtask	Task Description	Responsible Organizations
3.1	Fuel material property measurements	Purdue
3.2	Develop material property correlations for ThO_2-UO_2 fuel	INEEL, Purdue
3.3	Update FRAPCON-3 code to define the input fraction of ThO_2 in the fuel and call MATPRO functions appropriate for this type of fuel	INEEL
3.4	Develop a fission product release model for ThO_2-UO_2 fuel	INEEL, MIT
3.5	Extend SCDAP/RELAP5 to define the input the fraction of ThO_2 in the fuel and call MATPRO functions appropriate for this type of fuel	INEEL
3.6	Evaluate behavior of ThO_2-UO_2 fuel rods during normal operation using the extended FRAPCON-3 code	INEEL, MIT
3.7	Evaluate behavior of ThO_2-UO_2 fuel rods during large break LOCAs using the extended SCDAP/RELAP5 code	INEEL
3.8	Evaluate innovative ThO_2-UO_2 fuel designs	MIT

Task 3.1 is significantly behind schedule and it does not appear that Purdue intends to make any material property measurements in support of this NERI project. Tasks 3.2 and 3.3 were essentially completed during Year 1 of this NERI project. Tasks 3.4 through 3.7 were completed for the homogeneous thoria-urania fuel during Year 2. Tasks 3.6, 3.7, and 3.8 were completed during Year 3 for the various micro-heterogeneous fuels of interest.

Progress at MIT on Subtask 3.4 Fuel Performance Modeling for ThO_2/UO_2 Fuel

Y. Long, M. S. Kazimi, R. G. Ballinger, J. E. Meyer

The objective of this subtask is to develop fuel performance models for ThO_2-UO_2 fuel. These models include a fission gas release model suitable for incorporation into the FRAPCON-3 fuel performance code and a Reactivity Initiated Accident (RIA) model that will be used to modify the transient fuel performance code FRAP-T6. Note that the term "Thoria fuel" will often be used in the following text as a shorthand notation for mixed ThO_2-UO_2 fuel.

3.4.1. Summary of Achievements as of September 2001

3.4.1.1. Fission Gas Release in Thoria Fuel

Fission gas release is an important factor in achieving satisfactory performance of fuel to high burnups in LWRs. It determines the internal pressure rise within the fuel rods and excessive fission gas release might lead to fuel-cladding gap reopening at high burnup. Efforts are being made to investigate the fission gas release from mixed thoria -urania fuels with newly developed models for the appropriate thermal conductivity, thermal expansion, radial power distributions, and fission gas yield fraction [Long et al. 2002]. Fission gas release predictions of the modified FRAPCON code were compared to measured fission gas release data for mixed thoria -urania fuels from the Light Water Breeder Reactor (LWBR) program. Sufficiently detailed information is available in the open literature for only few test rods, which therefore became the basis for validating our modeling efforts. Because the mechanisms of fission gas release in ThO_2-UO_2 fuel are expected to be essentially similar to that of UO_2 fuel, the general formulations of the existing fission gas release models in FRAPCON-3 were retained. However, the diffusion coefficient was adjusted to a lower level to account for the smaller release fraction in thoria fuel. The modified version of FRAPCON-3 predicted the measured fission gas release data reasonably well. It also predicted significantly lower fission gas release from thoria-based compared with urania fuel at the same burnup as shown in Figure 57.

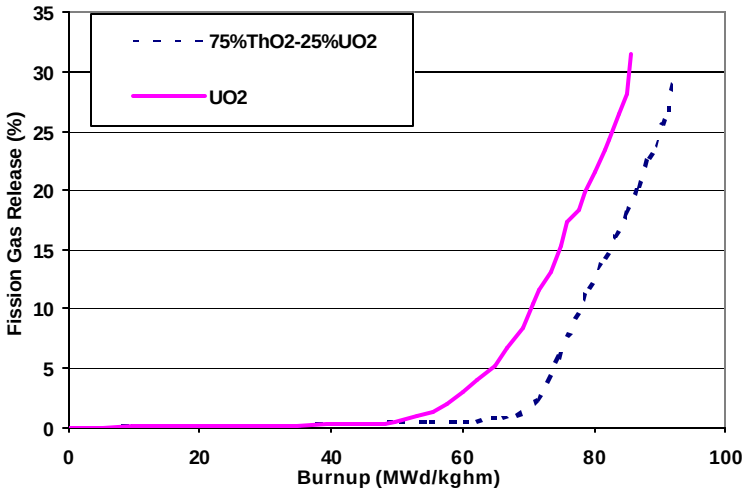

Figure 57. Fission gas release from UO_2 fuel and thoria-based fuel for a 17x17 fuel design (LHGR=25kW/m).

3.4.2. Fuel Performance Under RIA Conditions

A significant amount of energy is rapidly deposited in the fuel during a Reactivity Initiated Accident (RIA). The failure threshold of energy deposition is greatly reduced for fuel rods operated to very high burnup. There are several factors contributing to the reduction of this threshold: 1) the cladding becomes heavily oxidized, hydrided, and damaged by irradiation (thus

degraded by loss in ductility; 2) pellet-cladding mechanical interaction and/or transient induced fission gas release subjects the cladding to large forces; 3) degraded fuel thermal conductivity retains the energy in the fuel leading to higher gas pressures; and 4) large porosity in the rim region prevents heat transfer and abets gas release. The behavior of the high burnup fuel under RIA conditions is being modeled based on observations from UO_2 tests, and extrapolated to ThO_2–UO_2 fuels through the use of FRAP-T6. To properly model the deformation behavior of irradiated PWR fuels at RIA conditions for current high burnup application, efforts have been made to account for thermal fuel expansion and the fission gas induced deformation.

3.4.2.1. Thermal Expansion During an RIA

The pellet-cladding mechanical interaction (PCMI) failures in the CABRI test reactor (France) and in the NSRR test reactor (Japan) were mainly due to rapid fuel thermal expansion because most of the energy remained in the fuel pellet during the extremely small time scale of the reactivity pulse [Meyer et al. 1997]. Right after the pulse, the fuel enthalpy addition can be assumed close to the total energy deposited by the pulse. Therefore, the fuel thermal expansion during an RIA can be well correlated to the energy deposition by simply combining the effect of the heat capacity and thermal expansion coefficient. The combined effect is shown in Figure 58 for UO_2 and ThO_2 fuel. The mixed ThO_2–UO_2 fuel is expected to fall between those two lines. With the same amount of energy deposition, thoria fuel will have a higher fuel temperature due to the lower heat capacity. However this high temperature does not necessarily lead to a larger thermal expansion because of the lower thermal expansion coefficient of thoria fuel. With the same amount of energy deposition in the fuel and no energy transfer out, the thoria fuel will have slightly lower thermal expansion.

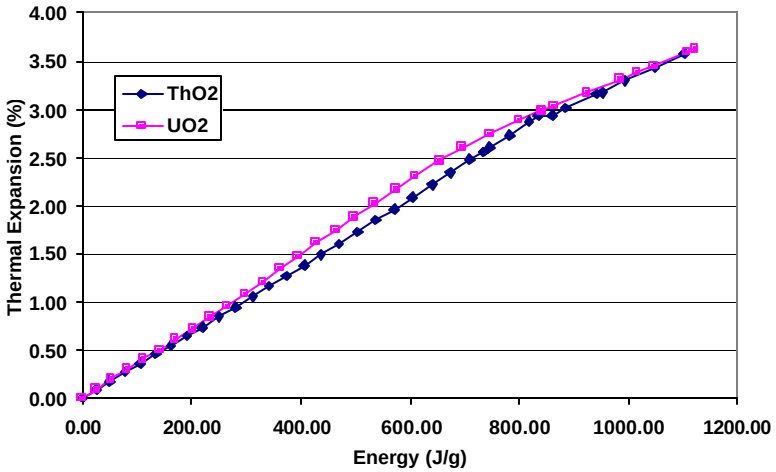

Figure 58. Relation between the thermal expansion and the enthalpy deposited in the fuel.

It is to be noted that uniform radial power distribution is assumed in the above analysis. The actual thermal expansion will be slightly different because more of the energy will be deposited near the surface of the fuel pellet. Table 30 shows the effect of thermal expansion on the cladding residual hoop strain. The thermal expansion has the largest contribution to fuel volume change in the low energy deposition case. The calculated residual hoop strains for the 2 lowest energy deposition cases, HBO2 and HBO4, are unreasonably low, which is due to a flaw in the mechanical model used in FRAP-T6. This problem is addressed in the cladding failure modeling work in the following section.

Table 30. Thermal expansion contribution to the residual hoop strain in the cladding.

	HBO02	HBO04	HBO03	HBO06	REPNa4	REPNa5	REPNa3	REPNa2
Calculated Residual hoop strain	0.00%	0.00%	0.88%	0.97%	0.72%	0.99%	1.13%	1.85%
Measured residual hoop strain	0.41%	0.20%	1.51%	1.11%	0.37%	1.10%	2.10%	3.50%
Energy deposition (J/g)	213	280	397	430	405	480	522	877

3.4.2.2. Fission Gas Swelling Behavior During an RIA

Although the fuel thermal expansion was the main contributor to the PCMI failures in the CABRI and NSRR tests, not taking into account the fuel swelling led to an unrealistic and underestimated calculated cladding strain as shown in Table 31. Clear evidence of the contribution of the fission-gas-induced swelling was demonstrated in the REP-Na-2 and REP-Na-3 tests. Fuel thermal expansion alone is not sufficient to explain the measured cladding strains. Fuel swelling occurred during the relatively low energy injection test REP-Na-3 only in the outer zones where the energy addition level was the highest, and led to a barrel-type deformation. In the high energy injection test REP-Na-2, fuel swelling occurred also in the innermost zones and led to an hourglass shape of the pellet, as observed on the cladding after the test.

Table 31. Swelling effect on residual hoop strain in the cladding.

	REPNa4	REPNa5	REPNa3	REPNa2
Residual hoop strain (Without swelling)	0.72%	0.99%	1.13%	1.85%
Residual hoop strain (Including swelling)	1.02%	1.68%	2.09%	3.17%
Measured residual hoop strain	0.37%	1.10%	2.10%	3.50%

Gaseous swelling has been investigated in our study using the GRASS model [Poeppel 1971], which was initially incorporated in FRAP-T6 to calculate the fission gas release. Although it was not developed for gaseous swelling calculations, the GRASS model has the gas volume information embedded in the calculations. This information can be used to calculate the corresponding swelling. To use the model, the initial state of the fission gas in the fuel is needed and unfortunately it is not available to us. An approximation was made by assuming a constant irradiation power history before the power pulse to calculate the initial gas state. The calculated residual hoop strain with the gas swelling effect is also shown in Table 31. The calculated results for the REPNa3 and REPNa2 tests are very close to the measured ones. However, the modified FRAP-T6 over predicts the strain for the REPNa4 and REPNa5 tests. The reason could be that the GRASS model assumes the bubble pressure is always balanced by the hydrostatic pressure. This may not be the case for fuel at low temperature because the fuel is too strong to yield around the bubble.

3.4.2.3. Cladding Behavior During an RIA

Two types of cladding failures were found in RIA simulation tests: cracking in the CABRI and NSRR tests, and ballooning in fresh/low-burnup fuel and irradiated VVER fuel rods in the IGR/BIGR tests. A third type of failure, melting is not likely to happen in a realistic RIA event.

Cracking: As cladding oxidation takes places during normal operation, about 20% of the hydrogen released from the reaction of the metal and water is absorbed in the Zircaloy cladding. When the concentration of hydrogen reaches about 120ppm, it is no longer soluble and zirconium hydride platelets precipitate out in the metal. These precipitates act as hardening centers along with oxygen, tin, and other alloying constituents. The hardness increases and the ductility decreases with burnup. Because heat flows through the cladding during normal operation of the fuel, a small temperature gradient is maintained across the cladding thickness (about 40^{o}C). This is sufficient to cause migration of the hydrogen toward the outer surface of the cladding as a result of hydrogen's tendency to move to cooler regions.

The residual hoop strain of the failed tubes in tube burst tests with artificially hydrided samples decreased with an increase in hydrogen concentration, and became less than 1% for

samples with hydride rims [Fuketa et al. 2000]. The cladding samples with accumulated hydrides failed at relatively low pressures. Even at an elevated temperature of 620 K, the residual hoop strain became less than 1% in samples with hydride rim thicker than 140 micrometers. These results demonstrate the important role of the hydride rim in the process of PCMI failure of high burnup PWR fuels.

The oxide layer on the outer surface supports a temperature gradient. Under certain conditions, heavy oxide layers begin to flake off, or spall, leaving local areas of the cladding in more intimate contact with the coolant. Those areas then run at cooler temperatures than average for the cladding surface, and hydrides migrate preferentially to those locations. Thus, when oxide spalling occurs, the underlying cladding will be very brittle in that region. Similar localized regions of hydrogen concentration can occur if there are large gaps between pellets in a fuel rod. High local hydride concentrations associated with spalling oxide are probably the reason that the REP-Na1 test rod failed with an unusually low enthalpy rise of 15 cal/g. This suggests that fuel rods that have high concentrations of hydrogen and spalling oxide or pellet gaps will have little resistance to PCMI failure during a reactivity accident.

The ductility of the cladding changes with temperature. At 600°C the cladding mechanical properties will be significantly degraded. Therefore, there is a significant risk of cladding ballooning and subsequent cladding failure because of the local internal overpressure from the transient fission gas release [Waeckel et al. 2000]. The cladding brittle failure in CABRI and NSRR tests may be partly due to an early failure before the cladding heated up.

Ballooning. Three types of VVER-type pressurized fuel rods were tested in the IGR reactor under RIA conditions: (a) Fresh fuel rods; (b) Fuel rods with pre-irradiated cladding and fresh fuel; and (c) High burnup VVER fuel rods. Ballooning was the failure mechanism for all the IGR test rods [Asmolov et al. 1997]. The peak fuel enthalpies that corresponded to the lower boundary of the failure threshold for the fresh and high burnup fuel rods were practically the same and equal to 160cal/g fuel. The fragmentation threshold of the high burnup fuel rods was not reached in these tests in spite of the fact that the central part of the fuel in one of the fuel rods became molten, a certain section of the cladding melted, and the cladding was oxidized up to 10μm. Some specific effects, that are characteristic of only high burnup fuel rod tests, were observed: (a) formation of two ruptures in the fuel cladding and (b) formation of large longitudinal ruptures. It can be noted that the ductile failures of the VVER high burnup rods (tested in IGR reactor) are in contrast to the brittle failures of the PWR high burnup rods tested in the SPERT, NSRR, CABRI reactors. Presently, a common understanding is that two factors may be responsible for this difference: (1) the high level of ductility of the irradiated Zr-1%Nb cladding of the VVER fuel; and (2) the much wider pulse duration of the IGR reactor. Measurements of the mechanical properties of the VVER irradiated claddings have shown that the yield stress and the ultimate strength of this cladding (at 60MWd/kgU) are higher than typical of PWRs by about 20-30%. This preservation of high clad ductility is a key factor in preventing PCMI failures of high burnup rods under RIA conditions.

Pulse irradiation tests of fresh fuel rods in the NSRR revealed rapid cladding deformation [Nakamura et al. 1996]. After the gap was closed, the cladding deformation was controlled by the pellet deformation and was mostly elastic. Failures occurred under conditions where the cladding reached its melting temperature at a peak fuel enthalpy of 887 J/g (212 cal/g) or higher. Under this condition, the cladding became locally thinner due to local melting. In addition, significant cladding embrittlement occurred due to the oxidation, which led to the cladding failure. When the rod internal pressure was higher than the system pressure by 0.6 MPa, cladding burst occurred at a peak fuel enthalpy of 712 J/g (170 cal/g) and at cladding temperatures below

the melting point. The fuel failure enthalpy decreased linearly as a function of the pressure difference, down to 368 J/g at a rod internal /external pressure difference of 4.4 MPa. For fresh fuels, the cladding temperature was of primary importance for fuel rod failure. The gap closure was important because it created a high thermal conductance at the pellet-to-cladding gap and subsequent cladding temperature rise. However, PCMI was of secondary importance in terms of failure of the fresh fuel rods.

Correction for Low Temperature Cladding Burst Stress. The calculated residual hoop strains for four of the NSRR tests are listed in Table 32. The calculated residual hoop strains for the two lowest energy deposition cases, HBO02 and HBO04, are unreasonably low. The problem is due to a flaw in the cladding mechanical model used in FRAP-T6. The material properties used in the FRAP-T6 simulations are calculated by MATPRO-Ver.11 [Allison 1993]. However, as shown in Figure 59, MATPRO predicts much higher burst stress in the low temperature range than measured in either the burst tests or extrapolated from the fast tensile data [Fuketa et al. 2000, Waeckel et al. 2000, Allison 1993].

Table 32. The effect of yield stress correction on residual cladding hoop strain of HBO tests.

	HBO02	HBO04	HBO03	HBO06
Residual hoop strain (original MATPRO model)	0.00%	0.00%	0.88%	0.97%
Residual hoop strain (yield stress corrected)	0.39%	0.61%	0.87%	0.95%
Measured residual hoop strain	0.41%	0.20%	1.51%	1.11%

For low temperatures (<750K), the burst stress is proportional to the strength coefficient in plastic stress-strain correlations:

$$s_B = 1.36K \quad (1)$$

Where, σ_B = tangential component of true stress at burst (Pa)

K = the strength coefficient from the plastic stress-strain correlation $s = Ke^n\left(\frac{\dot{e}}{10^{-3}}\right)^m$. (2)

Where, σ = true stress (Pa), ε = true effective plastic strain (unit less), $\dot{e}$ = rate of change of true effective plastic strain (s^{-1}), K, n, m = parameters which describe the metallurgical state of the cladding. To properly model the burst stress and the residual hoop strain during low energy deposition RIAs, the strength coefficient has been adjusted to 0.6 that of the original value. The predicted burst stress for the fully annealed cladding is shown in Figure 59. With this modification, the calculated HBO02 and HBO04 residual hoop strains are closer to the measured values, as shown in Table 32. It is to be noted that the higher calculated residual hoop strain than the measured value for HBO04 is due to the closed gap assumption.

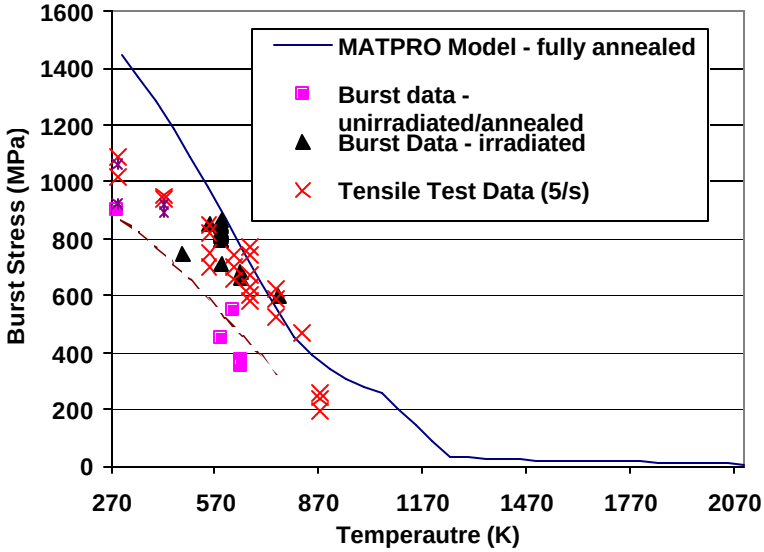

Figure 59. Burst stress and fast tensile failure stress data.

3.4.2.4. Extrapolation to PWR Conditions

There are some limitations for the RIA simulation tests because all the tests did not replicate the real LWR conditions [Schmitz and Papin 1999]:

- The CABRI tests were done in sodium coolant with low pressure. Sodium cooling keeps the clad temperatures low and the low internal pressure mitigates the dynamic gas effect.
- The NSSR tests were done in a capsule with low pressure and low temperature coolant and with a narrow power pulse (~5ms). The cladding remained during a significant time period below the brittle to ductile transition temperature.
- The IGR tests were done at low pressure, low temperature, and with a very wide power pulse (>500ms).
- The fuel rods used in the PBF tests were not fully representative of high burnup PWR fuel rods.

Thus the fuel performance during an RIA in a PWR could be different from the simulation tests. To properly model the differences, we used the MIT modified FRAP-T6 code to simulate the behavior of a high burnup fuel rod (78 MWd/kgU) during an RIA. The HBO3 test was used as the starting point to compose a case with a pressurized-water environment. The initial conditions of the HBO3 rod were adjusted to reproduce the state at end-of-life of the corresponding PWR rod (full length fuel rod; coolant condition: T=280°C, P=15.5MPa, and mass flux 3600kg/m^2-s). Since the pulse width in the HBO3 test was extremely small – only 4.4 ms, it was increased by a factor of 10 to 44 ms, which falls in the range of the pulse width for a regular PWR as shown in Table 33. To achieve the same amount of energy deposited in the fuel, the linear heat rate was reduced by a factor of 10 correspondingly. The two pulses are shown in Figure 60.

Table 33. Pulse widths for LWRs and test reactors [Meyer et al. 1996].

Reactor	Pulse width (ms)
NSRR	4.3 to 9.0
CABRI	9.5
PBF	11 to 22
SPERT	13 to 31
IGR	630 to 850
LWRs	30 to 75

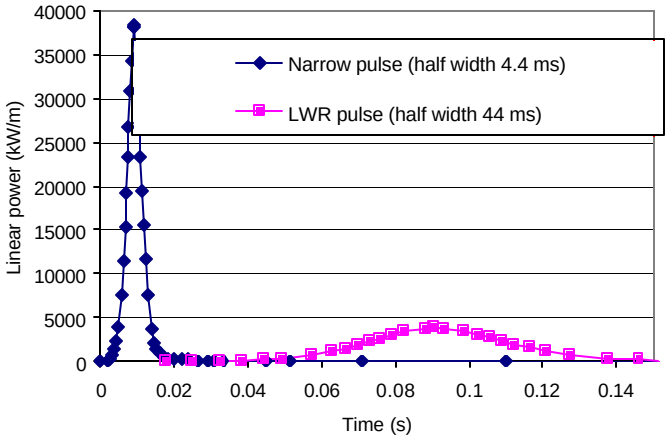

Figure 60. Pulse power history for test HBO3 and in a PWR.

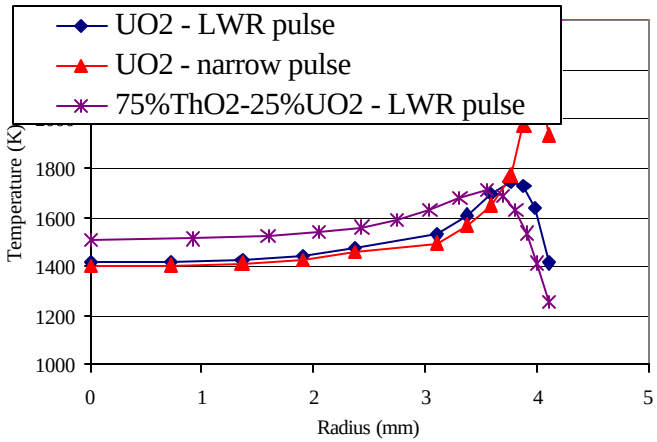

Figure 61. Maximum temperature profiles in the fuel pellets subjected to different pulse conditions.

Figure 61 shows the radial temperature profiles for both a narrow and a regular PWR pulse, when the maximum local fuel temperatures are reached. The rapid energy deposition plays the role of an envelope in

the initial phase of the transient. The profile of the energy deposition is the same as the power distribution during steady state. The high power peaking in the rim region leads to a high temperature in that area. However, a wider pulse with the same energy deposited will lead to a much lower peak fuel temperature due to the heat transfer during the process of energy deposition. The calculated peak temperature for the wider pulse case is almost 500 K lower than the narrow pulse case. This definitely will reduce the gaseous swelling and grain boundary separation in the rim region. The thoria fuel can further reduce the rim temperature due to its somewhat flatter power distribution.

The cladding temperature at the time of failure initiation will affect the threshold for PCMI failures, specifically; an increase in temperature will increase the material's fracture toughness. Also, for partly ductile PCMI failures, such as in the NSSR specimen HBO1, an increase in temperature will increase ductility hence accommodates more of the fuel pellet expansion. Thus an increase in temperature would always appear to be beneficial. Figure 62 shows the histories of cladding surface temperatures and residual hoop strains for the two pulse cases for the UO_2 fuel. Although there is not much difference in the final residual hoop strain for the two cases, the narrow pulse case reaches its final value almost instantaneously while the cladding temperature has barely changed. The cladding of an ultra high burnup fuel would be very brittle at this stage. The strain in the rod subjected to a regular LWR pulse takes a longer time to reach its final value and the cladding temperature increases gradually during the process.

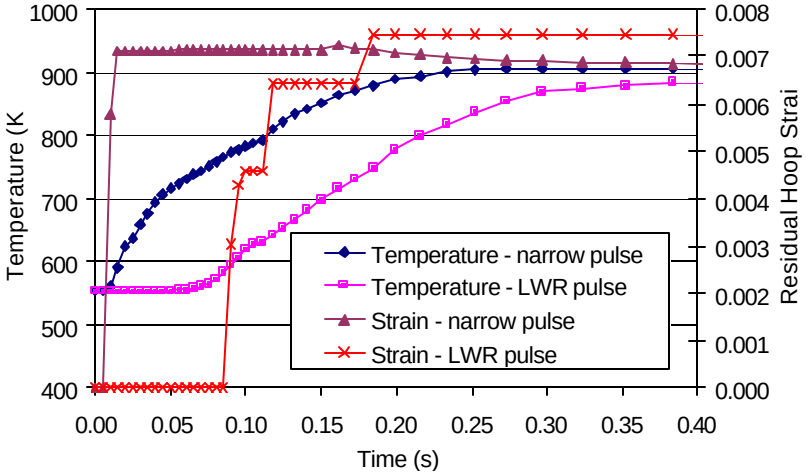

Figure 62. Cladding surface temperature and residual hoop strain during RIAs in a LWR.

Therefore, compared to the RIA simulation tests, the fuel in a real PWR will perform much better. The PWR cladding will be subjected to higher temperatures than the cladding in most of the RIA simulation tests, partly due to the difference in the temperature rise during the transient.

A similar calculation was also done for the 75%ThO_2-25%UO_2 fuel subjected to a LWR pulse. A comparison of the performance of the thoria and UO_2 fuel is shown in Figure 63.

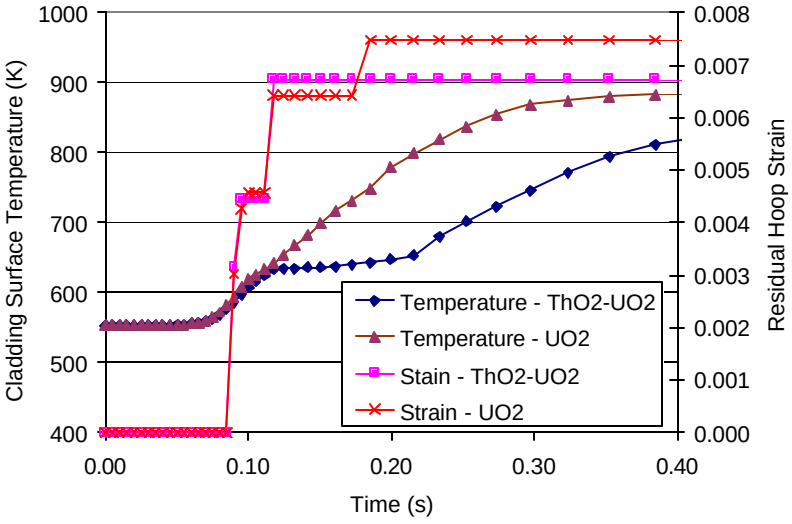

Figure 63. Cladding surface temperature and residual hoop strain of thoria and UO_2 fuel following an LWR pulse.

The thoria fuel cladding has a lower temperature and smaller residual hoop strain. The reason for the lower temperature is the lower power in the rim region of the fuel pellet. Because of this lower temperature, the cladding has more strength and thus smaller residual hoop strain. It is to be noted that the few steps in the residual hoop strain curve come from the cladding average temperature drop, although there is no drop in surface temperature.

3.4.3. Design and Operation Considerations

3.4.3.1. Introduction

New models for the rim effect, fission gas release, and fuel response to an RIA have been developed under the present task as described earlier. The results of this work show that thoria fuel performs better than UO_2 fuel during both normal operation and transient conditions. However, high burnup will still present significant challenges for burnup in the range 80-100MWd/kgHM. To achieve satisfactory performance, advanced fuel designs need to be developed, and care should be exercised in the power history of operating such fuel.

A set of criteria was proposed for acceptable performance that include limits on cladding stress and strain, cladding fatigue, circumferential cladding buckling, cladding oxidation and hydriding, cladding temperature, fretting wear, fuel rod bowing and growth, fuel maximum temperature, and fuel rod internal pressure [Bailly et al. 1999]. The same set of issues was re-evaluated for high burnup safety in [NEA, 2001]. Fuel element leaks during reactor operation must be avoided to control the primary circuit contamination and prevent forced shutdowns. Thus in PWRs, the probability for leaking rods must be maintained below about 10^{-5} per cycle to be tolerated, which corresponds to a few defective rods at most per reactor cycle. Fuel elements and assemblies must also have limited geometric strain, to avoid deteriorating the cooling conditions, hindering the operation of the reactivity control systems (absorber materials), and hindering or endangering the fuel loading and unloading operations.

3.4.3.2. Extrapolation of Current Fuel Designs

The thoria fuel concepts in this work are intended for use in PWRs with as little design change as possible. The current PWR fuel design, but with the thoria fuel, will first be assessed to determine its limitation for high burnup applications. The reference plant used for this study is a standard Westinghouse 4-loop 1150 MWe PWR. Within the US fleet of reactors, there are 72 operating PWRs, and 27 of them are such Westinghouse 4-loop reactors. In addition, this class of PWRs has a fairly high power density (104.5 kW/L) when compared to other PWRs, and thus represents a demanding application. The key system parameters are presented in Table 34, of particular note is that the fuel rod cladding material is standard Zircaloy-4. The growth rate of the corrosion layer for this material is generally larger than that for modern PWR fuel cladding, such as low tin Zircaloy-4 or ZIRLO cladding.

Table 34. Key reference reactor operating parameters and fuel design features [Garcia-Delgado et al. 1998].

Operating parameters	Value
Pressure (MPa)	15.51
Core inlet temperature (^oC)	292.7
Coolant mass flux (kg/m^2s)	3628
Core average linear heat rate (kW/m)	18.29
Cladding material	Std Zircaloy-4
Cladding outer diameter (mm)	9.5
Cladding thickness (mm)	0.57
Rod pitch (mm)	12.6

Figure 64 displays the relative axial power shapes for a typical PWR fuel rod as a function of its cycle of operation. The distributions reflect the expected results with use of burnable poison for an operation cycle of about 18 months. To achieve higher burnup, the cycle length was extended, but the core average power was kept the same for this work.

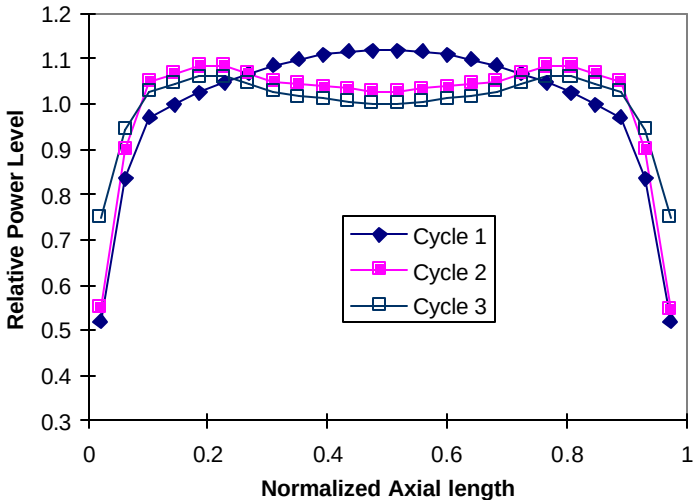

Figure 64. Relative axial power distribution.

A demanding situation of a constant pin average linear power of 25 kW/m was assumed in assessing the fuel performance of the current PWR fuel designs (a fuel pin with 25%UO_2-75%ThO_2 was considered). The cladding corrosion and fission gas release were calculated using the fuel performance code FRAPCON-3 [Berna et al. 1997] with the modifications discussed in the previous chapters. The predicted oxide thickness of the Zircaloy-4 cladding at end-of-life is very large for 100MWd/kgU PWR fuel as shown in Figure 65 and beyond the capability of the code. The cladding corrosion model in FRAPCON-3 can only handle an oxide thickness up to 150μm, which is why there is an apparent cutoff at 150μm in Figure 65. This large oxide thickness will lead to spallation of the oxide. The calculated fission gas release and rod internal pressure are shown in Figure 66. The fission-gas release from the 75%UO_2-25%ThO_2 fuel is around 40% at end-of-life and leads to a rod internal pressure exceeding the system pressure.

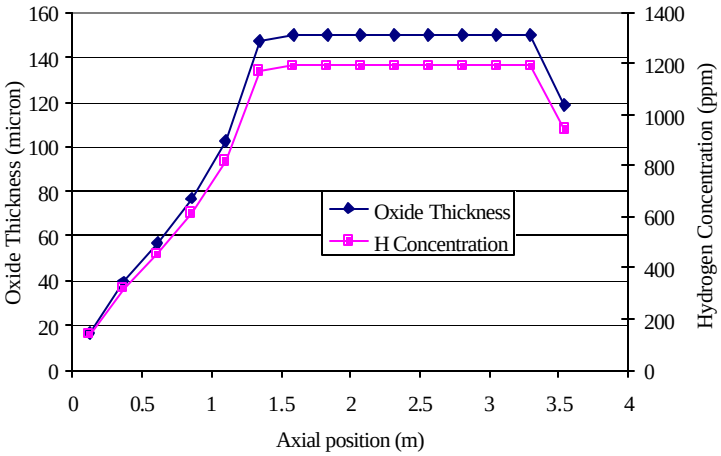

Figure 65. Maximum oxide thickness of Zry-4 cladding of a rod irradiated at constant average linear heat generation rate of 25kW/m up to 100MWd/kgU.

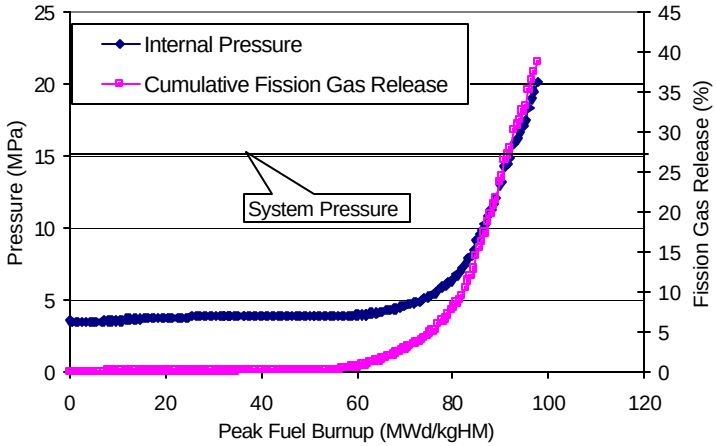

Figure 66. Cumulative fission-gas release and internal pressure for the current fuel design at constant power of 25kW/m.

The above analysis of the cladding corrosion and fission gas release indicates that satisfactory fuel performance at high burnup fuel (up to 100MWd/kgHM)

cannot be achieved using the current fuel designs. A new design, including new cladding materials and operation strategy, have to be adopted to improve the fuel performance, especially the fission gas release and cladding corrosion.

3.4.3.3. Advanced Cladding Materials.

The low-alloyed zirconium-base alloys Zircaloy-2 and -4 were developed for fuel rod cladding and for fuel assembly and other in-core structural components in the late 1950s and early 1960. The technical progress in the field of the zirconium-based alloys for reactor use together with the progress in the UO_2 fabrication area has driven discharge burnups to be increased from initially about 10MWd/kgU (BWR) and 20MWd/kgU (PWR) to currently about 45 to 50 MWd/kgU. Within this wide range of burnup, zirconium-based alloys were able to provide very good performance and are now exclusively used in LWRs. However, the increasing demand for higher discharge burnup and longer cycle lengths has led to the need for higher coolant lithium levels, reactor power up-ratings, and higher local power peaking factors. Therefore, waterside corrosion of the cladding has become one of the limiting factors in fuel rod performance. Unfortunately, the existing fuel performance models and even the traditional cladding itself can not meet the requirement of the general trend to higher fuel burnups and longer residence times. Extensive research on corrosion enhancement at high burnup has been conducted recently at both industry and research institutes. LiOH and hydride effects have been paid special attention as affecting the mechanism of accelerated corrosion.

The cladding development has focused on reducing the corrosion and thus reducing the hydrogen content of the cladding and maintaining appropriate mechanical properties at high burnup levels. Because of the extended exposure of the cladding material to the core environment, the fuel vendors are moving to advanced zirconium alloys with proprietary compositions and processing techniques. In general, these advanced alloys are low in Sn and high in Fe and Cr compared to the original Zircoly-2 and -4. The Zirconium/niobium alloys are also being evaluated for their ability to maintain ductility at high burnup levels. Zirconium/niobium alloys have long been recognized for their superior corrosion performance and have been used in a wide variety of reactors. ZIRLO from Westinghouse [Westinghouse 1991], DUPLEX from Simmons [Sabol et al. 1994, Seibold et al. 2000] and M5 from Framatome [Forat and Florentin 1999] represent the innovative claddings and they have been demonstrated to have good in-pile performance. The M5 alloy, in the re-crystallized state for cladding tube material, exhibits better results acquired up to 63 MWd/kgU, when compared to those obtained with any low tin Zircaloy-4 alloy [Forat and Florentin 1999]:

- The overall oxidation is reduced by a factor of 3 to 4,
- The hydriding is reduced by a factor of 5-6,
- The free growth is lowered by a factor of 2-3,
- The irradiation creep is reduced by a factor of 2-3.

Corrosion of the fuel rod cladding leads to a wall thickness reduction, and is limited by NRC regulation to 10% for LWR fuel rods to comply with the mechanical stability requirements under transient conditions [Groeschel and Hermann 1996]. For standard Zircaloy-4, three transitions in high burnup fuel cladding corrosion have been identified and their mechanisms have been proposed, based on extensive research. The first transition is stress and microstructure transformation controlled. The second transition is due to high irradiation in the reactor. Current high burnup transition investigations are more focused on lithium and hydride effects and several hypotheses are available.

Currently, FRAPCON-3 uses a two-stage corrosion model by Forsberg et al. (1995) for standard Zircaloy-4. The oxidation proceeds via a cubic rate law until the transition thickness (taken to be 2.0μm) is accumulated. That is,

$$\frac{ds}{dt} = \left(A / s^2\right)\exp\left(-Q_1 / RT_i\right) \tag{3}$$

After transition, the oxidation proceeds according to a linear rate law; that is,

$$\frac{ds}{dt} = C(\Phi)\exp\left(-Q_2 / RT_i\right) \tag{4}$$

where,

ds/dt = Oxidation rate (μm/day)

T_i = temperature at oxide-to-metal interface (K)

R = 1.98 cal/mol/ K

For Standard Zircaloy-4, $A = 6.3 \times 10^9$ μm^3/day, Q_1 = 32,289 cal/mol, Q_2 = 27,354 cal/mol.

The factor for the post-transition corrosion in Equation (4) is a function of neutron flux F, which captures the irradiation effect on the cladding corrosion:

$$C(\Phi) = C_0 + U\left(M\Phi\right)^p \tag{5}$$

Where,

F= fast neutron flux (E>1 MeV), n/(cm^2·s),

For Standard Zircaloy-4, $C_0 = 8.04 \times 10^7$ μm/day, $U = 2.38 \times 10^8$ μm/day, $M = 1.91 \times 10^{-15}$ cm^2-sec/n, and the superscript p = 0.24.

However, the oxide thickness did not show any irradiation or high burnup transition up to 64 MWd/kgU for M5 and 82 MWd/kgU for DX Zr1Nb cladding [Willse and Garner 2000, Seibold et al. 2000]. The corrosion behavior of these two cladding materials shows less sensitivity to temperature and exhibits less data scatter than Zircaloy-4. Oxide thickness data scatter is indicative of a low sensitivity to irradiation conditions, including reactor power histories and differences in operating conditions from one plant to another.

Thus, in modeling the corrosion behavior of M5 and DX Zr1Nb cladding, the neutron fluence term C(?) of the post-transition equation was removed to represent the relative insensitivity to irradiation and the activation energy Q_2 was adjusted to a lower value due to the low sensitivity to temperature. The pre-factor C(?) was adjusted accordingly by orders of magnitude.

Since M5 and DX Zr1Nb are both zirconium alloys with 1%Nb, they have the same corrosion behavior and should be modeled the same. For M5 and DX Zr1Nb cladding materials,

the pre-transition corrosion equation was kept the same as for the standard Zircaloy-4 cladding, while the corrosion rate of post-transition state was changed to:

$$\frac{ds}{dt} = C \exp\left(-Q_2 / RT_i\right) \qquad (6)$$

Where, $C = 1.367 \times 10^2$ μm/day, $Q_2 = 11{,}078.4$ cal/mole.

The model gives a very reasonable prediction of the axial oxide thickness profile (Figure 67) and the peak oxide thickness versus burnup (Figure 68). In this study, a constant linear heat rate of 18.29 kW/m (which corresponds to the core average power) was assumed and this inevitably causes some uncertainty. But, given the insensitivity of the M5 corrosion to the power history [Willse and Garner 2000], the uncertainty should be almost the same as the data scatter, which is small compared to Zircaloy-4.

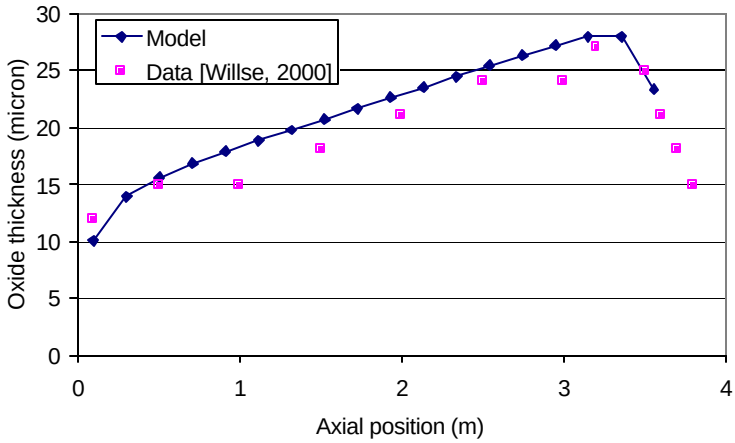

Figure 67. Prediction of the axial oxide thickness profile of M5 cladding at 63MWd/kgU.

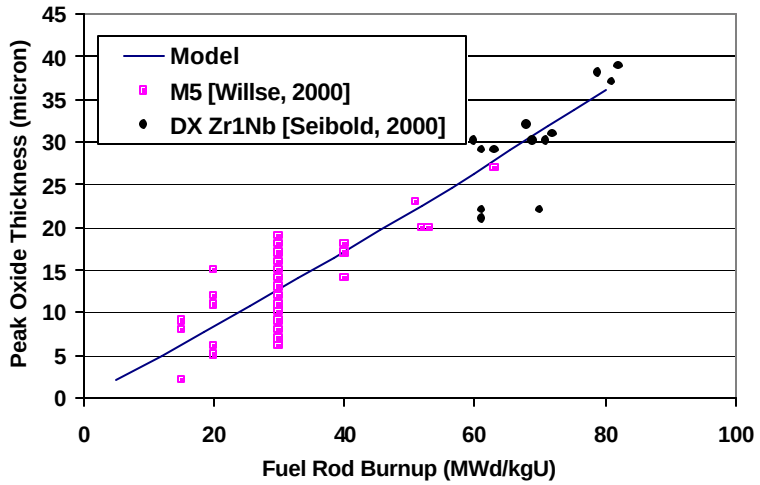

Figure 68. Prediction of M5 and DX Zr1Nb corrosion with rod burnup.

Hydrogen produced in the corrosion process penetrates into the metal, forming brittle zirconium hydride, which reduces the ductility of the metal. Regulation limits the acceptable average hydrogen concentration to about 500ppm [Groeschel and Hermann 1996]. Due to the much lower corrosion rate and considerably lower hydrogen pickup, M5 and DX Zr1Nb will have much lower hydrogen concentration. The 500ppm threshold hydrogen content will not be exceeded at burnups up to 100MWd/kgHM.

The measured hydrogen pickup ratio of DX Zr1Nb is only 0.28 of that for the Zircaloy-4 [Seibold et al. 2000]. Preliminary calculations, using this low hydrogen pickup ratio, show that the hydrogen concentration in the advanced cladding remains below 100ppm. With hydrogen concentrations this low, the hydrogen will not have any impact on the mechanical properties of fuel cladding.

Since cladding brittleness is of concern during an RIA event and hydride is the main contributor, the advanced cladding material will certainly improve the fuel performance during such events. Then, the remaining concern would be the impact of the neutron fluence on the cladding brittleness. Unirradiated M5 cladding is very ductile, but the ductility is reduced in a reverse manner with burnup. At 350°C, the total elongation in a tensile test can be reduced from 40% for the unirradiated material to 9.7% at 38MWd/kgU [Mardon et al. 1997]. Further increasing the irradiation exposure, may reduce the ductility to unacceptable values.

3.4.3.4. Large-Grained Fuel Pellets.

Grain size enlargement has been evaluated as one means to mitigate the rim effect and the consequent enhanced gas release [Spino 1996]. Various types of large grain fuels have been tested in-pile, namely un-doped urania, UO_2 doped with metal oxides of Nb_2O_5, TiO_2, Cr_2O_3, and La_2O_3, and UO_2 doped with Al and Ti-silicates [Kubo et al. 1994, Killeen 1975, Killeen 1980, Une et al. 2000, Nogita et al. 1997]. Under steady state operation, the rim effect, fission gas release, and swelling were improved in all cases.

Grain size effects on the fission gas release. It will take longer times for the gas atoms to diffuse to the grain boundaries of larger grains, and there is also less swelling. Several types of large grained pellets were irradiated in the Halden Boiling Water Reactor. Besides the standard grain size pellets (grain size: 9~ 12 μm), two types of large-grained -pellets of un-doped (51-63μm) and alumino-silicate doped fuel (46-58μm) were fabricated and loaded in these fuel rods [Hirai et al. 2000]. The fission gas release estimates were derived from the rod internal pressure data, during both reactor shutdown and operation, and from post irradiation examinations. The fission-gas release estimates from the rod internal pressure data agreed with each other and were consistent with the post irradiation examination results. It was concluded that the fission-gas release was suppressed by 20 to 50% due to enlarging the grain size, regardless of the additive type and additive content.

However, under simulated power transient conditions after a burnup of ~25 MWd/kgU, only un-doped and silicate doped large grained fuels showed better behavior than standard UO_2. The Nb_2O_5 and TiO_2 doped fuels showed a high gas release under transient heating [Kubo et al. 1994]. Since doping of large grained UO_2 is necessary to counter its otherwise worse creep and pellet-cladding interaction behavior, the above results suggest the preferable use of silicates as plasticizers (for grain boundary sliding) than of dissolved niobia and titania. However, in-reactor ramp testing of silicate-doped fuels is needed to prove their actual effectiveness as a pellet-cladding mechanical interaction remedy, as was the case with niobia [Howl et al. 1994].

While it is possible to change the grain size in FRAPCON-3 and get a reduction in fission-gas release, the match between the predictions and the observed fission-gas release is not good. This improvement is a development to be undertaken in the future.

Grain size effects on the rim structure. The improvement in the fission-gas release due to larger sized grains has long been recognized, but the improvement to the rim structure formation is a recent finding. The mechanism of this improvement has been under extensive investigation using various techniques, such as optical microscopy, SEM, EPMA, XRD, and TEM [Une et al. 2000, Nogita et al. 1997]. TEM observations have shown an inhomogeneous accumulation of dislocations along the grain boundary. This indicates that the grain boundaries inhibit the climbing motion of dislocations and then are important sites for inhomogeneous dislocation accumulation, namely for formation of nuclei for re-crystallization. Consequently, a smaller as-

fabricated grain-size leads to a higher dislocation density because of the larger grain boundary surface area per volume. From a simple geometrical consideration, the grain boundary area per volume is inversely proportional to grain size, i.e. $\propto d^{-1.0}$.

The SEM fractography has shown some sub-divided grain structure that appeared to be localized along the grain boundaries [Une et al. 2000]. The SEM results support the inhomogeneous accumulation of dislocations near and/or on the grain boundaries. Recent re-evaluation of the rim structure width for LWR pellets of the HBEP program has shown that a PWR pellet irradiated to 63 MWd/kgU with a grain size of 78 μm significantly impeded the microstructure change, although the local burnup at the pellet rim had exceeded the threshold burnup 80 MWd/kgU for small grain fuel [Mogensen et al. 1999]. Consequently, large-grained pellets with higher resistance to the rim structure formation also show lower rim bubble swelling and lower fission gas release at high burnup.

3.4.3.5. Use Of Annular Fuel Pellets and Large Plenum Volumes.

The fuel rod is pressurized at the time of fabrication to mitigate cladding creep and to increase initial gap conductance. Under normal reactor operating conditions, this pressure must be lower than a value that will lead to dimensional instability or heat transfer impairment at high burnup. This criterion is such that the hot internal pressure, due to the accumulation of the pressure of the initial helium of the new rod and that of the fission gases released during irradiation, must be lower than the pressure needed to open the diametrical gap between the pellets and the cladding by tensile creep of the cladding. The purpose of this criterion is to avoid thermoplastic instability, where by the increase of the gap causes pellet column heating and, therefore, an acceleration of fission gas release, thus an abnormal increment of the internal pressure of the rod.

The current fuel design cannot meet this criterion because the internal pressure in a conventional fuel rod at 100MWd/kgHM will be significantly higher than the primary coolant pressure. A large-sized grain design will have a little lower fission gas release and thus lower internal pressure, but the improvement is unknown at present. To make the fuel operable at very high burnup, additional gas accommodation volume has to be provided. One approach to increase the free gas volume in the rod is to use annular fuel pellets. Another one is to increase the gas plenum volume.

Annular fuel pellets. There has been a modest increase in the use of annular fuel pellets because of their improved thermal margins and larger fission product gas accommodation volume. Annular fuel pellet use is now common in the natural uranium or low enrichment pellets used as axial blankets in LWRs. All the fuel in the Russian VVER-1000PWR is annular, having a 10% volume central void. The benefits of using annular fuel include:

- Increased space for accumulation of fission gas, and hence reduced rod internal pressure;
- Delayed and reduced pellet-clad-interaction (PCI);
- Lower peak fuel temperatures; and
- Lower stored energy in the fuel pins, and therefore benefits for the LOCA limits.

An economic evaluation performed at B&W indicated that fuel cycle cost benefits are optimum for annular fuel with about 10% void volume [Badruzzaman 1980]. Therefore, the void volume fraction was set to 10% also in this study. The ratio of fuel pellet temperature difference

ΔT (center-surface) of annular (a) to solid (s) fuel pellets having the same external diameter and linear power is:

$$\frac{\Delta T_a}{\Delta Ts} = F = 1 - \frac{\ln\left(\frac{R_o}{R_i}\right)^2}{\left[\left(\frac{R_o}{R_i}\right)^2 - 1\right]} \qquad (7)$$

Where R_o, R_i = the outer, inner radii. At a void fraction $v = \left(\frac{R_o}{R_i}\right)^2 = 0.1$, it is found that F=0.74, thus the peak ΔT is ~25% lower. The ratio of the pellet-average temperature difference $\overline{\Delta T}$ values can be shown to be:

$$\frac{\overline{\Delta T_a}}{\overline{\Delta Tb}} = AF = 1 - \frac{2F}{\left[\left(\frac{R_o}{R_i}\right)^2 - 1\right]} \qquad (8)$$

For v=0.1 this ratio AF is 0.83, a ~17% reduction. This reduction also applies to the stored energy in the fuel pin (and assembly) when weighted by the fuel volume (1-v); hence total thermal energy reduction is 0.25 in this study.

The added free gas space is relative to solid pellet volume, which for v=0.1 is slightly more than the usual end-of-pin gas plenum volume (5 to 10% of active fuel length). Because the temperature in the central volume is very high, with the same initial filling gas pressure, the annular fuel will have higher internal pressure when the fuel is hot. To achieve a comparable internal pressure, the pressure of the initial fill gas was reduced from 1.4 MPa to 1 MPa in the annular fuel. The calculated fractional fission gas release was found, at 100 MWd/kgHM, to be 35% compared to 40% in the solid fuel. The calculated internal gas pressure was 14.7 MPa compared to 20 MPa for solid fuel. However, Hastings et al. [1985] has shown that annular fuel actually has a higher fission gas release than solid fuel. Therefore the benefit of annular fuel on the fission gas release may be modest.

Large gas plenum. A larger gas plenum can also accommodate the high fission gas release in the high burnup fuels. It is found to be more efficient than the annular pellet design in this aspect because the temperature in the plenum is much cooler than in the void of the annulus. By doubling the plenum from 0.4 m to 0.8 m, the internal pressure at end-of-life can be comparable to the annular pellet design. The larger plenum will increase the friction pressure drop. However, from an economics point of view, a large plenum is more desirable than the more costly annular pellet design. Furthermore, there is more room to increase the plenum, while a large central volume may cause the fuel to become unstable (i.e., fragmented fuel may fall into the central hole).

3.4.3.6. Techniques to Aid Fuel Management Decisions

The current standard practice in the industry is to burn the fuel to a batch average burnup of about 50MWd/kgHM. At this level of burnup, there is much less degradation of the fuel. Also, the power history shape has much less of an effect on the fission gas release because there is very

little fission gas release. However, at a burnup of 80-100MWd/kgHM, the internal gas pressure becomes a major problem, especially if the power history is constant.

A high linear power near end-of-life can cause many problems: (1) high oxide-cladding interface temperature due to thicker oxide acting as a thermal barrier; (2) high fuel temperature due to degradation of fuel thermal conductivity; (3) high gas temperature and pressure in the central volume of the annular fuel pellet. Therefore, it is always desirable to have a decreasing power history with burnup to counter these effects, i.e. more power is produced at the beginning to take advantage of the relatively high fission gas release threshold and low fission gas inventory at that time.

Eleven decreasing power histories with an average level of 25kW/m, shown in Figure 69, were used to analyze the fission-gas release at a burnup of 80MWd/kgU. Other operating conditions were kept the same as the reference Westinghouse PWR case. The cumulative fission gas releases for the various power histories at a burnup of 80 MWd/kgU are shown in Figure 70. Power History 6, in which the power begins at 35 kW/m and ends at 15 kW/m has the lowest cumulative percentage of fission gas released. Actual power histories in LWRs always include abrupt changes after each fuel reload and can not be so smooth as the ones in Figure 69 and the approach to an optimized power history will vary accordingly. But the concept demonstrated here can be utilized to guide the fuel design and operation (i.e. poison design to control the power history).

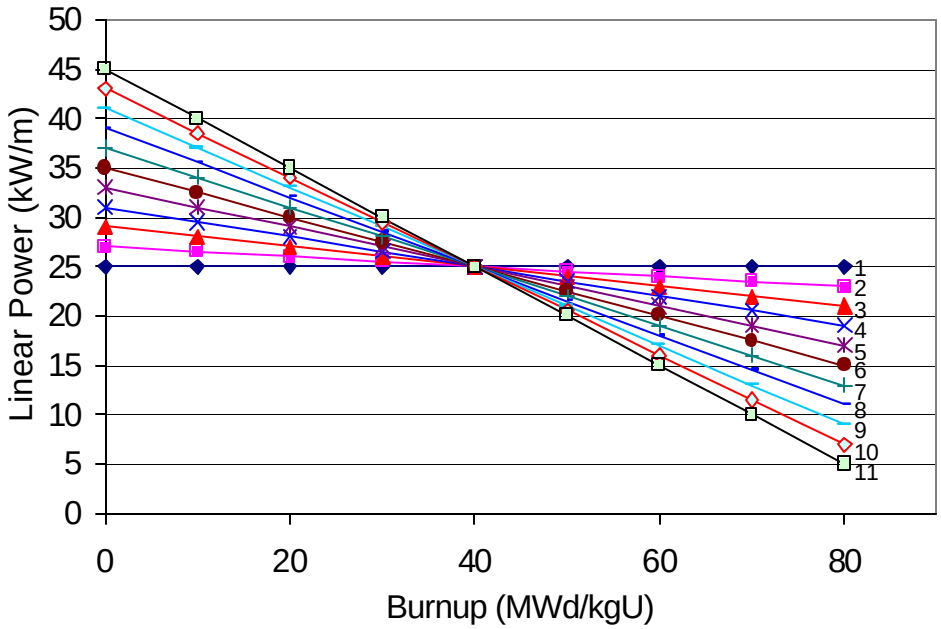

Figure 69. Decreasing power histories for constant burnup.

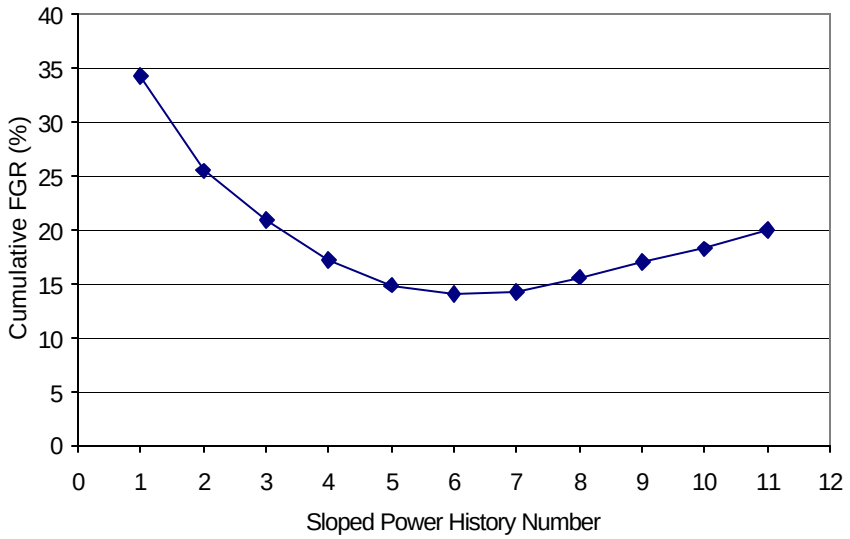

Figure 70. Cumulative fission gas release with various power histories.

3.4.3.7. Assessment of Micro-Heterogeneous Fuel

The key parameters for a micro-heterogeneous fuel design - DuUAx4 are given in Table 35. The configuration of this micro-heterogeneous fuel is very complicated and cannot be directly simulated by the modified FRAPCON-3 code. An approximate approach has to be adopted to investigate the fission-gas release and corrosion performance.

Table 35. Configuration and burnup performance of DuUAx4 design.

	Length (mm)	Annulus		Central pellet		B1 (MWd/kg HM)
		Outside Radius (mm)	Materials	Outside Radius (mm)	Materials	
Driver Pellet	40	4.127	UO_2 (19.5% enriched)	2.063	Graphite	55.94
Thorium Pellet	91	4.127	ThO_2	1.137	UO_2 (19.5% enriched)	

For the corrosion calculations, the conventional fuel rod is divided into 3 segments (1.27m, 1.11m, and 1.27m respectively), the middle segment represents all the driver pellets and the upper and lower segments represent the thorium pellets. The fuel format of each segment is specified the same, but at different power levels. At the beginning of life the power of the driver zone is about 2.4 times the average power, while the power of the thorium zone is about 0.38 the average power. The average discharge burnup in a 3-cycle batch

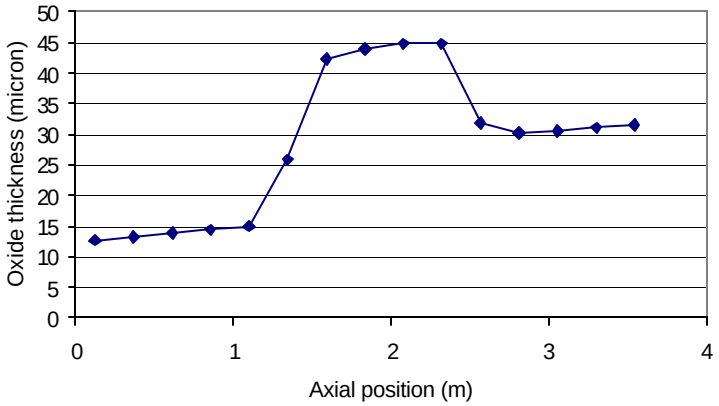

Figure 71. The corrosion performance of DuUAx4 fuel design with driver and thorium pellet position rearranged.

will be around 84 MWd/kgHM. For some rods the burnup may reach 100MWd/kgHM. In order to avoid a gap convergence problem, a lower constant power history of the average linear heat generation rate 18.29kW/m instead of a hot pin situation of 25kW/m were assumed. This is acceptable for M5 corrosion calculations because the reduced power level means a longer irradiation time and hence more corrosion. The calculated oxide thickness profile is shown in Figure 71. The peak oxide thickness in the driver zone is around 45μm and the value in the thorium zone is around 30μm.

Another concern about the axial heterogeneous design relative to corrosion is that the hydrides in the cladding will migrate to the cooler area surrounding the thorium pellets. The average hydrogen concentration in the 3 segments from bottom to top are around 30, 105, 75ppm respectively. Even if all the hydrogen migrates from the hot area to the cold area, the average hydrogen concentration in the cladding surrounding the cooler thorium would still be very low. However, attention should be paid to whether the hydride blisters will form at the oxide-metal interface.

For the fission-gas release calculation, however, the above approach cannot be used because FRAPCON can not handle different fuel pellets in one rod. This can be done by simply looking at the burnup of each fuel pellet. With an average burnup of 100MWd/kgHM, the burnup in the driver annulus is close to 300MWd/kgU. So is the central pellet in the thorium section. The fission-gas release will be rather large at these extreme high burnups. For athermal release only, it will be above 70%. It is very likely that the fission-gas release will be above 80% or even 90% when the thermal release is included. If the average burnup is limited to 70MWd/kgHM, the peak driver burnup may be around 200MWd/kgU. This level becomes closer to that of the seed pin in the WASB design, and similar design approaches may yield satisfying performance.

3.4.4. Summary

This summary is based on all the fuel performance work at MIT since the beginning of the project. The work has focused on developing fuel performance models that can be used to assess the performance of ThO_2-UO_2 fuels that may be operated up to 80-100MWd/kgHM in current and future LWRs. This involved development of models to evaluate the behavior of ThO_2-UO_2 fuel during normal and off-normal conditions. The models were incorporated by modifying the NRC licensing codes appropriately: FRAPCON-3 for normal operation and FRAP-T6 for transient conditions. Both codes had been developed for low to medium levels of burnup of UO_2 fuel. The codes were selected because the main mechanisms affecting the thermal and mechanical performance are the same for UO_2 fuel and ThO_2 fuel. These models were verified and compared to the results of previous thorium fuel studies and high burnup uranium fuel evaluations

Rim effect. The pellet rim structure formation at high burnup has been assessed by reviewing the evidence from UO_2 fuel and ThO_2 fuel irradiation studies. Modeling the rim effect in thoria fuel has led to the following conclusions:

(1) Due to its lower epithermal resonance absorption, the thoria fuel will have a much flatter distribution of the radial fissile products and flatter radial power distributions during operation as compared to urania fuel. The rim structure formation and its consequences in thoria fuel, therefore, are expected to occur at significantly higher average burnup levels than in urania fuels.

(2) The newly developed model – THUPS – which calculates the radial power shapes in thoria fuel provides power/burnup distributions that are very close to those calculated by the sophisticated neutronic code MOCUP, but it's much simpler and easier to incorporate into any fuel performance code.

(3) The formation of a rim structure can lead to larger fuel swelling and lower fuel thermal conductivity. In the process of restructuring, some fission gas will be released to the free volume. This would explain the accelerated fission gas release at high burnup observed in UO_2 fuel. Modeling the rim effects is of special concern in the analysis of RIA events because of the grain boundary separation in the rim region that may release a large amount of energy and lead to early brittle failure of the cladding.

Fission gas release. A fission gas release model to predict the performance of thoria based fuel using the FRAPCON-3 computer code package has been formulated. In addition to the modification of the radial power/burnup distribution and the rim porosity, the following changes have been made in the FRAPCON-3 code:

(1) Thoria fuel properties: thermal conductivity, thermal expansion, fuel density, etc have been incorporated in the code. Thoria fuel performs better than conventional urania fuel at fuel exposures near or above the current USNRC licensing limit of 62 MWd/kgU because thoria has a higher thermal conductivity at low and moderate temperatures typical of commercial plant operation. In addition, although thoria has a slightly higher fission gas production per fission, it has a much lower rate of fission gas release during irradiation. While the enhanced conductivity is evident for ThO_2, in a mixture of UO_2-ThO_2 the thermal conductivity enhancement is small. The lower thermal fuel expansion tends to negate these small advantages.

(2) Fission gas yield rate. For the thoria based fuel system, the production of Kr per U-233 fission is more than twice as much as per U-235 fission, which results in a total of approximately 10 percent more fission gas (Xe plus Kr) production. The disadvantage will be reduced when using U-235 as the initial fissile material. From the ORIGEN-2 calculation for a mixed oxide, the cumulative gas production would be about 3.37% more than for a UO_2 fuel for a burnup of 72 MWd/kgHM.

(3) Fission gas release model. Mechanisms of fission gas release in ThO_2-UO_2 fuel are expected to be essentially similar to that of UO_2 fuel, therefore the general formulations of the existing fission gas release models in FRAPCON-3 were retained. However, the gas diffusion coefficient was adjusted to a lower level to account for the smaller observed release fraction in thoria-based fuel. To properly model the accelerated fission gas release at high burnup fuel a new athermal fission gas release model was introduced.

The modified version of FRAPCON-3 was calibrated using the measured fission gas release data from the Light Water Breeder Reactor (LWBR) program information. Application of the new model to calculate the gas release in typical PWR hot pins indicates that the ThO_2-UO_2 fuel will have considerably lower fission gas release above a burnup of 50 MWd/kgHM than UO_2 fuel.

RIA performance A large amount of energy will be deposited in the fuel in a very short time during a Reactivity Initiated Accident (RIA). The failure threshold of energy deposition is greatly reduced for fuel rods operated to very high burnup. There are several factors contributing to the reduction of this threshold: 1) heavily oxidized and hydrided, thus degraded, cladding; 2)

reduced fuel thermal conductivity; 3) pellet-cladding gap closure due to fuel swelling; and 4) large porosity in the rim region allowing very fast gas release. Investigation of fuel performance under RIA events included:

(1) Reviewing the high burnup urania fuel simulation tests, and determining the important phenomena and mechanisms.

(2) Modeling the key contributors to the cladding failure. The failure of fuel rods during an RIA comes mostly from the pellet-cladding mechanical interactions (PCMI). For high burnup fuel with extremely large energy deposition, gaseous swelling will provoke additional cladding stress and strain. For very brittle fuel cladding, the possible high-energy gas liberated from the high burnup rim region can greatly increase the risk of cladding failure. The transient fuel performance code FRAP-T6 was modified to simulate the RIA tests. Modifications have been made for high burnup properties, gaseous swelling, and thoria fuel properties. Results using the modified code show that ThO_2-UO_2 fuel will have better performance than UO_2 fuel under RIA event conditions due to its lower thermal expansion and flatter power distribution in the fuel pellet.

(3) Evaluating the typically postulated RIA event in a real PWR. Most RIA simulation tests were done in a very different environment from the large LWRs and this has important effects for interpretation of the results. The biggest effect is probably due to test temperatures. A cold zero-power rod-drop accident is possible in a BWR, whereas a zero-power rod-ejection accident can only occur when a PWR is hot. Tests have been performed both ways. The next biggest effect of test conditions is probably due to the pulse width. Pulse widths that are too narrow produce enhanced stresses in the cladding at a time when the cladding is cooler than it would be in the real case. The real PWR fuel will have a higher safety margin than observed in the tests (except the IGR tests in Russia) due to the higher cladding temperature and wider power pulse.

Fuel design and operation. Based on the assessment using the modified FRAPCON-3, it is unlikely that current rod designs can achieve a rod peak burnup of 100MWd/kgHM. To achieve satisfactory performance, an advanced fuel design must be adopted to mitigate some of the high burnup effects, such as the rim effect, early brittle failure during RIAs, and accelerated fission-gas release and cladding corrosion.

Recommendations for fuel design and operation strategy were proposed for the thoria fuel to achieve the desired high burnup in several fuel design options (e.g. homogeneous ThO_2-UO_2 fuel, and micro-heterogeneous fuel). With the adoption of advanced cladding materials, for example M5 or DX Zr1Nb, corrosion and hydriding may not pose a problem for these fuel designs. However, larger fuel grain sizes and a decreasing power history might also be needed to mitigate the fission gas release, and an increased free gas volume (i.e. larger plenum volume) should be provided to accommodate the increased fission-gas release in all the designs.

The above-mentioned new models and assessments have shown that thoria fuel has the potential to be a better performer than urania in both normal and off-normal conditions. With advanced fuel designs (i.e. larger gas plenum, large fuel grains, advanced cladding material), carefully designed operating strategy and satisfactory investigation of other high burnup issues (such as LOCA effects), higher burnups on the order of 80 –100 MWd/kgHM can be achieved.

Progress at the INEEL on Subtask 3.8 Temperature Performance of ThO_2-PuO_2 Fuel

Larry Siefken

3.8.1. Design of ThO_2-PuO_2 Fuel

A previous study has proposed a homogeneous mixture of ThO_2 and PuO_2 as an advanced fuel for Light Water Reactors (LWRs) (MacDonald 2002). This fuel design decreases the stockpile of weapons grade fissile material and also has the advantage of increasing proliferation resistance. The basic characteristics of the proposed ThO_2-PuO_2 fuel rods are described in Table 36. Except for fuel composition, the ThO_2-PuO_2 fuel rods are the same as conventional 17x17 LWR fuel rods.

Table 36. Basic characteristics of ThO_2-PuO_2 fuel rods.

Characteristic	Value
Weight % PuO_2 in fuel	3.3 – 6.4
Weight % ThO_2 in fuel	96.7 – 93.6
Radius of fuel pellets (mm)	4.096
Thickness of fuel-cladding gap (mm)	0.082
Outer radius of cladding (mm)	4.750
Composition of cladding	Zircaloy-4
Pitch of fuel rods (mm)	12.60

3.8.2. Thermal Conductivity of ThO_2-PuO_2 Fuel

The thermal conductivity of ThO_2-PuO_2 fuel is required in order to calculate its temperature behavior. Only a few measurements of thermal conductivity have been made for ThO_2-PuO_2 fuel (Bakker et al 1997). The integrated, with respect to temperature, thermal conductivity of a mixture of 97.28wt% ThO_2 and 2.72 wt% PuO_2 was measured by irradiation of fuel elements with central thermal couples (Jeffs 1968). The thermal conductivity of a mixture of 96 wt% ThO_2 and 4 wt% PuO_2 was also measured using the laser flash technique (Basek et al 1989). The thermal conductivity was measured for the temperature range of 950 K to 1800 K. The measured thermal conductivity as a function of temperature is shown in Figure 72. The thermal conductivities of 100% ThO_2 and 100% UO_2 are also shown in the figure (Belle and Berman 1984, Siefken et al 2001). The thermal conductivities for all three compositions of fuel apply to fuel at 100% theoretical density. The measured thermal conductivity of the 96%ThO_2-4%PuO_2 changes linearly with temperature for temperature in the range of 950 K to 1100 K. Assuming the linear relationship continues for temperatures less than 950 K, the thermal conductivity of 96%ThO_2-4%PuO_2 at 700 K is extrapolated to be 6.6 W/m.K. The thermal conductivity of 100% ThO_2 at 700 K is somewhat greater, namely 7.2 W/m.K. At 1500 K, the thermal conductivities of these two compositions are 4.3 and 3.8 W/m.K, respectively. The higher thermal conductivity for 96%ThO_2-4%PuO_2 than for 100% ThO_2 at 1500 K is somewhat remarkable.

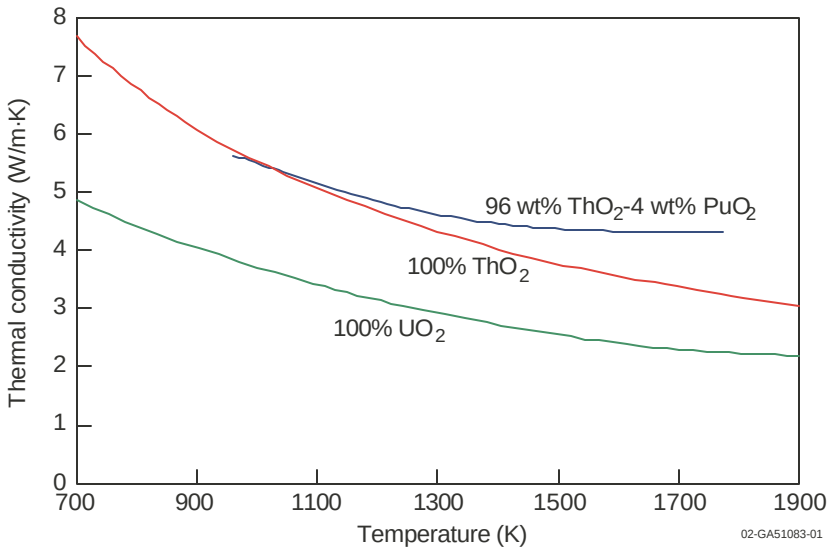

Figure72. Thermal conductivities of 96 wt%ThO_2-4 wt%PuO_2, 100 wt%ThO_2, and 100 wt% UO_2, each for 100% theoretical density.

Data for the heat capacity and linear thermal expansion of mixtures of ThO_2 and PuO_2 are not available (Bakker et al. 1997).

3.8.3. Temperature Behavior of ThO_2-PuO_2 Fuel

A steady state and transient temperature analysis of 96wt%ThO_2-4 wt%PuO_2 was performed using the thermal conductivity data obtained by Basek et al. and performing a linear extrapolation of the measured thermal conductivity for temperatures less than 950 K and greater than 1800 K. Other material properties, such as heat capacity and linear thermal expansion, were assumed to be the same as fuel composed of 96 wt% ThO_2-4 wt% UO_2.

The temperature behavior of the ThO_2-PuO_2 during in-service conditions in a Pressurized Water Reactor (PWR) and during a large break LOCA was calculated using the SCDAP/RELAP5/MOD3.3 code (Siefken et al. 2001). The characteristics of the analyzed fuel rods were described previously in Table 36. The calculations apply to fuel rods at beginning of life conditions. The power distribution in the fuel was assumed to be uniform in the radial direction.

The centerline temperature of fuel rods with 96%ThO_2-4%PuO_2 fuel during in-service conditions is calculated to be significantly less than that for fuel rods composed of 100% UO_2 fuel. Figure 73 shows the radial temperature distribution at the location of peak linear power in the reactor core for fuel rods composed of 96%ThO_2-4%PuO_2 fuel, 100% ThO_2 fuel, and 100% UO_2 fuel. The power at this location was 42 kW/m. The centerline temperatures for these three compositions of fuel were 1715 K, 1750 K, and 2035 K, respectively. The slightly less centerline temperature for the 96%ThO_2-4%PuO_2 fuel than for the 100% ThO_2 fuel is due to the thermal conductivity of the 96%ThO_2-4%PuO_2 being slightly greater than that for the 100% ThO_2 for temperatures greater than 1100 K. The centerline temperature of the 100% UO_2 fuel for the present calculations is about 300 K less than that calculated previously (MacDonald 2002). This difference is due to a higher but more typical fill gas pressure for the present calculations than for the previous calculations.

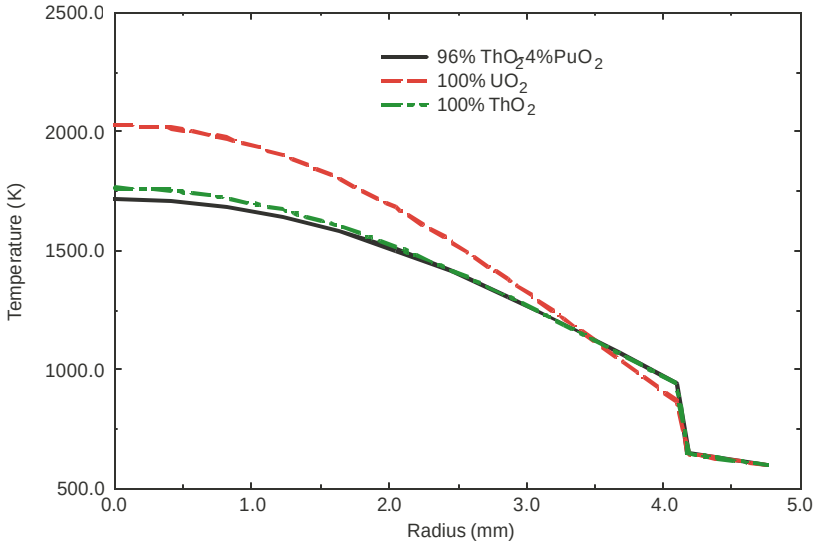

Figure 73. Radial temperature distribution at in-service conditions in fuel rods composed of 96 wt%ThO_2-4 wt%PuO_2, 100% ThO_2, and 100% UO_2, each at power of 42 kW/m.

The transient temperature behavior of the ThO_2-PuO_2 fuel was compared with that of 100% UO_2 fuel using the simplified bundle representation of a large break Loss of Coolant Accident (LOCA). This simplified representation applies transient boundary conditions to a fuel bundle that result in transient coolant conditions in the bundle similar to those in a fuel bundle in a PWR core during a large break LOCA (MacDonald 2002). The four distinct periods of a LOCA are represented by the simplified bundle representation; (1) steady state period just before the initiation of the LOCA, (2) blowdown and depressurization period during which a significant amount of stored energy is removed from the fuel rods, (3) almost adiabatic heatup period during which the fuel bundle is almost empty of liquid water, and (4) reflood period during which the fuel rods are gradually quenched. The calculations were performed for the hot bundle in the reactor core, where the peak linear fuel rod power at the start of the LOCA was 42 kW/m. The reflood rate was a 0.1 m/s and began 25 s after the start of the LOCA. Scram of the reactor was assumed to occur at the start of the LOCA. Although the decay heat in the 96%ThO_2-4%PuO_2 bundle may be slightly greater than that in the 100%UO_2 bundle, nevertheless the decay heat histories were assumed to be the same for the two fuel bundles. The SCDAP/RELAP5/MOD3.3 code represented the fluid in the fuel bundles with a stack of 40 equally sized control volumes. A total of 80 equally spaced axial nodes were used to represent the fuel rods in the fuel bundles.

The peak cladding temperature during the simulated large break LOCA for the bundle of 96%ThO_2-4%PuO_2 fuel rods was calculated to be significantly less than that for a bundle of 100% UO_2 fuel rods. The cladding temperature histories for these two fuel bundles are compared in Figure 74. The peak cladding temperatures in the 96%ThO_2-4%PuO_2 fuel bundle and 100% UO_2 fuel bundle were 895 K and 965 K, respectively. The lesser peak cladding temperature for the 96%ThO_2-4%PuO_2 fuel bundle is due to the lesser in-service fuel temperatures in this fuel bundle than in the 100% UO_2 fuel bundle. The 96%ThO_2-4%PuO_2 fuel bundle was completely quenched at a time of 95 s, while the 100% UO_2 fuel bundle was still not quenched for a time greater than 100 s.

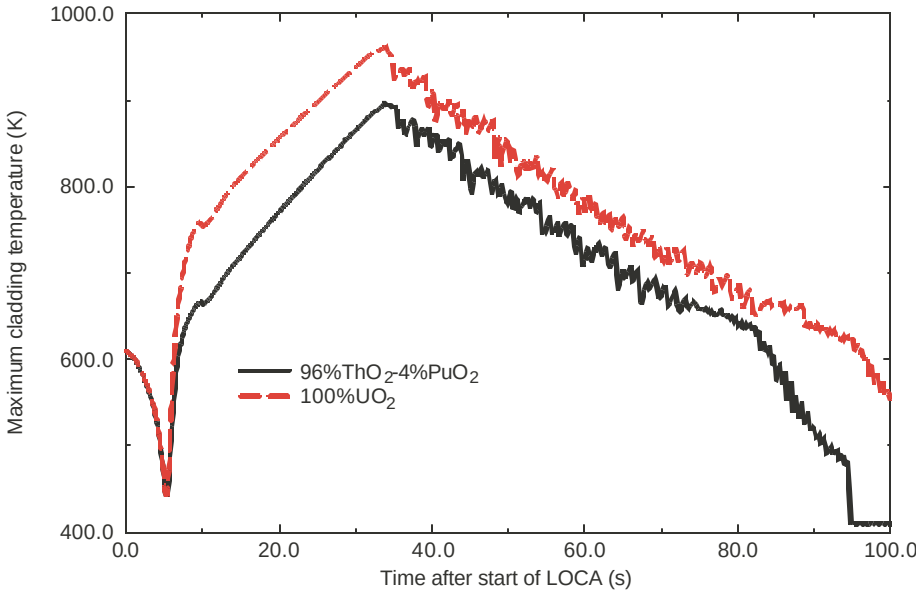

Figure 74. Peak cladding temperatures during simulated large break LOCA for bundle of 96% ThO_2-4%PuO_2 fuel rods and bundle of 100% UO_2 fuel rods.

In summary, the steady state and transient temperature performance of fuel rods with 96wt%ThO_2-4wt%PuO_2 fuel compares favorably with that of fuel rods with 100% UO_2 fuel. The in-service fuel temperatures of the 96%ThO_2-4%PuO_2 fuel rods are significantly less than those of 100% UO_2 fuel rods, and the cladding temperatures during a LOCA are significantly less in the 96%ThO_2-4%PuO_2 fuel rods than in the 100% UO_2 fuel rods. These favorable comparisons are primarily due to the thermal conductivity of the 96%ThO_2-4%PuO_2 fuel being greater than that of 100% UO_2 fuel. Since the model used for the thermal conductivity of the 96%ThO_2-4%UO_2 fuel was based on only one set of measurements, these results are preliminary in nature.

TASK 4. LONG TERM STABILITY OF THO_2-UO_2 WASTE - Progress at the University of Florida and at Argonne National Laboratory

Prof. James S. Tulenko, Dr. Ronald H. Baney, Dr. Darryl Butt, Dr. Paul Demkowicz, Lisa Argo, and Noriko Shibuya at the University of Florida and Dr. James C. Cunnane and Dr. James Jerden at ANL

4.1. Introduction

Background. The proposed long-term storage of spent nuclear fuel has given rise to concerns regarding the leaching of uranium and other hazardous radionuclides from the fuel matrix into the surrounding environment. It is believed that urania–thoria fuels may have a major advantage over the current commercial urania (UO_2) fuels as a more stable material for disposal in a geological repository, with significantly lower rates of aqueous dissolution. These mixed oxide $(U,Th)O_2$ solid solutions are currently being investigated to assess their behavior in long term geological storage.

Thoria (ThO_2) is a very stable and relatively insoluble oxide. The highest oxidation state for thorium is +4, and therefore Th(IV) in ThO_2 can not be oxidized further. However, uranium(IV) in UO_2 can exist in higher oxidation states, up to U(VI). Uranium oxide therefore may undergo extensive oxidation, forming a number of different oxygen-rich phases as the reaction proceeds (for example, UO_{2+x}, U_4O_9, U_3O_7, U_3O_8, UO_3). This reaction has a profound influence on the aqueous dissolution behavior, since higher oxidation states of uranium readily form soluble species in water. The oxidation of UO_2, therefore, leads to the formation of more soluble phases, which in turn affects the long-term stability of spent nuclear fuel materials in geological repositories in which eventual contact with groundwater is likely.

Urania and thoria share the same crystal structure and form solid solutions at all UO_2–ThO_2 compositions. The oxidation and dissolution behavior of such materials over a range of compositions has not been extensively studied. Of immediate interest is the extent to which thorium in the $(U,Th)O_2$ matrix is able to stabilize the material with regard to oxidation and dissolution. It has been hypothesized that uranium in a matrix of thorium ions will be less easily oxidized, and therefore the dissolution of uranium from such materials will be significantly lower than for pure UO_2 under similar conditions.

Objective. The objective of this research is to determine the oxidation and dissolution behavior of $(U,Th)O_2$ solid solutions, and to quantify the relative advantages and disadvantages of these materials versus conventional UO_2 fuel with respect to long term storage.

The dissolution behavior of both irradiated and unirradiated $(U,Th)O_2$ fuel has been investigated. Irradiated $(U,Th)O_2$ pellets with compositions ranging from 2–5.2% were acquired by Argonne National Laboratory East (ANL-E). Dissolution of these materials in J-13 well water at 90ºC was studied by measuring the concentration of ^{232}Th, ^{233}U, and a number of important fission products, including ^{137}Cs, ^{99}Tc, and ^{90}Sr.

Unirradiated $(U,Th)O_2$ fuel pellets were produced at the University of Florida by blending and sintering UO_2 and ThO_2 powders. The compositions under investigation are 5%, 23.6%,

36.8%, 50%, and 100% UO_2. Uranium dissolution of whole pellets was studied at 90ºC, and dissolution of crushed pellets was studied at room temperature. All dissolution studies were performed using J-13 water as the leachate solution. This study has the aim of ultimately comparing the dissolution rates of unirradiated $(U,Th)O_2$ fuels as a function of composition, as well as to compare the dissolution rates of irradiated and unirradiated 5% UO_2 fuels.

Thermal gravimetric analysis of unirradiated $(U,Th)O_2$ has been used to calculate the kinetic parameters governing the dry oxidation of the solid solutions. Compositions between 5–100% UO_2 are being analyzed. The goal of this study is to evaluate the effect of $(U,Th)O_2$ composition on the oxidation behavior to determine if ThO_2 is able to stabilize the materials with regard to oxidation of uranium.

4.2. $(U,Th)O_2$ Dissolution Studies

The aqueous dissolution of $(U,Th)O_2$ fuels is currently under investigation. The primary objectives of this study are (1) to determine the effect of fuel composition (%UO_2) on the dissolution behavior and (2) to compare the dissolution of irradiated and unirradiated fuels. Unirradiated fuels are being studied at UF, irradiated fuels at ANL.

4.2.1. Unirradiated Fuel

Unirradiated $(U,Th)O_2$ pellets with compositions ranging from 5 to 50% UO_2 were prepared by blending UO_2 and ThO_2 powders. Appropriate amounts of UO_2 (Siemens) and ThO_2 (Alfa Aesar) powders were weighed and placed in a zirconium jar along with two 10 mm YSZ milling media. The powders were then milled together for 60 minutes using a SPEX 8000M Mixer/mill. The milled powders were pressed into pellets in a 13 mm stainless steel die using a single action laboratory press and a pressure of 100MPa. Pure UO_2 pellets were pressed using pressures of 50MPa and 100MPa for comparison. The pressed pellets were sintered at 1650ºC for 20 hours in a 5%H in Ar gas mixture using a tube furnace.

Pellets were crushed manually in a zirconium container using an alumina pestle. The fragments were sieved using 60 mesh (250µm) and 170 mesh (90µm) screens. Generally about 51–61% of the powder was retained on the 170-mesh sieve and about 35–42% was collected below the 170-mesh. The -170 mesh portions of the crushed pellets were analyzed using x-ray diffraction. The specific surface area of both size ranges was analyzed using the BET method with krypton as the adsorbate gas. The 90 to 250µm powder samples for surface area analysis were rinsed in demineralized water and dried in a vacuum prior to analysis to remove all fine particulates.

The green and sintered densities of the pellets are shown in Table 37. The green densities were determined based on geometrical measurements and the sintered densities were measured by the immersion method. Figure 75 shows examples of the sintered pellets of all compositions.

Table 37. Green and sintered densities of $(U,Th)O_2$ pellets.

Composition (%UO_2)	Green density (%TD)[a,b]	Sintered density (%TD)[a]
5	65.9 ±0.2	98.2 ±0.6
23.6	63.5 ±0.1	96.8 ±0.3
36.8	62.6 ±0.2	96.2 ±0.2
50	61.4 ±0.1	95.3 ±0.2
100[c]	57.8 ±0.2	97.6 ±0.8

[a]Error represents the 95% confidence interval
[b]Green densities estimated from geometrical measurements.
[c]Data represents only pellets pressed at 100 MPa.

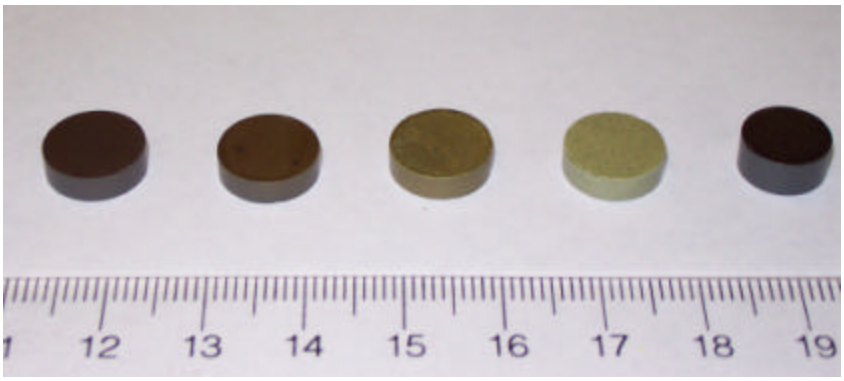

Figure 75. Sintered $(U,Th)O_2$ pellets prepared by blending UO_2 and ThO_2 powders. Pellet compositions are, from left to right: 50 %, 36.8 %, 23.6 %, 5 %, and 100 % UO_2.

XRD analysis of the crushed pellets confirms the presence of the $(U,Th)O_2$ solid solution. No extraneous peaks are found in the diffraction patterns. The surface areas of the powders are given in Table 38.

Table 38. Specific surface area of crushed unirradiated $(U,Th)O_2$ pellet fragments.

Composition ($\%UO_2$)	Specific surface area ($m^2\ g^{-1}$)	
	-170 mesh	-60 +170 mesh
5.0	0.206	0.0299
23.6	0.224	0.0199
36.8	0.201	0.0141
50.0	0.198	---
100	0.131	0.0120

4.2.2. Irradiated Fuel

Irradiated $(U,Th)O_2$ pellets have been acquired by Argonne National Laboratory–East (ANL-E). The following sections provide background information regarding the fabrication and irradiation history of the $(U,Th)O_2$ fuel rods previously examined at ANL, from which samples were taken to be used in these experiments.

Chemical composition, homogeneity and irradiation history of samples. The test materials consist of metallurgical specimens prepared as part of the end-of-life destructive examination of the Shippingport Light Water Breeder Reactor (LWBR) core (Richardson et al. 1987, Olson et al. 1999). Figure 76 shows a cross-section through the LWBR core and indicates the approximate locations of the spent rods from which the test materials were extracted. The fabrication and irradiation history of these samples are summarized below to provide background for the corrosion and dissolution results. For more detailed discussions of these samples see Richardson et al. (1987) and Olson et al. (1999). Pertinent observations made during the LWBR end-of-life destructive analyses program are summarized in Table 39.

Fuel pellet fabrication. The fabrication of chemically homogeneous (e.g. true binary solid solutions) thoria-urania pellets is complicated by the high melting temperature of ThO_2 (3390°C) relative to UO_2 (2827°C) and relatively low diffusion coefficients at normal sintering temperatures (Olsen et al. 1999). The estimate of the melting temperature for urania-thoria solids containing 2 to 6 weight percent UO_2 in $(U,Th)O_2$ is 3288°C (Olsen et al. 1999). The pellet homogeneity criteria for the LWBR fuels was achieved by multiple stages of blending and co-micronization of urania and thoria powders followed by pellet pressing and sintering at

approximately 1800°C (Olsen et al. 1999). The homogeneity of the as-fabricated LWBR pellets were assessed with an auto-radiographic technique and pellet batches not meeting a pre-determined criteria were rejected. This issue of fuel homogeneity is central to our experimental study as it is expected that the dissolution behavior of a binary solid solution of $(U,Th)O_2$ will differ from that of a micro-heterogeneous thoria-urania sample.

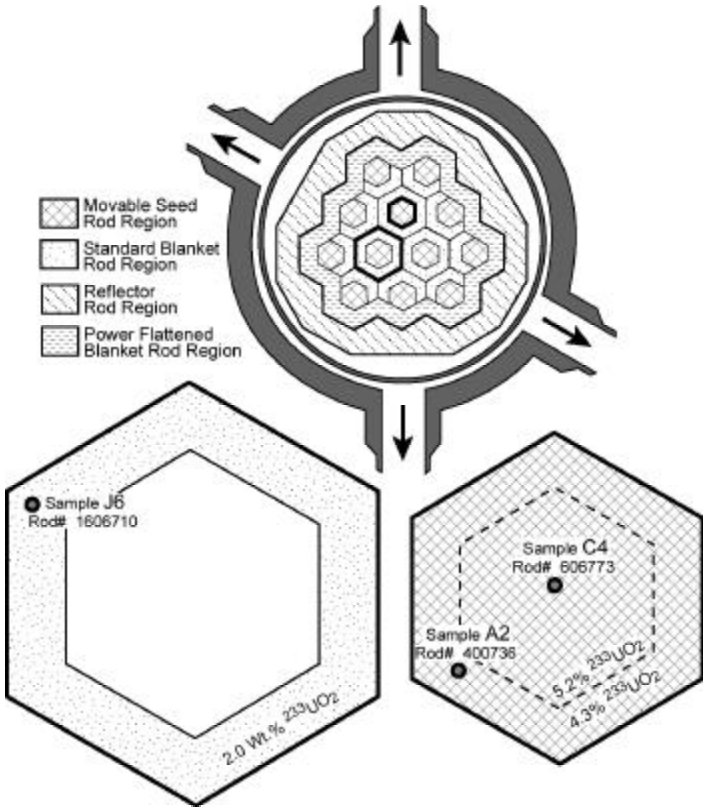

Figure 76. Cross-section of LWBR core showing different types of fuel modules. The two bottom images show, schematically, the blanket rod (left) and seed rod (right) modules from which the test materials for this study were extracted. The Shippingport thoria-urania reactor vessel was 10 m high with an inner diameter of 2.7 m (images adapted from Olsen et al. 1999).

Fission gas release and estimate of core temperature during irradiation. The LWBR end-of-life fission gas (Xe and Kr) measurements were made by puncturing fuel rods using a laser and analyzing the collected gas by mass spectrometry (Olsen et al. 1999). The rods analyzed included a broad range of burnup values, neutron fluence, and power density. The fuel to cladding gap and plenum inventories of the fission gas comprised less than 1% of the total gases measured from the rods. Most of the trapped gas (>94%) was helium, which was the initial fill gas. Other gasses included xenon and krypton produced during fission and minor amounts of H_2 and CO_2 that were residual from the pellet fabrication. The ratio of fission gases (Xe + Kr) to the total gas was used to develop a rough estimate of the core temperatures achieved during reactor operation. The estimate was made by normalizing the fission gas release percentages to 100% pellet density and plotting them against average rod depletion (Figure 15 of Richardson et al. 1987). The normalized fission gas release for the analyzed LWBR samples were less than 0.25% which yields a temperature estimate of 1415ºC. Because the rods analyzed included samples from the peak temperature and peak depletion locations in the core, this calculated operation temperature represents a maximum upper bound for the LWBR fuel (Richardson et al.

1987). Giovengo et al. (1982) suggest that relatively high fission gas release values (>5%) are related to microstructural changes that occur at temperatures greater than 1871ºC in thoria-urania fuels. These data therefore suggest that the temperatures in the LWBR core were not high enough to cause significant microstructural alteration of the fuels during burnup.

Table 39. Test results from the end-of-life analyses of fuel rods from the Shippingport Light Water Breeder Reactor program (adapted from Olsen et al. 1999, Table 5-5).

Property Tested	Purpose of Test	Results of Test	Number of Rods Tested
Fission gas release	Quantify fission gas release, which is an indication of fuel temperature achieved during reactor operation.	Operating temperature is <1416°C (Richardson et al. 1987). Fission gas in gap (plenum) is < 1% of total fission gas measured from the rods.	17 at ANL-E 12 at ANL-W
Metallography	Size and distribution of pores, cracks, grain-size, corrosion, mechanical and chemical behavior of cladding.	Low burnup thoria pellets show no cracking. $(U,Th)O_2$ pellets commonly cracked but not disaggregated. Fine porosity. No evidence for bonding of fuel to cladding in seed.	12 at ANL-E
Cladding	Zircaloy-4 cladding adequacy	No through-going cladding defects detected.	12 at EFC
U isotopic composition	Determine post burnup U isotopic inventory for proof of breeding study and to calibrate fissile inventory calculations.	Fissile inventory (pre-burnup) / Fissile inventory (post-burnup) = 1.0139 providing proof that breeding of U-233 was accomplished. The initial isotopic data is given in Table 40.	17 at ANL-E
Concentrations of La-139 and Nd-148 in spent rods.	Calculate burnup of different types of fuel rods (HNO_3-HF digestion) and calibrate non-destructive burnup calculations.	The average burnups of the seed rods ranged from 41,200 to 53,400 MWD/MTM*. The average burnups of the blanket rods ranged from 18,700 to 24,400 MWD/MTM.	2 at ANL-W
Concentrations of I-129 and Cs-137 in fuel and cladding	Determine amount of I and Cs that migrated to gap region and into cladding.	Small quantities of I-129 in fuel (< 400 mg/kg) and in negligible amounts associated with cladding. Cs-137 mostly in fuel (~1300 mg/kg, seed rods) with minor amounts associated with cladding (<10 mg/kg).	11 samples at ANL-E

ANL-E: Argonne National Laboratory-East; ANL-W: Argonne National Laboratory-West; EFC: Naval Reactors Expended Core Facility, *MWD/MTM = megawatt days per metric ton of thorium plus uranium.

Microstructural characterization of samples. Although minor fission gas porosity is noted in the samples used in the current study, there is no optical or microscopic evidence for significant microstructural changes (e.g. recrystallization) in the fuel due to in-reactor heating. Metallographic and optical observations indicate that many of the urania-thoria pellets contain both through-going, lateral, and circumference-parallel fracture patterns. The samples used in the dissolution experiments are fractured but have remained intact during testing. Thus, except for minor fission gas porosity and pellet fracturing, the experimental samples generally retain microstructural characteristics (e.g. grain size range and distribution) of the as-fabricated pellets.

Uranium isotopic measurements. The initial (as-loaded) uranium isotopic composition of the fuel pellet types used in the current study is summarized in Table 40. Two types of seed rods were produced for the LWBR program: highly-enriched rods containing 5.195 weight percent $^{233}UO_2$ in $(U,Th)O_2$ and lower enriched rods containing 4.327 weight percent $^{233}UO_2$ in $(U,Th)O_2$. The blanket rod specimen used in the current study is from the standard blanket region of the LWBR core and contains 2.0 weight percent $^{233}UO_2$ in $(U,Th)O_2$.

The core was designed to burn ^{233}U as the fissile component and in the process breed more ^{233}U from fertile ^{232}Th by neutron absorption and decay. The ratio of the initial amount of fissile material in the rods over the amount of fissile material in the spent rods was = 1.0139, thus demonstrating that breeding was achieved. The neutron absorption and subsequent decay involved in the breeding processes determined the uranium isotopic composition of the post-burnup LWBR samples. This process is summarized in Figure 77. The end-of-life uranium isotopic inventories for 5 seed rods and 4 standard blanket rods were measured by thermal ionization mass spectrometry at ANL-E (Olsen et al. 1999). These data are summarized in Table 41.

As the data in Table 41 indicate, the spent LWBR rods are highly enriched in ^{233}U. Therefore, the ^{233}U is the main monitor nuclide for uranium release for the dissolution and corrosion experiments.

Table 40. Initial (as-loaded) uranium isotopic inventory and total thorium content of the seed and standard blanket fuel rods used in the LWBR core.

	Totals for Seed Rods (kg)	Totals for Blanket* Rods (kg)	Seed Rods (percent)	Blanket Rods (percent)
^{232}U	0.001	0.001	< 0.01	< 0.01
^{233}U	198.441	116.202	98.35	98.29
^{234}U	2.581	1.577	1.28	1.33
^{235}U	0.143	0.110	0.07	0.09
^{236}U	0.031	0.031	0.02	0.03
^{238}U	0.574	0.303	0.28	0.26
Total U	201.771	118.223	----	----
Total Th	5,206.55	9,487.14	----	----
Number of Rods	7,428	3,234	----	----

*Inventories for standard blanket rods only

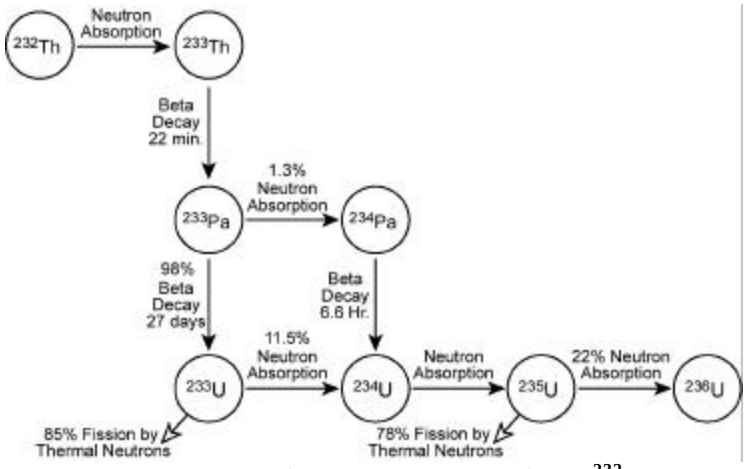

Figure 77. Production of uranium isotopes from ^{232}Th by neutron absorption and radioactive decay in the LWBR system (adapted from Olsen et al. 1999).

Concentrations of ^{137}Cs and ^{129}I in the fuel and estimates of gap inventories. Relatively mobile fission products such as cesium and iodine may migrate during reactor operation to sites in the fuel from which they may be readily released on contact with an aqueous phase. To estimate the inventories of readily leachable ^{137}Cs and ^{129}I in the spent LWBR rods, samples of cladding and fuel were separated and leached in 2 molar HCl for 30 minutes (Richardson et al. 1987; Olsen et al. 1999). For these leaching tests the gap region was operationally defined as the gap between the fuel and cladding, cracks in the fuel, and open, interconnected pores in the fuel. After leaching,

Table 41. Post-burnup uranium isotopic inventory (in percent) for seed and standard blanket rods analyzed as part of the LWBR end-of-life, proof of breeding program (Olsen et al., 1999).

	Seed (%) (n = 5)	Blanket* (%) (n = 4)
^{232}U	0.1 +/-0.02	0.1 +/-0.03
^{233}U	87.3 +/-1.1	89.3 +/-0.7
^{234}U	10.4 +/-0.8	8.8 +/-0.6
^{235}U	1.8 +/-0.2	1.5 +/-0.1
^{236}U	0.2 +/-0.05	0.1 +/-0.03
^{238}U	0.3 +/-0.04	0.2 +/-0.04

*Inventories for standard blanket rods only.

the fuel and cladding samples were completely digested (separately) in concentrated HNO_3 + HF and the solution was analyzed for ^{137}Cs and ^{129}I. Results of these analyses indicate that both the fuel and the cladding contained minor amounts of ^{129}I and that the gap inventory of ^{137}Cs was less than 0.5 % of the total amount present in a given sample (Table 42). As will be discussed in the experimental results section below, the most abundant nuclide present in our experimental leachate samples was ^{137}Cs, which was most likely leached from the gap inventory.

Table 42. Estimates of ^{137}Cs inventories associated with the fuel, cladding and gap regions. Values based on acid leaching and complete digestion of fuel (Richardson et al. 1987, Table 17).

Rod Type	Burnup (MWD/MTM)	^{137}Cs in Fuel (mg/kg)	^{137}Cs Fuel leach (mg/kg)	^{137}Cs in Cladding	^{137}Cs total (mg/kg)	% ^{137}Cs in gap	% ^{137}Cs in cladding	% ^{137}Cs in fuel
Seed	53,400	1609.8	1.8	2.8	1614.4	0.11	0.17	99.71
Seed	53,400	1261.5	4.3	5.9	1271.7	0.34	0.47	99.19
Seed	47,300	1355.2	2.4	5.8	1363.4	0.18	0.43	99.39
Seed	47,300	1317.0	BDL	6.2	----	----	0.47	----
Average	----	1311.2	3.4	6.0	1320.6	0.26	0.46	99.29
Blanket	22300	622.1	0.4	2.8	625.3	0.06	0.45	99.49
Blanket	22300	812.7	0.6	NM	----	0.07	----	----
Blanket	22300	571.6	0.4	2.9	574.9	0.07	0.51	99.42
Average	----	668.8	0.5	2.9	672.1	0.07	0.48	99.45

Serial numbers of the rods from which the seed rod samples were extracted are 0205071 and 0507672 and the standard blanket samples were taken from Rod 1606710. BLD = below detection limit, NM = not measured.

Characteristics of samples used in dissolution and fission product release experiments. The experimental samples for the current study came from the three spent LWBR rods characterized by Richardson et al. (1987) and discussed above. Two of these were seed rods and one was a standard blanket rod. The locations of these rods within the core module are shown in Figure 76. The individual pellets sampled were chosen to provide variations in initial uranium content and extent of burnup (Table 43). The tests were performed on cut and polished disks as well as crushed and sieved samples.

Table 43. Characteristics of irradiated thoria/urania fuel samples chosen for corrosion tests.

Rod Serial Number	Sample Number	Initial $^{233}UO_2$ (Wt.%)	Fuel Burnup (MWD/MTM)	Pellet OD (inches)[1]	Theoretical Density[1]	Grain Diameter in Microns[2]	
						Edge	Center
0400736 (T)	A2	4.327	24,850	0.252	97.71	60	70
0606773 (T)	C4	5.195	40,870	0.252	97.55	70	80
1606710 (T)	J6	2.000	22,350	0.5105	98.11	150	80

[1]Average as fabricated fuel characteristics from (Olsen 1999, Table 3-4, p.23).
[2]Grain size measurements from metallographic analyses of (Richardson 1987, Table 8, p.55).
MWD/MTM = megawatt days per metric ton of metal (uranium + thorium).

4.2.3. Experimental Procedures For Dissolution Studies

4.2.3.1. Unirradiated Fuel – UF

Unirradiated pellets of all five compositions (see Table 37) were polished on all sides by hand using 600 grit SiC paper and deionized water as a lubricant. The polished pellets were rinsed with deionized water and cleaned ultrasonically in deionized water for 5 minutes to remove all particulates. The pellets were weighed and the dimensions were measured using digital calipers.

The pellets were then placed on gold mesh sample holders in stainless steel vessels. The vessels were fabricated at ANL-E by welding 304L stainless steel caps onto 304L stainless steel tubes and sealed using Swagelok™ tube fittings. Within the reaction vessels, the samples are supported on gold mesh or gold foil holders spot-welded onto the 304L stainless steel lifting bails (Figure 78). Each sample vessel was filled with 25mL J-13 well water and sealed. The sealed vessels were then placed in a laboratory oven at 90ºC (Figure 79).

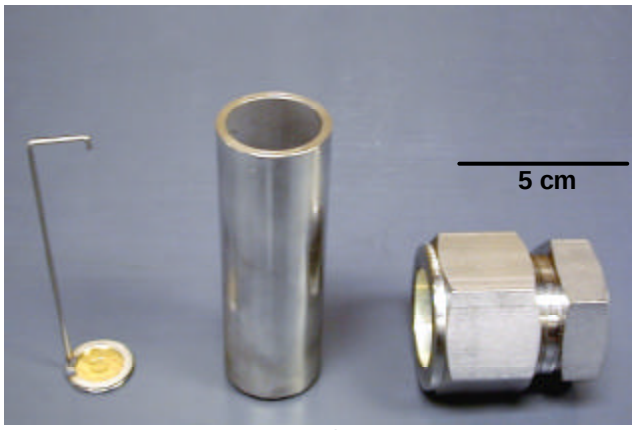

Figure 78. Components of experimental vessels: gold mesh sample holder, 50mL stainless steel tube, and Swagelok™ cap.

Figure 79. Stainless steel sample vessels, containing unirradiated fuel pellets immersed in J-13 water, inside a laboratory oven.

The leachate solutions were sampled by removing all of the solution and replenishing with fresh J-13 water. Approximately 10-15mL of the solution was filtered with 20 nm pore size syringe filters. Both the filtered and unfiltered portions of the leachate solutions were acidified with 1 drop of concentrated (70%) nitric acid.

For the powder dissolution studies, both the 90–250µm and <90µm portions of the crushed pellets were placed in 250mL glass flasks with 200mL J-13 water. The 90–250µm powder fraction was first rinsed in ~30mL J-13 water and filtered with 25µm pore size filter paper prior to starting the experiments to remove the fine particulates. The flasks were sealed with rubber stoppers and the solutions were stirred for the entire experiment duration by means of magnetic stir bars. The dissolution experiments were carried out at room temperature (24 ±2ºC). The experimental setup is shown in Figure 80.

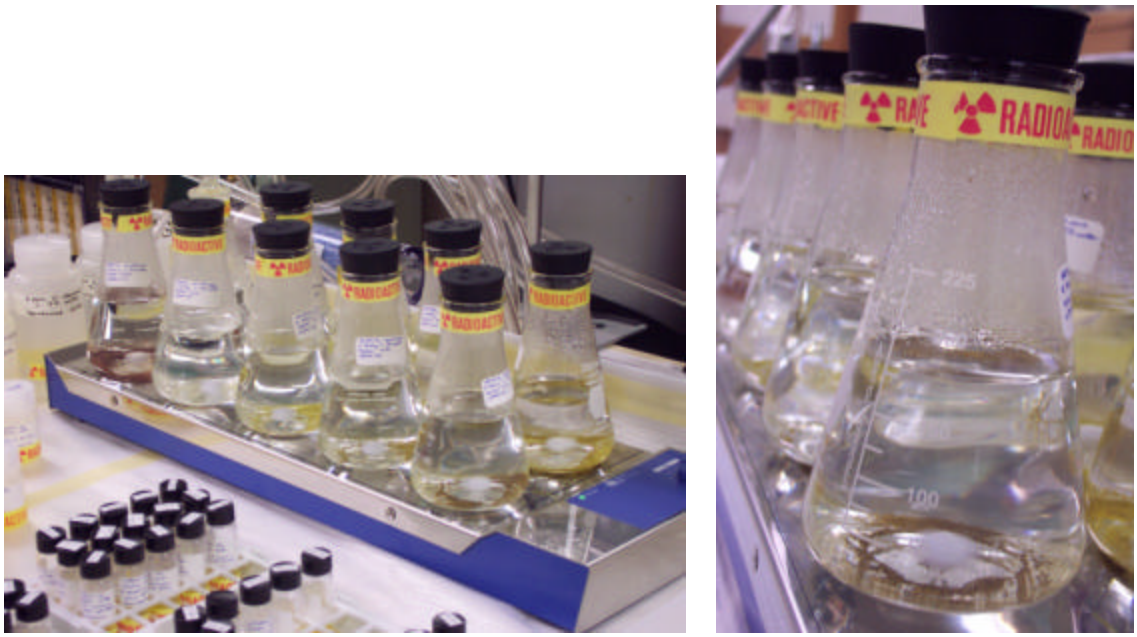

Figure 80. Experimental setup for unirradiated crushed pellets in J-13 water. Crushed and sieved pellet fragments are immersed in J-13 water inside stoppered glass flasks and stirred with magnetic bars.

Samples of the leachate solutions were withdrawn in 5mL aliquots and filtered immediately through 20 nm pore size syringe filters. The filtered solutions were then acidified to approximately 0.16% acidity with 1 drop of 3M nitric acid. In the case of the <90µm 100% UO_2 powder, 3mL of the leachate solution was passed through 20 nm filters and 2mL was analyzed unfiltered. Both the filtered and unfiltered were acidified with 3M nitric acid.

The concentration of U^{+6} in the acidified leachate solutions from both the pellet and powder experiments was analyzed using a Scintrex UA-3 Uranium Analyzer. The technique and calibration of this instrument has been discussed in previous reports. Generally 3–6 measurements were made on each sample for statistical reliability.

The pH of the solutions was measured at selected intervals throughout the experiments using a glass combination electrode. The electrode was standardized with buffered solutions at pH 4, 7, and 10 prior to sample analysis. The pH values for all of the solutions was found to be between 8.2 and 8.5 for the period 0–25 days.

4.2.3.2. Irradiated Fuel – ANL-E

All sample preparations and experiments were performed in the Chemical Technology Division, Class III Hot Cell Facility (located at ANL-E). The dissolution and fission product release experiments involved submersion of the irradiated thoria-urania samples in ground water from well J-13 near Yucca Mountain, Nevada. The tests were preformed at 90°C in 50 mL stainless steel batch reaction vessels identical to those used for unirradiated pellets (Figure 78).

Disk samples of irradiated pellets were cut in the hot cells using a diamond blade saw. The disks were polished using 600 grit silicon carbide paper (deionized water lubricant), rinsed, and immersed in an ultrasonic bath of deionized water for 5 minutes to remove fine particles from the

sample surfaces. The thickness of each sample disk was measured after polishing using digital calipers. The sample thickness and weights are shown in Table 44. Granular samples were prepared by crushing rod segments with a steel mortar-pestle and sieving to obtain the desired size fraction. The grain-size used for the tests is 75-150 microns. After crushing, the samples were rinsed thoroughly with deionized water to remove the fine particles. Both the disk and granular samples were examined at 10–20x magnification using a camera mounted in the hot cells prior to starting the experiments. At the beginning of each test interval the reaction vessels were filled with approximately 25mL of J-13 well water, leaving approximately 25mL of air-filled head space within the vessels. No effort has been made to control the fugacities of O_2(g) and CO_2(g) during the experiments.

Table 44. Test matrix for dissolution and fission product release experiments on irradiate fuel pellets and crushed fragments.

Test ID	Form of Sample	Samp. ID	Initial UO_2 (Wt.%)	Fuel Burnup (MWD/MTM)	Sample Wt. (mg)	Thickness (mm)	Initial Vol. J-13 (mL)
ANL-1	Polished Disk (1)	A2	4.327	24,850	630	1.57	23.53
ANL-2	Polished Disk (2)	A2	4.327	24,850	820	1.93	23.39
ANL-3	Polished Disk (1)	C4	5.195	40,870	540	1.11	25.27
ANL-4	Polished Disk (2)	C4	5.195	40,870	730	1.19	22.51
ANL-5	Granular	C4	5.195	40,870	140	----	20.29
ANL-6	Polished Disk	J6	2.000	22,350	2330	1.69	21.41
ANL-7	Granular (1)	J6	2.000	22,350	960	----	26.39
ANL-8	Granular (2)	J6	2.000	22,350	640	----	23.97
ANL-9	----	Blank	----	----	----	----	25.05

MWD/MTM = megawatt days per metric ton of metal (uranium + thorium)

The samples were taken by the following process: removal of vessels from oven, cooling at ambient temperature, weighing of vessels, removal of gold sample holders, and decanting of leachate into high density polyethylene (HDPE) bottles (all done remotely in hot cells). All of the leachate solution for a given test was extracted and the test restarted for the next test interval with 20 to 25mL of fresh J-13 water. The leachate samples were surveyed for α, β, and γ radiation and, if within radiation safety limits, removed from the hot cell for filtering. All the samples were below the administrative gamma dose rate limit of 200mR/hr and thus no sample dilution was necessary for removing samples from the hot cells. The leachate samples were filtered through 0.45 micron and/or 30,000 molecular weight (~5 nanometer) millipore membranes. Both filtered and unfiltered samples were acidified to pH < 2 with ultra-pure nitric acid and analyzed by ICP-MS. Due to mass interferences, the nuclides ^{137}Cs and ^{241}Am were analyzed by high-resolution gamma counting. The reacted solid samples were examined at 10–20x magnification during each sampling interval (see results section for description of reacted samples). On termination of two of the tests, the samples were removed and vessels were leached overnight in 1% nitric acid to determine the amount of nuclides that may have been retained in the base of the vessels.

3.2.4. J-13 Well Water Chemistry

The starting composition of the J-13 water used in the experiments on irradiated and unirradiated (U,Th)O_2 was analyzed at ANL-E. The cations were measured by inductively coupled plasma, atomic emission spectrometry (ICP-AES) and the anions were measured by ion chromatography (IC). These data are shown in Table 45 (ANL1 and ANL2 are replicate samples of J-13 used at Argonne; UF1 is the J-13 used at UF). The ions Al^{3+}, Fe^{2+}, PO_4^{3-} and NO_2^- were all below detection limits of 0.1, 0.1, 0.5, and 0.4 mg/L respectively. More sensitive anion

analyses by Harrar et al. (1990) report total dissolved inorganic phosphate concentrations for J-13 waters of 0.12 mg/L (as HPO_4^{2-}). The dominant oxidant in our leachant solutions, dissolved oxygen, is estimated assuming that the fluid samples have approached equilibrium with atmospheric oxygen. This yields a dissolved oxygen concentration of approximately 8 mg/L (solubility of O_2(g) in dilute water at 25°C; e.g. Langmuir 1997).

Table 45. Chemistry of J-13 well water used for tests on irradiated $(U,Th)O_2$.

Species	Concentration (ppm)		
	J13 (ANL1)	J13 (ANL2)	J13 (UF1)
SiO_2(aq)	61.8	62.0	63.7
Na^+	44.2	43.9	43.4
K^+	4.7	4.8	4.7
Mg^{2+}	1.9	1.9	1.9
Ca^{2+}	12.0	11.8	12.2
NO_3^-	6.6	6.6	8.7
F^-	2.2	2.4	2.13
Cl^-	8.1	8.1	7.8
SO_4^{2-}	18.3	18.5	18.5

For all of the tests at elevated temperature, the sealed reaction vessel containing the sample and J-13 leachant is heated from ambient temperature to 90°C at the initiation of each test interval. Increases in gas fugacities associated with this heating process were calculated using the geochemical modeling software "Geochemist's Workbench™" and are shown in Figure 81. Heating results in an overall pressure increase to approximately 2 bars. In this closed system the dissolved concentrations of oxygen and carbonate are anticipated to remain relatively constant during heating as decreases in solubility with increasing temperature are balanced by the increasing partial pressures of the corresponding gasses (Figure 81). The pH, which starts at approximately 7.4, decreases during heating to a value of approximately 7.1. Thus, during the tests, the irradiated thoria-urania samples are interacting with nearly neutral solutions that are saturated with oxygen.

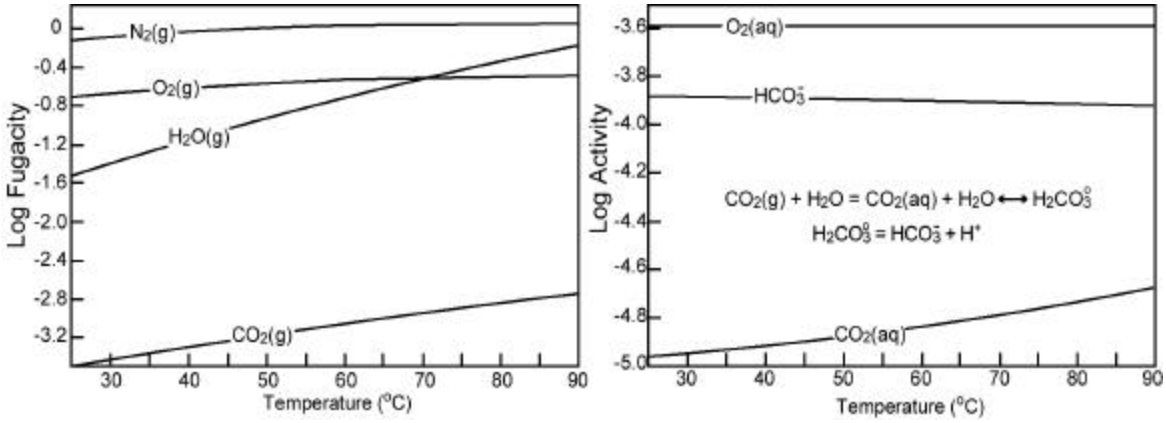

Figure 81. Left image: gas fugacity vs. temperature for J-13 water and air-filled head space in a sealed vessel heated to 90°C. Right image: activity of dissolved oxygen and dissolved carbonate corresponding to the partial pressures shown on the left image. The reactions summarize how carbonate may effect pH within the system.

The J-13 at 90ºC is theoretically supersaturated with respect to the smectite clay minerals nontronite and saponite; however, the formation of these minerals appears to be kinetically inhibited, as no precipitates have been noted in any of the samples. The activities of the dissolved cations and anions within the J-13 water at 90ºC were also calculated using the Geochemist's Workbench™ software, which employs an extended form of the Debye-Huckle equation (Helgeson, 1969) for activity modeling. The results of these calculations (Table 46) are used to create the activity diagrams presented in the experimental results section below.

4.2.5. Experimental Results: Dissolution of Irradiated Fuel

4.2.5.1. Macroscopic Examination Of Reacted Irradiated $(U,Th)O_2$ Fuel Samples

Equilibrium thermodynamic calculations predict that, given the amount of dissolved oxygen in the leachant solutions used in our experiments ($10^{-3.6}$ molal), the U(IV) in the $(U, Th)O_2$ samples should oxidize to U(VI) (thermodynamic calculations made using the data base of Grenthe et al. 1992). Hexavalent uranium in this system is predicted to have a solubility in the range of 10^{-6} to 10^{-7} molal, with the uranyl oxy-hydroxide dehydrated schoepite being the solubility controlling phase. The stability of dehydrated schoepite and other uranium species are shown as a function of oxidation potential and pH in Figure 82. Thus, if uranium were released relatively rapidly from the corroding samples it is predicted that dehydrated schoepite would precipitate on reacting surfaces as a corrosion product.

Table 46. Results of activity calculations for J-13 well water at 90°C.

T	90°C		
pH	7.1		
Eh*	0.7 Volts		
Ionic Strength	$3.3x10^{-3}$		
	Molal	**Activity**	**Log Activity**
SiO_2(aq)	$1.03x10^{-3}$	$1.03x10^{-3}$	-2.99
Na^+	$1.92x10^{-3}$	$1.79x10^{-3}$	-2.75
K^+	$1.21x10^{-4}$	$1.13x10^{-4}$	-3.95
Mg^{2+}	$7.74x10^{-5}$	$6.18x10^{-5}$	-4.21
Ca^{2+}	$2.99x10^{-4}$	$2.29x10^{-4}$	-3.64
HCO_3^- + CO_2(aq)	$1.43x10^{-4}$	$1.35x10^{-4}$	-3.87
NO_3^-	$1.07x10^{-4}$	$9.90x10^{-5}$	-4.00
O_2(aq)	$2.57x10^{-4}$	$2.57x10^{-4}$	-3.59
F^-	$1.17x10^{-4}$	$1.09x10^{-4}$	-3.96
Cl^-	$2.05x10^{-3}$	$1.91x10^{-3}$	-2.72
$H_2PO_4^-$ + HPO_4^{2-}	$1.25x10^{-6}$	$1.06x10^{-6}$	-5.97
SO_4^{2-}	$1.72x10^{-4}$	$1.29x10^{-4}$	-3.89

*Theoretical Eh calculated assuming equilibrium for all redox couples in solution. Species Al^{3+}, Fe^{3+}, Mn^{4+} all have activities less than 10^{-8}. Dissolved oxygen and carbonate concentrations are from Figure 67. The phosphate starting concentration is from Harrar et al., 1999.

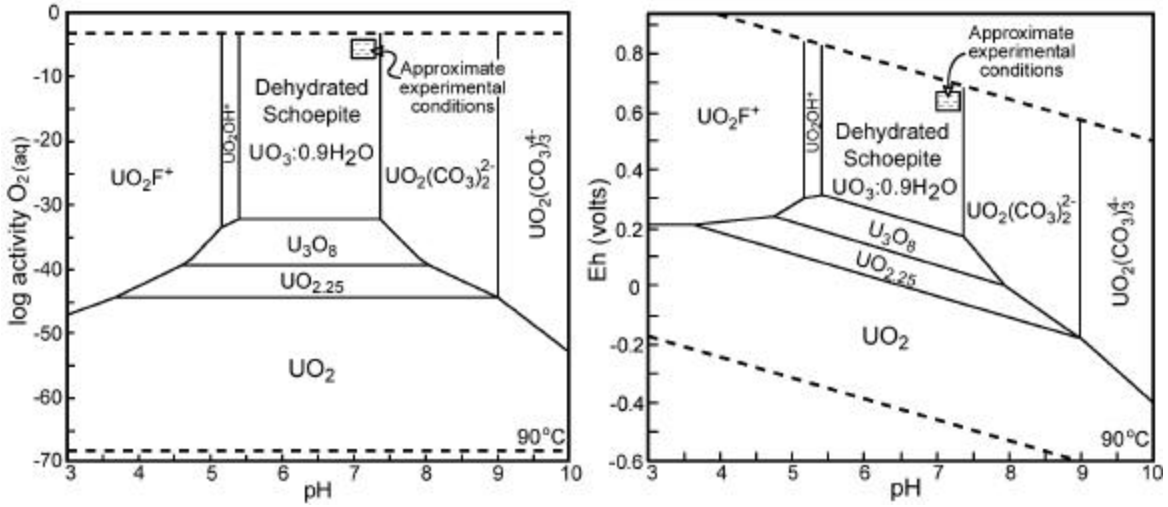

Figure 82. Uranium species stability (solid and aqueous) plotted on dissolved oxygen vs. pH (left) and oxidation potential vs. pH (right) diagrams. Plotted for 10^{-6} molal dissolved uranium and CO_2(g) fugacity of $10^{-2.7}$.

Macroscopic examination of the irradiated thoria-urania fuel samples from our experiments reveals no evidence for the growth of corrosion products after 195 days of reaction. Surfaces of reacted disks (Figure 83) are black with individual grains visible. Crushed and sieved samples also show no evidence for the precipitation of secondary phases (Figure 84). These observations

agree with solution data indicating that the leachates are undersaturated with respect to potentially important uranyl phases.

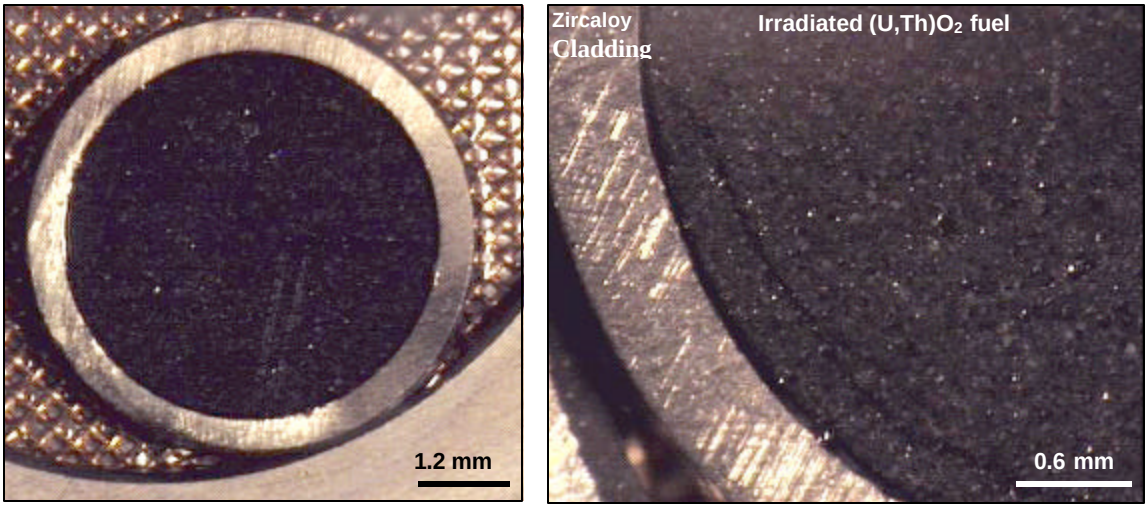

Figure 83. Optical images of sample disk C4 after 138 days of interaction with J-13 water at 90°C. Left image is of sample disk on gold mesh sample holder. Right image is enlarged view of cladding and fuel. Crystal faces of individual fuel grains are clearly visible (white reflections on right image) and there is no evidence for corrosion product precipitation.

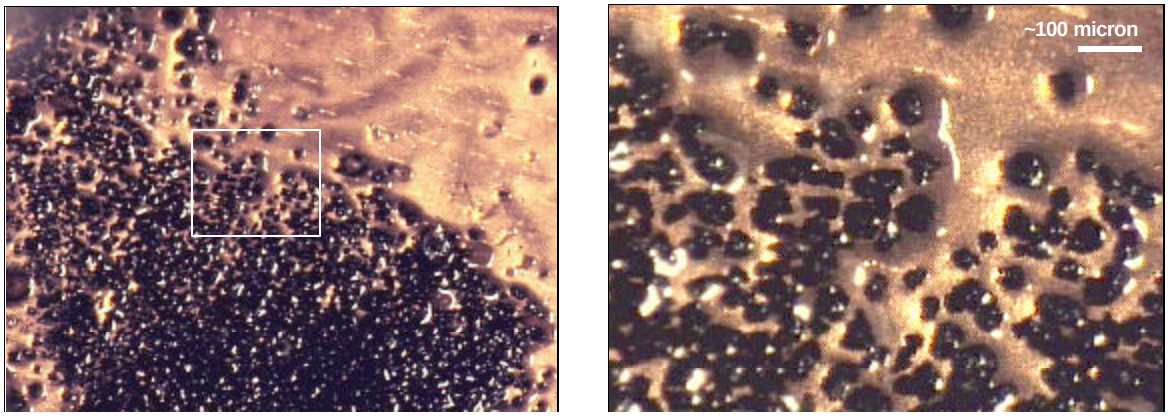

Figure 84. Optical photographs of crushed and sieved sample C4 after 124 days of interaction with J-13 well water at 90°C. Individual fuel grains (black) show no evidence for reaction at this scale and secondary alteration products have not been observed. The images show the fuel grains resting on gold foil (yellow). The right image is an enlarged view of the area indicated by the white box in the left image showing individual fuel grains.

4.2.5.2. Solubility Of Actinides And Other Fission Products in J-13 Leachate Solutions

The concentrations of actinides and fission products in the filtered and unfiltered leachate samples are presented in Tables 47 and 48 respectively. These data are discussed in the context of equilibrium thermodynamic constraints and presented on activity diagrams where activity is nominally equal to the molal concentration of the species in question. The kinetic implications (e.g. actinide and fission product release rates) of these data are discussed in the subsequent section.

Table 47. Concentrations of actinides and selected fission products in filtered leachate samples.

Test ID	C4D4	C4D4	C4D4	C4D4	C4D4	C4D13	C4D13	C4D3	C4D15	C4D15	A2D2	A2D2	A2D2	A2D5	J6D20	J6D20
Test Interval (days)	53	53	95	138	195	95	138	195	81	124	53	53	138	195	39	39
Filter	~5 nm	0.45 µm	~5nm	~5 nm	~5nm	~5 nm	~5 nm	~5nm	~5 nm	~5 nm	~5 nm	0.45 µm	~5 nm	~5nm	~5 nm	0.45 µm
Species	**Concentration (µg/L)**															
Sr-90	1.29	1.27	0.16	0.1	<0.08	2.75	0.11	0.133	0.42	0.32	1.25	1.31	0.3	15.0	0.3	0.33
Mo-97	5.8	5.77	4.5	4.5	4.45	13.9	1.14	6.36	5.35	4.18	6.07	6.32	6.14	5.34	6.06	5.71
Tc-99	3.62	3.32	2.73	2.74	3.57	6.09	0.87	5.23	6.72	2.6	4.71	4.42	7.01	4.88	5.8	5.23
Cs-134	0.04	0.04	<0.01	<0.01	<0.01	0.09	0.01	<0.01	0.02	<0.01	0.04	0.04	<0.01	<0.01	0.02	0.02
Cs-137	14.79	14.80	0.45	0.12	0.41	35.22	0.96	0.29	8.55	1.34	14.51	14.7	0.57	19.52	6.92	6.74
Th-232	0.22	0.15	0.17	0.50	<0.56	0.11	0.39	<0.56	0.05	0.15	0.18	0.09	0.29	<0.56	0.18	2.65
U-233	0.28	0.27	0.32	0.44	0.23	0.66	0.06	0.62	0.08	0.89	0.15	0.16	0.26	0.12	0.84	0.92
U-234	0.05	0.06	0.06	0.09	<0.12	0.11	0.04	0.126	0.04	0.12	0.02	0.02	0.04	<0.12	0.12	0.13
Np-237	<0.02	<0.01	<0.05	<0.04	<0.16	<0.05	<0.04	<0.16	<0.05	<0.04	<0.02	0.01	<0.04	<0.16	<0.02	<0.01
U-238	14	14.4	9.94	11.9	4.64	26.4	0.65	18.2	<0.65	31.5	28	29.3	24.5	2.53	10.5	10.7
Pu-239	<0.02	<0.01	<0.06	<0.04	<0.2	<0.06	<0.04	<0.2	<0.06	<0.04	<0.02	<0.01	<0.04	<0.2	<0.02	<0.01
Pu-240	<0.02	<0.01	<0.04	<0.08	<0.08	<0.04	<0.08	<0.08	<0.04	<0.08	<0.02	<0.01	<0.08	<0.08	<0.02	<0.01
Am-241	<0.01	<0.01	<0.01	<0.01	<0.02	<0.01	<0.01	<0.02	<0.01	<0.01	<0.01	<0.01	<0.01	0.05	<0.01	<0.01

*Test identifications are listed as sample type (C4, A2, J6) followed by the reaction vessel identification number. The estimated accuracy for these data is +/-30%.

Table 48. Concentrations of actinides and selected fission products in unfiltered leachate samples.

Test ID	C4D4	C4D4	C4D4	C4D4	C4D13	C4D13	C4D13	C4D15	C4D15	A2D2	A2D2	A2D5	J6D20	Blank	C4D13	A2D5
Test Interval (days)	53	95	138	195	95	138	195	81	124	53	138	195	39	81	Acid Rinse	Acid Rinse
Filter	Unfil.	Unfil.	Unfil.	Unfil	Unfil.	Unfil.	Unfil	Unfil.	Unfil.	Unfil.	Unfil.	Unfil	Unfil.	Unfil.	Unfil.	Unfil.
Species	**Concentration (µg/L)**															
Sr-90	1.3	0.22	0.18	1.76	0.58	1.30	2.57	2.93	0.51	1.3	0.2	1.54	0.33	0.08	0.86	0.50
Mo-97	5.90	4.41	2.58	4.75	5.37	3.75	6.61	14.4	1.47	6.49	3.04	5.4	6.46	5.24	0.67	0.22
Tc-99	3.70	2.96	1.55	4.01	6.85	2.41	5.59	6.36	1.18	5.0	3.44	4.72	6.35	0.03	0.06	0.03
Cs-134	0.03	<0.01	<0.01	<0.01	0.02	0.01	<0.01	0.1	<0.01	0.04	<0.01	<0.01	0.02	<0.01	<0.01	<0.01
Cs-137	12.55	0.45	0.12	0.41	8.47	0.96	0.29	38.12	1.34	15.26	0.57	19.52	7.06	<0.01	0.24	0.23
Th-232	0.32	1.94	9.20	91.9	49.60	44.80	83.5	0.74	137.0	0.39	8.16	6.6	15.4	0.16	4.27	0.86
U-233	0.3	0.42	0.66	3.86	2.73	2.81	3.79	0.75	6.98	0.18	0.45	0.32	1.44	0.02	1.29	0.79
U-234	0.07	0.08	0.11	0.63	0.39	0.48	0.62	0.13	1.11	0.02	0.05	<0.06	0.22	0.04	0.24	0.08
Np-237	0.01	0.05	0.01	<0.08	0.05	0.03	<0.08	0.05	0.01	0.01	0.01	<0.08	0.01	0.05	<0.04	<0.04
U-238	14.8	13.6	11.7	11.6	3.7	70.0	26.7	27.5	5.77	31.4	18.3	3.81	13.1	0.65	126.0	30.0
Pu-239	0.01	0.06	0.08	0.58	0.06	0.37	0.37	0.06	0.06	0.01	0.04	<0.1	0.01	0.06	0.81	<0.05
Pu-240	0.01	0.04	0.02	0.09	0.04	0.13	0.04	0.04	0.02	0.01	0.02	<0.04	0.01	0.04	0.23	<0.02
Am-241	<0.01	<0.01	<0.01	<0.02	<0.01	<0.01	<0.02	<0.01	<0.01	<0.01	<0.01	0.05	<0.01	<0.01	0.08	<0.01

*Test identifications are listed as sample type (C4, A2, J6) followed by the reaction vessel identification number. The estimated accuracy for these data is +/-30%.

Thorium. The thorium (^{232}Th) concentrations in the filtered (~5 nanometers) leachate solutions ranged from <0.05 to 0.5 µg L^{-1} (roughly $10^{-9.7}$ to $10^{-8.7}$ molal). These concentrations are only slightly higher, on average, than the hot cell J-13 blank, which contains 0.16 µg L^{-1} thorium. The concentrations do not systematically vary with sample type (e.g. disk versus crushed and sieved) or the amount of time the sample has reacted. As shown in Figure 85, these measured concentrations are orders of magnitude higher than the predicted ThO_2 solubility of approximately 10^{-14} molal, but are lower than the predicted solubility of $Th(OH)_4$(solid). No thorium hydroxides or thorium hydrous oxides have been noted in the reacted samples. It is unclear why these concentrations are higher than the thermodynamically predicted values. However, it can be concluded from these data that only trace (to ultra-trace) amounts of dissolved thorium have been released from the samples during these test experiments.

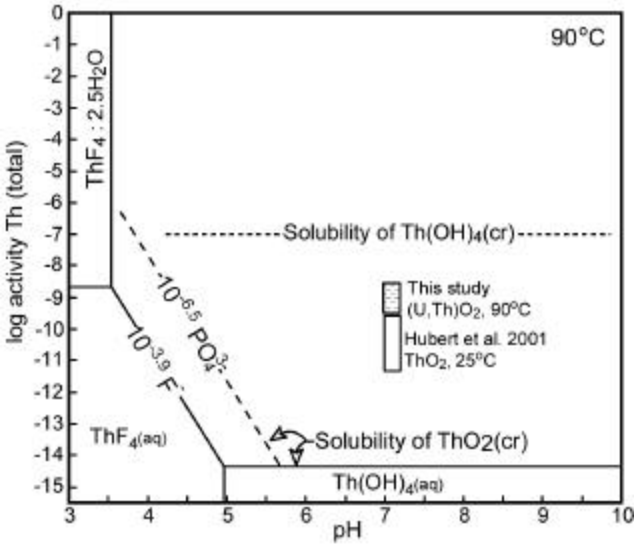

Figure 85. Solubility of ThO_2(cr) and $Th(OH)_4$(cr) vs. pH (plotted using activities listed in Table 42). The data fields compare the experimental results from this study with the results from the 25ºC dissolution experiments on ThO_2 powders reported by Huber et al. (2001).

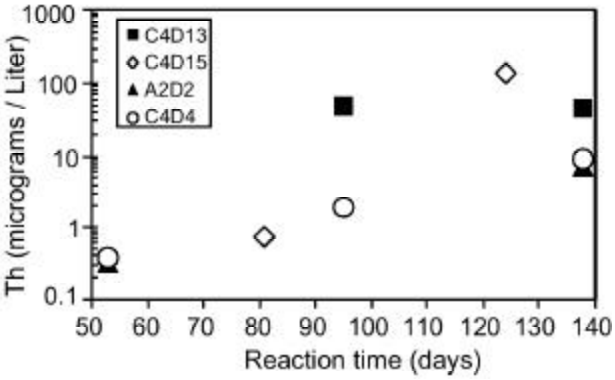

Figure 86. Concentrations of thorium in unfiltered samples.

The unfiltered samples have concentrations ranging from 0.3 up to 137 µg L^{-1}. The highest concentrations are associated with the crushed and sieved samples and thus are interpreted to reflect the analyses of fine solid particles produced during sample preparation (e.g. crushing). Sequential filtering of the J6 leachate sample suggests that approximately 17% of the particulate material in this sample falls within the colloidal size range (0.45 µm to ~5 nm).

However, the disk samples also show notable amounts of filterable thorium. For all sample types the particulate thorium concentrations increase in the later sampling periods (Figure 86), suggesting that minor physical degradation of the samples is occurring. Thus, the solution data suggest that the most important mechanism for thorium release from these types of materials at pH near 7 is by particulate rather than solute transport.

Uranium. Based on the end-of-life isotopic analyses (Table 41), the monitor nuclide for uranium release in our experiments was ^{233}U. The concentrations of the ^{233}U in the filtered (~5

nanometers) leachate solutions ranged from 0.06 to 0.9 μg L^{-1} ($10^{-9.6}$ to $10^{-8.4}$ molal). The ^{233}U concentrations did not vary systematically with burnup or initial uranium content. However, in general, the highest concentrations of leached ^{233}U (0.8–0.9 μg L^{-1}) were from the crushed and sieved samples, suggesting that the increased surface areas of these crushed samples leads to minor but measurable increases in uranium release. As shown on Figure 87, all the leachate solutions were undersaturated with respect to dehydrated schoepite and the uranium is predicted to be present in solution dominantly as a uranyl carbonate species (e.g. $UO_2(CO_3)_2^{2-}$). The data field labeled "This Study" on Figure 87 is plotted for our ^{233}U concentrations only; if the total uranium concentration is plotted (including minor ^{238}U contamination) the field increases to around 10^{-7} molal and is thus still undersaturated with respect to dehydrated schoepite.

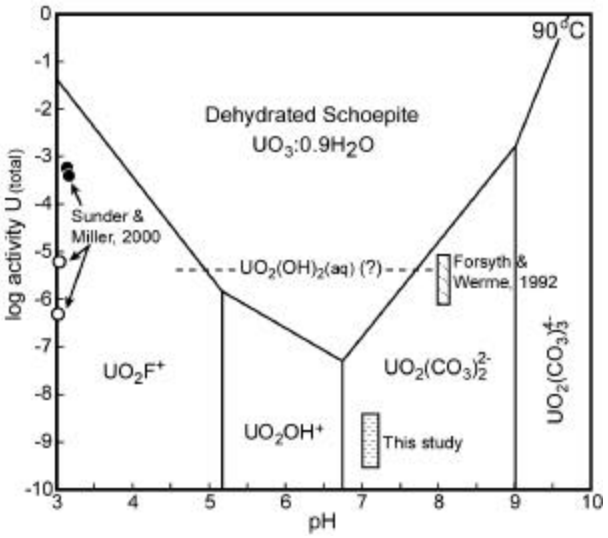

Figure 87. Solubility of uranium vs. pH (plotted using activities listed in Table 42). Data fields compare experimental results from this study with results from other dissolution experiments performed on urania and thoria-urania samples.

The uranium concentrations in the unfiltered leachate samples show the same general trend as for the thorium, with concentrations increasing with time. However, the amounts of filterable uranium are all less than ten μg L^{-1} and are thus considered to be of minor importance in terms of nuclide release.

The leachate solutions also contain measurable ^{238}U and ^{235}U, both of which are minor constituents of the fuel samples (0.3 and 1.8 percent respectively). Thus the presence of these nuclides appears to represent minor (micrograms) contamination from sample processing in the hot cells. The hot cell blank contained less than 1 μg L^{-1} ^{238}U thus narrowing the contamination source down to the sample processing such as disk cutting and crushing of the samples. The contamination of the leachates with minor amounts of ^{238}U does not, however, effect the calculation of uranium release rates or fuel dissolution, as greater than 85 weight percent of the uranium isotopic inventory in the fuel is ^{233}U.

Sunder and Miller (2000) report dissolved uranium concentrations ranging from 100 to 1300 μg L^{-1} in leachates from dissolution experiments on unirradiated $(U_{0.024}Th_{0.976})O_2$ and $(U_{0.015}Th_{0.985})O_2$ disks performed at 95ºC. These relatively high concentrations are explained by the fact that the experiments of Sunder and Miller (2000) involved pH values ranging from 3 to 5, at which uranium (and thorium) solubility increases by orders of magnitude relative to more neutral conditions (e.g. Figure 87).

Forsyth and Werme (1992) performed dissolution experiments on clad segments and fragments of UO_2-based spent nuclear fuel of moderate burnup (~43,000 MWD/MTM) at 25ºC in basic (pH~8) bicarbonate ground water. These tests, which were performed in oxic conditions, showed dissolved uranium concentrations ranging from 10^{-6} to 10^{-5} mol L^{-1} after 100 to 200 days of reaction. These data are also shown on Figure 87 for comparison with the irradiated $(U,Th)O_2$ samples.

Neptunium, Plutonium and Americium. The concentrations of ^{237}Np, ^{239}Pu, ^{240}Pu and ^{241}Am in the filtered leachate samples are all less than 0.08 μg L^{-1} ($<10^{-9.5}$ molal) with many less than 0.02 μg L^{-1} ($<10^{-10}$ molal). The concentrations of these actinides are also insignificant within the unfiltered samples, which contain less than 0.4 μg L^{-1}.

The low concentrations of plutonium are consistent with thermodynamic calculations, which predict a solubility of approximately 10^{-12} molal under these conditions, with PuO_2 being the solubility-controlling phase (Figure 88). However, the predicted solubility of neptunium under these conditions is approximately $10^{-6.5}$ molal, which is higher than our measured concentrations (Figure 89). This discrepancy is explained by the fact that the actinides are likely contained within the fuel matrix, which has remained relatively inert during these experiments.

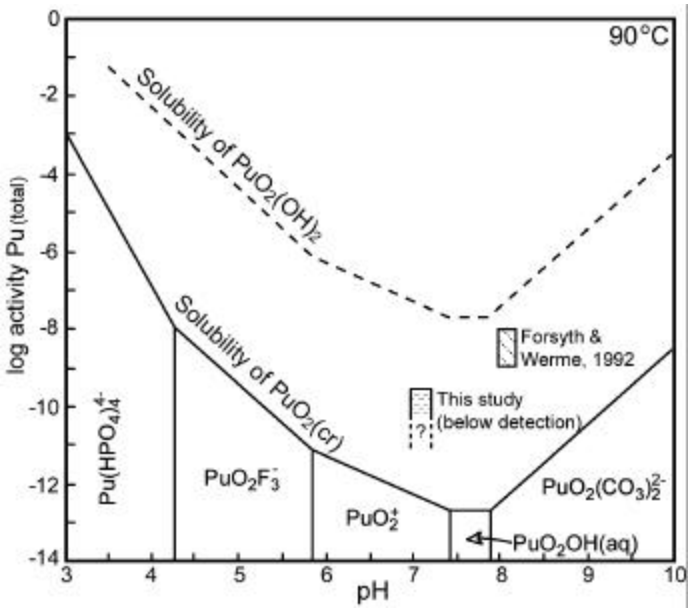

Figure 88. Solubility of plutonium vs. pH (plotted using activities listed in Table 42). Data fields compare experimental results from this study with results from leaching tests on UO_2-based spent fuel reported by Forsyth and Werme (1992).

The dissolution experiments of Forsyth and Werme (1992) on clad segments and fragments of UO_2-based spent nuclear fuel at 25ºC showed dissolved plutonium concentrations ranging from around 10^{-8} to 10^{-9} mol/L after 100 to 200 days of reaction in oxic conditions. Assuming that plutonium is released congruently as the fuel matrix dissolves this observation suggests that the matrix dissolution of the UO_2-based fuel is faster than the irradiated thoria-urania samples.

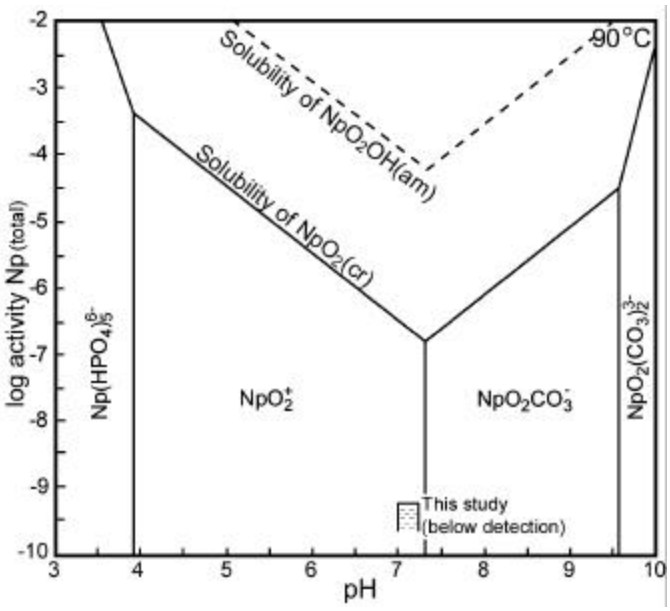

Figure 89. Solubility of neptunium vs. pH (plotted using activities listed in Table 46).

Cesium, Strontium, Iodine, Technetium, and Molybdenum. Cesium (^{137}Cs + ^{134}Cs) is the most soluble nuclide present in the experiments. Concentrations of ^{137}Cs in the filtered leachates ranged from below 1 μg L^{-1} to as high as 35 μg L^{-1}. The highest concentrations were measured during the early sampling intervals and decrease in the later ones (Figure 90). This trend suggests that there is a readily leachable

inventory of cesium that may be removed relatively rapidly (on the order of weeks) in near neutral waters at 90ºC. This leachable fraction however, does not account for all of the "gap" fraction present in these samples, which were estimated by acid leaching (e.g. Table 42). This highly mobile ^{137}Cs component is most dramatically demonstrated for sample C4D13, which contains 35µg L^{-1} in leachate for its first interval, but drops to less than 1µg L^{-1} for the second interval.

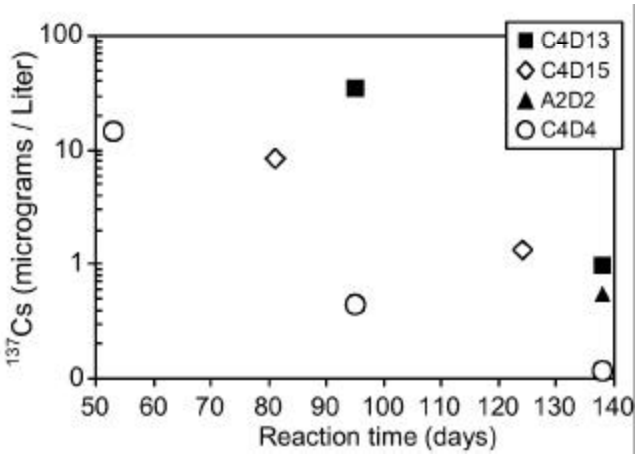

Figure 90. Cesium-137 concentrations as a function of reaction time.

The strontium-90 concentrations show a trend similar to that of the cesium, with concentrations decreasing from greater than one microgram per liter in the early sample intervals to less than one for later intervals. The iodine-129 is below the detection limit of approximately 50 µg L^{-1} in these samples. The technetium-99 concentrations in the filtered samples ranged form approximately 1 to 7µg L^{-1}, which is similar to the range for the ^{97}Mo. The leachate concentrations for these lighter fission products do not vary for the unfiltered sample groups and show no consistent trends with respect to the sample type (e.g. U content or burnup). There is a general correlation between the concentrations of the ^{97}Mo and ^{99}Tc in the leachate samples. This suggests that the ^{99}Tc releases may be influenced by the presence of a Mo/Tc-bearing, metallic phase, perhaps similar to the epsilon (5-metal) phase observed in spent UO_2 fuels. Metallographic examinations of samples used in our experiments (Richardson et al. 1987) also suggest the presence of a metallic phase within grain-boundaries, however, its composition has not yet been confirmed.

4.2.5.3. Fractional Release Rates of ^{233}U, ^{232}Th, and ^{137}Cs and Dissolution Rates of Irradiated (U,Th)O_2

The fractional release term is defined by normalizing the amount of a nuclide lost to solution to the total amount of that nuclide initially present in the sample:

$$Fr = (Ci_{sol.})\ (m_{sol.}) \ / \ (Ci_{fuel})\ (m_{fuel}) \qquad [9]$$

Where $Ci_{sol.}$ is the concentration of nuclide (i) in solution (g/g), $m_{sol.}$ is the total solution mass (g), Ci_{fuel} is the concentration of nuclide (i) in the fuel (g/g), and m_{fuel} is the total mass of the fuel sample (g).

The fractional release rate (Rf) is thus defined by dividing Fr by the number of days that the sample has been reacted:

$$Rf = Fr \ / \ days \qquad [10]$$

Additionally, surface area normalized fractional release rates can be obtained by dividing the fractional release rate by the surface area (SA) of the sample:

$$Rf \ / \ SA = Fr \ / \ days\ (SA) \qquad [11]$$

The use of fractional release rates and surface area normalized fractional release rates is particularly useful when comparing data from compounds with different compositions. The fractional values normalize the data with respect to the element of interest.

The dissolution rate (DR) of the solid can be calculated by dividing the amount of the monitor nuclide released into solution to amount of time the solid was reacted and the solid surface area of the sample. The monitor nuclide is one that is released congruently during corrosion of the sample (e.g. not incorporated into secondary deposits).

$$DR = (Ci_{sol.})\,(m_{sol.}) / (days)\,(SA) \qquad [12]$$

Where $Ci_{sol.}$ is the concentration of nuclide (i) in solution (mg/g), $m_{sol.}$ is the total solution mass (g), days refers to the test interval duration and SA is the solid surface area in m^2.

The fractional release per day and surface area normalized fractional release (leach) rates (calculated using equation 11) for ^{137}Cs are shown in Figures 91a and b. Samples reacted for 53 days have release fractions per day of 10^{-5} $days^{-1}$ while those reacted for >140 days drop to 10^{-7} $days^{-1}$. This trend is interpreted to reflect the relatively rapid depletion of the readily mobilized ^{137}Cs fraction, which is probably associated with macro-pores within the fuel (e.g. fuel/cladding gap and open fractures). The ^{137}Cs surface area normalized fractional release data follow the same trend (Figure 91b). The ^{137}Cs fractional release data for UO_2-based spent fuel reported by Forsythe and Werme (1992) ranged from approximately 10^{-5} $days^{-1}$ to 10^{-6} $days^{-1}$ during a 21 to 182 day leaching period. Thus the ^{137}Cs release from the irradiated thoria-urania fuel is comparable to, but somewhat lower than that for UO_2-based spent fuel in near neutral ground waters.

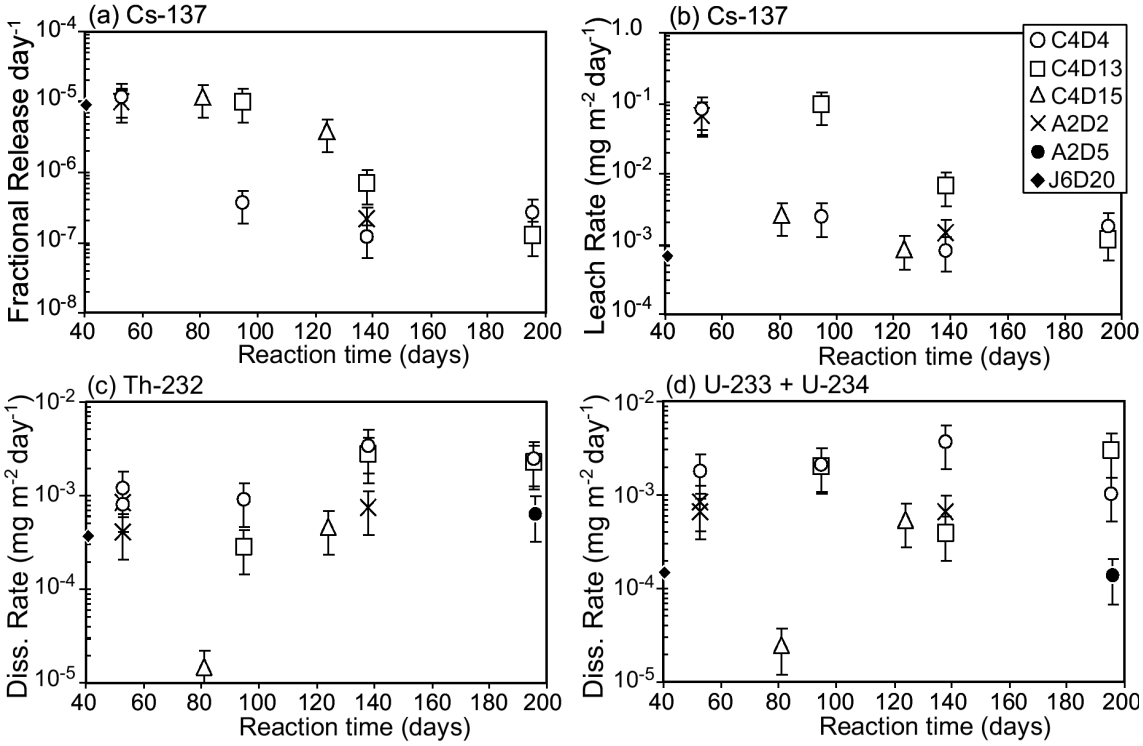

Figure 91. Fractional release and dissolution rate data for irradiated thoria-urania samples (the estimated accuracies, shown as error bars, are 50%).

The release fraction per day for ^{232}Th is $<10^{-9.1}$ day^{-1} and the corresponding fuel matrix dissolution rate ranges from $3.4x10^{-3}$ to $<1.5x10^{-5}$ mg m^{-2} day^{-1} (Figure 91c). These rates are orders of magnitude lower than the dissolution rates reported for UO_2 spent fuel, which are generally >1.0 mg m^{-2} day^{-1} in oxidizing solutions (Shoesmith et al. 2000). The uranium in the samples used in our experiments consisted of >98% ^{233}U and ^{234}U. Thus, the uranium fractional releases and dissolution rates were calculated using the sum of these two nuclides. The uranium fractional releases range from $<10^{-9.2}$ day^{-1} to $10^{-7.1}$ day^{-1} (average is $10^{-8.2}$ day^{-1}) thus indicating that the uranium is released incongruently relative to the thorium on a fractional release basis. However, the surface area normalized dissolution rates calculated using the uranium concentrations range from $3.7x10^{-3}$ to $3.7x10^{-5}$ mg m^{-2} day^{-1} (Figure 91d) and are thus not dramatically different from those calculated using ^{232}Th. This observation further supports the conclusion that the rate of dissolution/corrosion of the irradiated thoria-urania fuel samples are at least two orders of magnitude lower than those for UO_2 spent nuclear fuel in oxic groundwaters.

4.2.6. Experimental Results: Dissolution of Unirradiated Fuel

4.2.6.1. Dissolution of Unirradiated Crushed Pellets

The concentrations of dissolved uranium in the leachate solutions from the crushed pellet experiments ranged from approximately 1 to 900µg L^{-1}. The amount of dissolved uranium in the leachate solutions for the powder dissolution experiments is shown in Figure 92. The values are normalized to the surface area of the powders. Specific surface areas of the powders were given in Table 38.

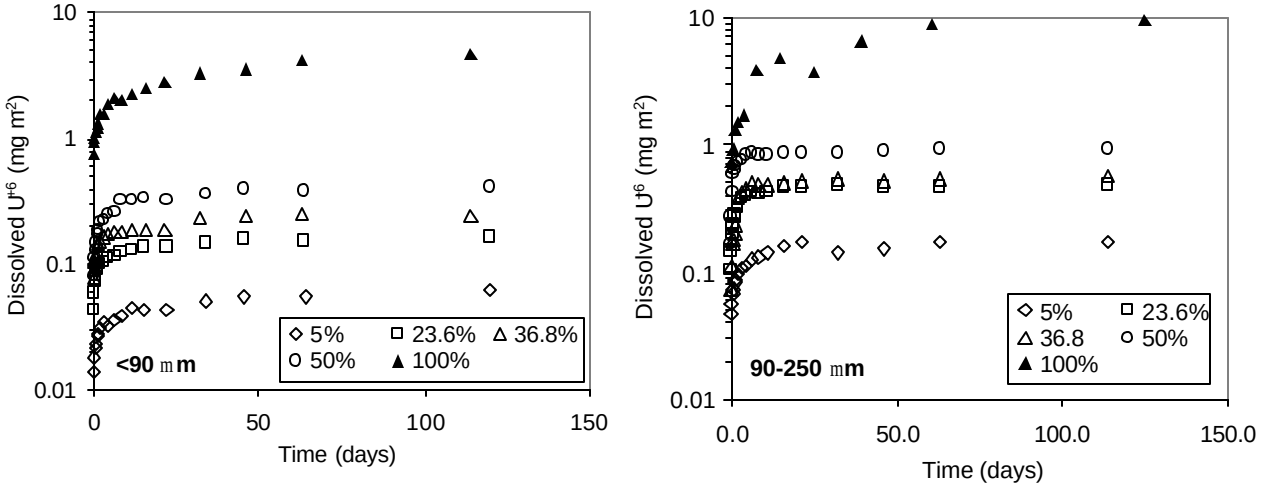

Figure 92. Dissolved uranium (mg) per square meter of powder surface area for <90 µm (left) and 90–250 µm (right) crushed and sieved (U,Th)O_2 pellets. The composition of the powders is listed as % UO_2.

The surface area normalized fractional release data for the powders is presented in Figure 93. This data normalizes the results with respect to the amount of uranium available in the fuel, based on initial composition and powder surface area.

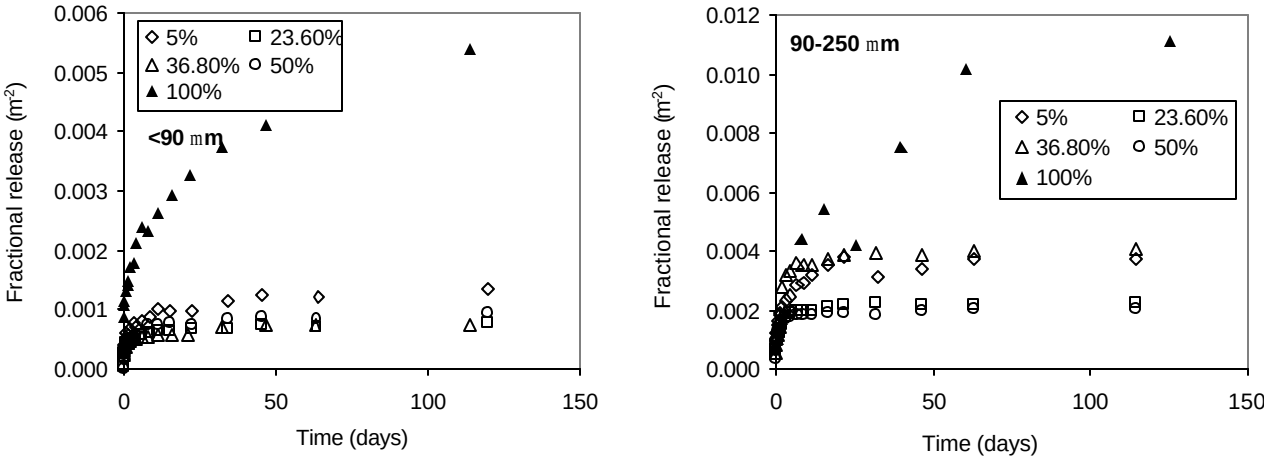

Figure 93. Surface area normalized fractional U^{+6} release from crushed and sieved $(U,Th)O_2$ pellet samples. The composition of the powders is listed as $\%UO_2$.

Trend lines were applied to the dissolution data in Figures 92 and 93 to determine the best fit. Power law ($y = Ax^B$) trend lines produced the best fit for the 100% and 5% UO_2 data, and logarithmic ($y = A(\ln x) + B$) trend lines gave the best fit for the remaining compositions. This held true for both the <90 µm and 90-250 µm powder sizes. Examples of data with the applied trend lines are shown in Figure 94. Correlation coefficients (r^2) for the trend lines were all above 0.9 with one exception (the 50% UO_2 90–250 µm powder).

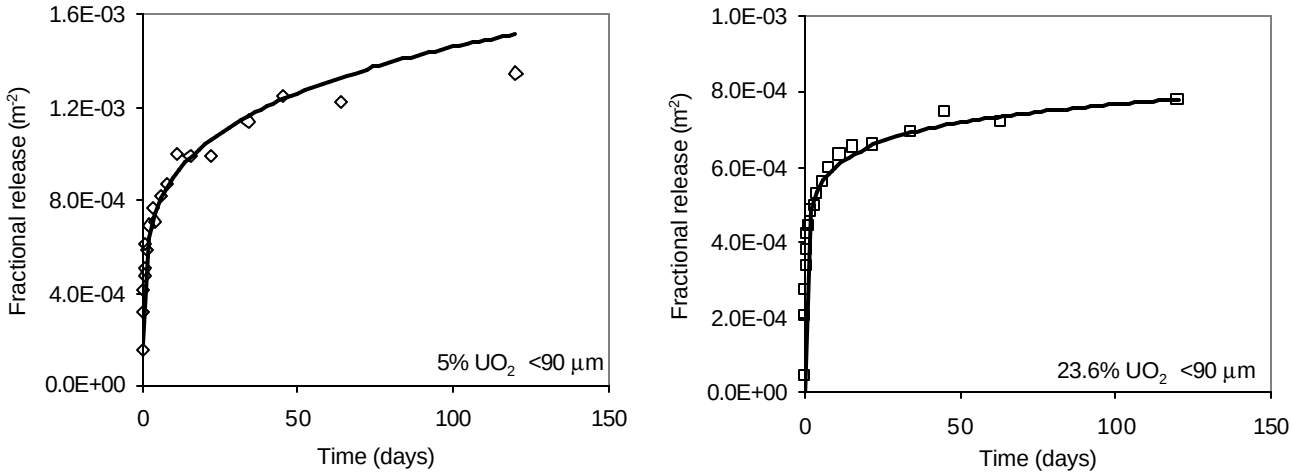

Figure 94. Trend lines applied to surface area normalized fractional release data, showing examples of power law (left) and logarithmic (right) curves.

The uranium dissolution rates (mg m^{-2} d^{-1}) and surface area normalized fractional uranium release rates (m^{-2} d^{-1}) were calculated by differentiating the best-fit trend lines of the dissolution data. The calculated rate data are shown in Figures 95 and 96. Each data point in these figures corresponds to the differential of the trend line at that time value.

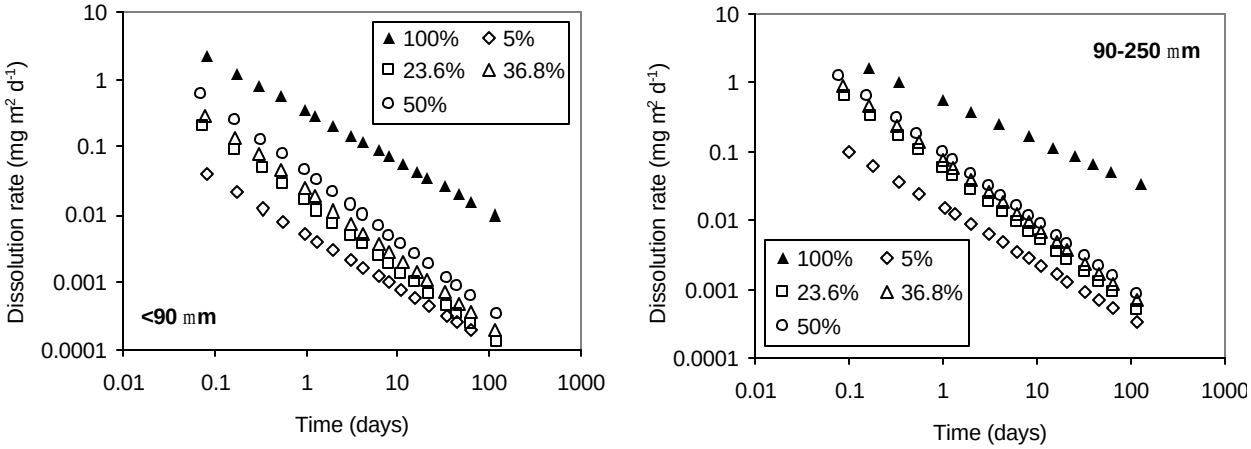

Figure 95. Uranium dissolution rates for crushed and sieved (U, Th)O_2 pellets. The values were calculated by differentiating the trend lines of the dissolution data. The composition of the powders is given in %UO_2.

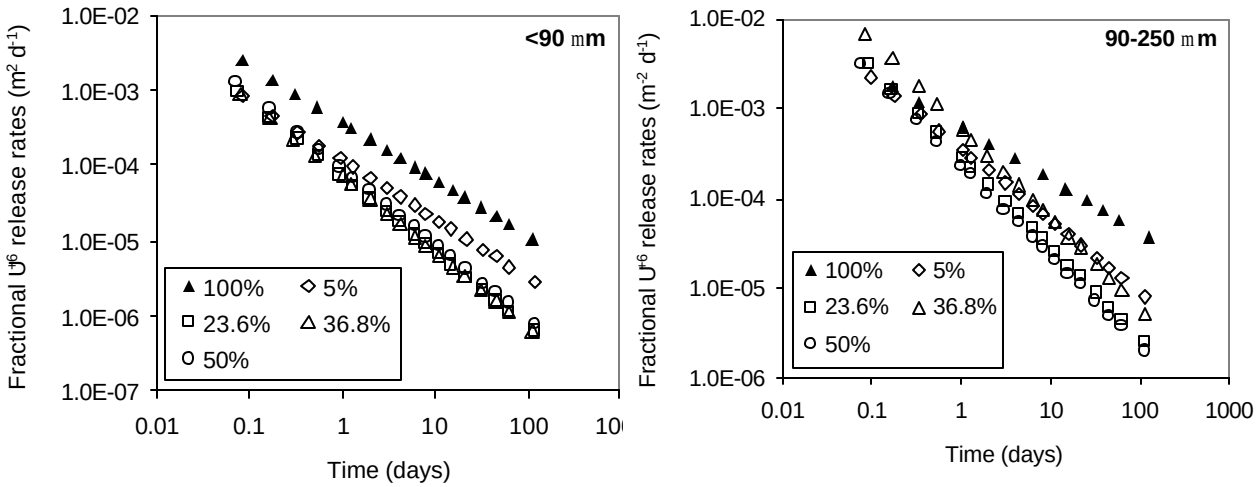

Figure 96. Surface area normalized fractional uranium release rates for crushed and sieved (U,Th)O_2 pellets. The values were calculated by differentiating the trend lines of the surface area normalized fractional release data. The powder composition is given in %UO_2.

For all powder compositions and both particle size ranges, the dissolution rates decrease with time. The observation of higher initial dissolution rates that decrease after several days is consistent with studies reported previously in the literature (see, for example Bruno et al. 1995, and Casas et al. 1993). The calculated dissolution rates for the 90–250µm powder were consistently slightly higher than those for similar compositions of the <90µm powder.

The dissolution rates of pure UO_2 found in this study range between approximately 2–0.01 mg m^{-2} g^{-1} at times between 0.1 and 125 days. Dissolution rates for unirradiated fuel reported in the literature exhibit a large range of values, depending on the specific experimental conditions, such as solution pH, carbonate concentration, temperature, and the O/U ratio of the starting material. The values obtained in this study are comparable to those found in the literature for unirradiated UO_2 under similar experimental conditions. Bruno et al., for example, reported dissolution rates between 0.67 and 2.41 mg m^{-2} g^{-1} for unirradiated UO_2 in a $NaCl/NaHCO_3$

solution at pH 8.5. Casas et al. have reported initial and final dissolution rates of 0.33 and 2.48×10^{-3} mg m^{-2} g^{-1}, respectively, for crushed UO_2 pellets in $NaClO_4$ solutions at pH 8.

The dissolution rates for the 5% UO_2 crushed pellets are generally about 1 to 2 orders of magnitude lower than for pure UO_2, with values for the intermediate compositions (23.6%, 36.8%, and 50% UO_2) falling in between. The dissolution rates for the 5% UO_2 powders are between 2×10^{-3}–1×10^{-4} mg m^{-2} d^{-1} for times between 10–120 days. These values are very similar to the range of values found for ~5% ^{233}U irradiated pellets at 90ºC and times between 50 to 140 days (Figure 91).

The surface area normalized uranium fractional release rates (Figure 96) present the dissolution data normalized both for powder surface area and composition, and present a meaningful comparison of all of the powder dissolution data. The data for the <90 µm powders indicates that the normalized fractional U^{+6} release rates for all of the $(U,Th)O_2$ materials were less than for the pure UO_2. The differences between the $(U,Th)O_2$ compounds and the UO_2 are small at the initial sampling times but increase with time. At 0.2 days the normalized fractional release rate for UO_2 is between 3 and 8 times higher than for the $(U,Th)O_2$ compositions, while at ~120 days the rate for the UO_2 is between 10 and 37 times higher. At all times the difference between the $(U,Th)O_2$ compositions was small, and followed the trend $(U_{0.5}Th_{0.5})O_2$ > $(U_{0.368}Th_{0.632})O_2$ > $(U_{0.236}Th_{0.764})O_2$. The 5% UO_2 powder exhibited slightly different behavior, initially exhibiting the lowest rate, but ending the experiment with the highest rate of all the $(U,Th)O_2$ compositions.

The 90–250 µm powder exhibited similar results with a few notable exceptions (Figure 96). Differences in fractional release rates between the pure UO_2 and the $(U,Th)O_2$ fragments were negligible initially, with the $(U_{0.368}Th_{0.632})O_2$ fragments exhibiting rates slightly higher than UO_2. At ~120 days, however, the rate for the UO_2 is between 9 and 30 times higher than those for the solid solutions. Differences among the $(U,Th)O_2$ materials is again minor, with the exception of the higher rates for $(U_{0.368}Th_{0.632})O_2$.

If the calculated curves in Figure 96 are extrapolated to 5 years, the surface area normalized fractional uranium release rates for UO_2 become 10 to 70 times higher (<90 µm powder) and 20 to 100 times higher (90–250 µm fragments) than the rates for the $(U,Th)O_2$ fuel.

Analysis of the filtered and unfiltered leachate solutions from the <90µm 100% UO_2 powder experiment revealed that significant amounts of suspended solids >20 nm were present in the leachate solutions. It was found that approximately 62% of all uranium in the leachate solutions was present as suspended particulate material after 2 hours. This value diminished to approximately 15% after 10 days.

The pH of all the leachate solutions was between 8.0 and 8.6 throughout the duration of the experiments. These values are slightly higher than those of the J-13 water used for the study of irradiated pellets at ANL-E (pH values of ~7.4 at room temperature). The discrepancy could be due to differences in carbonate concentration between the two batches of J-13 water.

4.2.6.2. Dissolution of Unirradiated Pellets

The concentration of U^{+6} in the sampled leachate solutions from pellet dissolution experiments is shown in Figure 97. The U^{+6} concentration measured in blank J-13 solutions under similar conditions was approximately 0.5 µg L^{-1} (shown as the dotted line on Figure 97). The measured $[U^{+6}]$ value for a number of the sample solutions, particularly those for pellets with

low UO_2 content, were found to be near or below this blank level. As a result, interpretation of the data for these samples is difficult.

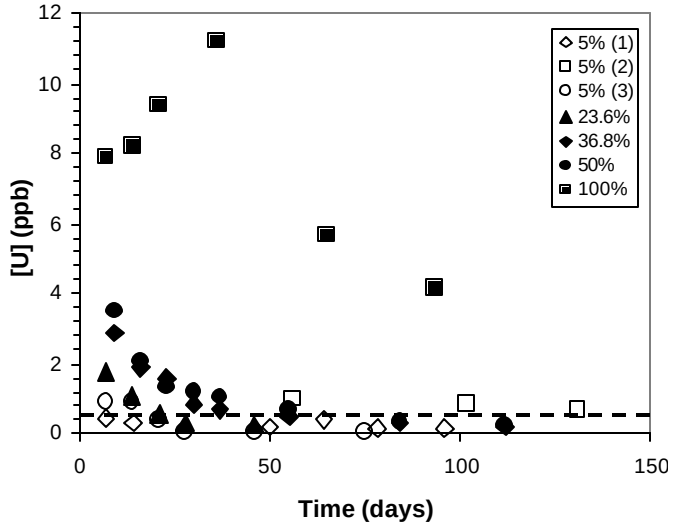

Figure 97. Dissolved uranium concentration in pellet dissolution leachate samples. The pellet compositions (% UO_2) are shown. Dashed line shows the approximate U^{+6} concentration of the blank solutions.

The dissolution rates for 100% UO_2 are calculated to be between approximately 0.1–0.01 mg m^{-2} d^{-1} over the period from 7–93 days. The dissolution rates for 36.8% and 50% UO_2 pellets are between 0.02–0.003 mg m^{-2} d^{-1} during the same experimental period. The dissolution rates and surface area normalized fractional release rates for unirradiated whole pellets are shown in Figure 98. The dissolution rates for the 23.6% and 5% UO_2 pellets cannot be reliably determined because the measured U^{+6} concentrations are near or below the background level.

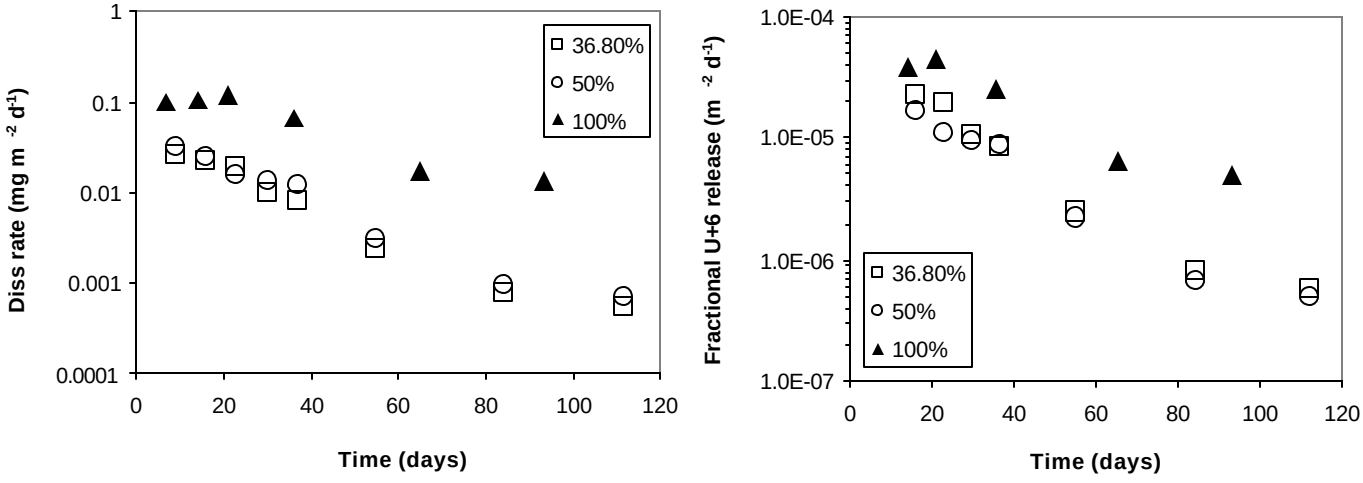

Figure 98. Dissolution rates (left) and surface area normalized fractional release rates (right) of whole (U,Th)O_2 pellets in J-13 water at 90°C. The composition of the pellets is given in percent UO_2.

The dissolution rates for the 23.6%, 50%, and 100% UO_2 whole pellets at 90ºC are very similar to the values for crushed pellets of the same composition at room temperature (Figure 95). It should be noted that geometric surface areas were used in calculating the dissolution rates of whole pellets. Actual surface areas are expected to be slightly higher, and would yield dissolution rates slightly lower than those in Figure 98.

4.2.7. Summary Of Dissolution Results

The dissolution of irradiated thoria-urania fuel in J-13 groundwater was found to be minimal and its corrosion negligible over a 195 day reaction period. The early or "instant" release of ^{137}Cs, however, is similar to that measured for irradiated UO_2 fuels under similar experimental conditions. Concentrations of ^{90}Sr are also relatively high for early sample intervals, suggesting that significant fractions of Cs and Sr are distributed within fluid-accessible macro-pores within the fuel (fuel/cladding gap, open fractures and grain-boundaries). Concentrations of ^{99}Tc in the filtered leachates are correlated with ^{97}Mo, suggesting that its release may be influenced by a Mo/Tc-bearing metallic phase similar to the epsilon particles found in UO_2 fuels. This conclusion is supported by metallographic observations. The actinides ^{237}Np, ^{239}Pu, ^{240}Pu and ^{241}Am remained insoluble throughout the experiments. There is minor incongruent release of U relative to Th on a fractional release basis, however, the matrix dissolution rates calculated using Th and U consistently yield values ranging from $3x10^{-3}$ to $<3x10^{-5}$ mg m^{-2} day^{-1}. These tests demonstrate that the dissolution rate of irradiated thoria-urania fuels are at least two orders of magnitude lower those measured for UO_2 spent fuels in oxidizing, near neutral ground-waters.

The surface area normalized fractional uranium release rates for the unirradiated crushed UO_2 pellets at room temperature were found to be as much as ~40 times higher than the rates for the unirradiated $(U,Th)O_2$ fuel materials after ~120 days. The differences in rates among the various $(U,Th)O_2$ compositions, however, were relatively small.

The dissolution rates of unirradiated whole pellets at 90ºC and crushed pellets at room temperature are very similar (Figures 98 and 95). This result in itself suggests that there is little temperature dependence in the temperature range of 25–90ºC on the dissolution rates for these materials in J–13 ground water.

The uranium dissolution rates for unirradiated 5% UO_2 crushed pellets were between 2×10^{-3}–1×10^{-4} mg m^{-2} d^{-1} for times between 10–120 days. These values are in relatively good agreement with those for irradiated pellets of the same composition, and suggest that there is little effect of burnup on the matrix dissolution. In addition, the dissolution rates (mg m^{-2} d^{-1}) for unirradiated 5% UO_2 crushed pellets (Figure 95) were between approximately 25–100 times less than the rates measured in this study for pure unirradiated UO_2. This decrease is of lower magnitude than found for irradiated 5% UO_2 pellets, which were found to have dissolution rates at least two orders of magnitude less than UO_2. However, it should be noted that the comparison in the case of irradiated 5% UO_2 fuel is made with published studies of irradiated UO_2 dissolution, and not a side-by-side comparison using the same experimental procedure.

The findings of this study indicate that there is a decrease in the normalized uranium dissolution rates of unirradiated $(U,Th)O_2$ solid solutions by a factor of approximately 10 to 37 times compared to pure UO_2. However, only minor differences in the normalized dissolution rates of the solid solutions are observed as a function of the composition. The results presented

here, therefore, provide evidence that (U,Th)O_2 fuels have an advantage over UO_2 fuels with respect to aqueous dissolution in groundwater.

4.3. Thermal Gravimetric Study of (U, Th)O_2 Dry Oxidation

The aqueous dissolution of UO_2 invariably involves the oxidation of U(IV) to higher oxidation states and subsequent formation of soluble U(VI) species. As part of the study of (U, Th)O_2 stability, therefore, the oxidation of these materials in air was also investigated. Because oxidation involves the addition of oxygen atoms to the (U, Th)O_2 lattice, there is an associated weight gain. Thermal gravimetric analysis was used to monitor the oxidation by measuring the mass of the samples heated in air at different temperatures and heating rates. The objective of this work was to quantify the kinetic parameters governing oxidation in these materials as a function of composition, and to determine if oxidation is significantly inhibited by the presence of ThO_2.

4.3.1. Experimental Approach

The unirradiated (U, Th)O_2 materials described in previous sections were used for the dry oxidation studies. The 90–250µm crushed pellet fragments were used in this part of the study. Gravimetric analysis was performed using a TA Instruments TGA 2050. Both isothermal and non-isothermal heating conditions were used. Oxidation was performed in air flowing through the sample chamber at 90 cm^2/min. Sample sizes were approximately 8–20 mg for each experiment. The non-isothermal heating rates chosen for this study were 1, 3, and 5ºC/min. Temperatures for isothermal experiments were then chosen based on the non-isothermal weight gain curves.

The samples were analyzed using powder x-ray diffraction both before and after the oxidation experiments. Characterization was performed using a Phillips APD 3720 diffractometer with a Cu anode target, where the $K_{\alpha 1}$ wavelength is 1.54056Å. Generator voltage and current were 40 kV and 20 mA, respectively. Scans were made between 10º and 139º 2Θ with a step size of 0.02º. An internal Si standard was used for all measurements. The lattice parameters were calculated by a graphical and numerical least squares method and a method utilizing angular separation reported by Popovic (1973). Additional information about the measurement error was calculated using Cohen's method (Cullity 1978).

The solid-state kinetic analysis was based on a single step kinetic equation:

$$f(a) = k(T) \cdot t, \qquad [13]$$

and the Arrhenius relationship:

$$k(T) = A \exp\left[-\frac{E}{RT}\right], \qquad [14]$$

where α is the fraction reacted, f(α) is the reaction model, T is temperature, k(T) is the rate coefficient, t is time, A is the frequency factor, and E is the activation energy. Two methodologies for calculating A and E were used in this work: traditional model fitting and a model-free method reported by Vyazovkin and Wight (1999).

Model-fitting method. Traditional kinetic analysis of isothermal data entails a comparison of the measured values with theoretical functions derived from models based on the geometry of interface initiation and advance and/or diffusion processes occurring in the solid. Some common kinetic models are given in Table 49 (based on Bamford and Tipper, 1980).

Table 49. Reaction models.†

Reaction model	**f(a)**
Acceleratory rate equations	
Power Law	$\alpha^{1/n}$
Exponential Law	$\ln\alpha$
Sigmoid rate equations	
Avrami – Erofe'ev	$[-\ln(1-\alpha)]^{1/2}$
	$[-\ln(1-\alpha)]^{1/3}$
	$[-\ln(1-\alpha)]^{1/4}$
Prout – Tompkins	$\ln[\alpha/(1-\alpha)]$
Deceleratory rate equations	
(Based on diffusion mechanisms)	
One-dimensional diffusion	α^2
Two-dimensional diffusion	$(1-\alpha)\ln(1-\alpha) + \alpha$
Three-dimensional diffusion	$[1-(1-\alpha)^{1/3}]^2$
Ginstling – Brounshtein	$[1-(2\alpha/3)] - (1-\alpha)^{2/3}$
(Based on geometric models)	
Contracting area	$1-(1-\alpha)^{1/2}$
Contracting volume	$1-(1-\alpha)^{1/3}$
(Based on order with respect to a)	
First order	$-\ln(1-\alpha)$
Second order	$(1-\alpha)^{-1}$
Third order	$(1-\alpha)^{-2}$

†Based on Bamford and Tipper (1980), p. 74

Under isothermal conditions, agreement with a known reaction model $f(\alpha)$ is confirmed by linear behavior when the function $f(\alpha)$ is plotted versus time, *t*. Rate coefficients at each isotherm are obtained from the slope of the linear $f(\alpha)$ vs. *t* plot, as in equation [15]:

$$f(\alpha) = k(T) \bullet t + \text{intercept} \qquad [15]$$

Overall values for E and A are simultaneously solved from the $k(T)$ at each known T, using Equation [14] and assuming Arrhenius behavior.

For non-isothermal experiments, the function $f(\alpha)$ obtained from the isothermal analysis is applied to non-isothermal rate data, yielding a plot of $\ln k(T)$ vs T^{-1}. Again, linear behavior suggests obedience to the reaction model, $f(\alpha)$. Values for E and A are calculated from the slope and intercept of the linear plot according to the relationship:

$$\ln k(T) = \left(-\frac{E}{R}\right)\left(\frac{1}{T}\right) + \ln A \qquad [16]$$

Model-free method. The model-free method was applied solely to the isothermal rate data in this study. Under isothermal conditions, the reaction model is assumed to be independent of heating rate. The single step kinetic and Arrhenius equations are combined:

$$-\ln t_{a,i} = -\left[\frac{E}{RT}\right] + \ln\left[\frac{A}{f(a)}\right] \qquad [17]$$

The slope of linear regions of $-\ln t$ vs. T^{-1} plot, using data for a specific a value, yields E_a without making assumptions about f(a). Frequency factors (A) cannot be determined in this fashion without identifying f(a). The benefits, however, are such that process complexities may be revealed by illuminating any dependence of activation energy (E) on a, instead of simply yielding an overall value for the process.

4.3.2. Thermogravimetry Results

The low specific surface areas of the 90–250µm pellet fragments used in this study (0.01–0.03 m^2 g^{-1}) influence the thermogravimetric results such that bulk reactions outweighed the contribution of surface reactions. This was particularly evident with UO_2, which generally has a characteristic two-step transformation from cubic UO_2 to tetragonal U_3O_7 to orthorhombic U_3O_8. Thermal gravimetric analysis of the <45µm UO_2 powder oxidized in air showed the expected two-step curve, whereas the larger fragments only exhibited the net bulk reaction to U_3O_8. The absent surface contribution can be attributed to the lower surface to volume ratio of the pellet fragments as compared to fine powders. A single-step TGA oxidation curve for UO_2 pellet fragments oxidized at 3ºC/min to a target temperature of 900ºC is shown in Figure 99. The arrows indicate the temperatures used in subsequent isothermal experiments carried out on the UO_2 pellet fragments.

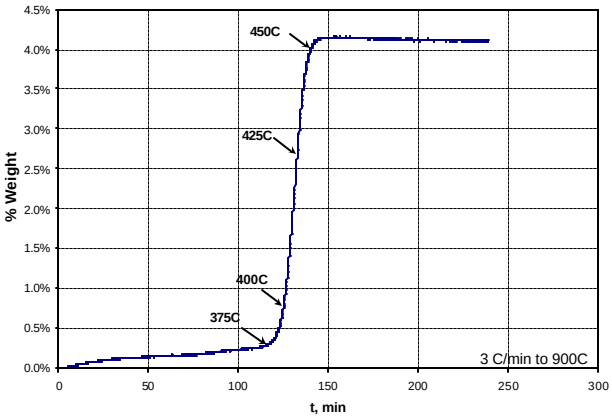

Figure 99. Non-isothermal air oxidation of UO_2 fragments (90–250 µm) heated at 3ºC/min. Temperatures for isothermal experiments are indicated with arrows.

The same approach was employed to selected temperatures of isothermal interest for all (U, Th)O_2 compositions. Pellet fragments that were sieve classified between 90 and 250µm were subjected to heating rates of 1, 3, and 5ºC/min under flowing air. Single step curve behavior was observed for all samples. Temperatures from the sloped linear region of each curve were selected for isothermal investigation. Non-isothermal TGA curves are shown in Figures 100, 101, and 102 for (U, Th)O_2 compositions of 23.6, 36.8, and 50% UO_2. The weight gain upon oxidation of the 5% UO_2 material was found to be too small to be accurately resolved, and is not discussed further.

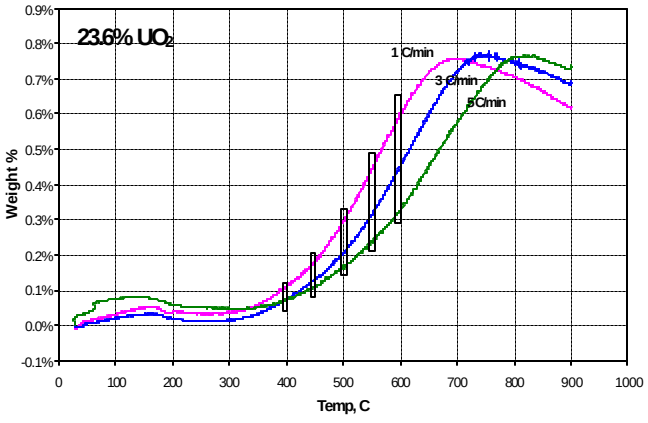

Figure 100. Thermal gravimetric data for non-isothermal oxidation of 23.6% UO_2 fragments at 1, 3, and 5ºC/min. Bars indicate temperatures used in isothermal analysis.

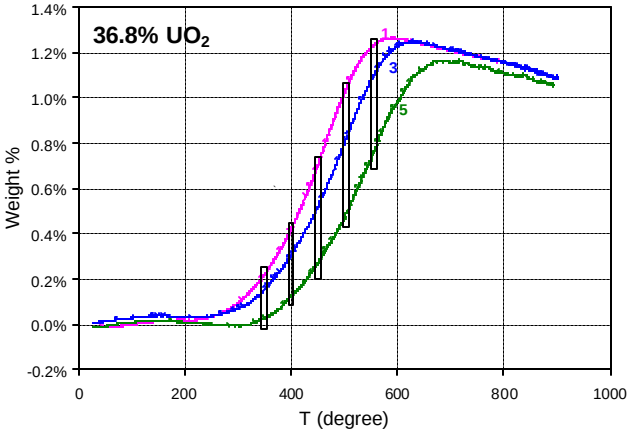

Figure 101. Thermal gravimetric data for non-isothermal oxidation of 36.8% UO_2 fragments at 1, 3, and 5ºC/min. Bars indicate temperatures used in isothermal analysis.

The bars across each set of curves in Figures 100–102 indicate the temperatures chosen for isothermal analysis. It was noted that when each (U, Th)O_2 sample reached its peak, the sample weight began to decrease. Examinations of the instrument setup and XRD conclusions did not yield any clues as to the cause of the weight loss. The observed decrease could be due to a buoyancy effect, an instrument-related artifact that is independent of reactions taking place in the sample.

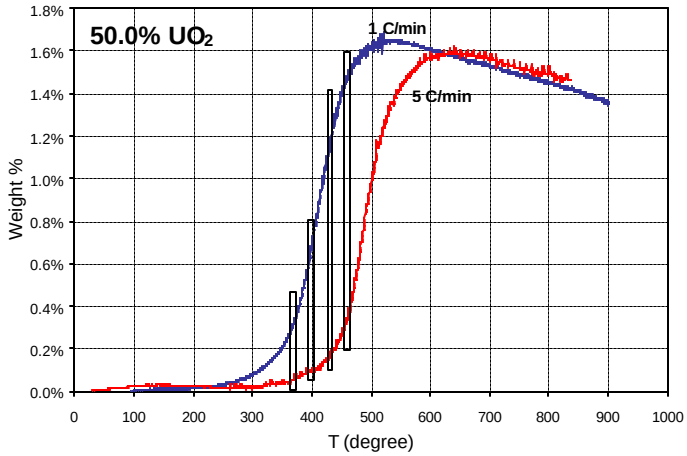

Figure 102. Thermal gravimetric data for non-isothermal oxidation of 50.0% UO_2 fragments at 1 and 5ºC/min. Bars indicate temperatures used in isothermal analysis.

Based on the non-isothermal oxidation data, pellet fragments were subjected to isothermal oxidation in air at the appropriate temperatures. Those results are presented as fraction reacted, a, versus time, t-t_o, plots (Figures 103–106) where t_o is the time required to reach the desired isothermal temperature. Weight gain, assumed to be from oxidation, does occur during this ramp up period. The fraction reacted (a) is determined assuming the starting weight represents 0% reacted, and the final (oxidized) weight is 100% reacted. It was observed that the percent weight gain increased with higher UO_2 content. Considering the lengthy dwell times required for complete reaction of the (U, Th)O_2 compositions (in excess of 1000 minutes) it was observed that the weight increases during the initial 8–15 minute ramp period had little effect on the overall curve shape. Oxidation of the 100% UO_2 fragments, on the other hand, reached completion between 20–120 minutes, depending upon temperature. Contributions to the

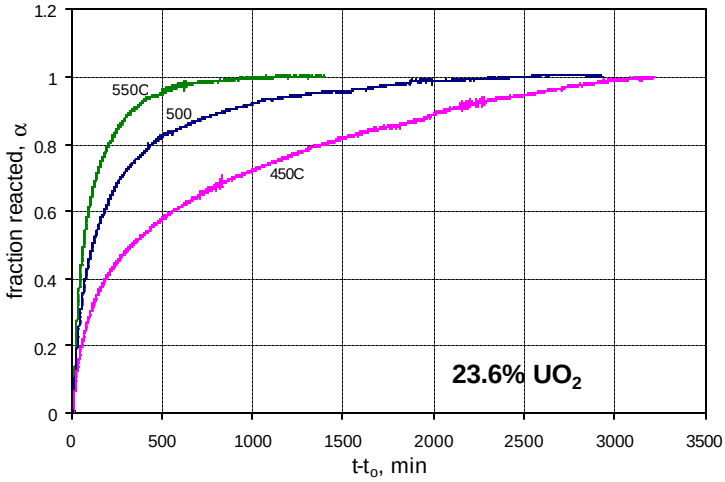

Figure 103. Thermal gravimetric data for isothermal air oxidation of 23.4% UO_2 fragments.

overall weight gain during the ramp period for 100% UO_2, therefore, significantly affected the curve shape.

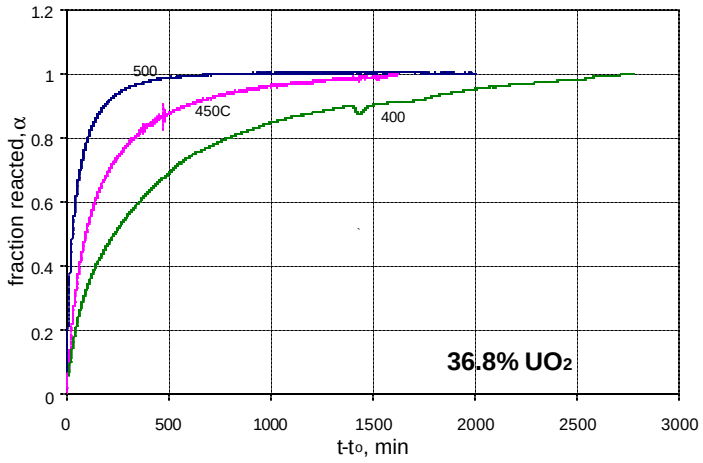

Figure 104. Thermal gravimetric data for isothermal air oxidation of 36.8% UO_2 fragments.

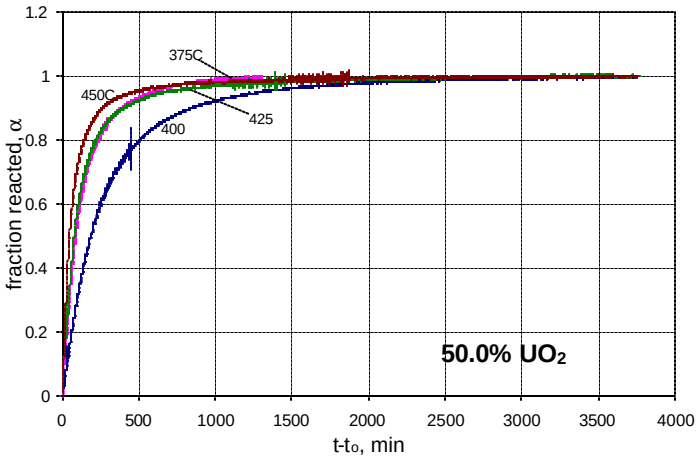

Figure 105. Thermal gravimetric data for isothermal air oxidation of 50% UO_2 fragments.

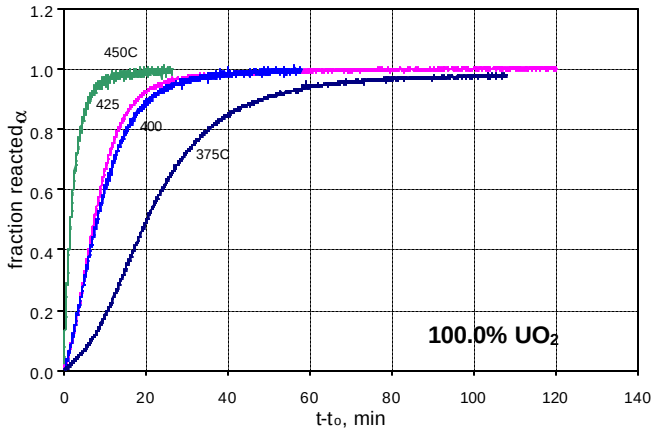

Figure 106. Thermal gravimetric data for isothermal air oxidation of 100% UO_2 fragments.

The oxidation of several samples did not reach completion by the end of the experimental duration. This data, therefore, cannot be used in the subsequent kinetic analysis. This includes data for the 23.6% UO_2 at 400ºC and the 36.8% UO_2 at 300ºC and 350ºC. The isothermal gravimetric curves for these samples have been omitted from the following discussion.

Xray diffraction measurements showed that the lattice parameter of unoxidized (U, Th)O_2 decreases linearly with increasing UO_2 content (Figure 107). The diffraction patterns for all (U, Th)O_2 materials exhibited no evidence for phase transformations as oxidation proceeded, with the crystal structure of the compounds remaining cubic after oxidation at all temperatures. In contrast, the diffraction patterns of oxidized UO_2 exhibited the characteristic transformation from cubic to tetragonal to orthorhombic structures. The error bars shown in Figure 107 include the

scatter associated with three calculation methods (least squares method, Cohen's method, and Popovic's method).

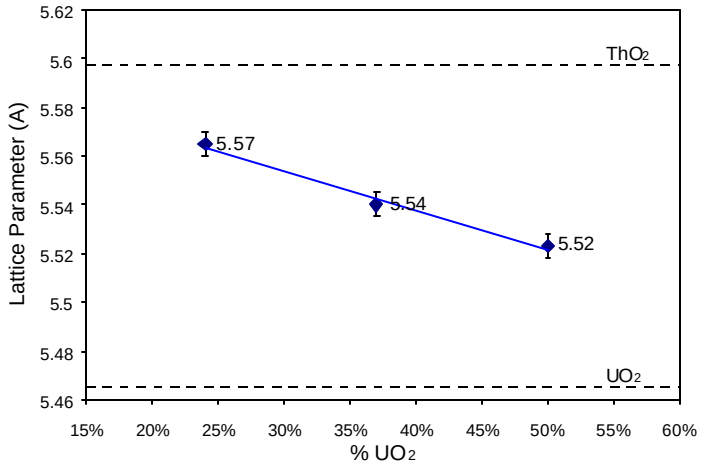

Figure 107. Lattice parameter, a (in Angstroms), of unoxidized (U,Th)O_2 solid solutions as a function of UO_2 content oxide content. Lattice parameters for ThO_2 and UO_2 indicated by dashed lines.

4.3.3. Results Of Kinetic Analysis

Since the temperature is held constant, time is the only dependent variable in the isothermal runs. The isothermal data, therefore, are typically assumed to be more reliable for calculating kinetic parameters. The isothermal data were fitted to the reaction models from Table 49. Linear behavior suggests a good fit of the model. However, it should be noted that the various models were not verified by complementary techniques in this study. The results of isothermal rate data for 23.6% UO_2 fit to two and three dimensional diffusion reaction models are shown in Figure 108 (next page).

Based on the correlation coefficients for the linear trend lines in Figure 108, traditional model-fitting applied to the 23.6% UO_2 isothermal rate data suggests two dimensional diffusion at the lower temperature (450ºC), followed by a shift to three dimensional diffusion at 500ºC and 550ºC. At the lower temperature, it is difficult to definitively state which of the two diffusion models fit best. Rate coefficients obtained from the slopes are 2×10^{-4} to 7×10^{-4} min^{-1} across all four temperatures. The activation energy (E) and frequency factor (A) were calculated by solving equation [14]. The calculated activation energies are shown in Table 50. The calculated values for A exhibited extremely large error for most of the data analyzed, and have not been included. The reason for the large error in these values is unclear at this time.

The linearity of the non-isothermal rate data was also tested after having identified possible reaction models with isothermal data. Since model-fitting provides an overall value, differentiating whether curve behavior is a result of the oxidation mechanism, or interactions from the variable temperature and time, is not within the capability of this analysis technique. Plots of log*k* vs 1/T were constructed with 2D and 3D diffusion models. Both models presented linear behavior in the region of interest. The linear fit results are shown in Table 50.

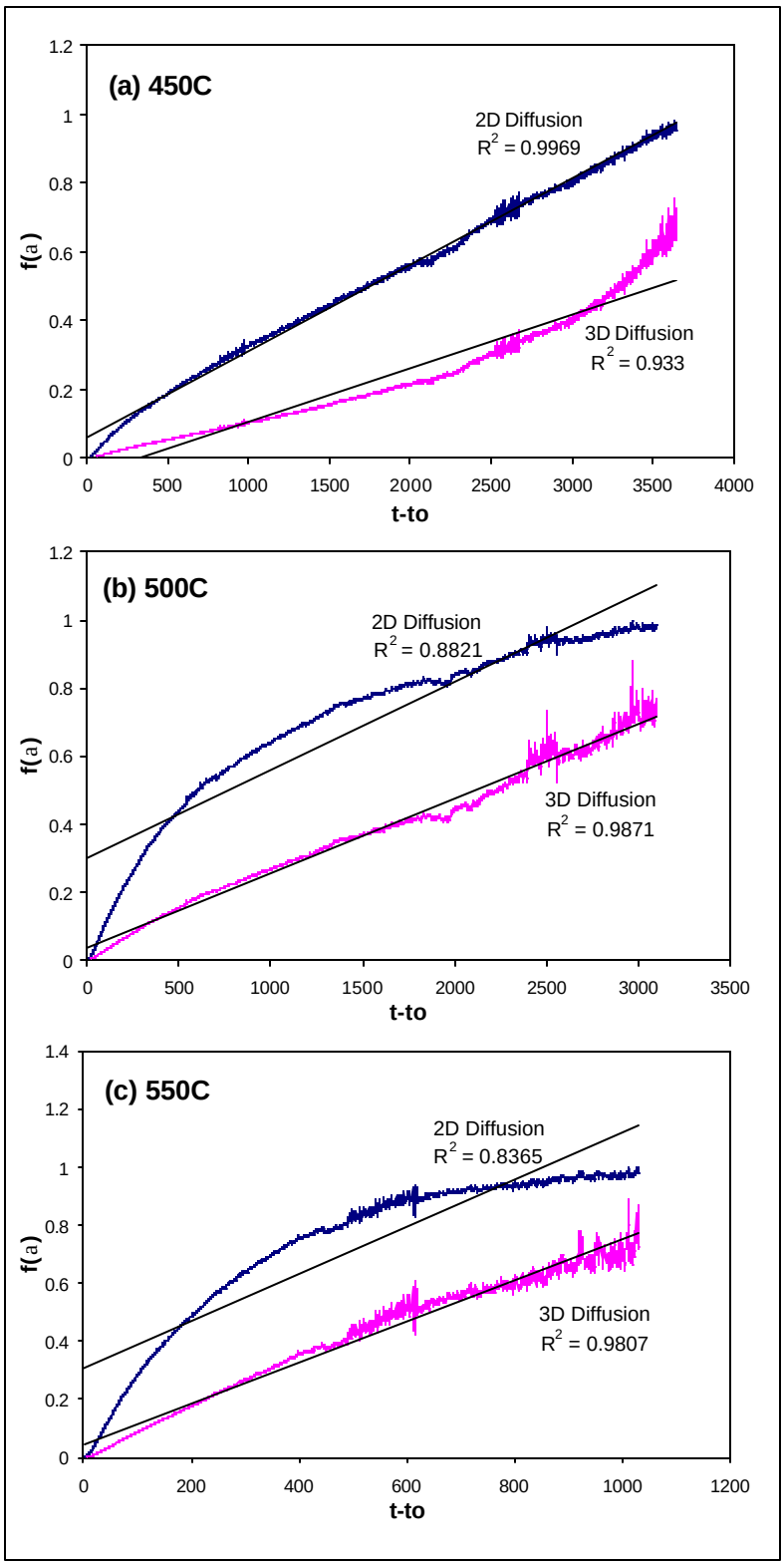

Figure 108. Isothermal oxidation rate data for 23.6% UO_2 fit to 2D and 3D diffusion reaction models for (a) 450ºC, (b) 500ºC, and (c) 550ºC isotherms.

Table 50. Activation energy (E) for oxidation calculated by model-fitting of 23.6% UO_2 rate data.

Heating method and reaction model		E (kJ/mol)
Isothermal	3D Diffusion	87 ± 64
Nonisothermal	2D Diffusion at 1ºC/min	81.2
	2D Diffusion at 3ºC/min	78
	2D Diffusion at 5ºC/min	82
	3D Diffusion at 1ºC/min	94
	3D Diffusion at 3ºC/min	92
	3D Diffusion at 5ºC/min	92
Isothermal	a = 0.5	88
(model-free)	a = 0.9	91

The model-free technique reported by Vyazovkin and Wight (1999) and discussed above was used to corroborate the values calculated by model-fitting. The model-free method was applied solely to the isothermal rate data. Under isothermal conditions, the reaction model is assumed to be independent of heating rate. Combining the single step kinetic and Arrhenius equations into:

$$-\ln t_{a,i} = -\left[\frac{E}{RT}\right] + \ln\left[\frac{A}{f(a)}\right] \qquad [18]$$

The slope of the linear regions of $-\ln t$ vs. T^{-1}, with a = 0.5 and 0.9, yields E_a without making assumptions about f(a). For the 23.6% UO_2 isotherms, the $-\ln t$ vs. T^{-1} plot is shown in Figure 109. The calculated values of E_a are 88 kJ/m and 91 kJ/mol for a = 0.5 and 0.9, respectively.

The same analysis as described here for the 23.6% UO_2 samples was applied to the 36.8% and 50.0% UO_2 pellet fragments. Those results are presented in the figures and tables below.

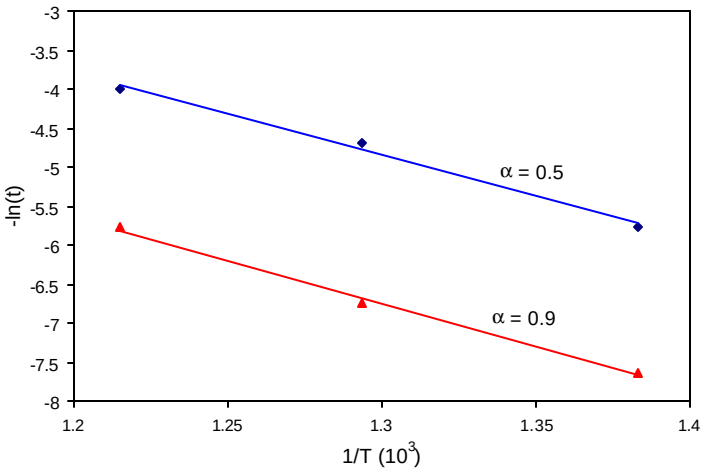

Figure 109. Plots of $-\ln t$ vs. T^{-1} for isothermal oxidation rate data for 23.6% UO_2. Slope of the curves gives the activation energy, E_a.

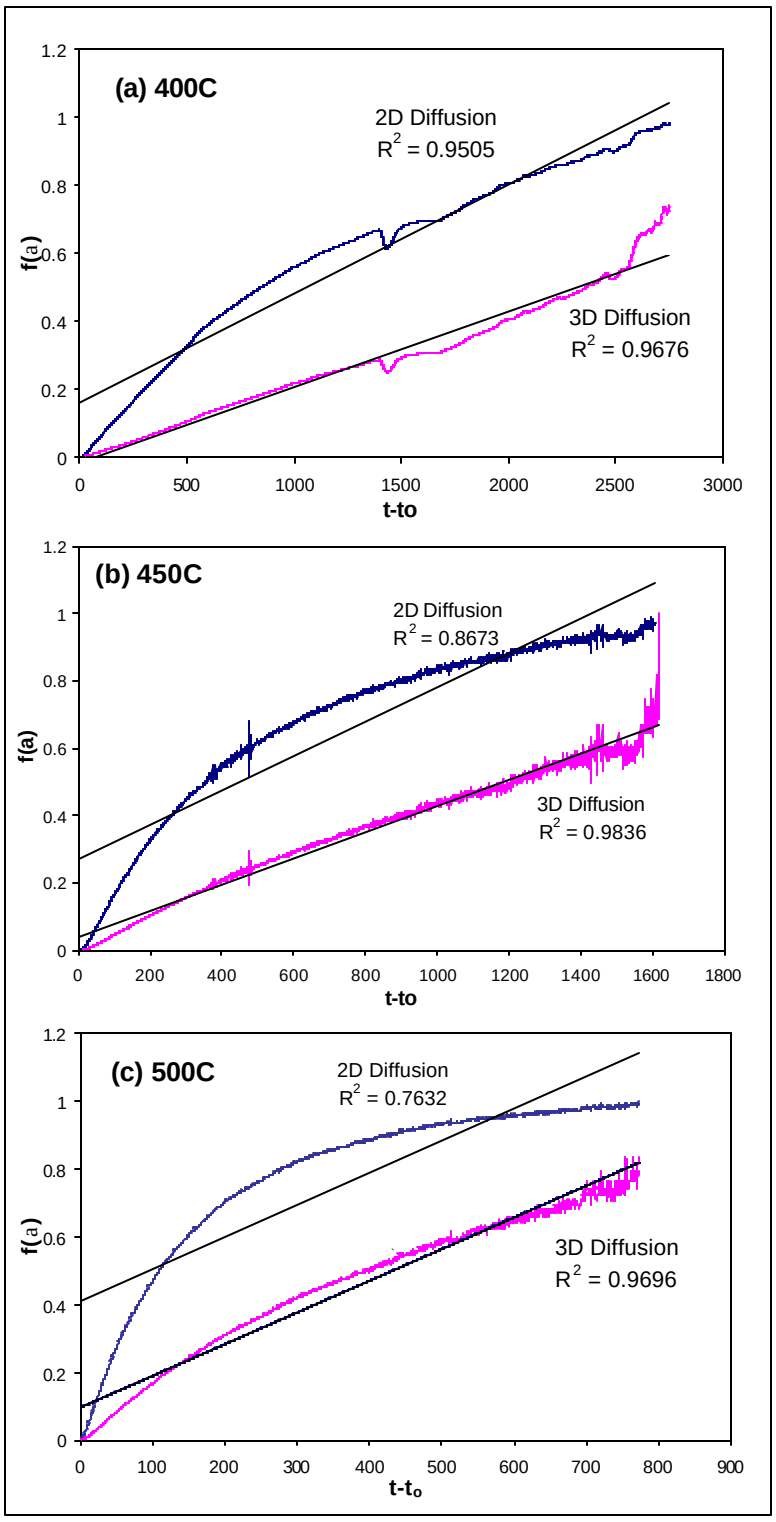

Figure 110. Isothermal oxidation rate data for 36.8% UO_2 fit to 2D and 3D diffusion reaction models for (a) 400ºC, (b) 450ºC, and (c) 500ºC isotherms.

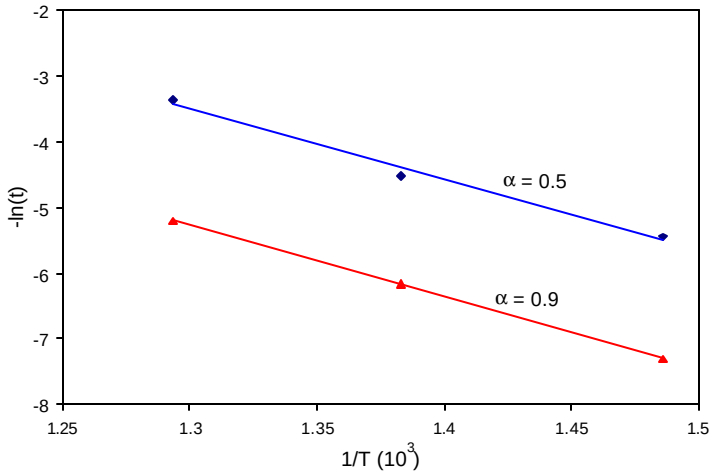

Figure 111. Plots of –ln*t* vs. T^{-1} for isothermal oxidation rate data for 36.8% UO_2. The slope of the curves provides the activation energy, E_a.

Table 51. Activation energy (E) for oxidation, calculated by model-fitting and model-free analysis of 36.8% UO_2 rate data.

Heating method and reaction model		E (kJ/mol K)
Isothermal	3D Diffusion	66 ± 10
Nonisothermal	3D Diffusion at 1ºC/min	92
	" " at 3ºC/min	93
	" " at 5ºC/min	108
Isothermal	a = 0.5	90
(model-free)	a = 0.9	91

Unlike the 23.6% and 36.8% UO_2 data, the 50.0% UO_2 fragments did not display linear behavior with any of the typical reaction models. With regard to the raw data (Figure 105), the oxidation was more than 50% complete within the first 500 minutes for all the isothermal runs. Inserting the data into each reaction model yielded only two possibilities, Avrami-Erofe'ev and 3D Diffusion. However, it can be observed in Figure 112 that the models are roughly linear at times greater than 200 minutes. Within the first 100–200 minutes of interest, none of the reaction models produced a satisfactory linear fit to the data. The validity of using either reaction model to calculate A and E parameters therefore comes into question.

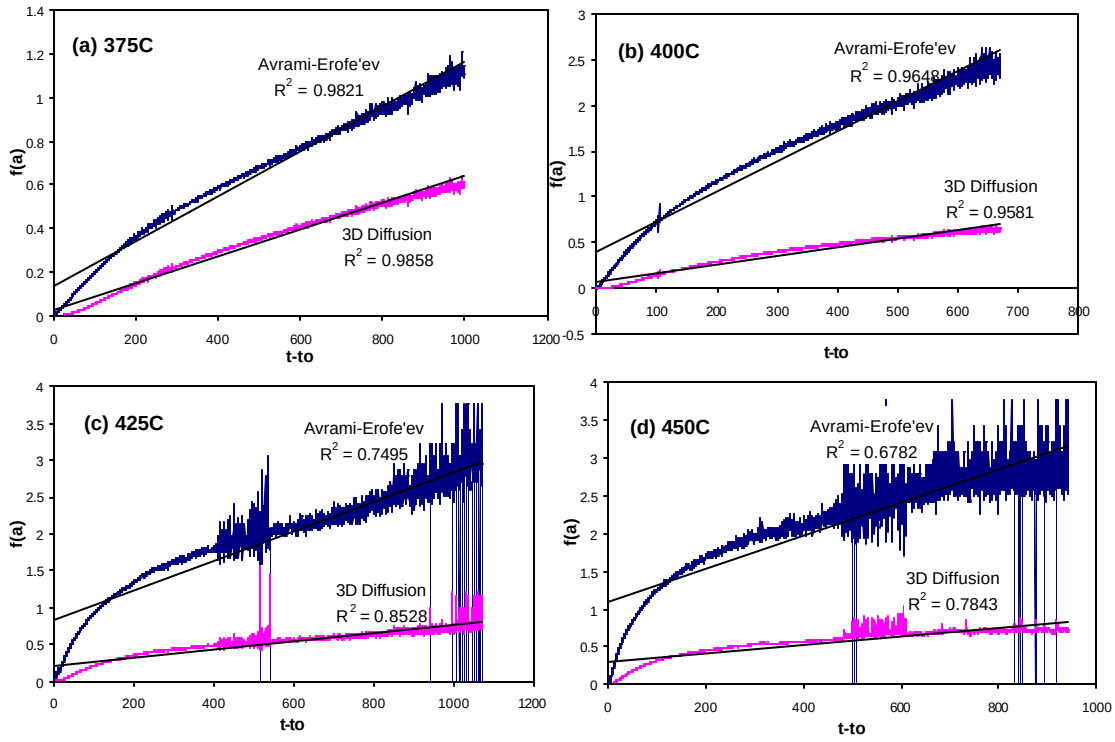

Figure 112. Isothermal oxidation rate data for 50% UO_2 fit to Avrami-Erofe'ev and 3D diffusion reaction models for (a) 375ºC, (b) 400ºC, (c) 425ºC, and (d) 450ºC isotherms .

Attempts to fit non-isothermal data to a known reaction model also met with inconclusive results. At the slower heating rate of 1ºC/min, linearity was observed in both the Avrami-Erofe'ev and 3D diffusion models within the temperature range of interest. Data obtained at a heating rate of 5ºC/min, however, was not linear. This incongruity may be a result of a lag between reaction rate and heating rate, where the temperature rises faster than the material is able to react. Without complementary microscopic techniques, the appropriate reaction model could not be confirmed in this study. As a consequence, the calculations presented here were obtained solely by the model-free methodology. A plot of $-\ln t$ vs. T^{-1} based on the model-free method using isothermal data for the 50% UO_2 material is shown in Figure 113. Unlike the 23.6% and 36.8% UO_2 compositions, the data does not suggest multi-step behavior.

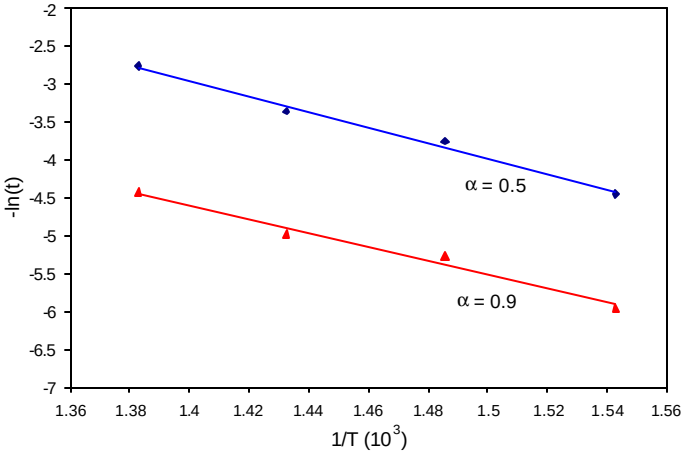

Figure 113. Model-free calculations for 50.0% UO_2 isothermal rate data.

Table 52. Activation energy (E) for oxidation, calculated by model-free analysis of 50.0% UO_2 rate data.

Heating method and reaction model		E (kJ/mol K)
Isothermal	a = 0.5	86
(model free)	a = 0.9	76

Kinetic analysis of pure UO_2 pellet fragments produced results similar to the 50.0% UO_2 material. None of the reaction models applied to the isothermal or non-isothermal oxidation data produced linear plots. This system, however, is a highly studied material and it is unlikely that conclusions drawn from numerous other researchers are inapplicable in this study. Particle size is a known variable of influence upon kinetic analysis. The fragments in this research reduced the ratio of surface reactions to bulk reactions. Since a particle size component was not included in the reaction models, this is a possible explanation for poor fit of the reaction models. This also demonstrates the limitations of the model-fitting method.

Since oxidation of 100% UO_2 was pursued as a control for comparison purposes, the model-free determination of E was employed. The plot of $-\ln t$ vs. T^{-1} (Figure 114) does not suggest a multi-step process. However, knowing that UO_2 oxidation is a two-step process, the influence of particle size is apparent. With a low surface to volume ratio, it is likely that Figure 114 mainly reflects the bulk contribution to oxidation. Overall E values calculated for a = 0.5, 0.7, and 0.9 are 116, 104, and 100 kJ/mol, respectively, which are in agreement with values typically reported in the literature.

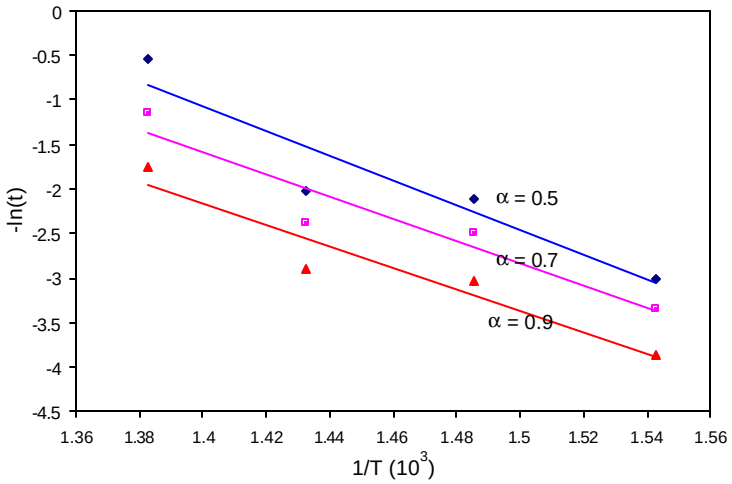

Figure 114. Model-free calculations for 100% UO_2 isothermal rate data.

The activation energies obtained in this study and those reported by Anthonysamy et al. (2000) are compiled in Table 53 below. The data from the model-free method are the averages of the activation energies calculated at each a value examined. In general there is relatively good agreement between the isothermal and non-isothermal values determined in this work, with the exception of the low value for 36.8% UO_2 determined using the isothermal data and the three-dimensional reaction model. The activation energies for the (U, Th)O_2 materials of all compositions are relatively similar (most are between 80-100 kJ/mol), and are slightly lower than the value of 108 (±7) kJ/mol determined for UO_2 using the model-free method. This differs from the results reported by Anthonysamy et al., who found lower activation energies (~30–50 kJ/mol) for low UO_2 content compositions, and higher energies (46–91 kJ/mol) for high UO_2 content compositions.

Table 53. Overall activation energies (kJ/mol) for $(U,Th)O_2$ oxidation found in this study and by Anthonysamy et al. (2000).

Sample Composition	Heating rate (K/min)	E (kJ/mol) Anthonysamy et al.	E (kJ/mol) This Study
$(U_{0.15}Th_{0.85})O_2$	0.5	45 ± 0.3	
	1	42 ± 0.3	
	5	31 ± 0.2	
	Isothermal	51 ± 1	
$(U_{0.236}Th_{0.764})O_2$	1		94
	3		92
	5		92
	Isothermal (model fit)		87 ± 64
	Isothermal (model-free)		89 ± 3
$(U_{0.30}Th_{0.70})O_2$	0.5	51 ± 0.6	
	1	49 ± 0.5	
	5	49 ± 0.4	
	Isothermal	45 ± 1	
$(U_{0.368}Th_{0.632})O_2$	1		92
	3		93
	5		108
	Isothermal (model fit)		66 ± 10
	Isothermal (model-free)		90 ± 1
$(U_{0.50}Th_{0.50})O_2$	Isothermal (model-free)		81 ± 7
$(U_{0.72}Th_{0.28})O_2$	0.5	81 ± 0.4	
	1	70 ± 0.6	
	2	70 ± 0.6	
	5	46 ± 0.4	
	Isothermal	91 ± 1	
$(U_{0.77}Th_{0.23})O_2$	0.5	90 ± 0.6	
	1	79 ± 0.4	
	2	67 ± 0.8	
	5	66 ± 0.8	
	Isothermal	82 ± 1	
UO_2	Isothermal (model-free)		107 ± 8

4.3.4. Degree of Oxidation

From the initial and final weights of each isothermal run, a final O/U ratio was calculated to evaluate the extent of oxidation. In the calculations, thorium was assumed to maintain a constant value of +4, and therefore an O/Th ratio of 2. Additional starting assumptions were that the initial state of the $(U, Th)O_2$ samples was stoichiometric, such that O/U = 2, and that oxidation of the samples was the sole contributor to the weight gain. With the experimental observation that the crystal structures of the mixed oxide materials all remained as the cubic fluorite type, it was expected that the hyperstoichiometry would not exceed that associated with U_3O_8.

The results are presented in Figure 115 as mean uranium valence. Each data point represents a single thermal gravimetric experiment, so no estimation of error is presented. At all temperatures studied, UO_2 oxidized to a U valence equivalent to U_3O_8, as expected. None of the (U, Th)O_2 materials achieved this extent of oxidation. Additionally, the lower U content oxides did not go beyond the transitional U_3O_7 edge at lower temperatures. This result gives qualitative evidence of an oxidation inhibiting effect for (U, Th)O_2 as compared with pure UO_2.

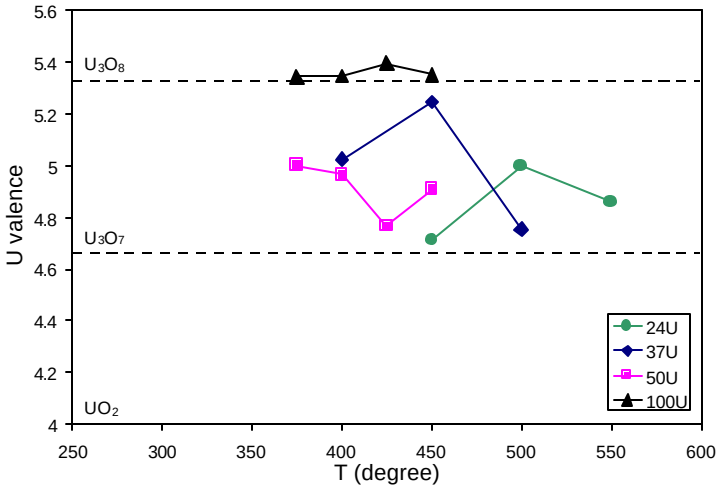

Figure 115. Mean uranium valence for (U, Th)O_2 samples isothermally oxidized in air. Dashed lines indicate the uranium valence for reference compounds U_3O_7 and U_3O_8.

4.3.5. Summary of Dry Oxidation Results

All the non-isothermal weight gain data exhibited single-step behavior. The isothermal data suggest a three-dimensional diffusion model for oxidation of (U, Th)O_2 for the 23.6% and 36.8% UO_2 compositions with activation energy values of 87 ±64 and 66 ±10 kJ/mol, respectively. No suitable reaction models could be found for the data from the 50% and 100% UO_2 materials. The model-free method of determining activation energy was applied to the isothermal data, and produced relatively similar activation energy values (81–90 kJ/mol) for all of the 23.6%, 36.8%, and 50% UO_2 compositions. The activation energy for 100% UO_2 was found to be 107 (±8) by the model-free method. Thus, the data available suggest little dependence of activation energy on (U, Th)O_2 composition, and only slightly lower values for the mixed oxide compared to pure UO_2. In addition, the relatively low surface-to-volume ratio of the fragments used in this study was found to influence the thermal gravitational data significantly, resulting in single step oxidation curves even for 100% UO_2, instead of the characteristic two-step behavior typically seen with higher surface area powders.

Task 5. Korean Work

(Chan Bock Lee, KAERI)

KAERI has been working on four tasks in support of this NERI project to assess the feasibility of urania-thoria fuel: core design analyses, fuel pellet manufacturing technologies, fuel rod performance analysis, and xenon diffusivity measurements.

Task 5.1 Core Design Analysis

(Hyung Kook Joo, Jae Man Noh, Jae Woon Yoo, Jin Young Cho, Sang Yoon Park KAERI)

5.1.1. HELIOS/MASTER Code Preparation for Thorium Fuel Core Analysis

The HELIOS/MASTER code system was modified for the neutronic analyses of thorium-fueled reactor cores. HELIOS1.6 is two-dimensional transport code, which uses a current coupling collision probability method for the neutron transport calculations. The HELIOS code with a 45-neutron group design library will be used for generation of the group constants for the thorium fuel assemblies. MASTER, a nodal core simulator developed by KAERI, will be used for the calculations of the core physics with thermal-hydraulic feedback. The nuclide chain in the MASTER code was extended to include Th-232 and associated nuclides such as Pa-233, U-233, and U-234 for the thorium core analysis, as shown in Figure 116.

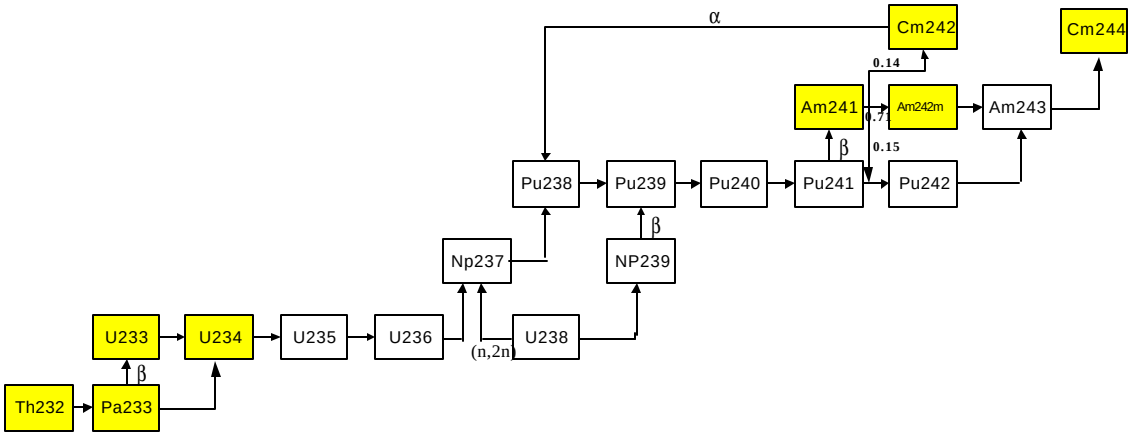

Figure 116. The extended nuclide decay chain in MASTER.

5.1.2. PWR Thorium Pin-Cell Burnup Benchmark Calculation With HELIOS-1.6

As a part of the verification of the HELIOS calculation capability for thorium-based fuel, the k-infinite and isotopic number densities of 25% UO_2 + 75% ThO_2 fuel pins were calculated and compared with the results of CASMO4 and MOCUP calculations (both the MIT and INEEL versions). Table 54 shows the calculated k-infinites for a 25%UO_2+75%ThO_2 pin cell at selected burnup steps. The isotopic number densities at 60MWd/kgHM are compared in Table 55. The differences between the HELIOS, MIT-MOCUP, and INEEL-MOCUP calculated k-infinites and

the values calculated with CASMO4 are shown in Figure 117. Based on these results, HELIOS is in a good agreement with MOCUP and CASMO4.

Table 54. Comparison of eigenvalues for the 25%UO_2+75%ThO_2 pin-cell model.

Burnup (MWd/kg)	CASMO-4	MIT MOCUP	INEEL MOCUP	KAERI HELIOS-1.6
0.000	1.23782	1.23354	1.22347	1.22843
0.114	1.20071	1.19708	1.18051	1.19164
5.835	1.14828	1.14466	1.13563	1.14101
10.411	1.12108	1.11662	1.11325	1.11517
19.563	1.07245	1.07154	1.06648	1.07023
31.004	1.02014	1.02168	1.01906	1.01992
40.156	0.98190	0.98453	0.98514	0.98313
49.308	0.94636	0.95383	0.95035	0.94899
51.596	0.93817	0.94477	0.94063	0.94084
60.749	0.90701	0.91851	0.91447	0.91058
72.189	0.87348	0.88449	0.87942	0.87811

Table 55. Fractional Difference in Isotopic Number Densities at 60.749 MWd/kgHM.

Isotopes	CASMO-4	MIT MOCUP	INEEL MOCUP	KAERI HELIOS-1.6
Th-232	1.53769e+22	-0.003	-0.003	-0.002
Pa-231	1.70440e+18	0.048	0.018	-
Pa-233	1.95229e+19	0.035	0.045	0.031
U-232	1.56006e+18	0.034	-0.003	-0.061
U-233	2.74202e+20	0.040	0.044	0.043
U-234	5.15172e+19	0.176	0.174	0.032
U-235	1.78104e+20	-0.021	-0.033	-0.009
U-236	1.39420e+20	0.054	0.057	0.057
U-238	3.88419e+21	0.004	0.003	0.003
Np-237	1.82660e+19	-0.058	-0.035	-0.069
Np-238	5.46097+e16	-0.037	-0.096	-0.074
Np-239	7.61806e+17	-0.043	-0.019	-0.037
Pu-238	8.90932e+18	-0.026	-0.099	-0.061
Pu-239	5.37090e+19	-0.071	-0.050	-0.013
Pu-240	1.82233e+19	-0.032	0.021	0.033
Pu-241	1.90707e+19	-0.024	-0.041	-0.026
Pu-242	9.96772e+18	-0.036	0.027	-0.082

5.1.3. Fuel Cycle Analysis for UO_2 Cores and $(Th,U)O_2$ Cores

A 900MWe PWR currently operated in Korea was adopted as the reference plant to construct various conceptual cores with thorium-uranium fuel. Three kinds of homogeneous thorium-

uranium fueled cores were investigated with three different weight fractions of ThO_2: 75, 70, and 65w/o in the thorium-uranium fuel. The U-235 enrichment of the UO_2 in the thorium-uranium fuel was 19.5 w/o. For the purpose of comparison, a series of reference UO_2 only cores were also analyzed. The enrichment levels of the uranium in the uranium fuel assemblies were 4.5 w/o for the core with a 15-months cycle scheme, 7.2 w/o and 8.0 w/o for the cores with 24-month cycle schemes. The reference plant core has 157 fuel assemblies. Fifty-two fresh fuel assemblies were newly loaded for each cycle according to a three-batch reloading strategy in both the thorium-uranium cores and the uranium only cores. The fuel assemblies with low reactivity at the end-of-cycle were discharged during the reload. The fuel loading pattern was determined with a trial-and-error method according to the low-leakage-loading concept.

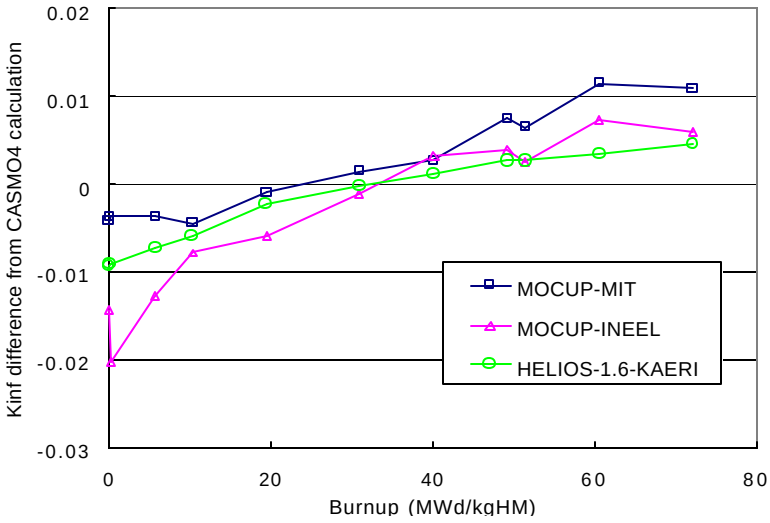

Figure 117. K-infinite differences of HELIOS, MIT MOCUP, and INEEL MOCUP from CASMO-4 as a function of burnup. The calculations were performed at hot full power with a pin-cell model and 25%UO_2 – 75%ThO_2 fuel.

The power distribution in the core was controlled by using gadolinia rods, in order to meet the peak power limit. The gadolinia rods were placed in the fresh fuel assemblies. The total number in the core was 336 for the uranium core with a 15-month cycle and 880 for the uranium core with a 24-month cycle. For the thorium-uranium fueled cores, the number of gadolinia rods were decreased to 160 in the thorium-uranium core with 75w/o of ThO_2 and 208 in the thorium-uranium core with 70 or 65w/o of ThO_2.

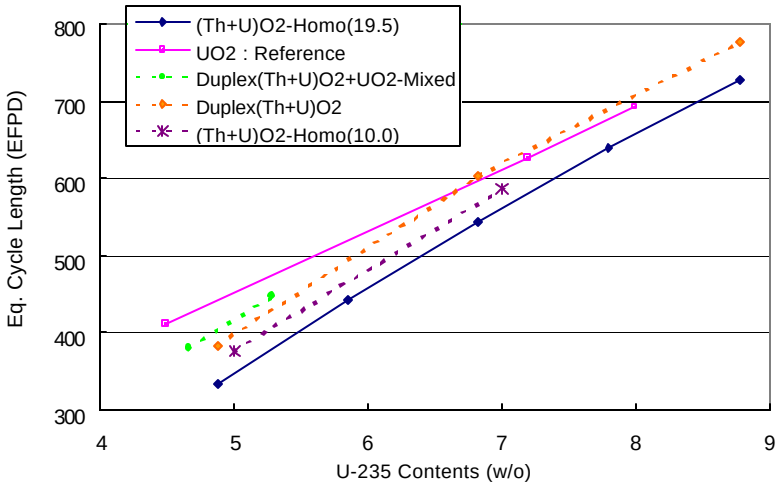

Figure 118. Equilibrium cycle lengths as a function of initial U-235 content of various thorium- uranium cores and the reference uranium cores.

The cycle lengths of each core are plotted in Figure 118 versus the initial content of U-235 in the fresh fuel. (Figure 118 also contains the results of some alternative designs discussed in the next section below.) As shown in Figure 118, the cycle lengths of the homogeneous thorium-uranium fuel cores are shorter than that of the reference uranium cores (at any given initial U-235 enrichment level). However, the differences

between the cycle lengths of the thorium-uranium cores and the reference uranium core become smaller as the cycle length becomes longer.

The core reactivity parameters including the Doppler temperature coefficients, moderator temperature coefficients, soluble boron worths, and control rod worths of the cores fully loaded with homogeneous $(Th,U)O_2$ fuel have been analyzed and compared with those of the reference UO_2 cores. These results are shown in Figures 119 through 121, and Table 56. The Doppler temperature coefficients of the cores with thorium-based fuel are more negative than that of the reference UO_2 cores as shown in Figure 119. Except the Doppler temperature coefficient, there are no significant systematic differences in the other physics parameters between the various thorium-based fueled cores and the reference UO_2 cores.

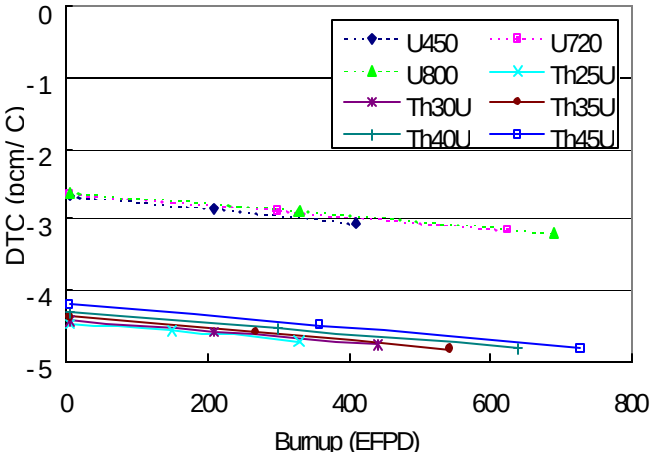

Figure 119. Doppler temperature coefficients of various homogeneous thorium-uranium cores and the reference uranium cores.

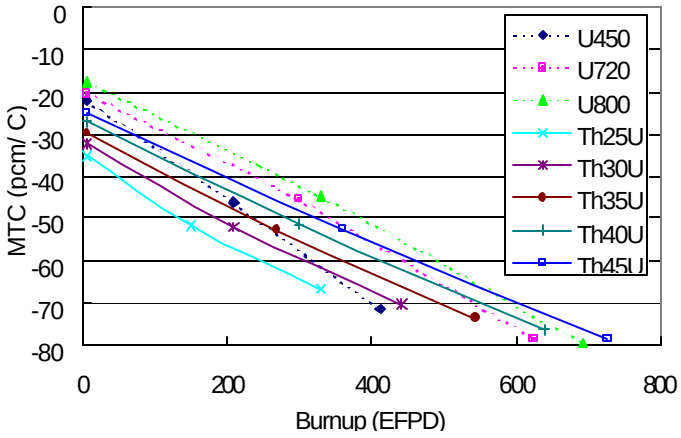

Figure 120. Moderator temperature coefficients of various homogeneous thorium-uranium cores and the reference uranium cores.

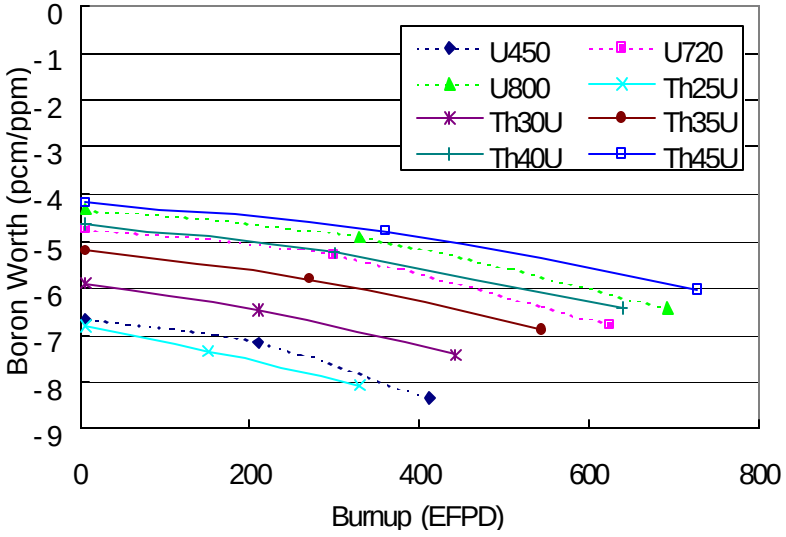

Figure 121. Soluble boron worth of various homogeneous thorium-uranium cores and the reference uranium cores.

Table 56. Control Rod Worth of Homogeneous Thorium-Uranium Cores and Uranium Cores, at End of Cycle, HFP condition.

Control Rod Configurations	UO_2 Core			ThO_2+UO_2 Core				
	U-235 Enrichment (w/o)			UO_2 Weight fraction (%) (U-235 Enrichment = 19.5w/o)				
	4.5	7.2	8.0	25	30	35	40	45
D	1.39	1.24	1.21	1.36	1.32	1.28	1.25	1.22
D+C	2.96	2.68	2.63	2.89	2.79	2.71	2.64	2.57
D+C+B	4.59	4.15	4.05	4.55	4.36	4.20	4.07	3.94
D+C+B+A	5.56	5.11	4.99	5.40	5.24	5.09	4.96	4.84
D+C+B+A+S	9.41	8.48	8.25	9.52	9.01	8.60	8.25	7.94

5.1.4. Alternatives To Homogeneous (Th,U)O_2 Fuel to Enhance the Fuel Economy

A 19.5w/o U-235 enrichment of the uranium in the (Th,U)O_2 fuel decreases the SWU utilization, and is very costly. However, mixed cores with both (Th,U)O_2 and UO_2 fuel assemblies with various reload batch schemes have better economics [Joo et al. 2001]. Also, some of the duplex (Th,U)O_2 fuel designs proposed by MIT resulted in increased discharge burnup in the range of 7 to 16%, compared with the homogenized (Th,U)O_2 fuel.

Therefore, in order to enhance the economic potential of the thorium cycle in PWRs three alternative thorium-based fuel cores were investigated: the duplex (Th,U)O_2 fuel, the mixed core of duplex (Th,U)O_2 and UO_2 fuels, and homogeneous (Th,U)O_2 fuel with a rather lower U-235 enrichment of 10w/o.

The duplex fuel pellet consists of UO_2 in the inner region and ThO_2 in the peripheral region. The infinite neutron multiplication factors for the duplex fuel with burnup are 7 to 16% higher compared to that of the homogeneous (Th,U)O_2 fuel. However, since the fissile isotopes at the beginning of irradiation exist only in the inner UO_2 region, a higher power must be produced in the small volume UO_2 region to maintain the total power. The volumetric power in the UO_2 region of the duplex pellet is about three to four times higher than that of conventional UO_2 fuel, which causes fuel melting in the UO_2 region. Therefore, a lower U-235 enrichment of 10w/o, instead of 19.5w/o, was applied to the UO_2 region, the rest of the U-235 inventory was mixed with the ThO_2 in outer region. This modified duplex pellet, 10w/o enriched UO_2 in the inner region and (Th,U)O_2 in the peripheral region, provides a lower k-infinite value than the original duplex fuel, but provides higher k-infinite values than the homogeneous (Th,U)O_2.

The mixed core of homogeneous (Th,U)O_2 fuel assemblies with UO_2 fuel assemblies with various reload batch schemes showed an enhanced economic potential for (Th,U)O_2 fuel [Joo et al. 2001]. To further enhance the economic potential of the (Th,U)O_2 fuel, a mixed core of duplex (Th,U)O_2 fuel assemblies with UO_2 fuel assemblies has been also tested.

The cycle lengths of each core were plotted versus the initial U-235 content in Figure 118. As shown in Figure 118, the cycle lengths of the three alternative thorium cores with duplex fuel or mixed ThO_2-UO_2 fuel and UO_2 only fuel assemblies are longer than the cycle lengths of the homogenous ThO_2-UO_2 cores. And, the differences between the cycle lengths of the thorium cores and uranium cores are getting smaller as the cycle length becomes longer. It should also be noted that the number of fresh fuel assemblies that need to be loaded into the mixed cores is 48, which saves four fuel assemblies compared to the cores fully loaded with thorium-uranium fuel or in the reference uranium cores loaded with 52 fresh fuel assemblies. Taking the number of fresh fuel assemblies loaded into the core into account, the mixed core concept further improves the economic potential of the thorium fuel cycle.

In order to assess the economic potential of the homogeneous thorium-uranium fuel and the alternative thorium fuel cycles, the natural uranium utilization and the separative work unit (SWU) utilization were considered. The weight fraction of U-235 in the tails was assumed to be 0.25w/o. The cost of uranium ore and the SWU costs were assumed to be 50US$ /KgU and 110US$ /SWU-Kg, respectively. The results of the fuel economics assessment as a function of cycle length are shown in Figure 122. Compared to the homogeneous (Th,U)O_2 fuel, the uranium ore and SWU costs per MWD of the alternative thorium cores are improved. The fuel costs of the thorium-based fuel cycles are decreased as the cycle lengths become longer, while that of uranium fuel cycle increases with cycle burnup.

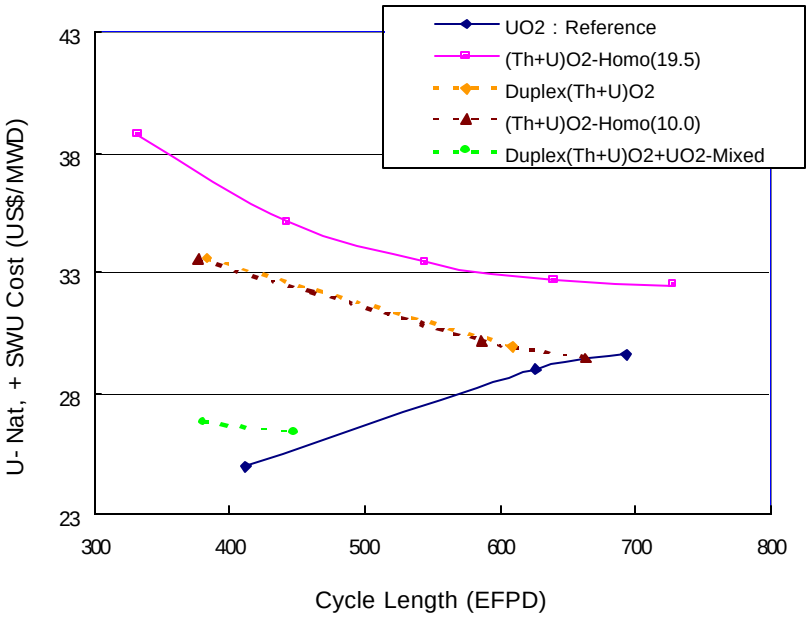

Figure 122. Uranium ore purchase and SWU costs of homogeneous thorium-uranium cores, uranium cores, and alternative thorium cores versus cycle length (110US$/Kg-SWU).

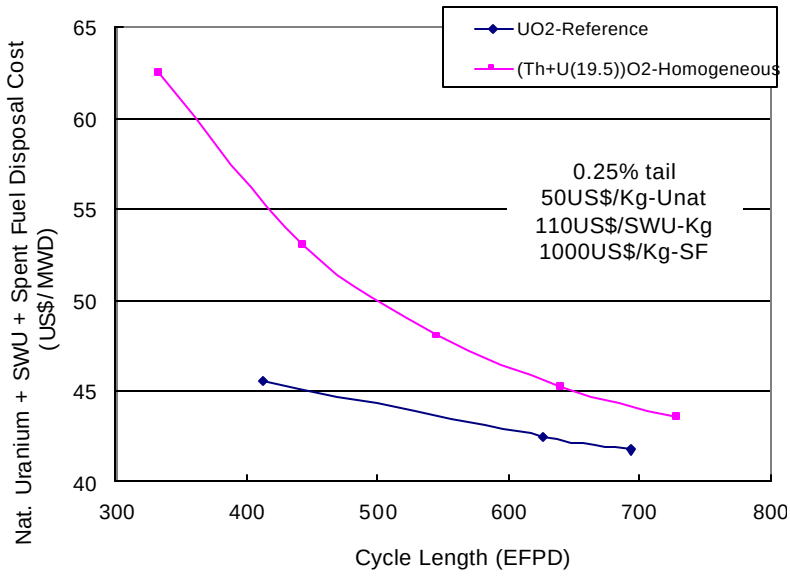

Figure 123. Uranium ore purchase, SWU, and spent fuel disposal costs of homogeneous thorium-uranium cores and uranium cores as a function of cycle length (1000US$/Kg-SF).

In Figure 123, the costs for spent fuel disposal were

additionally included in the economics assessment for the homogeneous thoria-urania case. As seen in Figures 122 and 123, some of the thorium based fuel options with longer cycles may show a superior economic potential to the UO_2 fuel.

5.1.5. Utilization of Homogeneous $(Th,U)O_2$ Fuel in a Small/Medium Sized Reactor

The utilization of homogeneous $(Th,U)O_2$ fuel in a 330 MWth LWR was also investigated. A small/medium sized uranium core loaded with 5% enriched UO_2 was considered as the reference core for comparison. The equilibrium cycle length of the reference UO_2 core was about 3 years, while the (60w/o Th, 40% U)O_2 core has about a 5-year equilibrium cycle length. The results of the $(Th,U)O_2$ fuel economic assessment for the small/medium sized core is compared to the UO_2 case in Figure 124 for three different disposal costs: 0, 500 US$/kg, and 1,000 US$/kg. The homogeneous $(Th,U)O_2$ fuel has better economics than the UO_2 fuel when the spent fuel disposal costs are higher than 700 US$/kg,.

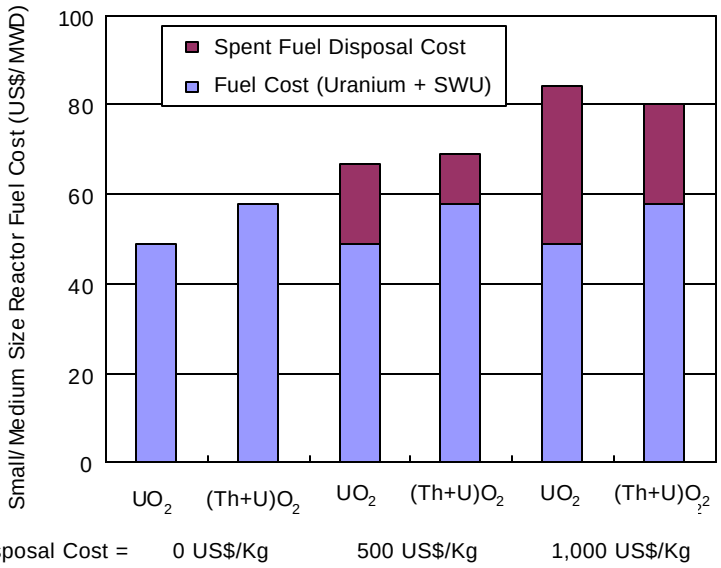

Figure 124. Uranium ore purchase, SWU, and spent fuel disposal costs of homogeneous $(Th,O)_2$ fuel and uo_2 fuel for small/medium sized core.

Task 5.2. $(Th,U)O_2$ Pellet Manufacturing

(Kun Woo Song, Ki Won Kang, Jae Ho Yang, KAERI)

5.2.1. Experimental Procedures

Thorium oxide (ThO_2) powder (>99.9% pure) was purchased from Indian Rare Earth LTD. According to the supplier's information, this powder was produced through calcination of thorium oxalate at temperatures above 800°C. Two kinds of powder with an average size of 2μm and 10μm were provided. The properties of the as-received powders were characterized using BET surface, X-ray diffraction, and SEM techniques. The X-ray diffraction was performed using Cu Ka radiation with monochromator. The pellet experiments were performed with only the 10μm-powder.

Dry milling. Three kinds of pellets -ThO_2, ThO_2-35%UO_2, ThO_2-65%UO_2 - were fabricated by conventional powder processing using the as-received and then milled powder. At first, the as-received thorium oxide powder was milled in a mortar for 40 min. Then the ThO_2 powder was mixed with the UO_2 powder ex-ADU in a tumbling mixer for 1 hour in order to form the various ThO_2-UO_2 powder mixtures. Each of the thoria-urania powder mixtures was then further milled 6 times using an attrition mill, which was designed to allow the powder charge to be removed from the mill and then loaded again. The attrition mill has a grid-shaped hole in the bottom of the vessel, so the milled powder passes continuously through the hole and then is stored in a bottle. The powder in the bottle is then pored into the attrition mill feeder hopper for another cycle of milling. The powder was milled by zirconia balls driven by an impeller rotating with a speed of 150 rpm. The structure of the attrition mill was previously reported in the 8th progress report.

Wet milling. In addition to the above dry milling, the ThO_2 powder was mixed with the UO_2 powder ex-ADU in a tumbling mixer for 1 hour to form the powder mixtures (as for dry milling). And then the powder mixtures were ball-milled for 24h in a jar containing zirconia balls and alcohol. Pure ThO_2 powder was also ball-milled in the same way.

Compaction, sintering, and thermal etching. The prepared powders were pressed at 2, 3 and 4 ton/cm^2 into compacts (green pellets). The compacts were heated up to 1700°C at 5°C/min and then held for 4 hours in H_2 atmosphere to sinter them. The density of the sintered pellets was determined by the water immersion method, and the theoretical density of the $(Th,U)O_2$ pellets was determined by combining the theoretical density of the ThO_2 and UO_2 in accordance with each mole fraction. The sintered pellets were sectioned longitudinally and polished. In order to observe the grain boundaries, thermal etching was carried out at 1600°C for 4 hours in a H_2 atmosphere, and the grain size was determined by the linear intercept method. X-ray diffraction was used to determine whether or not a ThO_2-UO_2 solid solution had been formed in the $(Th,U)O_2$ pellets.

5.2.2. Results

5.2.2.1. Characteristics of As-Received ThO_2 Powders

Figures 125(a) and (b) show SEM micrographs of the as-received 2μm ThO_2 and 10μm ThO_2 powders, respectively.

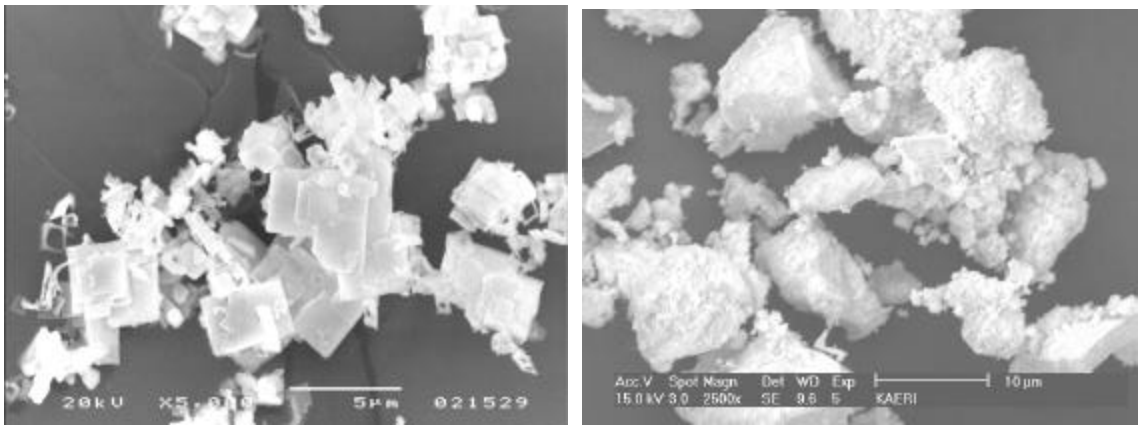

(a) 2㎛-powder **(b) 10㎛-powder**

Figure 125. SEM photographs of as-received ThO_2 powders.

The SEM photograph of the 2μm-powder shows that the powder appears to be significantly agglomerated and the particle has a plate-like shape. The particle surfaces seem to be smooth. But the photograph of the 10μm-powder shows that the particles are irregular in shape and the particle surfaces seem to be rough or porous. We found that the 2μm ThO_2 and 10μm ThO_2 had BET surface areas of 6.0m^2/g and 41.16m^2/g, respectively. In spite of its larger size, the 10μm ThO_2 had much higher surface area than the 2μm ThO_2. This might result from the difference in surface morphology between the two powders - smooth surfaces on the 2μm ThO_2 power and porous surfaces on the 10μm ThO_2 power.

Figures 126(a) and (b) show the XRD patterns of the as-received 2μm ThO_2 and 10μm ThO_2 powders, respectively. The full width at half maximum of the XRD peak for the 10μm powder is wider than the full width at half maximum for the 2μm powder. This means that the crystal size of the 10 μm powder is finer than that of the 2μm powder.

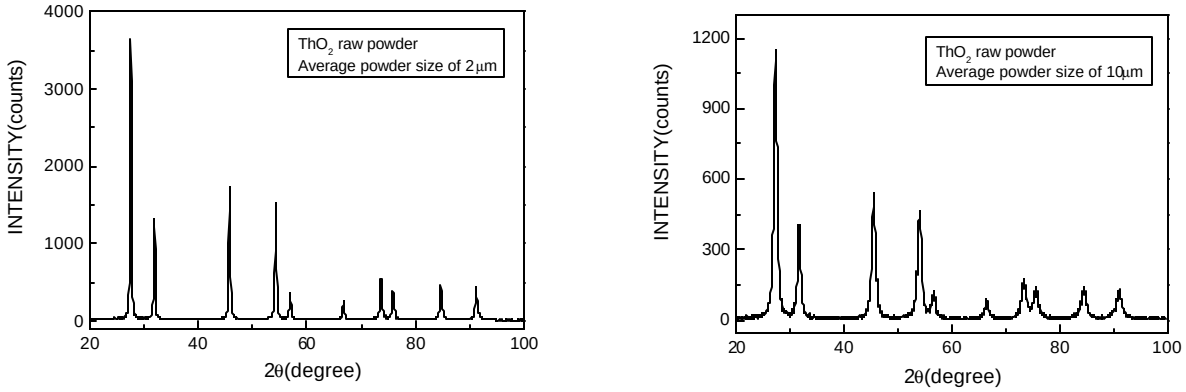

(a) 2μm-powder **(b) 10μm-powder**

Figure 126. X-ray diffraction patterns of as-received ThO_2 powders.

5.2.2.2. Pellets Fabricated By Dry Milling

Figure 127 shows the green density of the as-received ThO_2 and milled ThO_2 and UO_2-ThO_2 powders for a variety of compacting pressures. The green density increases with the compacting pressure. Milling can significantly improve the green density of the ThO_2 powder.

Figure 128 shows the sintered density of the as-received ThO_2, milled ThO_2 and $(U,Th)O_2$ pellets for a variety of compacting pressures. All the pellets have higher densities as the compacting pressure increases. A sintered density of 85-88%TD is obtained for the as-received ThO_2 powder. It is known that the sintered density of pure ThO_2 powder depends greatly on the calcination temperature [Harada et al. 1974], and this range of density agrees well with other reported values for

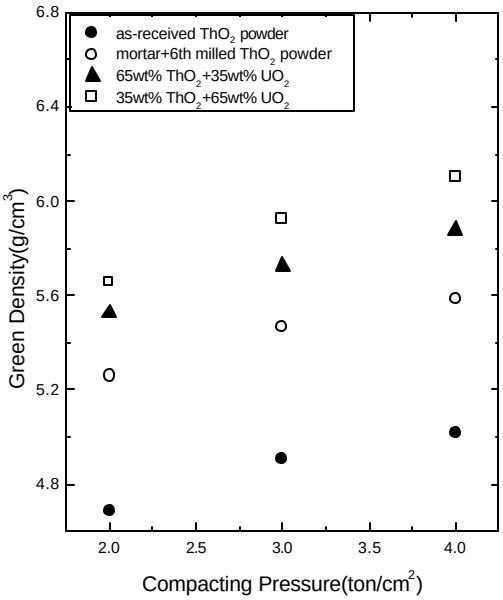

Figure 127. Green density as a function of compacting pressure.

powders calcined above 800°C [Pope and Radford 1974]. The sintered density of the milled ThO_2 pellets is 92-95%TD depending on the compacting pressure, and this density is higher by about 10% than the density of the pellets made with the as-received powder. This means that the combined milling - mortar and attrition- is effective in increasing the sintering activity of the ThO_2 powder. The density of the $(U,Th)O_2$ pellets ranges from 91% to 94%TD, which is slightly lower than that of the ThO_2 pellets made with milled powder.

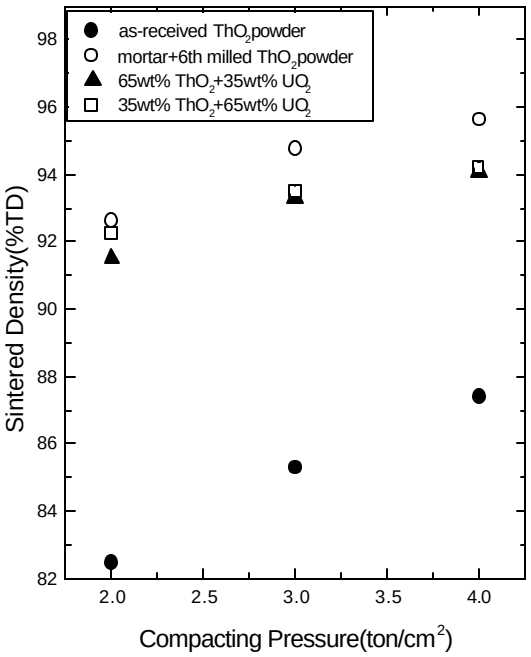

Figure 128. Sintered density as a function of compacting pressure.

Figure 129 shows the XRD patterns for the pure UO_2, ThO_2, and $(U,Th)O_2$ pellets, at normal angles (left) and high 2? angles (right). Figure 129(b) shows that the ThO_2 has a larger lattice constant than the UO_2, and that the peaks shift toward the high angles as the content of the UO_2 increases. The $65wt\%ThO_2$-$35wt\%UO_2$ and $35wt\%ThO_2$-$65wt\%UO_2$ pellets show single peaks similar to the UO_2 or ThO_2 pellets, indicating that solid solutions were formed. But it is supposed that the solid solution is not yet fully formed since the full width at half maximum of the thoria-urania peaks is wider than that of the pure UO_2 or ThO_2 pellets.

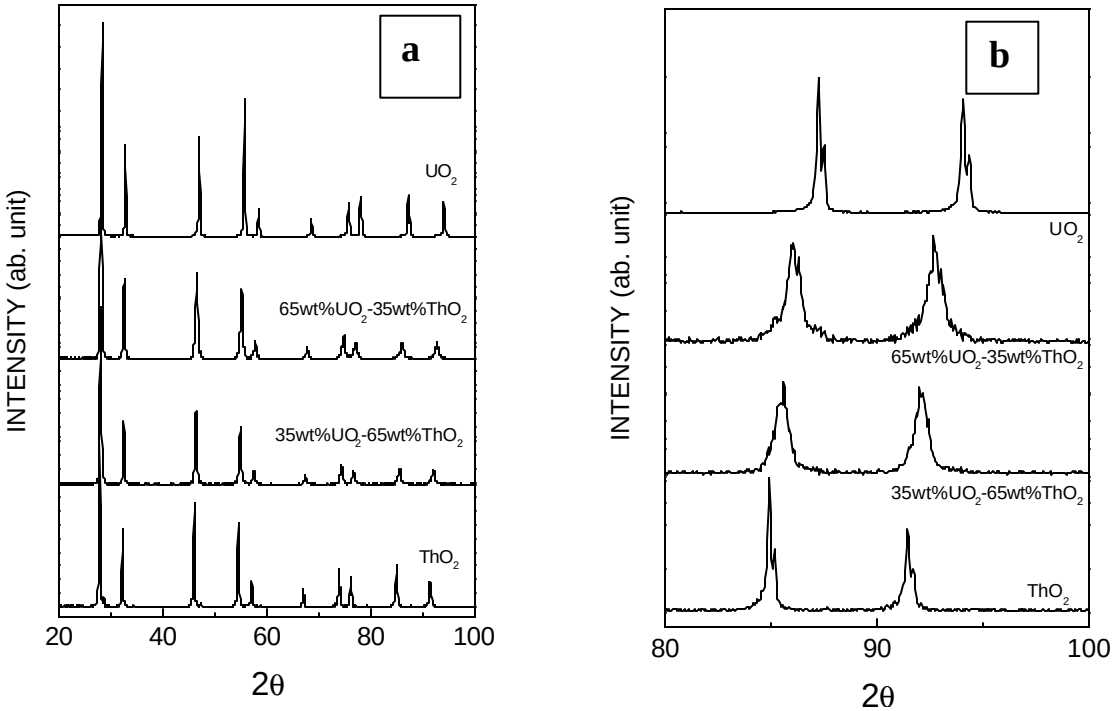

Figure 129. X-ray diffraction patterns for pure UO_2, ThO_2 and $(U,Th)O_2$ pellets, normal 2q angles left, high 2q angles right.

Figures 130(a), (b) and (c) show the pore structures of the ThO_2, 65wt%ThO_2-35wt%UO_2 and 35wt%ThO_2-65wt%UO_2 pellets, respectively. The grain structures of the same pellets are shown in Figures 131(a), (b) and (c), respectively. Some round areas that were different in color from the surrounding matrix were observed in Figure 130(b) and 130(c), suggesting that a complete solid solution was not formed. The above-mentioned X-ray diffraction pattern also indicated that a solid solution of (Th,U)O_2 was not completely formed. The grain size for the ThO_2 fuel pellets is 8.6μm and 5.5μm for the 65wt%ThO_2-35wt%UO_2 fuel pellets and 5.3μm for the 35wt%ThO_2-65wt%UO_2 fuel pellets.

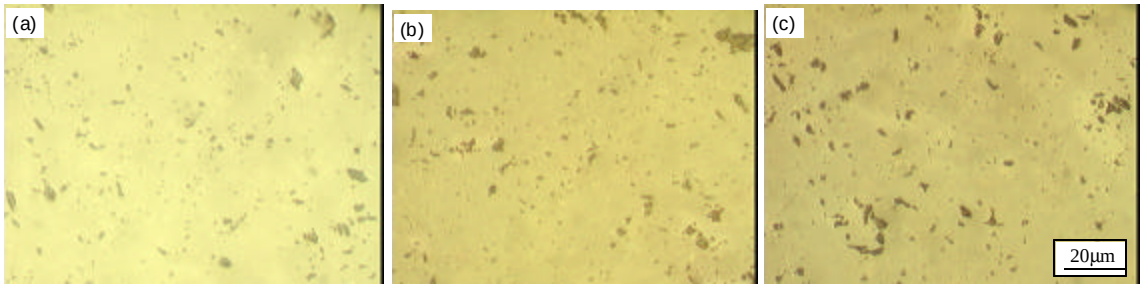

(a) 100% ThO_2 **(b) 35wt%UO_2+65wt%ThO_2** **(c) 65wt%UO_2+35wt%ThO_2**

Figure 130. Pore structure of pellets fabricated with dry milled powder.

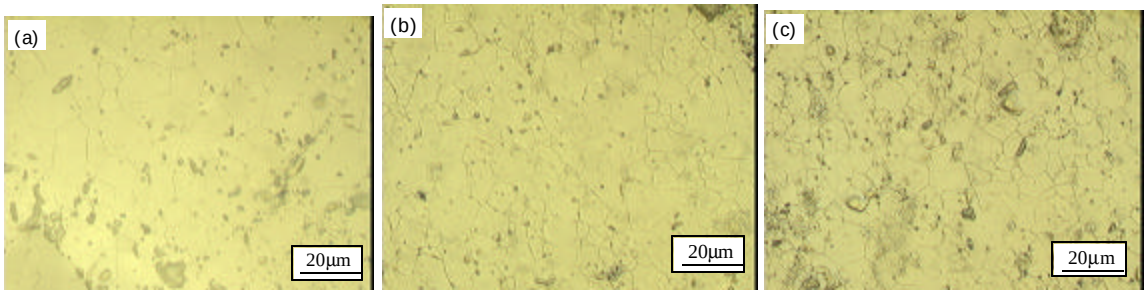

(a) 100% ThO_2 **(b) 35wt%UO_2+65wt%ThO_2** **(c) 65wt%UO_2+35wt%ThO_2**

Figure 131. Grain structure of pellets fabricated with dry milled powder.

5.2.2.3. Pellets Fabricated By Wet Milling

Figure 132 shows the green densities of the wet milled ThO_2 and UO_2-ThO_2 powders for a variety of compacting pressures. The green density increases with the compacting pressure. It is found that the wet-milled powders tend to have a lower green density than the dry-milled powders.

Figure 133 shows the sintered densities of the milled ThO_2 and (Th,U)O_2 pellets for a variety of compacting pressures. All the pellets have a higher density than 95%TD. The highest sintered density of the pellets for every composition is achieved at a compacting pressure of 3 ton/cm^2.

Figure 134(a) shows the XRD patterns for the ThO_2 and (Th,U)O_2 pellets, and Figure 134(b) shows the same results at high 2? angles. Figure 134(b) shows that the ThO_2 has a larger lattice constant than the UO_2, and that the peaks shift toward high angles as the content of UO_2 increases. The 65wt%ThO_2-35wt%UO_2 and 35wt%ThO_2-65wt%UO_2 pellets show single peaks

with widths that are similar to those of the UO_2 or ThO_2 pellets, indicating that solid solutions were almost completely formed. The full width at half maximum of the peaks is narrower than that of the dry milled pellets, so it is supposed that the $(Th,U)O_2$ solid solution is more homogeneous in the wet-milled powder pellets than in the dry-milled powder pellets.

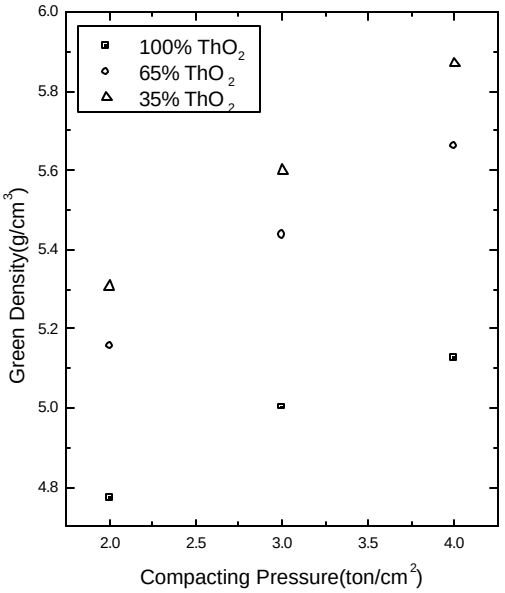

Figure 132. Green density as a function of compacting pressure.

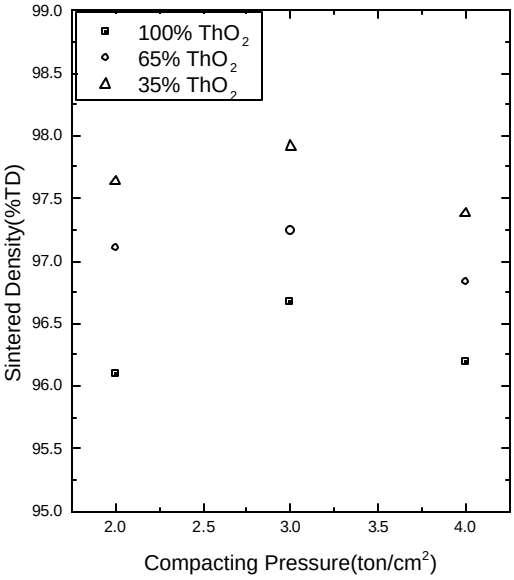

Figure 133. Sintered density as a function of compacting pressure.

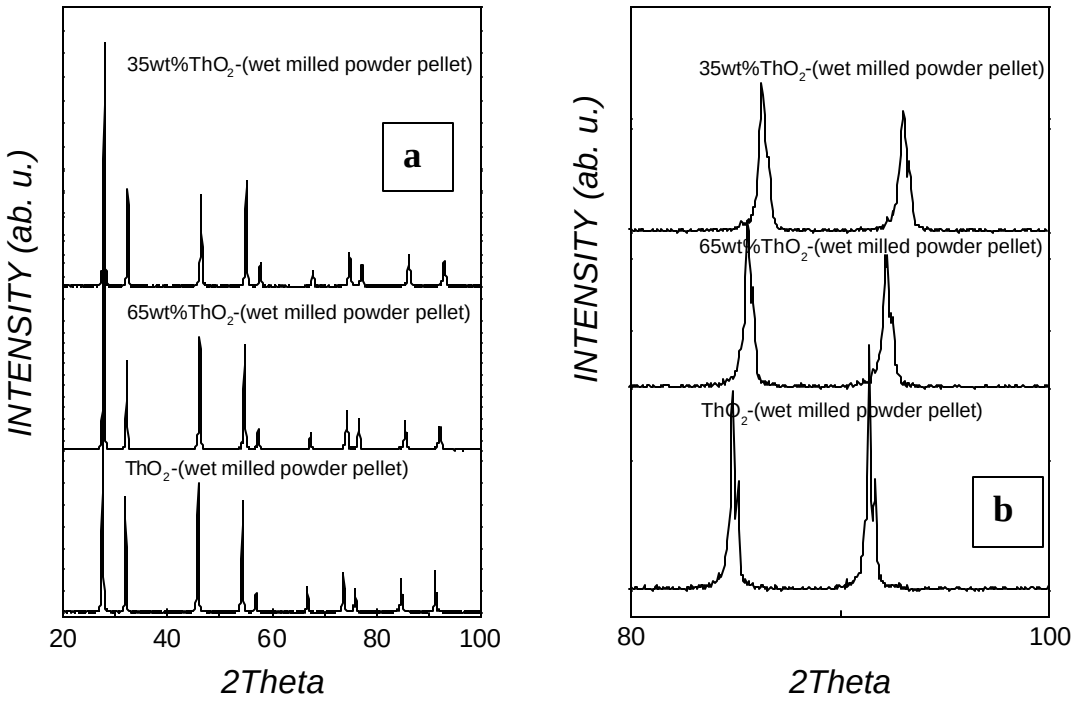

Figure 134. X-ray diffraction patterns for ThO_2 and $(Th, U)O_2$ pellets with wet milled powder, normal 2q angles left, high 2q angles right.

Figures 135(a), (b) and (c) show the pore structures of the ThO_2, 65wt%ThO_2-35wt%UO_2 and 35wt%ThO_2-65wt%UO_2 pellets fabricated with wet milled powder, respectively. The grain structures of the same pellets are shown in Figures 136(a), (b) and (c), respectively. The ThO_2 fuel pellet grain size was 11.2μm, the 65wt%ThO_2-35wt%UO_2 fuel pellet grain size was 9.2μm, and the 35wt%ThO_2-65wt%UO_2 fuel pellet grain size was 7.5μm. It appears that (Th,U)O_2 pellets with densities greater than 95%TD and good homogeneity can be obtained by the wet milling process.

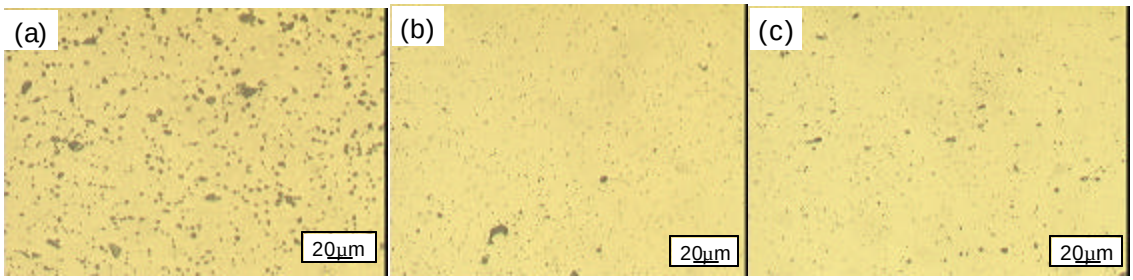

(a) 100% ThO_2 **(b) 65wt% ThO_2** **(c) 35wt% ThO_2**

Figure 135. Pore structure of pellets fabricated with wet milled powder.

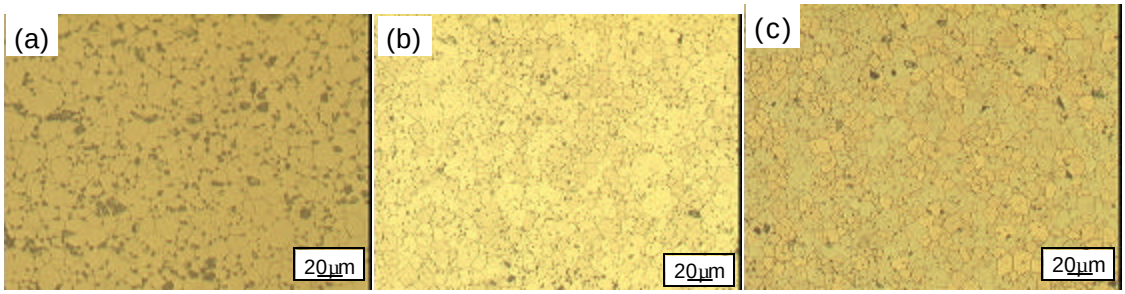

(a) 100% ThO_2 **(b) 65wt% ThO_2** **(c) 35wt% ThO_2**

Figure 136. Grain structure of pellets fabricated with wet milled powder.

Figures 137(a) and (b) show the results of area mapping (uranium scanning) of the 65wt%ThO_2-35wt%UO_2 and 35wt%ThO_2-65wt%UO_2 pellets. Figures 137(a) and (b) show that the uranium distribution in both these pellets was relatively homogeneous.

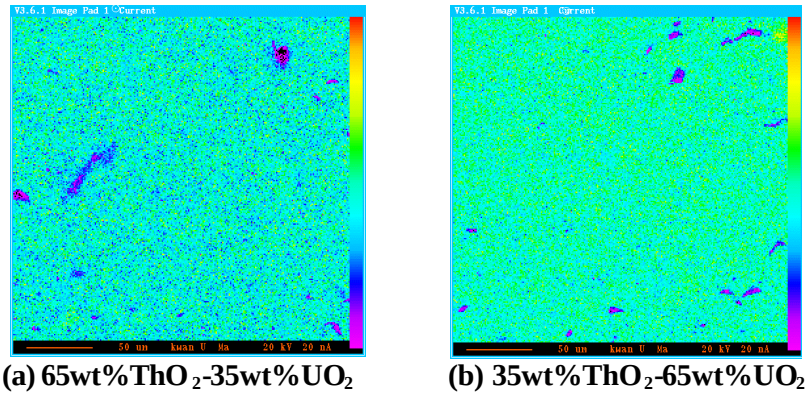

(a) 65wt%ThO_2-35wt%UO_2 **(b) 35wt%ThO_2-65wt%UO_2**

Figure 137. EPMA of the 65wt%ThO_2-35wt%UO_2 and 35wt%ThO_2-65wt%UO_2 pellets (uranium scanning).

5.2.3. Thermal Conductivity of $(Th,U)O_2$ Pellets

Samples for measuring the thermal properties were fabricated using the wet milled powder. From the measured thermal diffusivity, the thermal conductivity was calculated using the following relation:

$$k = aC_p r \tag{15}$$

where ?, α, ρ, C_p are the thermal conductivity, thermal diffusivity, the bulk density, and the specific heat capacity of the sample, respectively. The thermal diffusivity of the pellets was measured by the laser-flash method (Laser-flash 2000, Sinku Rico). The heat capacity was measured with a differential scanning calorimeter (DSC). Figure 138 is a schematic diagram of the thermal diffusivity experimental apparatus.

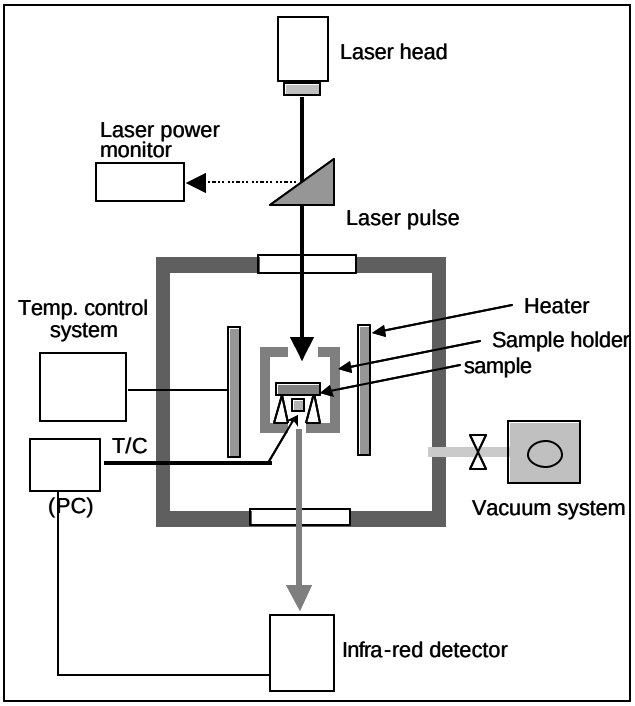

Figure 138. Schematic diagram of the experimental system for measuring thermal diffusivity.

The thermal diffusivity was determined from the rear-surface temperature rise to half its maximum value, after the front surface of a sample was heated by a laser beam.

$$a = \frac{w}{p^2}\frac{L^2}{t_{1/2}} \tag{16}$$

where, L is the sample thickness. The thermal conductivity was normalized to 95% of the theoretical density(TD) using modified Loeb equation[3]:

$$k = k_{TD}\left(1 - b\left(1 - \frac{r}{r_{TD}}\right)\right) \tag{17}$$

where, β is a constant.

Figure 139 shows the variation of the thermal conductivity as a function of temperature. The thermal conductivity decreases with UO_2 content. The measured thermal conductivity of the 100% ThO_2 is slightly higher than the other values [Bakker et al. 1997]. The thermal conductivities of the 65 and 35wt% ThO_2 mixtures are similar to that of the UO_2.

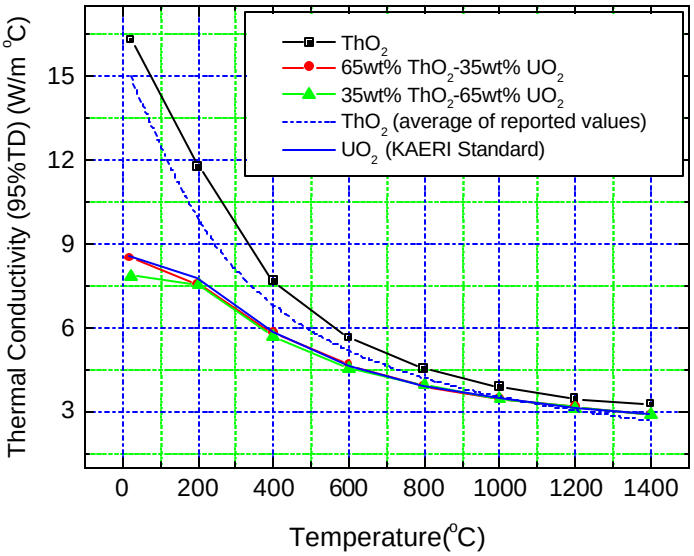

Figure 139. Plot of thermal conductivity as a function of temperature.

5.2.4. Conclusions

- Milling of the ThO_2-UO_2 powders and sintering at 1700°C can produce (Th,U)O_2 pellets with densities ranging from 93% to 98% TD.
- Compared to the dry milling method, wet milling of the ThO_2-UO_2 powders increases the density of the pellets and enhances the homogeneity of the uranium and thorium distribution.
- ThO_2 has a higher thermal conductivity than UO_2, but (Th,U)O_2 - 65 or 35wt% ThO_2 - is similar in thermal conductivity to UO_2.

Task 5.3. Fuel Rod Performance Analysis

(Chan Bock Lee, Yong Sik Yang, Young Min Kim, KAERI)

5.3.1. Evaluation of ThO_2-UO_2 fuel performance analysis code INFRA-Th

An irradiation test, called IFA-652.1, of ThO_2-UO_2 fuel was started in June 2000 in the Halden Reactor, located in Halden Norway as an international project. The purpose of the IFA-652.1 irradiation test is to study the basic characteristics of ThO_2-UO_2 fuel such as thermal conductivity, fission gas release, densification, and swelling. Thermo-couples and pressure transducers were used to instrument the IFA-652.1 test rods. The test rod fabrication data are summarized in Table 57. The burnup of the test rods reached about 5 MWD/kgHM in October 2000. The test will continue until 2005 and the discharge burnup will be about 45.6 MWD/kgHM.

Table 57. Fabrication data for the IFA-652.1 ThO_2-UO_2 test rods.

Pellet diameter (mm)	8.19	Clad material	Zr-2
Pellet length (mm)	10.2	Clad inside diameter (mm)	8.36
Pellet density (%TD)	82	Clad outside diameter (mm)	9.5
U-235 enrichment (wt%)	93	Clad thickness (mm)	0.57
ThO_2 contents (%)	88.3	Diametral gap (mm)	170
Dish depth (mm)	9.84e-3	Initial gas/pressure (atm)	He/10
Dish spherical radius (mm)	18.1	Thermocouple diameter (mm)	1.8

Since the burnup is low, the effects of the pellet densification and relocation upon the fuel gaps and temperatures are currently the key fuel behavior parameters of interest. Figures 140, 128 and 129 show the measured power level, fuel centerline temperature, and rod internal pressure in two of the IFA-652.1 ThO_2-UO_2 rods, called, Rods 4 and 5, respectively.

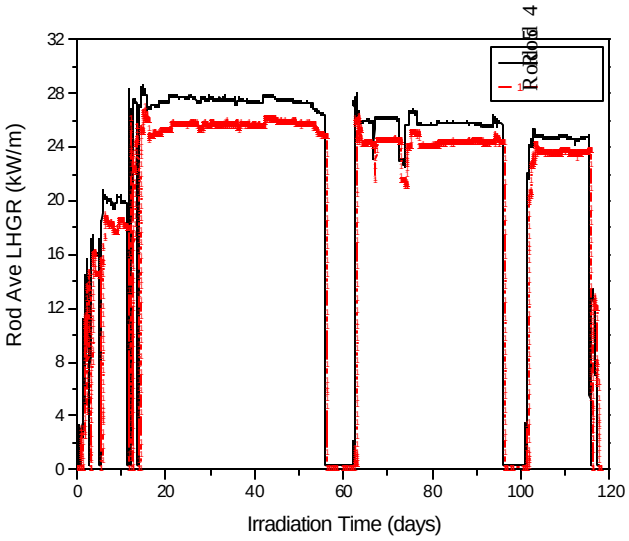

Figure 140. IFA-652.1 power histories.

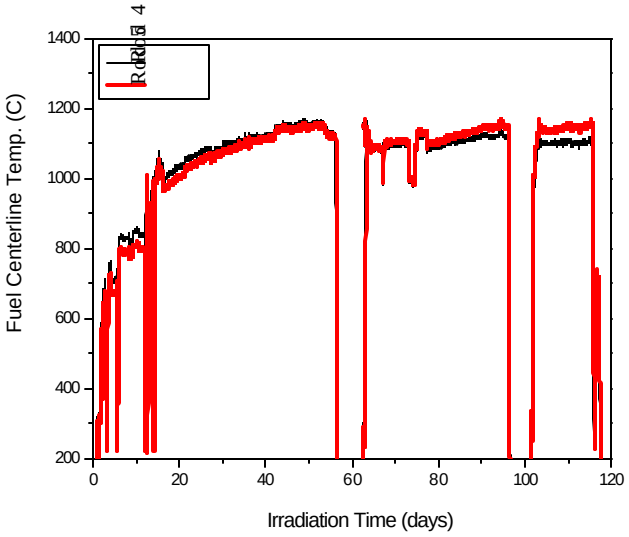

Figure 141. IFA-652.1 fuel centerline temperatures.

Rod 4 has a higher linear heat generation rate than Rod 5 by about 10%. However, after 60 days, Rod 5 apparently has a higher centerline temperature than Rod 4. Considering that there is no significant fission gas release at low burnup, this reversed temperature results seems to have resulted from fuel to cladding gap width differences due to more fuel densification in Rod 5. The bwer rod internal pressure in Rod 5 shown in Figure 128 also indicates higher densification.

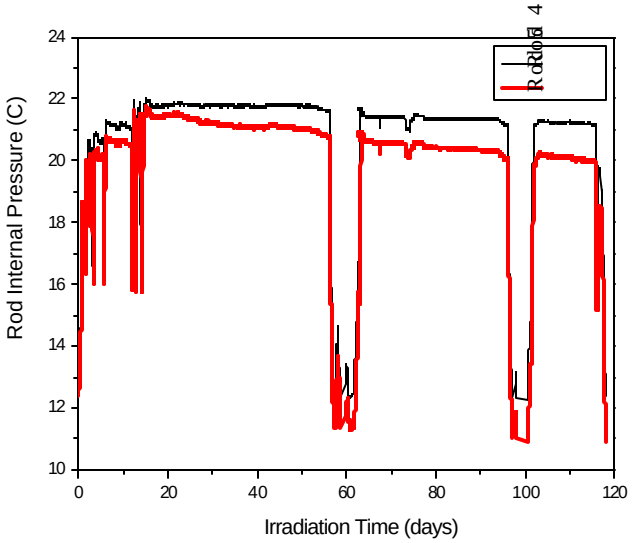

Figure 142. IFA-652.1 rod internal pressures.

Figures 143 and 144 compare the INFRA-Th predictions with the measured fuel centerline temperatures in Rods 4 and 5 during the power ramp at the initial start-up period. There is good agreement, between the INFRA-Th predictions and the measurements, indicating that the INFRA-Th code has the capability to predict the initial gap width as well as the thermal conductivity during the initial start-up period.

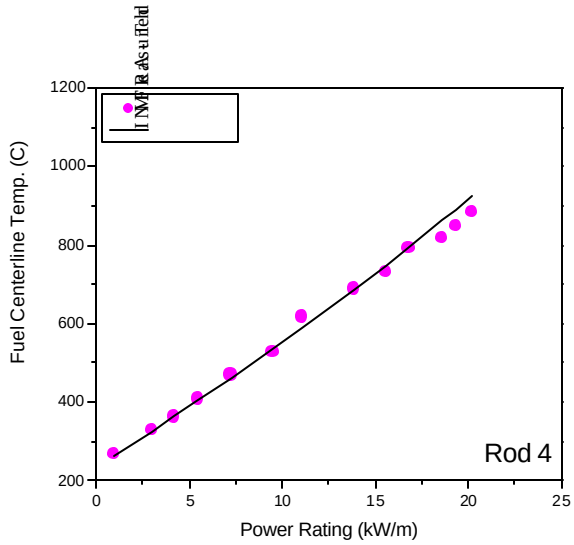

Figure 143. Fuel centerline temperature during start-up power ramp(Rod 4).

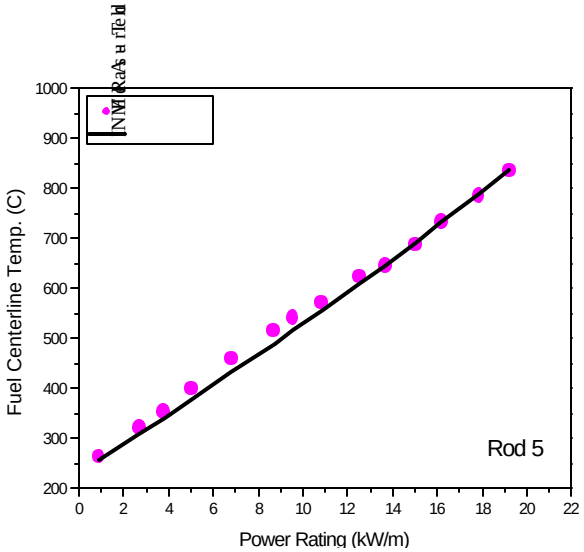

Figure 144. Fuel centerline temperature during start-up power ramp(Rod 5).

Figures 145 and 146 compare the INFRA-Th fuel centerline temperature predictions with the measured data during the power ramp at about 4.9 MWd/kgHM burnup. Even though INFRA-Th slightly under-estimates the Rod 5 fuel centerline temperatures, there is generally good agreement between the temperature predictions and the measurements. In the 11th Quarterly Report (MacDonald et al. 2002), it was reported that for Rod 5, a reduction of the fuel relocation by 60 % resulted in good agreement with the measured temperatures indicating less relocation of the ThO_2-UO_2 fuel than UO_2. However, after analysis of both Rods 4 and 5, it seems that there is not much difference in relocation behavior between the ThO_2-UO_2 and UO_2 fuel rods.

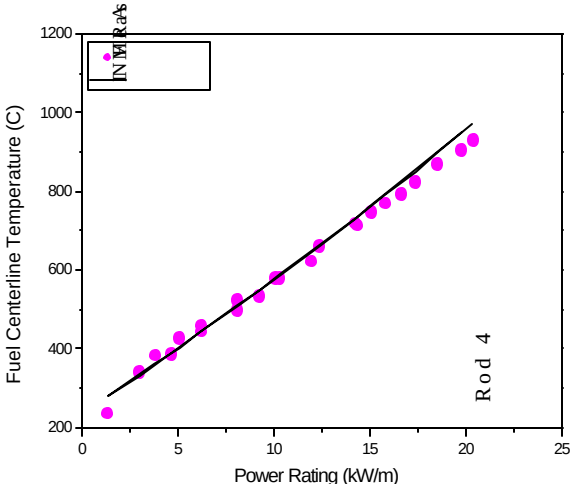

Figure 145. Fuel temperature during power ramp at 4.9 MWd/kgHM (Rod 4).

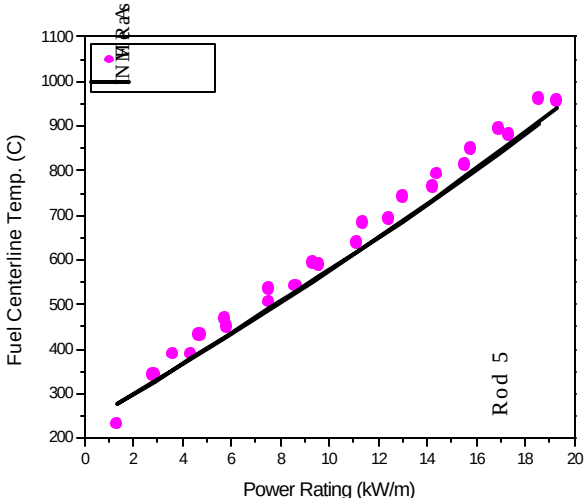

Figure 146. Fuel temperature during power ramp at 4.9 MWd/kgHM (Rod 5).

Figures 147 and 148 compare the rod internal pressure predictions with the measured data. The over-estimation of the rod internal pressure for Rod 5 indicates that there occurred more densification than expected in Rod 5, which is consistent with the under-estimation of the fuel centerline temperature for Rod 5 shown in Figure 146.

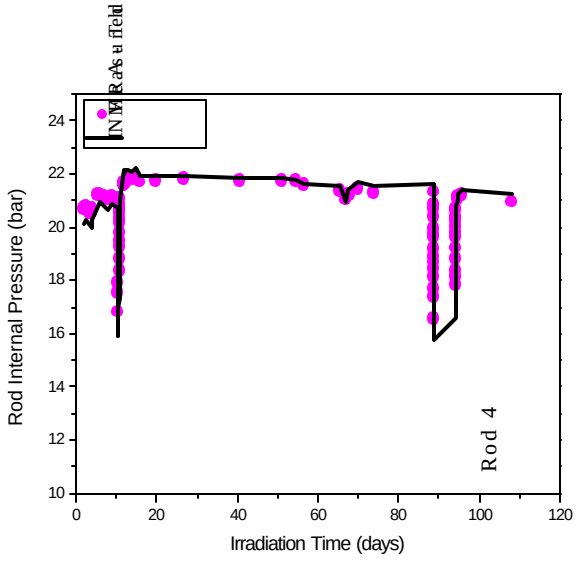

Figure 147. Rod internal pressure (Rod 4).

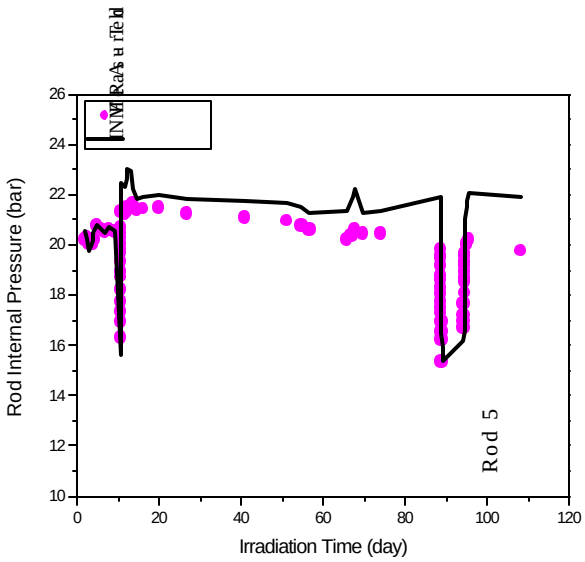

Figure 148. Rod internal pressure (Rod 5).

In the low burnup range up to 4.9 MWd/kgHM, the thermal conductance of the fuel gap is primarily affected by gap width, which depends upon such parameters as pellet densification, radial relocation, and thermal expansion. Since INFRA-Th uses the densification and relocation models based upon UO_2, it indicates that the densification and relocation behavior of the ThO_2-UO_2 fuel is similar to UO_2 fuel.

The agreement of the INFRA-Th predictions with the measured fuel centerline temperatures and rod internal pressures from Rods 4 and 5 in the Halden IFA-652.1 ThO_2-UO_2 experiment indicates that the models for the ThO_2-UO_2 fuel in the INFRA-Th code such as the thermal conductivity, thermal expansion, and radial power and burnup distributions are appropriate.

5.3.2. Analyses of Homogeneous ThO_2-UO_2 Fuel Rods

The performance of homogeneous ThO_2-UO_2 fuel rods during irradiation in both a 900 MWe PWR and the 330 MWth SMART reactor were analyzed.

Four different power histories were considered for the 900 MWe PWR case, as shown in Figure 149. The INFRA-Th fuel rod performance calculations are summarized in Table 58, indicating that the integrity of the ThO_2-UO_2 fuel rods would be maintained up to a burnup 100 MWD/kgHM.

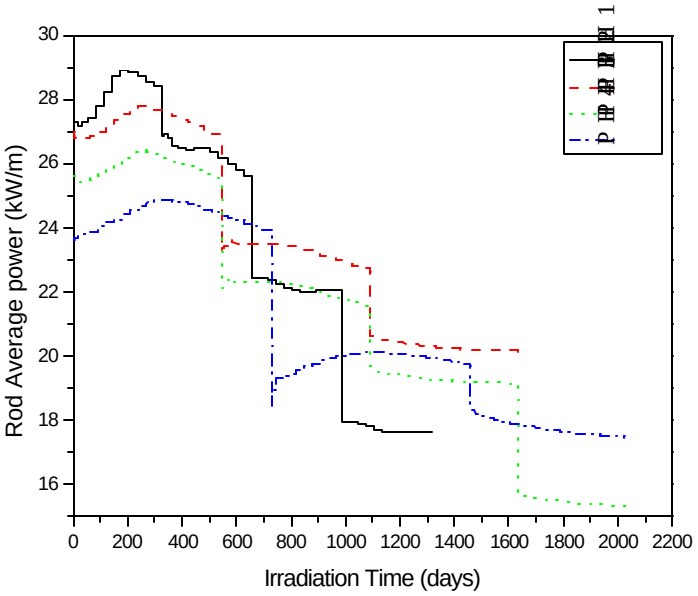

Figure 149. Rod average linear heat generation rate for PWR rods.

Figures 150 and 151 show the variations in the fuel centerline temperatures and fission gas release for the four power histories. The high power and high fuel centerline temperature fuel rods start to release significant fission gas at a relatively low burnup of around 30 MWD/kgHM. The fission gas release is enhanced as the burnup increases for all the cases. Therefore, to accommodate the released fission gases, annular pellets

were used for the high burnup fuel rods to satisfy the cladding non-lift off design limit. For the cladding materials, a Zr-Nb alloy cladding with a relatively high corrosion resistance was assumed.

Table 58. ThO_2-UO_2 PWR rod description and calculation results.

	PH1	PH2	PH3	PH4
Burnup (MWd/kgHM)	65	80	93	100
Fission gas release (%)	8.5	20.1	21.1	21.2
Rod internal pressure (MPa)	13	18.6	18.5	19.2
Oxide thickness (micron)	57.9	79.8	90.9	97.4

PH1 = ThO_2-25%UO_2, All solid pellets
PH2 = ThO_2-35%UO_2, Axial blanket (15 cm at both ends) of annular pellet (inner dia. of 3 mm)
PH3 = ThO_2-35%UO_2, Axial blanket (15 cm at both ends) of annular pellet (inner dia. of 3 mm)
PH4 = ThO_2-40%UO_2, All annular pellets (inner dia. of 3 mm)

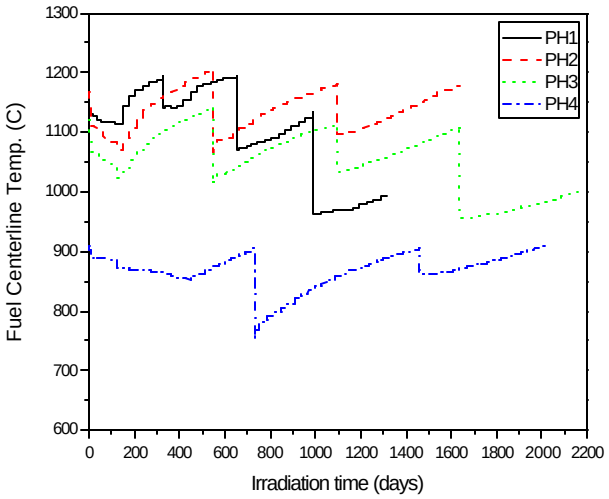

Figure 150. PWR fuel centerline temperature.

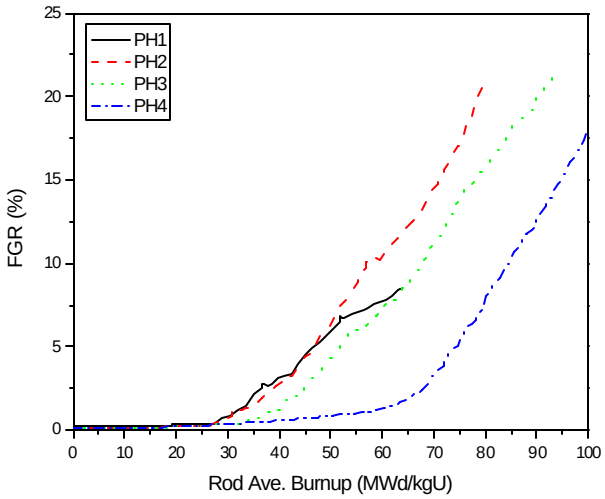

Figure 151. PWR fission gas release.

For the 330 MWth SMART reactor, ThO_2-UO_2 fuel with a 1680 effective-full-power-day refueling interval was analyzed. The fuel rod design parameters and INFRA-Th calculation results are summarized in Table 59, indicating that fuel rod integrity will be maintained.

Table 59. ThO_2-30 %UO_2 fuel rod design and calculation results.

Density (%TD)	Initial Pressure (bar)	Plenum Length (mm)	Plenum Volume (cc)
94.9	21.7	18.5	7.42
Burnup (MWd/kgHM)	**Fission Gas Release (%)**	**Rod Internal Pressure (MPa)**	**Oxide Thickness (micron)**
61	4.7	8.4	87.5

Figure 152 shows the power history of the limiting fuel rod with the highest burnup (61 MWd/kgHM). Figure 153 shows the peak fuel centerline temperature. Since SMART fuel rod has a relatively larger plenum volume than the PWR fuel rod, the cladding non-lift off criterion

(which depends upon the fission gas release and subsequent fuel rod internal pressure) is satisfied without using annular pellets.

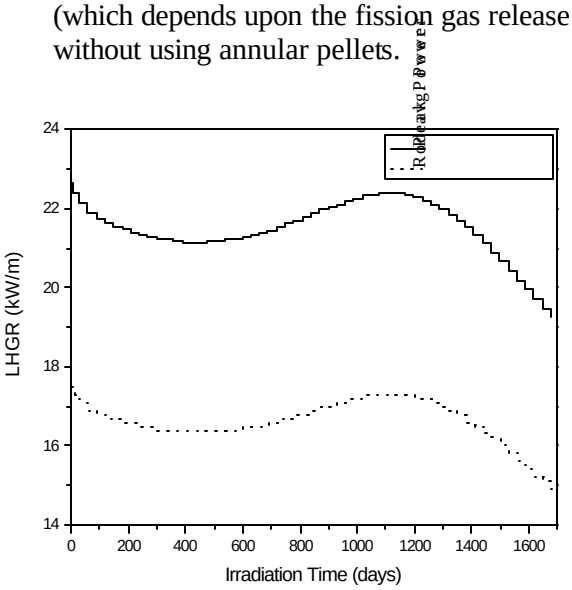

Figure 152. Power history.

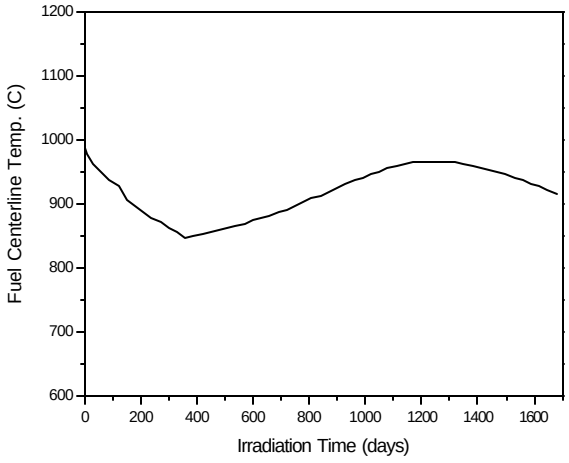

Figure 153. Peak fuel centerline temperature.

Task 5.4. Measurements of the Xenon Diffusivity in ThO_2/UO_2

(Kwang Heon Park, Hee Moon Kim, Kyunghee Univ.
Bong Goo Kim, Yong Sun Choo, Keon Sik Kim,
Kun Woo Song, Kwon Pyo Hong, Young Hwan Kang, KAERI)

Polycrystalline $(Th,U)O_2$ and UO_2 specimens were used to measure the diffusion coefficients of Xe-133 under various ambient gas oxygen potentials. The thoria-urania mixture was 35% ThO_2 and 65% UO_2. Three cubes were made, and each cube was about 2mm in each width. The diameter of an equivalent sphere, thereby simplifying the cubes, was obtained from the surface to volume ratios. The three cubes (300mg total) were irradiated in the HANARO reactor for 30 minutes. After cooling for 10 days, the annealing tests were performed. Figures 154 and 155 show the microstructure and the shape of the $(Th,U)O_2$ specimens, respectively. Table 60 lists the properties of the specimens.

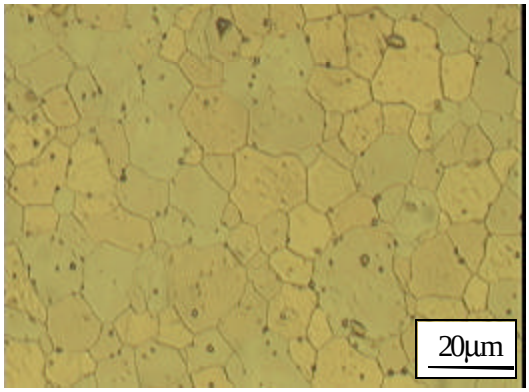

Figure 154. Microstructure of polycrystalline $(Th,U)O_2$.

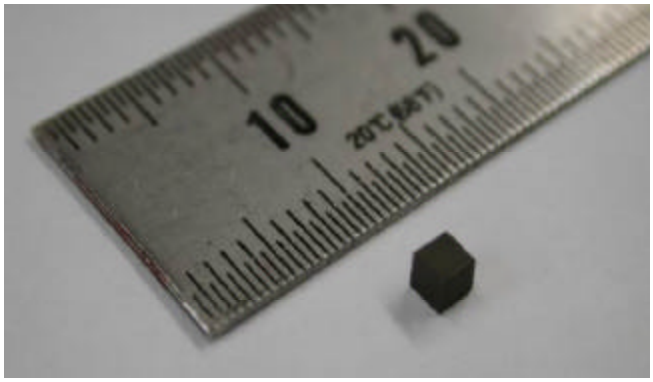

Figure 155. Cube of $(Th,U)O_2$.

Table 60. Properties of $(Th,U)O_2$ and UO_2.

Specimen	Type	Irradiation time (min.)	Grain size	TD
Polycrystalline $(Th,U)O_2$	Cube	30	7.5±1 μm	96.8% (10.62 g/cm^3)
Polycrystalline UO_2	Cube	20	8.1±1 μm	97% (10.642 g/cm^3)

Two annealing tests were performed, differing in the oxygen potential of the ambient gas, ΔG_{O2} = -370kJ/mol and -160 kJ/mol, respectively. The first annealing test was performed continuously at three different temperatures: 1600°C, 1500°C, and 1400°C for 10 hours at each temperature. Gamma scans were performed before and after the annealing tests to obtain the total released fractions of the Xe-133. The second annealing test was performed for 2 hours at 1400°C, for 3 hours at 1500°C, and for 3 hours at 1600°C, continuously. During the annealing test, a gamma detector was activated every 20 minutes to count the gamma rays from the Xe-133 in the trap system. Figures 156 and 157 show the square of the release fraction of Xe-133 with time. The diffusion coefficient was obtained by least square fitting of the slope of the f^2 versus time at each temperature. The diffusion coefficient and the slope are related as:

$$f^2 = \frac{36D}{\pi a^2} \times t \qquad (18)$$

where f is the release fraction at the current step (a fixed temperature) during the annealing test.

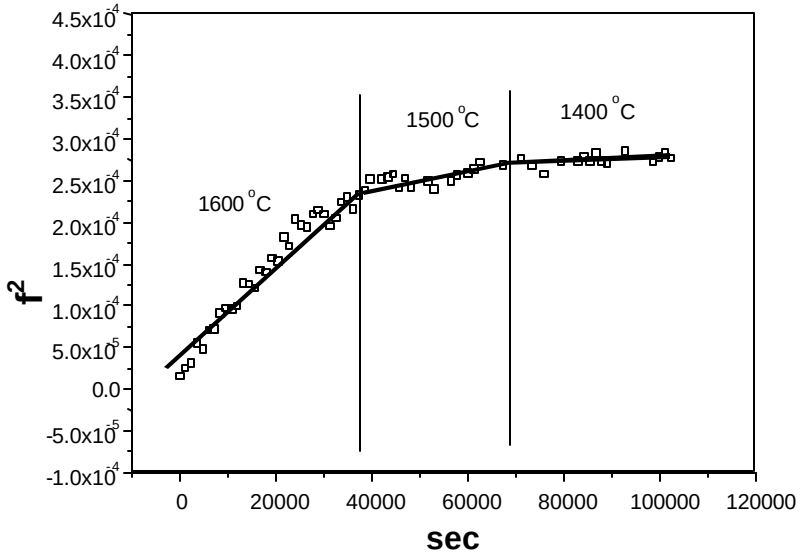

Figure 156. Plot of f^2 vs. time, ΔG_{O2} = -370 kJ/mol ($(Th,U)O_2$).

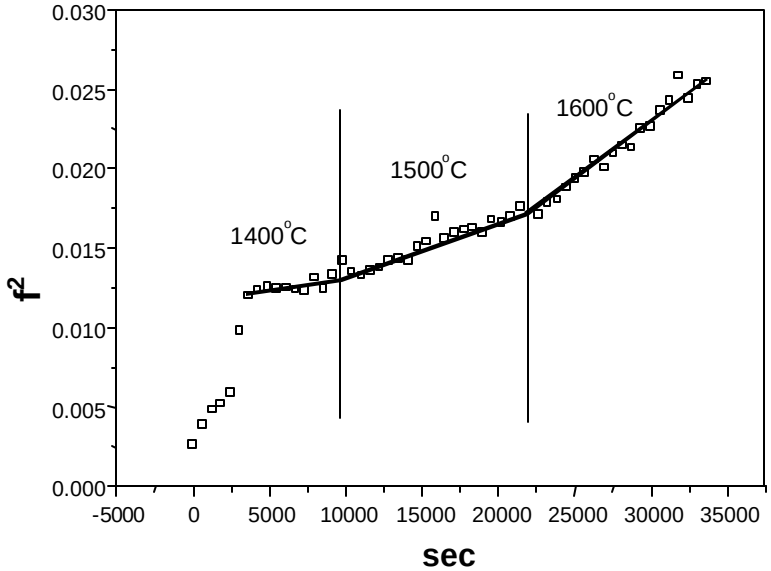

Figure 157. Plot of f^2 vs. time, ΔG_{O2} = -160 kJ/mol ($(Th,U)O_2$).

Polycrystalline UO_2 specimens were made in the same cubic shape and tested to provide data to compare with the polycrystalline

$(Th,U)O_2$ data. The UO_2 properties are also listed in Table 60. Figure 158 shows microstructure of the polycrystalline of UO_2. In addition, the diffusion coefficients of a single crystal of UO_2 were measured, which were reported in a previous Quarterly for this project.

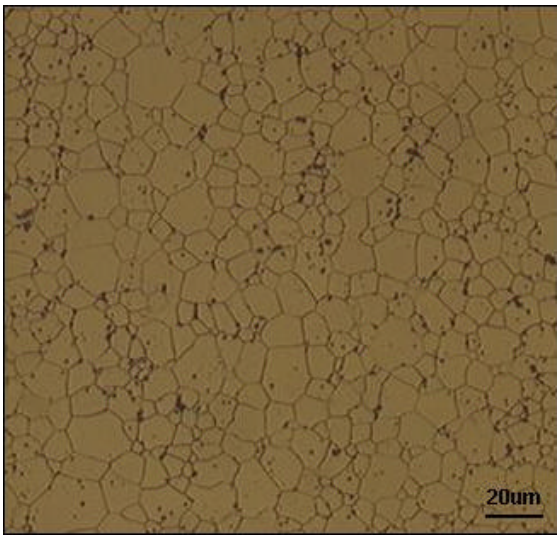

Figure 158. Microstructure of polycrystalline UO_2.

The annealing test for the polycrystalline UO_2 (with ΔG_{O2} = -370kJ/mol) was performed continuously for 8 hours at 1400°C, for 6 hours at 1500°C and for 9 hours at 1600°C. The diffusion coefficients for the polycrystalline $(Th,U)O_2$, polycrystalline UO_2, and single crystal of UO_2 are shown Table 61. The diffusion coefficients for the single crystal UO_2 were obtained with a –370 kJ/mol oxygen potential.

Table 61. Diffusion coefficients of $(Th,U)O_2$ and UO_2.

Specimens	Diffusion Coefficient (m^2/s)		
	1400°C	1500°C	1600°C
Poly -$(Th_{0.35},U_{0.65})O_2$ ΔG_{O2} = - 370 kJ/mol	$3.0X10^{-17}$ ±$1.5X10^{-17}$	$6.8X10^{-17}$ ±2 $X10^{-17}$	$5.5X10^{-16}$ ±$2.1X10^{-17}$
Poly -$(Th_{0.35},U_{0.65})O_2$ ΔG_{O2} = - 160 kJ/mol	$3.1X10^{-14}$ ±$8.0X10^{-15}$	$3.3X10^{-14}$ ±$3.5X10^{-15}$	$6.8X10^{-14}$ ±$3.1X10^{-15}$
Polycrystalline UO_2	$3.2X10^{-17}$	$1.1X10^{-16}$	$3.1X10^{-16}$
Single-crystal UO_2	$7.95X10^{-19}$	$2.35X10^{-18}$	$8.71X10^{-18}$

As shown in Figure 159, the diffusion coefficients from the polycrystalline $(Th,U)O_2$ are coincident with or lower than those from polycrystalline UO_2. The diffusion coefficient for the polycrystalline $(Th,U)O_2$ under a high oxygen potential (–160kJ/mol) turned out to be higher than that under a lower oxygen potential(–370 kJ/mol). Based on the comparison between the diffusion coefficients from the single-crystal (work previously reported in these quarterlies) and the polycrystalline UO_2, the diffusion coefficients in a single crystal of $(Th,U)O_2$ are expected to be much lower than in polycrystalline of $(Th,U)O_2$ (may be lower by two orders).

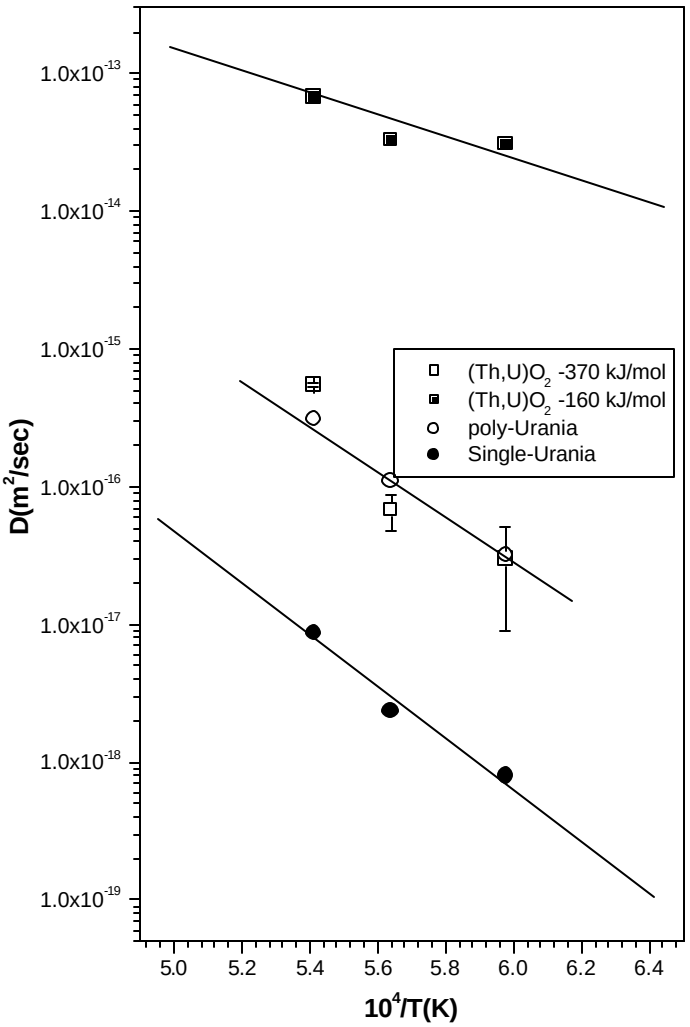

Figure 159. Plot of diffusion coefficients in $(Th,U)O_2$ and UO_2.

References

- Allison C. M., Berna G. A., and et al, "SCDAP/RELAP5/MOD3.1: Code Manual, Volume IV: MATPRO A Library of Materials Properties for Light-Water-Reactor Accident Analysis," NUREG/CR-6150, Nov. 1993.
- Anthonysamy, S., J. Kitheri, T. Gnanasekaran, and R. Vasudeva, "Studies on the kinetics of oxidation of urania-thoria solid solutions in air," *Journal of Nuclear Materials*, 280 (2000) 25-32.
- Aronson, S., Roof, R.B., Belle, J., "Kinetic study of the oxidation of uranium dioxide," *Journal of Chemical Physics*, 27 (1957) 137-144
- Asmolov V., and Yegorova L., "Investigation of the behavior of VVER fuel under RIA conditions," *Proceedings of the International Topical Meeting on LWR Fuel Performance, Portland, Oregon*, March 2-6, 1997.
- Badruzzaman A., "Economic Implications of Annular Fuel in PWRs," *Trans. Am. Nucl. Soc*., vol. 34, p 384-385, 1980.
- Bailly H., et al., "The Nuclear Fuel of Pressurized Water Reactors and Fast Reactors: Design and Behavior," Intercept Ltd., 1999.
- Bakker, K., E. H. P. Cordfunke, R. J. M. Konings, and R. P. C. Shram, "Critical evaluation of the thermal properties of ThO_2 and $Th_{1-y}U_yO_2$ and a survey of the literature data on $Th_{1-y}Pu_yO_2$," *Journal of Nuclear Materials*, Vol. 250, pp. 1-12 (1997).
- Bamford, C.H. and Tipper, C.F.H., *Chemical Kinetics v.22: Reactions in the Solid State*, Elsevier, New York (1980)
- Basek, U., A. K. Sengupta, and C. Ganguly, "Hot hardness and thermal conductivity of ThO_2-PuO_2 and ThO_2-UO_2 sintered pellets," *Journal of Material Science Letters*, v 8, n 4, April, 1989, p 449-450.
- Belle, J., and R. M. Berman, *Thorium Dioxide: Properties and Nuclear Applications*, DOE/NE-060, 1984.
- Berna G. A., Beyer C. E., Davis K. L., and Lanning D. D., "FRAPCON-3: A Computer Code for the Calculation of Steady-State, Thermal-Mechanical Behavior of Oxide Fuel Rods for High Burnup," NUREG/CR-6534, Volume 2, Dec. 1997.
- Boase, D.G., Vandergraaf, T.T., "The Canadian spent fuel storage canister: some materials aspects," *Nuclear Technology*, 32 (1977) 60-71
- Briesmeister, Judith F., editor *MCNP - A General Monte Carlo N-Particle Transport Code*, LA-12625-M, Version 4B, Los Alamos National Laboratory, Los Alamos, NM, March 1997.
- Bruno, J., Casas, I., Cera, E., de Pablo, J., Gimenez, J., and Torrero, M.E., "Uranium(IV) dioxide and SIMFUEL as chemical analogues of nuclear spent fuel matrix dissolution. A comparison of dissolution results in a standard NaCl/$NaHCO_3$ solution," *Materials Research Society Symposium Proceedings*, 353 (1995) 601-608
- Casas, I., Gimenez, J., Marti, V., Torerro, M.e., and de Pablo, J., "Kinetically controlled dissolution of UO_2(s) under oxidizing conditions. A combined dissolution-oxidation model," *Materials Research Society Symposium Proceedings*, 294 (1993) 61-66
- Casas, I., Gimenez, J., Marti, V., Torrero, M.E., and de Pablo, J., "Kinetic studies of unirradiated UO_2 dissolution under oxidizing conditions in batch and flow experiments," *Radiochimica Acta*, 66/67 (1994) 23-27
- Childs K. W., Heating 7.2b User's Manual, ORNL/(tm)-12262, February 1993.
- Clayton, J. C., *In-Pile and Out-Of-Pile Corrosion Behavior of Thoria-Urania Pellets*, WAPD-TM-1548, January, 1987

- Cox, J.D., Wagman, D.D., and Medvedev, V.A., Codata, *Key Values For Thermodynamics*, Hemisphere Publishing, New York (1989)
- Croff, Alan G. *A User's Manual for the ORIGEN2 Computer Code*, ORNL/TM-7175, Oak Ridge National Laboratory, Oak Ridge, TN 37830, July 1980.
- Cullity, B.D., *Elements of X-ray Diffraction, 2nd Edition*, Addison-Wesley Publishing Company, Inc., 1978.
- Delpech M., Huang S. L., Iwasaki T., "Performance Assessment of a PWR Based Nuclear Park Providing Complete Pu and M.A. Recycling", *Proceedings of PHYSOR 96: International Conference on the Physics of Reactors, Mito, Japan*, 16-20 Sep 1996.
- Driscoll M. J., Downar T. J., Pilat E. E., "The Linear Reactivity Model for Nuclear Fuel Management," American Nuclear Society, LaGrange Park, 1990.
- Edenius M., Ekberg K., Forssen B. H., Knott D.,"CASMO-4, A Fuel Assembly Burnup Program: User's Manual", STUDSVIK/SOA-95/1, Studsvik of America, Inc., 1995.
- Forat C., and Florentin F., "The AFA 3G Fuel Assembly: A Proven Design For High Burnups," *TOPFUEL'99*, Avignon, September 13-15, 1999.
- Forsberg K., Limback M., Massih A. R., "A Model for Uniform Zircaloy Clad Corrosion in Pressurized Water Reactors," *Nuclear Engineering and Design*, Vol 154, p 157-168, 1995.
- Forsberg C. W., Hopper C. M., and Vantine H. C., "What is Nonweapons-Usable U-233?" *Trans. Am. Nucl. Soc*., Vol. 81, p. 62, Long Beach, California, November 14-18, 1999.
- Forsyth, R.S. and Werme, L.O., "Spent fuel corrosion and dissolution," *Journal of Nuclear Materials*, 190 (1992) 3-19
- Fuketa T., Nakamura T., Sasajima H., Nagase F., and Uetsuka H., "Behavior of PWR and BWR Fuels During Reactivity-Initiated Accident Conditions," *Proceedings of International Meeting on LWR Fuel Performance, Park City, Utah*, April 10-13, 2000.
- Garcia-Delgado L., Driscoll M. J., Meyer J. E., and Todreas N. E., "Design of an Economically Optimum PWR Reload Core for a 36-Month Cycle," MIT-NFC-TR-013, 1998.
- Ghosh *et al.*, "Metallography of Plutonium, Uranium and Thorium Fuels-Two Decades of Experience in Radiometallurgy Division." Report BARC/1993/E/022, Bhabha Atomic Research Centre, 1993.
- Giovengo, J.F., Goldberg, I., Sphar, C. D., *Fission Gas Release From High Burnup ThO_2 and ThO_2-UO_2 Fuels Irradiated at Low Temperature*, WAPD-TM-1350, May, 1982
- Grenthe, I., Fuger, J., Konings, R.J.M., Lemire, R.J., Muller, A.B., Nguyen-Trung, C., and Wanner, H., *Chemical Thermodynamics, Volume 1: Chemical Thermodynamics of Uranium*, North-Holland, Amsterdam (1992)
- Groeschel F. and Hermann A., "Experiments to Understand the Corrosion Process of Fuel Rod Claddings," Annual Reprot 1996, Annex IV, PSI (Paul Scherrer Institut) Nuclear Energy and Safety Research, p 59-64, 1996.
- Gruppelaar H. and Schapira J. P., "Thorium as a Waste Management Option," Final Report EUR 19142EN, European Commission, 2000.
- Harada, Y., Y. Baskin and J. H. Handwerk, *Journal of the American Ceramic Society* Vol. 45, pp. 253-257, 1962.
- Harrar J. E., Carley, J. F., Isherwood, W. F., Raber, E., Report of the committee to review the justification of J-13 well water in Nevada nuclear waste storage investigations, Lawrence Livermore National Laboratory, UCID-21867, Livermore California (1990)

- Hastings L. J., Hunt C. E. L., Lipsett J. J., and Delaney R. D., "Short-lived Fission Product Release from UO2: Annular versus Solid Pellets," *Journal of Nuclear Materials*, Vol. 135, 1985.
- Helgeson, H. C., "Thermodynamics of hydrothermal systems at elevated temperatures and pressures," *American Journal of Science*, 267 (1969) 729-804.
- Hirai M., et al, "Grain Size Effects on Fission Gas Release and Bubble Swelling at High Burnup," *Proceedings of the International Topical Meeting on LWR fuel Performance, Park City*, April 2000.
- Howl D. A., Palmer I. D., and Topliss I., "Niobia doped fuel as PCI remedy", *Proceedings of the International Topical Meeting on Light Water Reactor Fuel Performance, West Palm Beach, Florida*, April 17-21, 1994.
- Hubert, S., Barthelet, K., Fourest, B., Lagarde, G., Dacheux, N., Baglan, N., "Influence of the precursor and the calcinations temperature on the dissolution of thorium dioxide," *Journal of Nuclear Materials*, 297 (2001) 206-213
- Jeffs, A. T., *Thermal Conductivity of ThO_2-PuO_2 Under Irradiation*, AECL-3294, April, 1969.
- Joo, H. K., et al., "An Enhancement of Economic Potential of Homogeneous Thorium Fuel for PWR by Utilizing the Mixed Core with Uranium Fuel Assembly, GLOBAL2001, 2001.
- Killeen J. C., "The Effect of Additives on the Irradiation Behavior," *Journal of Nuclear Materials*, Vol. 58, 1975.
- Killeen J. C., "Fission Gas Release and Swelling in UO_2 doped with Cr2O3," *Journal of Nuclear Materials*," Vol. 88, 1980.
- Kubo T., et al, "Fission Gas Behavior in Advanced UO_2 with Controlled Microstructures," *Proceedings of the International Topical Meeting on Light Water Reactor Fuel Performance, West Palm Beach, Florida*, April 17-21, 1994.
- Kuchibhotla, S., and A. A. Solomon, "Rheological Characterization of U,ThO_2 Slurries for Spray Drying", *Transactions of the ANS Annual Meeting at Hollywood, FL, June 9-13, 2002*.
- Kuchibhotla, S., and A. A. Solomon, ANS Student Conference held at Penn State University, April 10-14, 2002.
- Langmuir, D., *Aqueous Environmental Geochemistry*, Prentice-Hall Inc., Upper Saddle River, New Jersey (1997)
- Langmuir, D., and Herman, J.S., "The mobility of thorium in natural waters at low temperatures," *Geochim. Cosmochim. Acta*, 44 (1980) 1753-1766.
- Laughter M., Hejzlar P., Kazimi M. S., "Self-Protection Characteristics of Uranium-233 in the ThO2-UO2 PWR Fuel Cycle", Department of Nuclear Engineering, MIT-NFC-TR-045, July, 2002.
- Loeb, A. L., *Journal of the American Ceramic Society*, Vol. 37, p. 96, 1954.
- Lombardi C., Mazzola A., Padovani E. and Ricotti M. E., "Neutronic Analysis of U-Free Inert Matrix and Thoria Fuels for Plutonium Disposition In Pressurized Water Reactors**",** *Journal of Nuclear Materials*, Vol. 274, 1-2, pp. 181-188, 1999.
- Long Y., Yuan Y., Kazimi M. S., Ballinger R. G. and Pilat E. E., "A Fission Gas Release Model for High Burnup LWR ThO_2-UO_2 Fuel", *Nuclear technology*, Vol. 138, June 2002
- Mardon J. P., Garner G., Beslu P., Charquet D., Senevat J., "Update on the Development of Advanced Zirconium Alloys for PWR Fuel Rod Claddings," *Proceedings of the 1997 International Topical Meeting on LWR Fuel Performance, Portland, Oregon*, March 2-6, 1997.

- Meyer R. O., McCardell R. K., Chung H. M., Diamond D. J. and Scott H. H., "A regulatory assessment of test data for reactivity-initiated accidents," *Nuclear Safety*, Vol. 37, No. 4, p 271-288, 1996.
- Meyer, R. O., R. K. McCardell and H. Scott, "A regulatory Assessment of the Test Data for Reactivity Accidents," *Proceedings of the International Topical Meeting on LWR Fuel Performance, Portland, Oregon*, March 2-6, 1997.
- MacDonald, P. E., et al., *Advanced Proliferation Resistant, Lower Cost, Uranium-Thorium Dioxide Fuels for Light Water Reactors*, NERI Project 99-0153, Progress Report for Work through May 2002, Idaho National Engineering and Environmental Laboratory, Idaho Falls, ID, INEL/EXT-02-00924.
- MacDonald P. E., et al., "Advanced Proliferation Resistant, Lower Cost, Uranium-Thorium Dioxide Fuels for Light Water Reactors", NERI 2nd Annual Report, INEEL/EXT-01-00804, August, 2001.
- Mogensen M., Pearce J. H., Walker C. T., "Behaviour of Fission Gas in the Rim Region of High Burnup UO_2 Fuel Pellets with Particular Reference to Results From an XRF Investigation," *Journal of Nuclear Materials*, Vol. 264, 1999.
- Moore R. L., Schnitzler B. G., Wemple C. A., Babcock R. S., and Wessol D. E., "MOCUP: MCNP-ORIGEN2 Coupled Utility Program", INEL-95/0523, Idaho National Engineering Laboratory, September 1995.
- Nakamura T., Sasajima H., Fuketa T. and Ishijima K., "Fission gas induced cladding deformation of LWR fuel rods under reactivity initiated accident conditions," *Journal of Nuclear Science and Technology*, Vol. 33, No. 12, p. 924-935, 1996.
- NEA, "Nuclear Fuel Safety Criteria Technical Review," Nuclear Energy Agency, OECD Publication, 2001.
- Nogita K., Une K., Hirai M., Ito K., Ito K., and Shirai Y., "Effect of Grain Size on Recrystallization in High Burnup Fuel Pellets," *Journal of Nuclear Materials*, Vol. 248, 1997.
- Olson, G.L., McCardell, R. K. and Illum, D. B., *Fuel Summary Report: Shippingport Light Water Breeder Reactor*, INEEL/EXT-98-00799 Rev.1, January 1999
- Poeppel R. B., "An Advanced Gas Release and Swelling Subroutine," *Proc. Conf. Fast Reactor Fuel Element Technology, American Nuclear Society, 1971*.
- Pope, J. M., and K. C. Radford, *Journal of Nuclear Materials*, Vol. 52, pp. 241-254, 1974.
- Popovic, S., "Unit-cell dimension measurements from pairs of x-ray diffraction lines," *Journal of Applied Crystallography*, 6 (1973) 122-128.
- Richardson, K. D., Campbell, W. R. Clayton, J. C. and Smith, B. C., *End-of-Life Destructive Examination of Light Water Breeder Reactor Fuel Rods* (*LWBR Development Program*), WAPD-TM-1606, October 1987.
- Ruetten H.-J. et al., "Potential of Thorium-based Fuel Cycles to Constrain Plutonium and to Reduce the Long-lived Waste Toxicity", Final Report on the Coordinated Research Program, Reg. No. I3.30.08, 2000, Draft, *In Press.*
- Sapyta, J. J., T. N. Ake, and M. Saglam, *Light Water Reactor Uranium-Thorium Fuels Report, Task 1 Fuel Cycle Analysis, Third Annual Report*, Framatome ANP, May, 2002.
- Sabol G. P., Comstock R. J., Weiner R. A., Larouere P., and Stanutz R. N., "In-reactor Corrosion Performance of ZIRLO and Zircaloy-4," ASTM Special Technical Publication *Proceedings of the 10th International Symposium on Zirconium in the Nuclear Industry*, n1245, 1994.

- Schmitz F. and Papin J.., "High Burnup Effects on Fuel Behaviour Under Accident Conditions: the Tests CABRI REP-Na," *Journal of Nuclear Materials*, vol. 270, p 55-64, 1999.
- Seibold A., Garzarolli F., and Manzel R., "Material Development for Simens Fuel Elements," *Proceedings of the International Topical Meeting on LWR fuel Performance, Park City*, April 2000.
- Shoesmith, D. W., "Fuel corrosion processes under waste disposal conditions," *Journal of Nuclear Materials*, 282 (2000) 1-31.
- Siefken, L. J., E. W. Coryell, E. A. Harvego, and J. K. Hohorst, *SCDAP/RELAP5/MOD3.3 Code Manual: Modeling of Reactor Core and Vessel Behavior During Severe Accidents*, NUREG/CR-6150, Vol. 2, Rev. 2, INEL-96/0422, January 2001.
- Siefken, L. J., E. W. Coryell, E. A. Harvego, and J. K. Hohorst, *SCDAP/RELAP5/MOD3.3 Code Manual: MATPRO – A Library of Material Properties for Light-Water Reactor Accident Analysis*, NUREG/CR-6150, Vol. 4, Rev. 2, INEL-96/0422, January 2001.
- Solomon, A. A., S. M. McDeavitt, V. Chandramouli, S. Anthonysamy, S. Kuchibhotla, T. J. Downar, "Thoria-Based Cermet Nuclear Fuel: Sintered Microsphere Fabrication by Spray Drying", *Proceedings of ICONE10: 10th International Conference on Nuclear Engineering, Arlington, VA, April 14-18, 2002*
- Spino J., "State of the Technology Review," Advances in Fuel Pellet Technology for Improved Performance at High Burnup, IAEA-TECDOC-1036, Proceedings of a Technical Committee Meeting, Tokyo, Japan, Oct. 28 – Nov. 1, 1996.
- Sunder, S. and Miller, N.H. "XPS and XRD studies of $(Th,U)O_2$ fuel corrosion in water," *Journal of Nuclear Materials*, 279 (2000) 118-126.
- Une K., Nogita K., Suzawa Y., Hayashi K., Ito K., and Etoh Y., "Effects of Grain Size and PCI Restraint on the Rim Structure Formation of UO_2 Fuels," *Proceedings of the International Topical Meeting on LWR fuel Performance, Park City*, April 2000.
- Vyazovkin, S. and C.A. Wight, "Model-free and model-fitting approaches to kinetic analysis of isothermal and nonisothermal data," *Thermochimica Acta*, 340-341 (1999) 53-68.
- Waeckel N., Bernaudat C. and Salles B., "EDF Proposed Safety Domain for Rod Ejection Accidents in a PWR," *Proceedings of International Meeting on LWR Fuel Performance, Park City, Utah*, April 10-13, 2000.
- Westinghouse, Commercial Nuclear Fuel Division, "ZIRLO™ Cladding: Meeting the Demanding Nuclear Fuel Performance Challengs of the 90's," Pittsburgh, PA, 1991.
- Willse J. T., Garner G. L., "Recent Results From the Fuel Performance Improvement Program at Framatome Cogema Fuels," *Proceedings of the International Topical Meeting on LWR fuel Performance, Park City*, April 2000.
- Xu Z., Hejzlar P., Driscoll M. J., and Kazimi M. S., "An Improved MCNP-ORIGEN Depletion Program (MCODE) and Its Verification for High burnup Applications," *Proceedings of PHYSOR 2002, Seoul, Korea*, October 7-10, 2002a.
- Xu Z., Driscoll M. J., Kazimi M. S., "Neutron Spectrum Effects on Burnup, Reactivity, and Isotopics in UO2-H2O Lattices", *Nuclear Science and Engineering*, Vol. 141, pp. 175-189, 2002b.
- Zhao X., Pilat E. E., Weaver K. D., Hejzlar P., "A PWR Thorium Pin Cell Burnup Benchmark", *Proceedings of PHYSOR 2000*, Pittsburgh, May 2000.
- Zhao X., Driscoll M. J. and Kazimi M. S., "Micro-Heterogeneous Thorium Based Fuel Concepts for Pressurized Water Reactors", MIT-NFC-TR-031, MIT, Dept. of Nuclear Eng., August 2001.

Cost-Performance

Argonne National Laboratory (ANL)

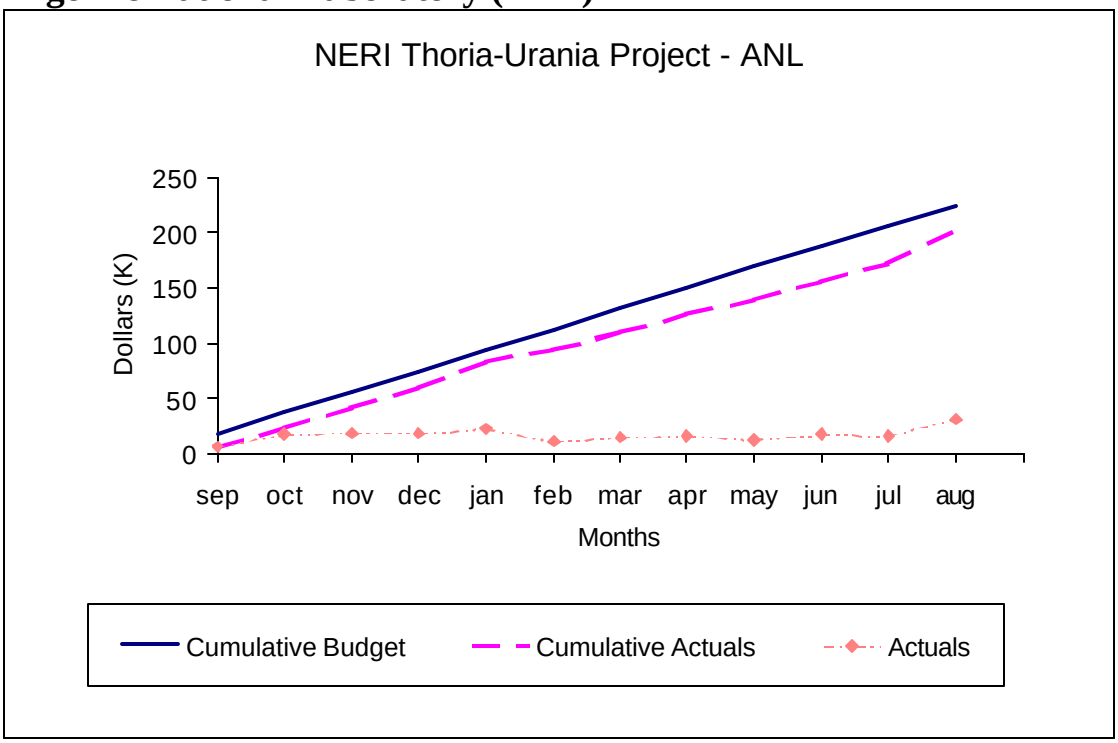

Framatome Technologies

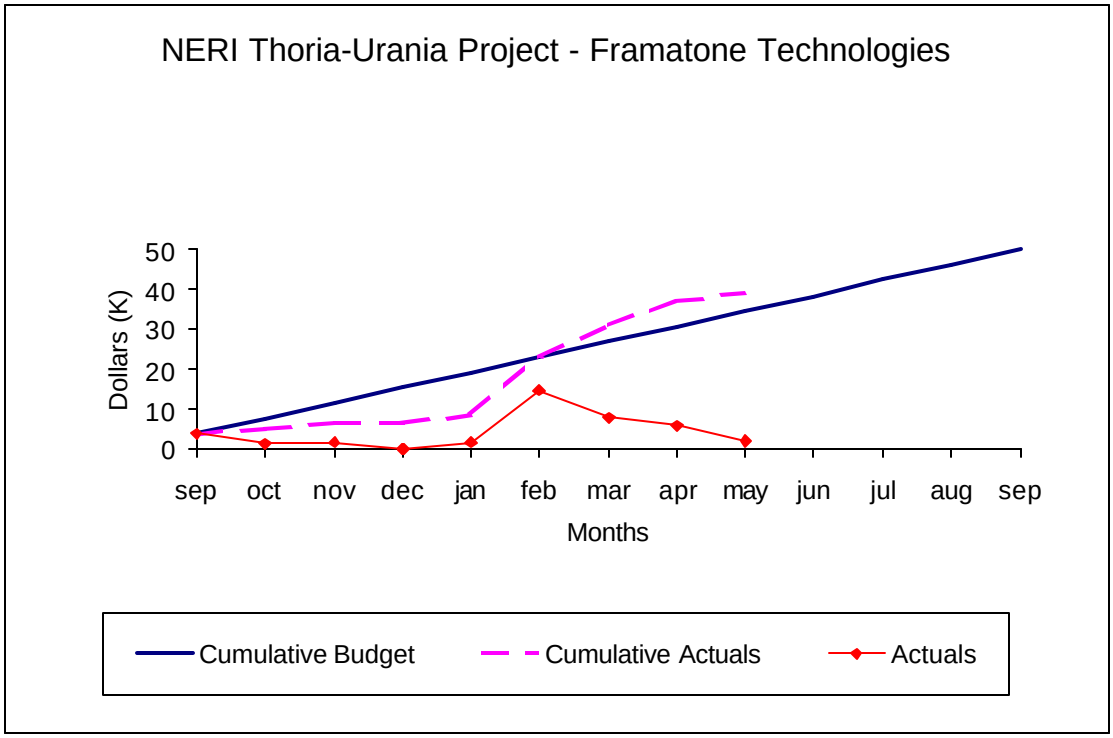

INEEL

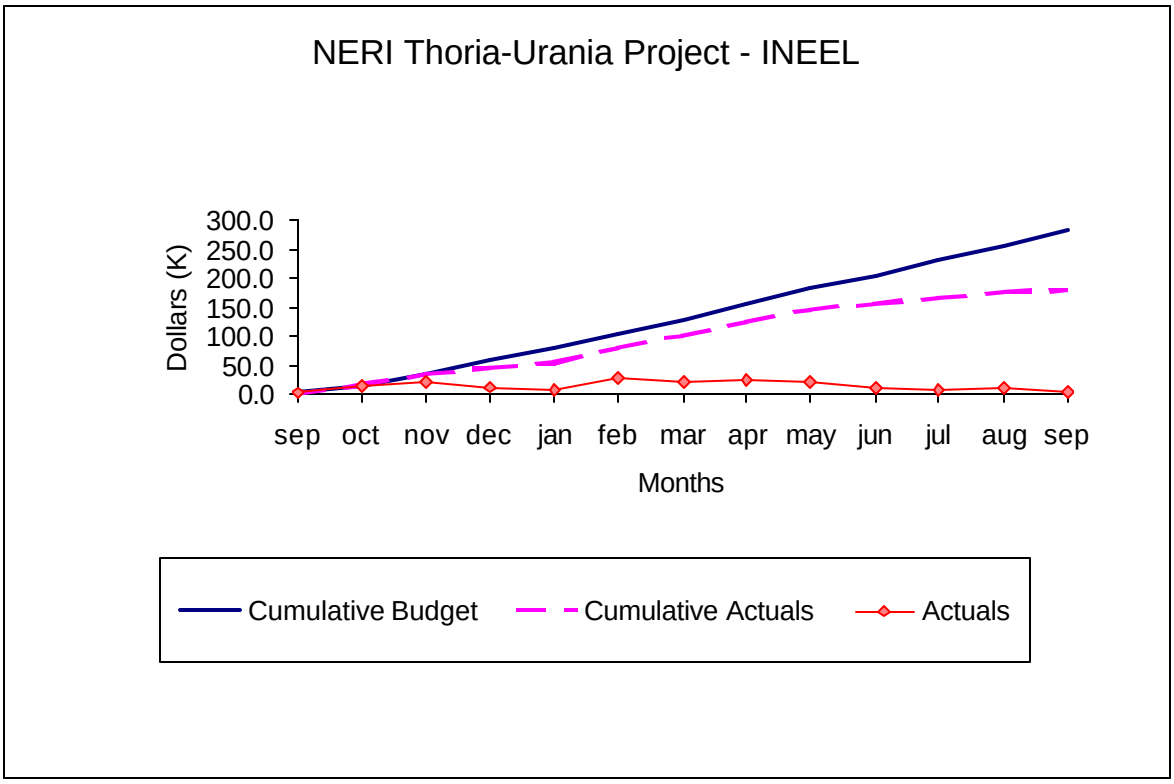
NERI Thoria-Urania Project - INEEL
Dollars (K)
300.0
250.0
200.0
150.0
100.0
50.0
0.0
sep oct nov dec jan feb mar apr may jun jul aug sep
Months
Cumulative Budget
Cumulative Actuals
Actuals

MIT

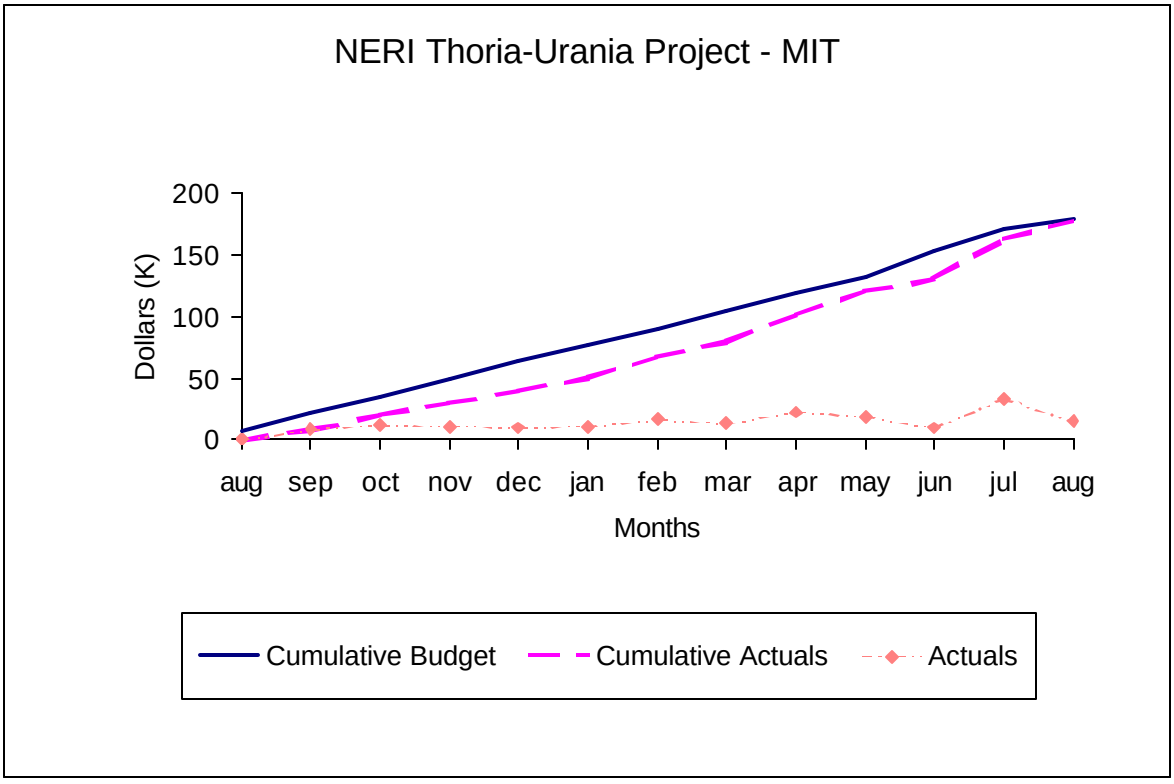
NERI Thoria-Urania Project - MIT
Dollars (K)
200
150
100
50
0
aug sep oct nov dec jan feb mar apr may jun jul aug
Months
Cumulative Budget
Cumulative Actuals
Actuals

University of Florida

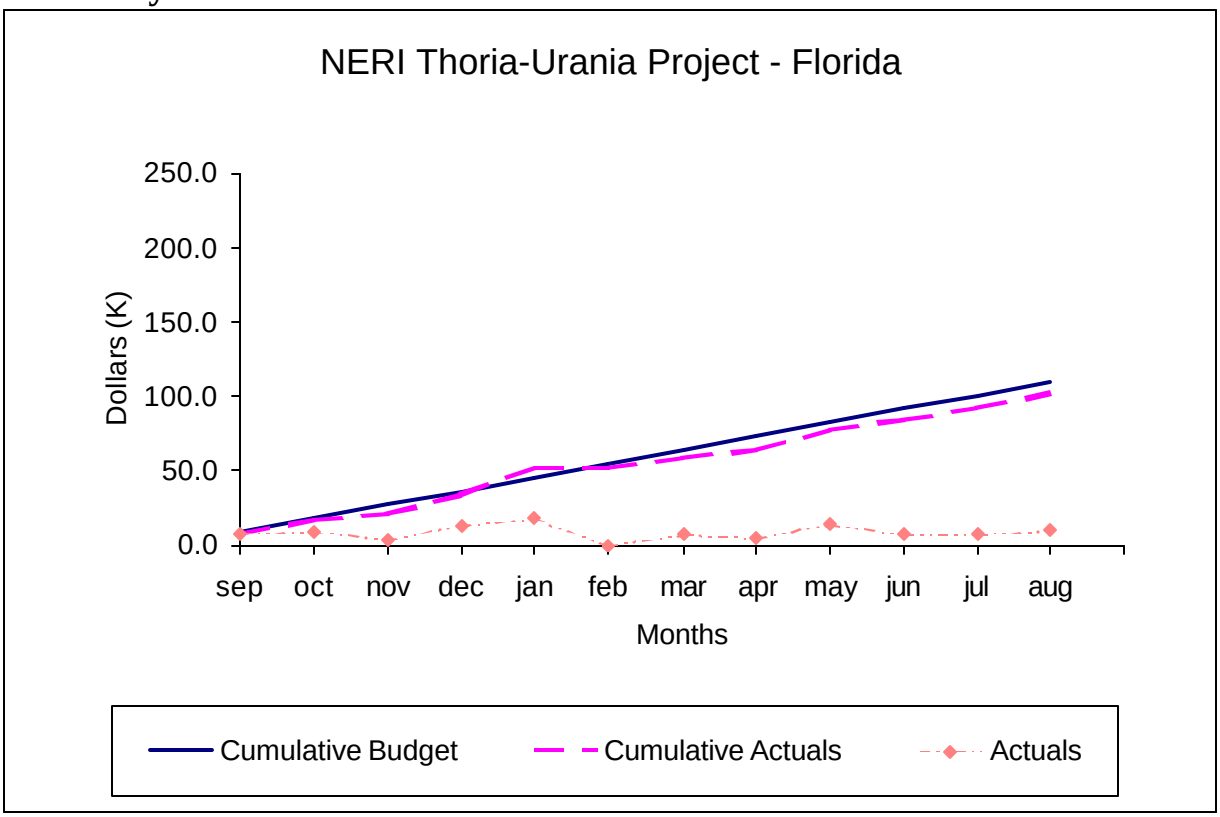

INEEL/EXT-02-01411

Advanced Proliferation Resistant, Lower Cost, Uranium-Thorium Dioxide Fuels for Light Water Reactors

Nuclear Energy Research Initiative
Project 99-0153

Progress Report for Work through September, 2002

12th Quarterly Report and 3rd Annual Report

Principal Investigator:

Philip E. MacDonald